Mapping the Magellanic Clouds using giant stars: Metallicities and substructures

Abinaya Ondivillu Omkumar

Universitätsdissertation
zur Erlangung des akademischen Grades

doctor rerum naturalium
(Dr. rer. nat.)

in der Wissenschaftsdisziplin
Astrophysik

eingereicht an der
Mathematisch-Naturwissenschaftlichen Fakultät
Institut für Physik und Astronomie
der Universität Potsdam
und
das Leibniz-Institut für Astrophysik Potsdam (AIP)

Datum der Disputation:

Betreuer

Prof. Dr. Maria-Rosa L. Cioni &
Leibniz Institute für Astrophysik Potsdam (AIP)

Dr. Smitha Subramanian
Indian Institute of Astrophysics (IIA)
Leibniz Institute für Astrophysik Potsdam (AIP)

Gutachter

Prof. Dr. Maria-Rosa L. Cioni
Leibniz Institute für Astrophysik Potsdam (AIP)

Prof. Dr. Dr. Stephan Geier
Universität Potsdam

Dr. Dorota Skowron
University of Warsaw

To my beloved grandmother, Indira,
I miss you deeply.

Abstract

In the framework of the Λ cold dark matter (ΛCDM) model, galaxies grow hierarchically through mergers that leave behind extended stellar haloes with stellar debris, whose properties encode their interaction history. Understanding galaxy evolution, therefore, requires investigating the consequences of such past dynamical interactions that have influenced the morphological and structural properties of galaxies over time. The Large and the Small Magellanic Clouds (LMC and SMC) or 'the Clouds,' our nearest pair of interacting dwarf galaxies located ~50 and 60 kpc from the Milky Way, reveal these processes through their tidal substructures spanning diverse stellar populations. This makes them an ideal laboratory for studying dwarf-dwarf and host-satellite interactions. This thesis explores how the past interactions of the Clouds with each other and with their host, the Milky Way, have imprinted these events across their stellar populations, from outermost substructures to crowded central regions. A comprehensive investigation of the metallicity of these stellar substructures is essential for understanding their origin and evolution. Although spectroscopic metallicities exist for a few thousand stars from various instruments, deriving consistent photometric distributions for populations that encompass the full spatial extent of the Clouds, including debris-rich outskirts, provides deeper insights into the interactions driving their evolution.

To trace these large-scale chemical patterns of the Clouds, Chapter 2 presents photometric metallicity maps for ~90 000 young (supergiant) stars and ~270 000 old (red giant branch; RGB) stars located within ~11 degrees of the SMC and ~20 degrees of the LMC. These maps are derived from a homogeneous dataset obtained from *Gaia* Data Release 3. Synthetic Strömgren magnitudes were computed using the XP spectra of these stars, by employing the GaiaXPy tool, while adopting calibration relations suitable for young and old stars from the literature to estimate the photometric metallicities. This extensive dataset enabled the application of piecewise-regression fitting to derive the metallicity gradients within different radial regions. The overall metallicity gradients, traced by both young and old stars, exhibit a decrease in metallicity from the centre to the galactic outskirts of both galaxies. Moreover, multiple breakpoints in the radial metallicity gradient are evident, indicating different radial regions following different and sometimes opposite trends. These radial slopes are interpreted as signatures of their interactions, their star formation history, and the chemical evolution of the Clouds.

Building on these maps, Chapter 3 of this thesis presents the analysis of the photometric metallicities derived in Chapter 2 for the LMC and SMC substructures, traced by young and old stellar populations. The study compares the metallicities of these substructures with those of the main body and the metallicity gradients across different quadrants, along with their metallicity distribution functions and kinematic properties relative to the Clouds, to shed light on their potential origins using a homogeneous dataset and metallicity estimates. The analysis, while confirming several of the previous trends, shows that the observed breaks in the metallicity gradient of the LMC and the SMC are

likely due to the mutual interactions between the LMC, SMC, and the Milky Way, which have created the peripheral stellar substructures.

Finally, Chapters 4 and 5 of this thesis focus on the crowded galactic centres, regions rendered observationally challenging by high densities of gas, dust, and stars. Studying these gravitationally-bound regions is crucial to understand how the dynamical interactions between dwarf galaxies, such as the Clouds and their interactions with their host, have shaped their crowded galactic centres. Chapter 4 presents the VMCDeep dataset, targeting the central 1.77 deg^2 of both clouds. I performed point-spread-function (PSF) photometry on individual epoch images and deep-tile images, then generated a band-merged catalogue for this crowded field of the Clouds. This chapter also demonstrates the potential of this dataset to probe the centres of the Clouds. A comparison with the VISTA survey of the Magellanic Clouds system (VMC) dataset shows that the newly obtained VMCDeep dataset has a more homogeneous spatial coverage of the same regions.

Chapter 5 of the thesis investigates the presence of distance bimodality of the Red Clump (RC) identified earlier in the outskirts from ~2 to 2.5 deg in the eastern regions of the SMC, towards the direction of the Magellanic Bridge and the LMC. The aim is to probe this bimodality observed in the luminosity distribution of the RC stars, to see whether they are present at the centre of the SMC. Using VMCDeep PSF catalogues, RGB contamination is modelled, and Gaussian fits are applied to RC luminosity distributions across central segments. This reveals, for the first time, clear signatures of bimodal RC populations in the innermost regions. Unlike most previous studies reporting single or heavily overlapping Gaussians with no significant peak separation, the dual Gaussian fits obtained with the VMCDeep dataset show statistically significant improvement across all central segments, indicating a bimodality in the SMC centre. Altogether, the thesis findings demonstrate that the structural and chemical complexity of the Clouds, from outskirts to their cores, arises directly from their long history of mutual encounters and Milky Way interactions.

Zusammenfassung

Das kosmologische ΛCDM (engl. cold dark matter; kalte dunkle Materie) Modell sagt voraus, dass Galaxien hierarchisch durch Verschmelzungen mit kleineren Galaxien wachsen, wodurch ausgedehnte Sternhalos mit den Überresten der einverleibten Galaxie entstehen. Die Eigenschaften dieser Galaxientrümmer spiegeln dabei die Wechselwirkungsgeschichte wider. Um die Entwicklung von Galaxien zu verstehen, müssen daher die Folgen solcher vergangenen dynamischen Wechselwirkungen untersucht werden, welche die morphologischen und strukturellen Eigenschaften der Galaxien im Laufe der Zeit beeinflusst haben. Die Große und die Kleine Magellansche Wolke (engl. Large and Small Magellanic Clouds; LMC/SMC) oder „die Wolken", befinden sich in einer Entfernung von etwa 50 bzw. 60 kpc von der Milchstraße und stellen unser nächstgelegenes Paar interagierender Zwerggalaxien dar. Ihre Gezeitenstrukturen, welche sich über verschiedene Sternpopulationen erstrecken, zeugen von ihrer vergangen Wechselwirkungsgeschichte. Dies macht sie zu einem idealen Labor für die Untersuchung von Wechselwirkungen zwischen zwei Zwerggalaxien einerseits und zwischen einer Haupt- und ihren Satellitengalaxien andererseits. Diese Arbeit untersucht, wie sich die vergangenen Wechselwirkungen der Wolken untereinander und mit ihrer Hauptgalaxie, der Milchstraße, auf ihre Sternpopulationen, von den äußersten Substrukturen bis hin zu den zentralen Regionen mit hoher Sternendichte, ausgewirkt haben. Dabei ist eine umfassende Untersuchung der Metallizität dieser stellaren Substrukturen für das Verständnis ihres Ursprungs und ihrer Entwicklung unerlässlich. Jedoch lieferten Daten von verschiedenen Instrumenten bisher nur für wenige tausend Sterne spektroskopische Messungen ihrer Metallizitäten. Daher stellt eine konsistente photometrische Bestimmung der Metallizitäten verschiedener Sternpopulationen, welche die gesamte räumliche Ausdehnung der Wolken umfassen, einschließlich der strukturreichen Randbereiche, ein wichtiges Werkzeug dar, um tiefere Einblicke in die Wechselwirkungen und die Entwicklung der Galaxien zu erlangen.

Um diese großräumigen chemischen Muster der Wolken nachzuzeichnen, werden in Kapitel 2 Karten der photometrisch bestimmten Metallizitäten für etwa 90.000 junge (Überriesen-) Sterne und etwa 270.000 alte (Rote-Riesen-Ast; engl. red-giant branch, RGB-) Sterne vorgestellt, welche sich in einem Umkreis von etwa 11 Grad um die SMC und etwa 20 Grad um die LMC befinden. Diese Karten wurden aus einem homogenen Datensatz abgeleitet, welcher aus der 3. Gaia Datenveröffentlichung stammt. Synthetische Strömgren-Magnituden wurden unter Verwendung der XP-Spektren dieser Sterne mit der Software GaiaXPy berechnet, wobei zur Abschätzung der photometrischen Metallizitäten aus der Literatur geeignete Kalibrierungsbeziehungen für junge und alte Sterne herangezogen wurden. Dieser umfangreiche Datensatz ermöglichte die Anwendung einer stückweisen Regressionsanpassung, um die Metallizitätsgradienten in verschiedenen radialen Regionen abzuleiten. Die generellen Gradienten der Metallizitäten, von jungen als auch von alten Sternen, zeigen in beiden Galaxien eine Abnahme der Metallizität vom Zentrum bis zu den galaktischen Randgebieten. Darüber hinaus sind mehrere Knickpunk-

te erkennbar, was darauf hindeutet, dass verschiedene radiale Regionen unterschiedlichen und manchmal entgegengesetzten Trends folgen. Diese radialen Gefälle werden als Folge der Wechselwirkungen, der Sternentstehungsgeschichte und der chemische Entwicklung der Wolken interpretiert.

Aufbauend auf diesen Karten präsentiert Kapitel 3 dieser Arbeit die Analyse der in Kapitel 2 abgeleiteten photometrischen Metallizitäten für die Substrukturen der LMC und der SMC, welche durch junge und alte Sternpopulationen nachgezeichnet werden. Die Studie vergleicht sowohl die Metallizitäten dieser Substrukturen mit denen des Zentralbereichs als auch die Metallizitätsgradienten über verschiedene Quadranten hinweg. Darüberhinaus werden die Verteilungsfunktionen der Metallizitäten und ihre kinematischen Eigenschaften im Verhältnis zu den Wolken untersucht, um mit Hilfe der homogenen Metallizitätsschätzungen Aufschluss über die möglichen Ursprünge dieser Substrukturen zu geben. Die Analyse bestätigt zwar mehrere der bisherigen Trends, zeigt jedoch, dass die beobachteten Knickpunkte im Metallizitätsgradienten der LMC und der SMC wahrscheinlich auf die gegenseitigen Wechselwirkungen zwischen der LMC, der SMC und der Milchstraße zurückzuführen sind, welche die Substrukturen in den Peripherien der Galaxien erzeugt haben.

Schließlich konzentrieren sich die Kapitel 4 und 5 dieser Arbeit auf die galaktischen Zentren mit hoher Sterndichte– Regionen, deren Beobachtung aufgrund der hohen Dichte an Gas, Staub und Sternen eine Herausforderung darstellt. Die Untersuchung dieser gravitativ gebundenen Regionen ist entscheidend für das Verständnis, wie die dynamischen Wechselwirkungen zwischen Zwerggalaxien, wie den Wolken, und den Wechselwirkungen mit ihrer Hauptgalaxie die galaktischen Zentren geprägt haben. Kapitel 4 stellt den VMCDeep-Datensatz vor, welcher die zentralen $1{,}77^2$ Grad beider Wolken abbildet. Ich führte eine Point-Spread-Funktion (PSF) Photometrie an den Einzelbildern und an den kombinierten Deep-Tile Bildern durch und erstellte anschließend einen finalen Katalog mit den Helligkeiten der Sterne in verschiedenen Filtern für diese dichten Sternenfelder der Wolken. Dieses Kapitel demonstriert zudem das Potenzial dieses Datensatzes zur Untersuchung der Zentren der Wolken. Ein Vergleich mit dem Datensatz der VISTA-Durchmusterung des Magellanschen Wolkensystems (VMC) zeigt, dass der neu gewonnene VMCDeep-Datensatz eine homogenere räumliche Abdeckung derselben Regionen aufweist.

Kapitel 5 der Dissertation untersucht das Vorhandensein einer Entfernungs-Bimodalität der Rote-Klumpen (engl. red clump; RC) Sterne, welche zuvor in den Randbereichen von etwa 2 bis 2,5 Grad in den östlichen Regionen der SMC in Richtung der Magellanschen Brücke und der LMC festgestellt wurde. Ziel ist es, diese in der Leuchtkraftverteilung der RC-Sterne beobachtete Bimodalität zu untersuchen, um festzustellen, ob sie auch im Zentrum der SMC vorhanden ist. Unter Verwendung der PSF-Kataloge der VMCDeep Beobachtungen wird zunächst der Einfluss der RGB-Sterne auf die Verteilung der RC-Sterne modelliert, und es werden die Leuchtkraftverteilungen der RC-Sterne über die zentrale Bereiche der Galaxie hinweg mit Hilfe von Gaußfunktionen angepasst. Dies zeigt zum ersten Mal eindeutige Anzeichen für bimodale RC-Populationen in den innersten Regionen. Im Gegensatz zu den meisten früheren Studien, welche einzelne oder stark überlappende Gaußverteilungen ohne signifikante Peak-Trennung berichteten, zeigen die mit dem VMCDeep-Datensatz erhaltenen dualen Gaußfunktionen eine statistisch signi kante Verbesserung über alle zentralen Teilbereiche hinweg, was auf eine Bimodalität im Zentrum der SMC hindeutet. Insgesamt belegen die Ergebnisse der Dissertation, dass die strukturelle und chemische Komplexität der Wolken, von den Randgebieten bis zu ihren Kernen, direkt aus ihrer langen Geschichte gegenseitiger Zusammentreffen und Wechselwirkungen mit der Milchstraße resultiert.

Contents

Abstract **v**

Zusammenfassung **vii**

Contents **xi**

1 Introduction **1**

1.1 Galaxies and their types 1
1.2 Evolution of galaxies 3
1.3 Dwarf galaxies and its importance 4
1.4 The Clouds 6
  1.4.1 The Magellanic System 7
  1.4.2 Stellar sub-structures of the Clouds 10
  1.4.3 Periphery of the Clouds 12
  1.4.4 Kinematics with *Gaia* 14
  1.4.5 Metallicities 15
  1.4.6 Photometric metallicities: Synthetic Strömgren photometry . . . 17
  1.4.7 Central region of the Clouds 18
1.5 Overview of the thesis 19

2 Strömgren photometric metallicity map of the Magellanic Cloud stars using Gaia DR3–XP spectra **21**

2.1 Introduction 21
2.2 Data 24
  2.2.1 Gaia DR3–XP spectra for SMC sources 24
  2.2.2 Gaia DR3–XP spectra for LMC sources 26
2.3 Synthetic Strömgren photometry using *Gaia* DR3–XP spectra 26
2.4 Estimation of photometric [Fe/H] 27
  2.4.1 Calibration relation for RGB stars 27
  2.4.2 Calibration relation for supergiant stars 29
2.5 Results 30
  2.5.1 Metallicity distributions 30
  2.5.2 Photometric metallicity recalibration 31
  2.5.3 Radial recalibration 32
  2.5.4 Metallicity maps of the RGB and supergiant stars 33
  2.5.5 Metallicity gradient of RGB stars 35
  2.5.6 Metallicity gradient of supergiants stars 39
  2.5.7 Metallicity catalogue 39
2.6 Discussion and conclusions 42
  2.6.1 SMC gradient 42

2.6.2 LMC gradient 43
2.6.3 Concluding remarks 45
2.A Metallicity recalibration using APOGEE 47
2.B Estimation of peak difference based on radius 48
2.C Voronoi binning 49
2.D Radial [Fe/H] gradient of the SMC and LMC sources in degrees 50

3 Investigating the origin of periphery stellar substructures of the Clouds using photometric metallicities 55
3.1 Introduction 55
3.2 Data 58
3.2.1 Photometric [Fe/H] catalogues 58
3.2.2 Substructure source selection 59
3.3 Results 59
3.3.1 Old stellar populations in the LMC substructures 59
3.3.2 Young stellar populations in the LMC substructures 62
3.3.3 Old stellar populations in the SMC substructures 62
3.3.4 Young stellar populations in the SMC substructures 64
3.3.5 Dual RGB population in the SMC 65
3.4 Comparison of various substructures 66
3.4.1 Metallicity distribution Functions 66
3.4.2 Comparison with the LMC and SMC gradients 69
3.4.3 Kinematics of substructures 70
3.5 Discussions 72
3.6 Summary 76
3.A Metallicity gradient without substructures 77
3.B Metallicity gradients in different quadrants 77
3.C Metallicity distributions 78
3.D Tabular summary 80

4 Deep VISTA observations of the Magellanic Clouds (VMCDeep) 83
4.1 Introduction 83
4.2 Observations 85
4.3 Data processing 87
4.3.1 CASU reduction 87
4.3.2 WFAU reduction 88
4.3.3 PSF photometry 89
4.4 Differences with respect to VMC 90
4.5 Content of the catalogue 91
4.5.1 Confusion 94
4.5.2 Data availability 94
4.6 Applications of the catalogue 96
4.6.1 Stellar kinematics 96
4.6.2 Variable stars 96
4.6.3 Star formation 97

4.6.4 Star formation history 99
4.6.5 Red clump substructure 100
4.7 Conclusions 101
4.A Additional (low-quality) observations 102
4.B VMCDeep: PSF photometry 102
4.B.1 Homogenised deep tile creation 103
4.B.2 PSF using DAOPHOT 104
4.C Photometric shifts 104
4.D Separate luminosity functions 107
4.E Maps from the VMC survey 107
4.F Confusion in the VMC survey 109
4.G Tile images 109

5 Probing the bimodality of Red Clump stars in the centre of the Small Magellanic Cloud 113
5.1 Introduction 113
5.2 Observations and data reduction 115
5.2.1 VMCDeep survey 115
5.2.2 Data reduction 116
5.3 Analysis of VMC deep data 117
5.3.1 Extinction correction 118
5.3.2 Selection of probable SMC members 118
5.3.3 Selection of RC stars 119
5.3.4 Presence of RGB stars 122
5.3.5 Exploring the effect of RGB contamination 125
5.4 Results and discussions 128
5.4.1 Presence of distance bimodality? 128
5.5 Summary 131
5.A CMD and Gaia selection 132
5.B Residual RC distribution 132

6 Conclusions and future prospects 137
6.1 Conclusions 137
6.2 Future prospects 139

Bibliography 141

Publications 157

Statement of own contribution 159

Acknowledgements 161

1

Introduction

1.1 Galaxies and their types

Galaxies are gravitationally bound systems comprising of stars, interstellar gas, dust, and a substantial amount of dark matter, exhibiting a broad diversity of masses, sizes, and morphologies. These systems consist of multiple structural components, including bars, bulges, discs, spiral arms, and haloes composed of both baryonic and dark matter, each displaying distinct structural, kinematical, and chemical properties. At first, this diversity fascinates us the most, but also hints at the complex nature of these objects, which necessitates a classification scheme to get a better picture. Among their most striking observational features is morphology, which varies greatly in both shape and size.

One of the earliest and still widely used classification schemes is the Hubble sequence, or the so-called “tuning fork diagram", named after its distinctive shape. Around a century ago, Edwin Hubble published his landmark paper titled “*Extra-galactic Nebulae*" (Hubble 1926), a statistical study of 400 extra-galactic nebulae in which he classified them into regulars (ellipticals and spirals) and irregulars based on photographic images. Traditionally, the galaxies were classified based on visual inspection of their morphologies. An adaptation of this sequence, first represented in Hubble (1936), is shown in Figure 1.1. Although the basic classification scheme has since been refined, most notably by de Vaucouleurs (1959); Sandage (1975); van den Bergh (1976) and many more, it remains fundamental in extragalactic astronomy. The main morphological types include early-type or elliptical galaxies (E0–E7, with 0 to 7 denoting increasing ellipticity), lenticulars (S0), late-type or spiral and disc galaxies (Sa–Sd), and irregulars (Irr). The morphological classification of galaxies provides information about the orbital motions of stars in galaxies, and correlates with star formation history and other physical properties. Importantly, many intrinsic properties such as luminosity, colour, and gas content vary systematically along it.

Elliptical and lenticular galaxies are typically gas-poor, dominated by old stellar populations, and exhibit smooth light distributions, whereas spiral galaxies display ongoing star formation and prominent blue discs (Strateva et al. 2001). Lenticulars (S0) are characterised by a central spheroidal bulge surrounded by a smooth, fainter disc lacking visible spiral arms, and consist mainly of old stellar populations. The S0 class was introduced as an intermediate type between ellipticals and spirals, indicate a progression from the most elliptical-like to the most disc-like forms. Spiral galaxies, represented on both prongs of the tuning fork diagram, share a disc-like structure with well-defined arms extending from a central, spheroidal bulge. The upper prong comprises normal spirals, characterised by a central bulge with increasingly open spiral arms from Sa to Sc. The lower prong shows barred spirals (SB), which represent similar characteristic features, and additionally includes a central bar linking the bulge and spiral arms.

Galaxies that do not fit these categories are classified as irregulars (Irr). These systems

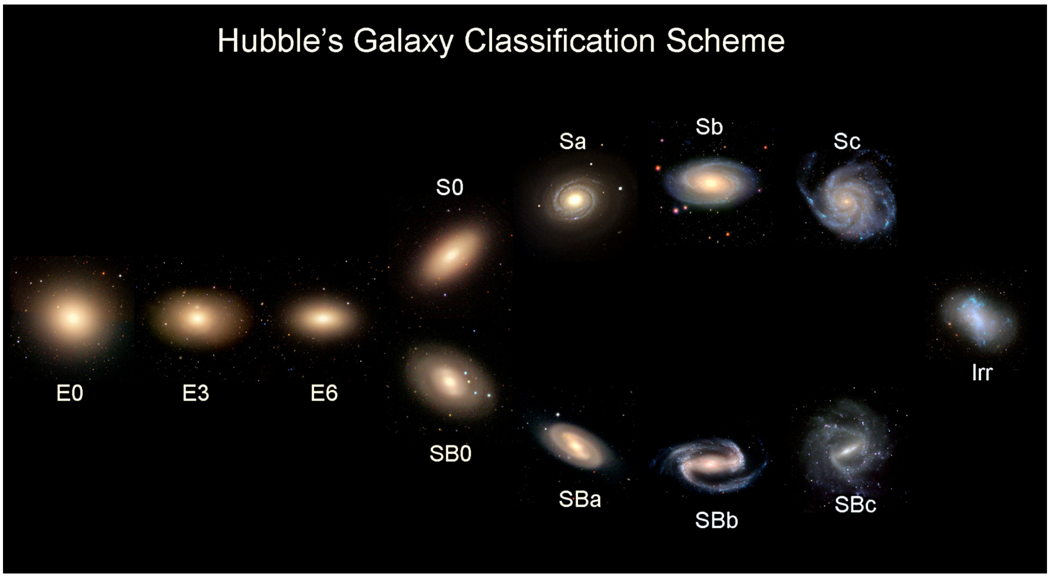

Figure 1.1: Figure illustrates the Hubble classification of galaxies, widely referred to as the Hubble tuning fork diagram, categorizes galaxies into several primary types based on their morphological characteristics. *Image Credit: ESO*

lack regular defining structures and often appear highly asymmetric. They are often low-mass, intensely star-forming, and exhibit patchy morphologies. Later, it was further divided into Type I and Type II. Type I irregulars are low-mass or dwarf-like spirals (de Vaucouleurs 1959), while Type II irregulars are even more chaotic.

A summary of many different nomenclatures for galaxy classifications is provided in Table 1 of Masters (2025). The advent of digital imaging introduced significant challenges for traditional visual classification methods, as we continue to obtain an enormous amount of data, as we are in the "Big data era" of astronomy, and manual inspection of images from large-scale surveys became increasingly impractical. Consequently, many astronomers have adopted more automated approaches, including the application of machine learning techniques (Masters 2025).

Deeper surveys revealed diverse low-surface-brightness features around most galaxies, including our home galaxy, the Milky Way (MW) (Figure 1.2). Among these are dwarf galaxies, the faintest and most numerous systems in the Universe, which serve as low-mass, less luminous counterparts to massive galaxies. There are several subclasses of dwarf galaxies, including dwarf ellipticals, dwarf spheroidals, and dwarf irregulars (Grebel 1997; McConnachie 2012). *dwarf ellipticals* exhibit elliptical morphologies but are smaller and typically bluer than their massive counterparts. Dwarf galaxies lacking gas and young stars appear diffuse and are termed *dwarf spheroidals*. In contrast, those with substantial gas reservoirs and active star formation display irregular structures and are classified as *dwarf irregulars*. Although dwarf galaxies were historically outliers in morphological classification schemes, modern surveys encompassing millions of galaxies have identified thousands of these systems (Koda et al. 2015), leading to several other sub-classes, such as Ultra-faint dwarf galaxies and tidal dwarf galaxies (Tillaboev et al. 2025), and offering profound insights into the field of galaxy evolution.

1.2 Evolution of galaxies

Galaxies exhibit a remarkable diversity in terms of type, size, and physical properties, reflecting the complexity of their formation and evolution. Scaling relations such as the Tully–Fisher relation (Tully & Fisher 1977), which correlates luminosity to maximum rotation velocity in disc galaxies, reveal underlying regularities in their assembly. Consequently, galaxies thus serve as natural laboratories for investigating these fundamental processes. Understanding the physical mechanisms that govern their formation and evolution remains one of the foremost open challenges in extragalactic astrophysics.

The Λ cold dark matter (ΛCDM) model suggests that structure in the Universe assembles hierarchically through a bottom-up scenario, in which larger dark matter haloes grow via successive mergers of smaller progenitors (Fall & Efstathiou 1980; Blumenthal et al. 1984; van den Bosch 2002; Agertz et al. 2011). The ΛCDM paradigm further predicts that most galaxies, including dwarf galaxies, host extended, metal-poor stellar haloes built from the tidal debris of past merging events (Bullock et al. 2001; Bullock & Johnston 2005; Cooper et al. 2010). Thus, it offers a concrete fossil record of their assembly histories that can, in principle, be studied in the present-day local Universe.

A key driver of galaxy evolution within this framework is the process of mergers and interactions, such as tidal, ram-pressure stripping, and strangulation (Eneev et al. 1973; Gunn & Gott 1972; Larson et al. 1980). Such environmental processes play a significant role in shaping the evolution of satellite galaxies, alongside internal secular evolution processes driven by bar instabilities, spiral structures, dark matter haloes and so on (Kormendy & Kennicutt 2004). Ram-pressure stripping removes a galaxy's interstellar gas through force exerted by the hot intracluster medium, sufficiently strong to overcome the gravity of the galaxy, quenching star formation and leaving behind a large tail of gas trailing (Gunn & Gott 1972; Abadi et al. 1999; McCarthy et al. 2008). Tidal interactions, on the other hand, distort morphologies by stripping and redistributing stars and gas through gravitational forces (Toomre & Toomre 1972; Eneev et al. 1973; Moore et al. 1996). Strangulation occurs more gradually, when the pressure from the intracluster medium strips off the halo gas, causing a slow decline in star formation activity and the galaxy eventually becomes red (Larson et al. 1980; Bekki et al. 2002).

Galaxy interactions can be broadly classified into mergers or fly-bys. They can be further sub-divided by the mass ratio of the two interacting systems into minor (stellar mass ratio <1:4) and major (stellar mass ratio >1:4) events. Major mergers can significantly distort galaxy morphology through tidal forces, induce radial gas inflows, and disrupt stellar rotation (Lynden-Bell 1967; Toomre 1977). It is well-established that collisions between disc galaxies of comparable masses lead to the formation of elliptical galaxies (Toomre 1977). Given that hierarchical assembly within the ΛCDM is scale-free, such interactions are anticipated across all mass scales (Fakhouri et al. 2010). Furthermore, the majority of mergers are predicted to occur amongst the most abundant population at all redshifts (Fontana et al. 2006; Karachentsev et al. 2013), namely dwarf galaxies ($M_* < 10^9$ M$_\odot$). As such, dwarf galaxies retain pristine signatures of these interactions and are ideally suited for testing the predictions of the ΛCDM model (Simon 2019).

1.3 Dwarf galaxies and its importance

The role of mergers and interactions in shaping galaxies has been extensively analysed in the high-mass regime ($M_* > 10^{10}$ M$_\odot$), both observationally (Ellison et al. 2010; Woods et al. 2010; Scudder et al. 2012; Ferreras et al. 2014; Cao et al. 2016; Shah et al. 2022) and theoretically (Toomre & Toomre 1972; Toomre 1977; Hernquist 1989; Hopkins et al. 2013; Brown et al. 2023; Byrne-Mamahit et al. 2023). These studies collectively show that major mergers cause significant morphological transformations, converting disc galaxies into spheroids, generating stellar and gaseous streams, triggering bursts of star formation, and channelling gas inflows that ignite nuclear starbursts and AGN activity.

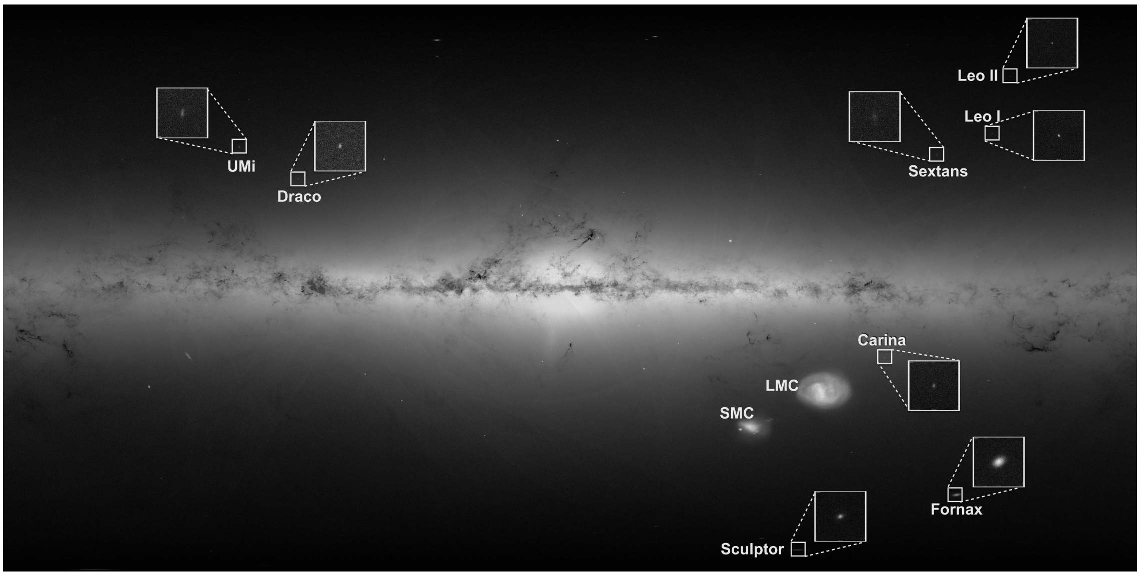

Figure 1.2: Figure presenting the MW galaxy along with the dwarf galaxies around it from *Gaia* telescope. *Image Credit: ESA/Gaia/DPAC*

Mergers are thus not merely destructive events but a fundamental creative process in galaxy evolution (Toomre & Toomre 1972; Toomre 1977). The low-mass regime, however, remains comparatively unexplored. Dwarf galaxies possess shallow gravitational potentials and more prone to environmental effects and baryonic feedback than their massive counterparts (Sawala et al. 2010; Venhola et al. 2019; Higgs & McConnachie 2021; Marasco et al. 2023 and references therein). Observationally, faint luminosities and complex surrounding substructures make these systems difficult to detect and characterise (e.g.Hopp et al. 2003; Whiting et al. 2007), while simulations face the challenge of simultaneously resolving the dwarf regime within a realistic cosmological volume (Vogelsberger et al. 2014; Naab & Ostriker 2017), though recent improvements have enabled more detailed modelling of dwarf–dwarf encounters (Dubois et al. 2021; Martin et al. 2021). This will be complemented by new and on-going observational surveys dedicated to study the assembly process of dwarfs (Annibali et al. 2020; Urbano et al. 2025).

Dwarf galaxies are often times found in associations (Tully et al. 2006; Bellazzini et al. 2013). This is consistent with the predictions of cosmological simulations that subhaloes are commonly accreted in small groups. Such a scenario may offer an explanation for the observed spatial alignment of several MW satellites with the orbital plane of the Clouds, supporting the hypothesis of group infall onto the MW (D'Onghia & Lake 2008; Koposov et al. 2015). Interactions between dwarf galaxies have been shown to enhance star formation rates by factors of up to ~2 compared to isolated systems (Stierwalt et al. 2015), with the triggered star formation being widespread and clumpy rather than nuclear as seen in massive galaxy mergers (Privon et al. 2017), and with the presence of tidal features correlating with elevated star formation activity (Lelli et al. 2014; Kado-Fong et al. 2020). Recent observational study by Subramanian et al. (2024) found enhanced star formation rates in interacting dwarfs with stellar masses of 10^6–10^9 $M_\odot$ in the Lynx-Cancer void. Subsequent studies reported that dwarf–dwarf interactions may both enhance and quench star formation (Kado-Fong et al. 2024; Chauhan et al. 2025).

Stellar streams serve as invaluable tracers of past satellite accretion around dwarf galaxies (e.g., Wheeler et al. 2015), but their detection remains exceedingly challenging due to their intrinsically low surface brightness. The scarcity of detections, with only 5.1% of inspected systems exhibiting accretion features in the low-mass galaxies (Sakowska et al. 2026) highlights that the vast majority of such structures around dwarfs remain undetected within the sensitivity limits of current observational surveys. Despite their significance in the Λ CDM framework, a detailed characterisation of their interaction histories, star formation efficiencies, and structural properties has less explored owing to the limited depth and resolution of surveys. Hence, it is not well understood whether dwarf–dwarf interactions drive morphological and star-forming changes analogous to those seen in massive systems, making it essential to study these processes.

The MW is surrounded by a substantial population of dwarf companions (see Figure 1.2), similar to most massive galaxies, though the faintness and relatively smaller sizes of dwarfs confine detailed observations largely to the nearby Universe. It can be seen in Figure 1.2 that amongst this population, the Large and Small Magellanic Clouds (LMC and SMC) clearly stand out as the two most prominent and nearest satellites of the MW. Being the interacting dwarf pair embedded within the gravitational potential of a massive host, they offer an unparalleled laboratory for simultaneously exploring dwarf–dwarf and satellite–host interactions. Their proximity and ongoing interaction with both each other and the MW provide unique and direct observational access to tidal forces, dark matter dynamics, and the evolutionary pathways of dwarf galaxies (D'Onghia & Lake 2008; Besla et al. 2012). Beyond their role as a dwarf interacting pair, the LMC has influence on the MW itself. Recent studies of stellar streams such as Orphan and Sagittarius reveal complexities in the MW's dark matter halo that can only be consistent by accounting for the dynamical perturbations exerted by the LMC (Vera-Ciro & Helmi 2013; Erkal et al. 2019; Helmi 2020). The LMC's gravitational influence perturbs the MW halo's density and kinematics, with mean velocities tracing LMC-induced perturbations and velocity dispersions constraining MW halo properties (Sheng et al. 2025) and contributing its own satellite population to the MW's halo (Battaglia et al. 2022). The LMC and the SMC therefore represent a uniquely rich system, serving simultaneously as laboratories for dwarf galaxy evolution and galaxy–galaxy interactions, and as essential probes within the broader context of ΛCDM galaxy evolution.

1.4 The Clouds

The LMC and SMC, collectively referred to as the Magellanic Clouds (hereafter, "the Clouds"), are our closest, interacting dwarf galaxy pair and largest satellites of the MW, prominently visible from the southern hemisphere. Knowledge of the Clouds predates European exploration, with indigenous South American cultures incorporating them into oral traditions for centuries; the Tupi-Guaranis of Brazil describe them as fountains from which a tapir (LMC) and a pig (SMC) drink, while the Mapuche of Chile characterise them as ponds. Dennefeld (2020) discussed that the earliest known written reference is attributed to Abd al-Rahman al-Sufi's *Book of Fixed Stars* (964 AD), with subsequent formalisation in the Western astronomical tradition through the works of Petrus Plancius (1598), Nicolas Louis de Lacaille (1755), and John Herschel (Herschel 1847). As noted in Dennefeld (2020), the Clouds came to bear the name of Ferdinand Magellan, who was an explorer but neither an astronomer nor made any notable contribution to their discovery. The appropriateness of this designation has been discussed by a number of astronomers and to consider renaming the Clouds, partly in light of historical concerns surrounding Magellan's conduct towards indigenous peoples (de los Reyes 2023).

Figure 1.3: Figure showing the homogeneous coverage of the Clouds (*Left:* LMC, *Right: SMC*) by VMC survey (Cioni et al. 2011).

The homoegeneous coverage of the LMC and the SMC obtained from the VMC survey are shown in left and right panels of Figure 1.3, respectively. Both the Clouds are gas-rich dwarf irregular galaxies exhibiting active star formation, and their proximity to the MW offers an unparalleled opportunity to resolve individual stars and examine the structural and morphological signatures of their mutual dynamical interactions in exceptional detail. The LMC lies at a distance of 50 ± 2 kpc (de Grijs et al. 2014a), and displays a complex morphology comprising an inclined disc, an off-centre bar (Bekki 2009; Subramaniam & Subramanian 2009), a prominent single spiral arm, and warped outer regions (Olsen & Salyk 2002; Choi et al. 2018a; Saroon & Subramanian 2022). The SMC, situated at 62 ± 1 kpc (de Grijs & Bono 2015a), is morphologically irregular, characterised by a wing-like extension oriented towards the LMC, and a substantial line-of-sight depth (Subramanian & Subramaniam 2009, 2012; Tatton et al. 2021), in particular of $\sim$ 20 kpc in its eastern regions (Nidever et al. 2013; Dias et al. 2021; Parisi et al. 2024), indicative of a triaxial structure and considerable dynamical complexity (Scowcroft et al. 2016; Jacyszyn-Dobrzeniecka et al. 2016, 2017a; Ripepi et al. 2017; Muraveva et al. 2017; Oliveira et al. 2023).

The Clouds are connected by a gaseous tidal feature first detected in neutral hydrogen by Hindman et al. (1963) by the Magellanic Bridge (MB), with its stellar counterpart later identified by Irwin et al. (1985). Subsequent investigations have established the MB as a tidal structure linking the eastern SMC to the western LMC, offering critical insight into the gas and stars stripped during their interaction (Harris 2007; Bagheri et al. 2013; Mackey et al. 2017; Gaia Collaboration et al. 2021b). Further low-density substructures trace the broader dynamical history of the system: the Leading Arm precedes the Clouds along their orbital path around the MW, and the Magellanic Stream extends prominently from the trailing edge, both clearly detected in H I maps (Mathewson et al. 1974; Moore & Davis 1994; Putman et al. 2003; Hammer et al. 2015; Chandra et al. 2023; Lucchini 2024; Zaritsky et al. 2025; Mishra et al. 2025). As the MW's most massive and proximate satellite pair, the Clouds are caught in the act of a rich, multi-body interaction, having experienced repeated close encounters with one another over several gigayears while simultaneously undergoing infall into the MW's gravitational potential (Vasiliev 2024; Besla et al. 2012). These interactions have left numerous imprints across both galaxies, in the form of disturbed morphologies like warped outer discs, and a plethora of peripheral substructures (Harris 2007; Mackey et al. 2018; Nidever et al. 2019; Cullinane et al. 2023).

1.4.1 The Magellanic System

Surrounding the Clouds, a wealth of low-density stellar and gaseous substructures bear testament to the complex dynamical history of the system as shown in Figure 1.4. The Magellanic Bridge (MB), connecting the eastern SMC to the western LMC, whereas the Leading Arm (Putman et al. 1998) and the Magellanic Stream (Putman et al. 2003) extend ahead of and behind the Clouds along their orbital trajectory, respectively. The Stream, in particular, constitutes one of the most spectacular gaseous features of the Clouds, spanning over 150 deg across the sky and serving as a direct record of material stripped from the Clouds (Lucchini 2024; Chandra et al. 2023; Zaritsky et al. 2025; Mishra et al. 2025). Beyond these large-scale gaseous structures, a growing number of stellar substructures have been identified using a variety of tracers, manifesting as morphological asymmetries, stellar over-densities, and extended peripheral features that collectively encode the dynamical interplay between the two Clouds and the broader influence of the MW (Mackey et al. 2016, 2018; El Youssoufi et al. 2019; El Youssoufi et al. 2021; Omkumar et al. 2021; James et al. 2021; Almeida et al. 2024; Massana et al. 2023).

Hydrodynamical simulations such as Besla et al. (2012) demonstrated that the large-scale gaseous features of the Magellanic system, including the Stream, the Leading Arm, and the Bridge (see Figure 1.5) could be reproduced through the mutual tidal interaction between the LMC and SMC alone, without requiring multiple pericentric passages around the MW. In this framework, the Stream arises primarily from material tidally stripped

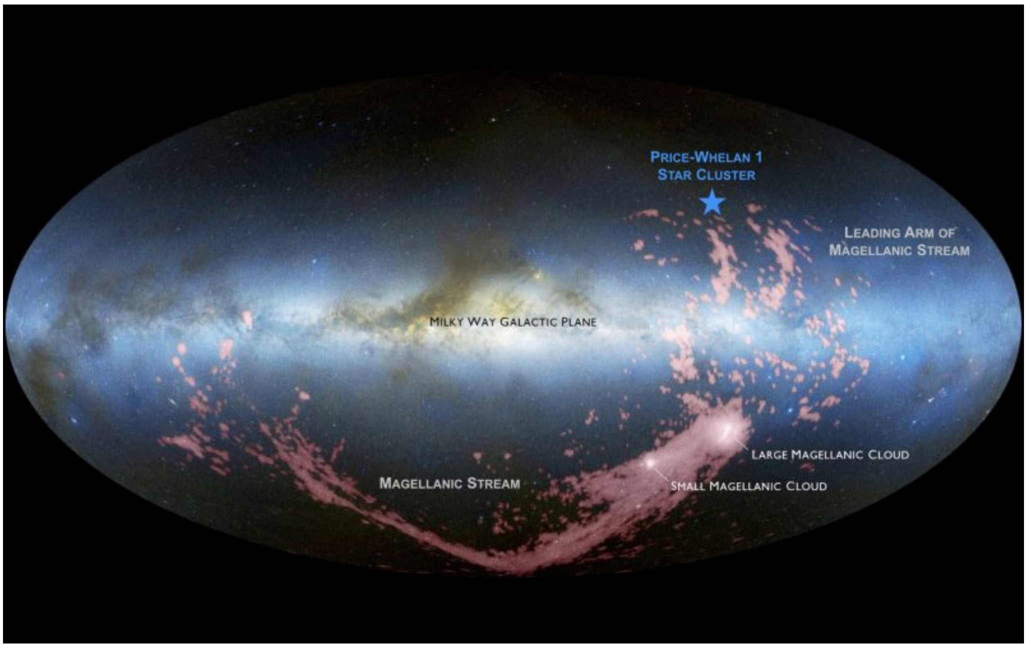

Figure 1.4: Figure showing the on-sky coverage of the Magellanic System including Magellanic Stream, Leading Arm, and the Clouds as traced by H I (pink; Nidever et al. 2010) along with an optical image of the MW (blue, white, and brown; Mellinger 2009).

from the SMC by LMC tides before the system's accretion by the MW, rather than through direct MW–SMC stripping as previously assumed. Two distinct interaction models were explored, Model 1 and 2, with the latter more successfully reproducing the observed morphology of the Stream and Bridge (Besla et al. 2012). Building upon this framework, Besla et al. (2013) extended the modelling to predict the existence of a stellar counterpart (see Figure 1.6) to the Magellanic Stream and Bridge, demonstrating that stars tidally stripped from the outer disc of the SMC during close LMC–SMC encounters. These predictions were pivotal in motivating observational searches for the stellar analogues of the well-characterised gaseous structures (e.g., Chandra et al. 2023; Viswanathan et al. 2024).

The orbital history that led to the formation of these structures has itself been subject to significant revision. Initially, the Clouds were thought to have completed multiple orbits about the MW (Tremaine 1976; Weinberg 2000), with repeated pericentric passages providing a natural mechanism for the production of the Stream and associated features. Recent precise proper motions based on HST by Kallivayalil et al. (2006); Kallivayalil et al. (2013) and *Gaia* challenged this view, suggesting instead that the system is on its first infall into the MW potential. The first-infall scenario was further supported by tidal models by (Besla et al. 2007, 2012), thereby indicating the formation of the observed structures on the mutual interaction between the two Clouds rather than on successive MW encounters. However, these models suffer from limitations such as the inability to reproduce the bifurcation observed in the Magellanic Stream. This first-passage scenario also accounts for the lack of extensive tidal disruption (Choi et al. 2022; Jiménez-Arranz et al. 2024) and

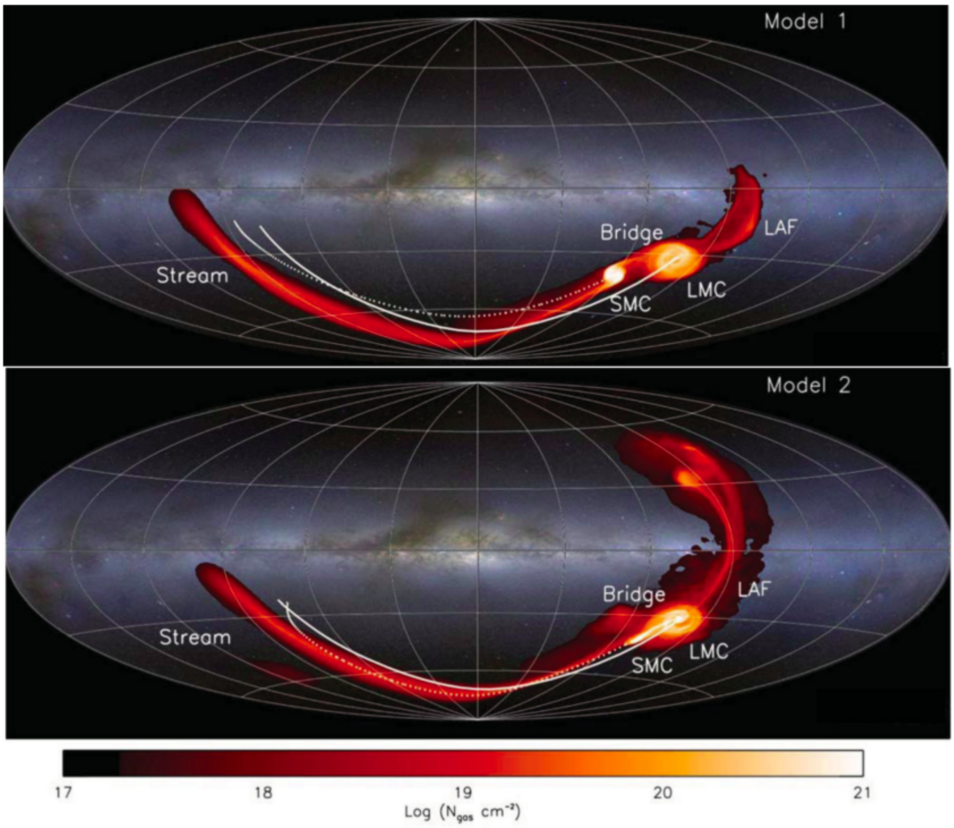

Figure 1.5: Hammer-Aitoff projection of the total gas distribution of the simulated Magellanic System (red scale) for Model 1 (top) and Model 2 (bottom) is over-plotted on the MW (blue, white and brown colours; (Mellinger 2009)). The orbital trajectory of the LMC (SMC) is denoted by the solid (dotted) white line. *Image adapted from Besla et al. (2012)*

the inclusion of the Magellanic Corona (Lucchini et al. 2020, 2021; Krishnarao et al. 2022; Mishra et al. 2024).

Moreover, several dedicated models have emerged to reproduce all the observed features (Diaz & Bekki 2012; Hammer et al. 2015; Tepper-García et al. 2019; Wang et al. 2019, 2022; Vasiliev 2024), but no single framework has yet achieved this. Notably, Tepper-García et al. (2019) revisited the formation of the Stream and Leading Arm in a first-infall scenario based on ram-pressure models, successfully recovering the location and extent of the Stream, whilst finding that the formation of the Leading Arm is inhibited by hydrodynamic interaction with the hot coronal component (Tepper-García et al. 2019). On the contrary, 'ram-pressure plus collision' models (Hammer et al. 2015; Wang et al. 2019; Tepper-García et al. 2019) naturally reproduce most observational properties associated with the Magellanic System, for instance, the observed dual filamentary structure of the Magellanic Stream, and a huge amount of ionised gas. Building upon this, Wang et al. (2022) successfully reproduce several other observed features, such as the offset between young and old stellar populations in the MB region as predicted by (Wang et al. 2019), and the stellar populations at two distances (e.g., Omkumar et al. 2021). More recently, the possibility of a second passage has been raised by Vasiliev (2024), reintroducing uncer-

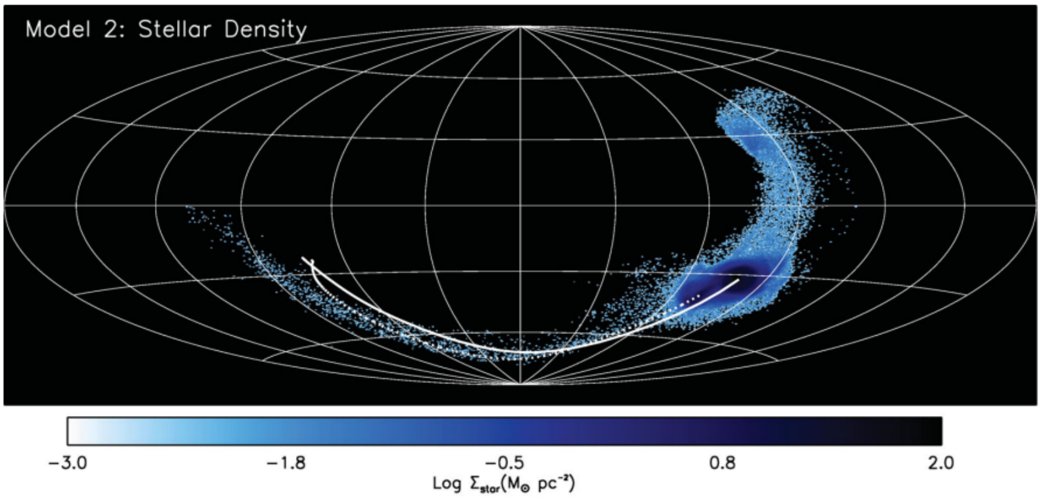

Figure 1.6: The stellar counterparts for the Model 2 (Figure 1.5) is shown in blue, adapted from Besla et al. (2013).

tainty into the picture. Hence, the fundamental character of the LMC–SMC interaction, whether a direct collision or a close fly-bys, tidal or ram-pressure stripping, together with the precise orbital history of the Clouds, is still a subject of ongoing debate.

However, the stellar populations associated with these substructures offer a particularly powerful diagnostic of the Clouds' interaction history. The MB is estimated to have formed ~300 Myr ago, and the Stream is thought to have originated ~1.5 Gyr ago. This implies that tidally stripped material should be dominated by intermediate-age to old stellar populations. Consistent with this expectation, previous studies have identified intermediate-age and old stars (>2 Gyr) in the vicinity of the Bridge (Nidever et al. 2011; Bagheri et al. 2013; Noël et al. 2013; Skowron et al. 2014; Noël et al. 2015; Belokurov et al. 2017; Jacyszyn-Dobrzeniecka et al. 2017a, 2020a; Massana et al. 2020), though the interpretation of their spatial distribution remains a matter of ongoing debate. Whilst Noël et al. (2013, 2015) and Carrera et al. (2017) favour a tidal origin for these intermediate-age populations, Jacyszyn-Dobrzeniecka et al. (2017a) and Wagner-Kaiser & Sarajedini (2017) argue instead that they represent the overlapping stellar haloes of the two Clouds. Identifying stellar counterparts to the Stream is considerably more challenging given its vast angular extent. However, debris tentatively associated with the Stream has been reported by Chandra et al. (2023), and a sample of around 40 very metal-poor stars has more recently been linked to this structure (Viswanathan et al. 2024), hinting at the ancient, tidally stripped nature of the Stream's stellar component.

1.4.2 Stellar sub-structures of the Clouds

The LMC disc exhibits warps across its radial extent, with multiple independent studies referring to a dynamically perturbed outer structure. Warp signatures are most clearly traced through variations in the position angle of the line of nodes. An inner south-west warp is detected at galactocentric radii of 2–4 deg (Olsen & Salyk 2002), with a more pronounced outer warp at ~7 in the south-west deviates by ~4 kpc towards the SMC (Choi et al. 2018a), likely driven by LMC–SMC tidal interactions. An additional outer warp in the north-east, displaying a comparable vertical deviation but smaller amplitude, has been reported by Saroon & Subramanian (2022), suggesting an asymmetric, possibly U-shaped warp morphology across the outer disc. An exponential fit to the vertical profile yields a scale-height increase from 1.3 to 1.9 kpc, with the older stellar component becoming increasingly dominant at large radii, a configuration consistent with both tidal perturbations from the MW (van der Marel & Cioni 2001a) and internal dynamical driven by LMC–SMC interactions (Besla et al. 2012).

The SMC is one of the metal-poor dwarf irregular satellites of the MW, and hosts an eastern extension known as the Wing (Shapley 1940). Despite the Wing's relatively low interstellar gas and dust content, it consists of young stars and ongoing active star formation (Cioni et al. 2000; Zaritsky et al. 2000; Rubele et al. 2018a; El Youssoufi et al. 2019). An additional shell-like stellar overdensity located ~ 1.9 deg north-east of the SMC centre has been identified by Martínez-Delgado et al. (2019), comprising a predominantly young population of ~150 Myr, suggestive of a relatively recent localised burst of star formation. In contrast to the LMC, the SMC's bar is considerably less prominent, and the north-eastern portion of the bar and disc lies systematically closer along the line of sight than its south-western counterpart (Jacyszyn-Dobrzeniecka et al. 2016).

The SMC's present-day structure bears the clear imprint of past tidal interactions, most visibly in its highly disturbed neutral atomic hydrogen distribution (Stanimirović et al. 2004). Moreover, older stellar populations exhibit a comparatively smooth and symmetric morphology, while the effects of tidal perturbation become increasingly pronounced in the younger stellar populations (Cioni et al. 2000; El Youssoufi et al. 2019; Gaia Collaboration et al. 2021b). Characterising the three-dimensional geometry of the SMC is further complicated by its substantial line-of-sight depth, which ranges from a few kpc to in excess of 20 kpc, with the precise extent and shape of this depth remaining uncertain (Jacyszyn-Dobrzeniecka et al. 2016, 2017b; Ripepi et al. 2017; Tatton et al. 2021).

Evidence for tidally stripped stellar material within the SMC has been identified through multiple independent studies. Using red clump (RC) stars, Nidever et al. (2013) identified a foreground stellar structure at ~55 kpc, offset by ~12 kpc from the main body at ~67 kpc, located in the eastern SMC at ~ 4.2 kpc from its centre, interpreted as material tidally stripped during the most recent LMC–SMC encounter. Subramanian et al. (2017) further analysed this feature and reported a foreground population lying 11.8 ± 2.0 kpc in front of the SMC main body, predominantly towards the south-east at 2–2.5 kpc from the centre, which they tentatively associate with material linked to the MB. Utilising the largest homogeneous dataset (~314 deg^2) from *Gaia* Data Release 2 (DR2; Gaia Collaboration et al. 2018a), Omkumar et al. (2021) traced this feature at ~ 2.5 deg to 5–6 deg from the optical centre of the SMC in the eastern regions. This finding was subsequently corroborated by an independent study using ground based optical data by Gatto et al. (2024). Extending this picture to larger radii, El Youssoufi et al. (2021) demonstrated that a structural bi-modality persists in the eastern SMC out to ~ 10°, with a background component between 7 deg and 10 deg in the north potentially associated with the Counter Bridge (Diaz & Bekki 2012), and a foreground component between 6 deg and 8 deg in the south possibly connected to the Old Bridge, a stellar tidal tail spatially offset from the gaseous MB.

1.4.3 Periphery of the Clouds

The Clouds have been studied extensively for decades, yet their outer regions remain a subject of study till date, as they remain far from fully understood. Stars at large galactocentric radii are weakly bound to their host galaxies compared to the central (inner), and are therefore the first to be affected by tidal forces arising from their mutual interaction and their host's gravitational potential. The peripheral regions of the Clouds thus act as a dynamical archive, preserving structural imprints of past interaction events. The combination of extremely low surface brightnesses of these sub-structures, the vast angular footprint of the Clouds made scrutiny of these regions severely limited.

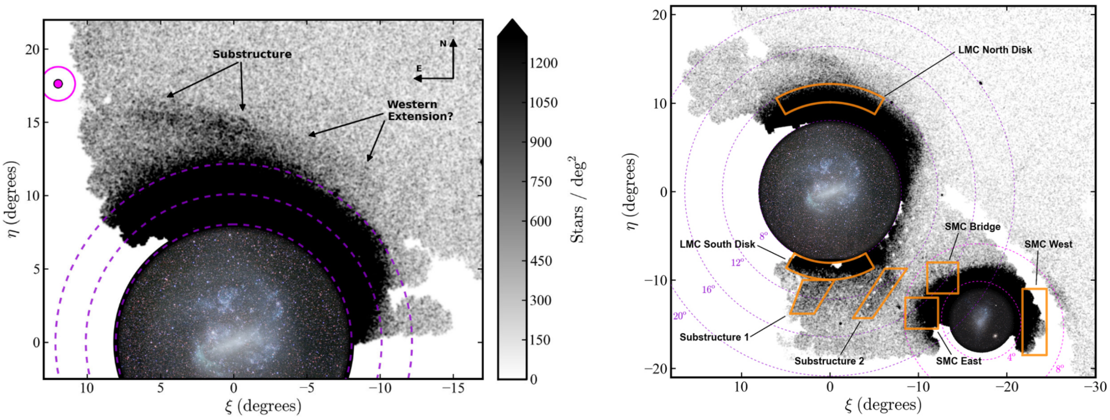

Figure 1.7: Left panel: Figure showing the stellar over-density in the northern region of the LMC (adapted from Mackey et al. 2016). Right panel: The Clouds along with the stellar substructures in the outskirts are marked with orange polygons; adapted from Mackey et al. (2018).

The identification of several such structures in recent years (Mackey et al. 2016, 2017, 2018; El Youssoufi et al. 2021) has demonstrated that the periphery of the Clouds are far from smooth or featureless, but are populated by a plethora of overdensities, streams, arcs, and tidal tails whose origins remain only partially understood. Figure 1.7 illustrates the substructures of the LMC's northern stellar periphery as revealed by Mackey et al. (2016). The left panel displays the arc-like Northern Substructure (North 1) detected at ∼13.5 deg from the LMC centre in DES imaging (Mackey et al. 2016), tracing old disc material perturbed by tidal forces. Extending this work, Mackey et al. (2018) mapped the southern periphery of the LMC and identified several substructures of the Clouds (right panel), the two hook-like southern substructures, South 1 and South 2, alongside the strongly distorted and truncated outer disc in the region closer to the SMC (Mackey et al. 2018), together underscoring the dynamically perturbed nature of the outermost regions of the Clouds. At least one of the southern substructures, South 2, was suggested to be physically associated with the RR Lyrae bridge (Belokurov et al. 2017) connecting the Clouds to the south of the gaseous MB. Moreover, the claw-like morphology of South 1 and its velocities exceeding 60 km s^{-1} point towards a highly dynamically perturbed origin

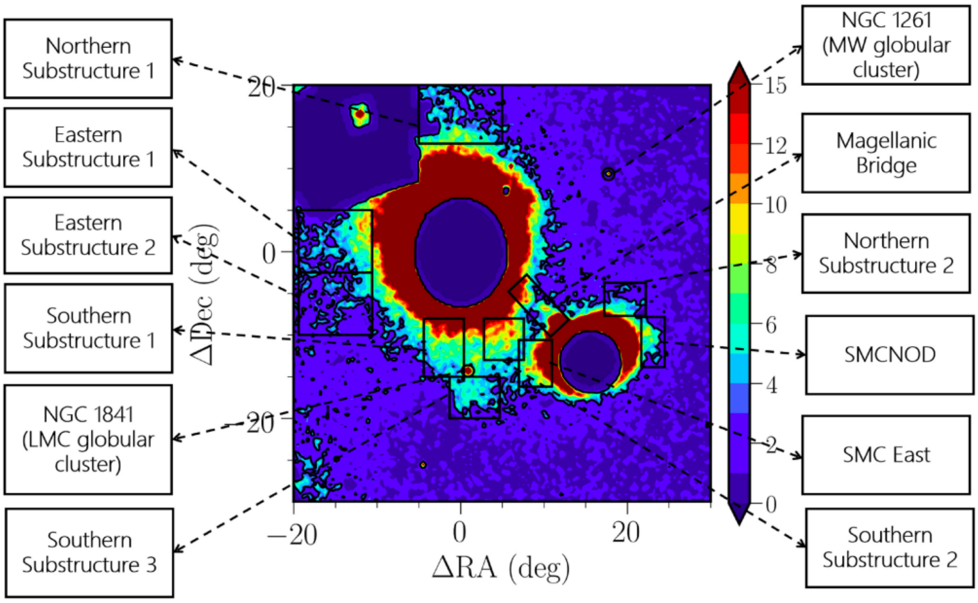

Figure 1.8: Figure shows the substructures detected as morphological features in the outskirts of the MCs studied in El Youssoufi et al. (2021), with the underlying density is that of young and old stars. The map is centred at (RA , Dec) = (81.24 deg, −69.73 deg). Elliptical and circular masks were used on the central region of the LMC and SMC, respectively, to enhance the distribution of stars in the outer regions.

(Cullinane et al. 2022b). The comprehensive morphological study of El Youssoufi et al. (2021), shown in Figure 1.8, presents the full network of peripheral stellar substructures identified across both Clouds in VISTA VHS near-infrared imaging, traced in both young and old stellar populations. Several of these substructures including the arc-like North 1 (Mackey et al. 2016), the southern features South 1 and South 2 (Mackey et al. 2018), the stream-like East 2 and the compact East 1 on the eastern LMC (El Youssoufi et al. 2021), and the SMC Northern Over-Density (Pieres et al. 2017), have been tentatively linked to either LMC–SMC tidal interaction or MW perturbation, yet their precise origins, stellar populations, and dynamical connections, that have thus far eluded a comprehensive and conclusive understanding.

It is in this context, a thorough investigation of the stellar periphery of the Clouds becomes indispensable. The substructures populating the outskirts of the Clouds encode age and metallicity gradients, kinematics, altogether a fossil record of the interaction sequence that has driven the morphological evolution of the system. Without a comprehensive characterisation of these features, any reconstruction of the orbital and interaction history of the Clouds and by extension, any comparison with the predictions of dynamical models (Besla et al. 2012; Diaz & Bekki 2012; Hammer et al. 2015), remains incomplete. This thesis addresses this gap directly, presenting a systematic investigation of the outermost stellar regions of both the LMC and SMC, with the aim of interpreting the substructures to better understand the past and ongoing dynamical evolution of the Clouds.

1.4.4 Kinematics with *Gaia*

The kinematic analysis of stellar substructures in the Clouds will provide some compelling hints for their origin. The advent of precise proper motion measurements from the *Gaia* (Gaia Collaboration et al. 2016a, 2018a, 2021b) has revolutionised kinematic studies, in particular of the Clouds to depict the internal streaming motions, tidal perturbations, and the kinematics of peripheral substructures across both Clouds with an astrometric precision unattainable by previous ground-based surveys. Omkumar et al. (2021) exploited the proper motion measurements from *Gaia* DR2 (Gaia Collaboration et al. 2018a) and demonstrated that the foreground RC stellar population identified by Hatzidimitriou et al. (1993); Nidever et al. (2013), exhibits kinematics systematically distinct from those of the SMC main body, with a slower tangential velocity.

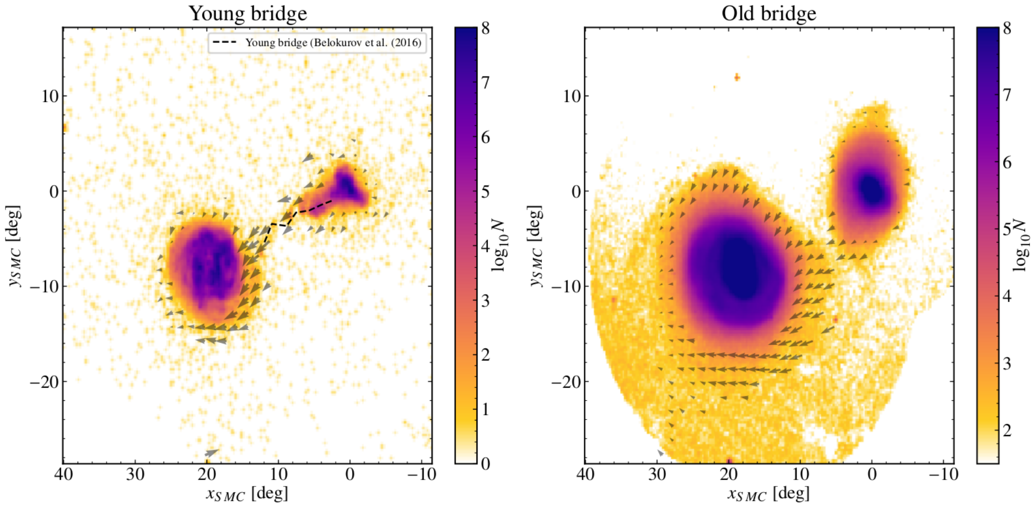

Figure 1.9: The proper motions of the stars in the Bridge region of the Clouds are shown with grey arrows. The underlying density is that of the young stars (left panel) and old stars (right panel), respectively. Image adapted from Gaia Collaboration et al. (2021b).

Complementing this, James et al. (2021) identified a bimodal distribution in the radial velocities (RVs) of red giant branch (RGB) stars in the eastern SMC through spectroscopic observations (Dobbie et al. 2014a; De Leo et al. 2020), with the two components separated by ~35–45 km s^{-1}. Incorporating these RV data alongside the proper motions from *Gaia* Early Data Release 3 (EDR3), James et al. (2021) identified that the lower- and higher-velocity RGB components align kinematically with the foreground substructure and the SMC main body identified with the RC stars, respectively. They also estimated that this foreground feature formed 307 ± 65 Myr ago, broadly consistent with the most recent LMC–SMC close encounter, as predicted by the simulations of the Clouds. In the western outskirts, El Youssoufi et al. (2021) identified a faint RC component that may trace the Counter-Bridge predicted by Diaz & Bekki (2012). Complementing this, a further bimodality in the RV distribution of RGB stars was detected by James et al. (2021) in the south-western regions of the SMC, notably absent in the RC population of the same region, hinting at a more complex interactions than our current understanding.

Figure 1.9 presents the homogeneous sampling and proper motions of stars across the Magellanic Bridge from Gaia Collaboration et al. (2021b), derived from *Gaia* EDR3, separately for young (left panel) and old (right panel) stellar populations. Gaia Collaboration et al. (2021b) exploited the proper motions to resolve the Bridge region along with the outer periphery of the Clouds, in detail. These plots further confirmed the old stellar population within the Bridge being spatially offset from its younger counterpart, consistent with the picture of an old tidal stellar bridge overlapping with a younger population formed more recently in situ during the LMC–SMC interaction (Gaia Collaboration et al. 2021b). These studies paint a picture of a dynamically complex periphery in which multiple stellar components with distinct spatial distributions and kinematics coexist, each reflecting a different epoch and/or interactions. Kinematic studies have proven instrumental in establishing the distinct dynamical nature of these substructures, they alone are insufficient to fully decipher their origins.

1.4.5 Metallicities

As outlined in the previous sections, the outer regions of the Clouds are enriched with substructures, including stellar arms, streams, and over-densities, each containing the imprint of repeated interactions between the Clouds. Deciphering the origin of these peripheral features is one of the key interest in study of the Clouds, as substructures in the outskirts can in principle arise from several distinct processes: tidal stripping of SMC material by the LMC, perturbation of the LMC's outer disc by the SMC or the MW, or ram-pressure effects as the Clouds move through the MW's circumgalactic medium (Cullinane et al. 2023; Muñoz et al. 2023). Kinematic data alone cannot fully differentiate between these scenarios, a detailed study of stellar metallicity is therefore essential (Carrera et al. 2017; Grady et al. 2021; Cheng et al. 2022; Cullinane et al. 2023; Muñoz et al. 2023; Massana et al. 2023). Stars serve as fossil records of their host galaxy's evolutionary history, with iron abundance [Fe/H] acting as a powerful tracer of nucleosynthesis that reflects how effectively a galaxy formed stars, retained enriched gas, and responded to external perturbations such as tidal stripping and accretion (McWilliam 1997). It is well-established that LMC and SMC have evolved along distinct chemical enrichment paths, with the LMC's metallicity distribution function (MDF) and the SMC's MDF being systematically more metal-poor (Carrera et al. 2008; Dobbie et al. 2014b; Choudhury et al. 2020), combining metallicity with kinematics thus beneficial to investigate their dynamical origin (Olsen et al. 2011; Muñoz et al. 2023). Spatially resolved metallicity maps reveal how chemical enrichment unfolded across a galaxy, tracing radial gradients driven by internal feedback, gas inflows, and dynamical interactions, and are therefore indispensable tools for connecting the present-day chemical structure of a galaxy to the sequence of physical processes that shaped it (Cohen et al. 2024a,b).

Significant progress has been made in characterising the metallicity distributions of both Clouds through different methods such as the RGB slope analyses and spectroscopic calcium triplet studies (Carrera et al. 2008; Choudhury et al. 2020, 2021; Dobbie et al. 2014b; Povick et al. 2021, 2023b,c). These studies have mapped the inner regions of both galaxies out to a few degrees from their respective centres, revealing negative radial metallicity gradients in both systems. For the SMC, reported gradient values range from

-0.075 ± 0.011 dex deg^{-1} (Dobbie et al. 2014b) to -0.031 ± 0.005 dex deg^{-1} (Choudhury et al. 2020), illustrating how different methodologies, tracer populations, and spatial coverages can yield conflicting results (De Bortoli et al. 2022). Previous studies have largely been restricted to the inner regions, leaving the outer regions, where the most of these substructures reside. Further complexity arises from the use of different calibration relations across studies for similar stellar tracers (Cioni 2009; Narloch et al. 2021, 2022), making a coherent, system-wide interpretation difficult.

Despite these collective advances, a fundamental limitation persists: no single homogeneous metallicity catalogue exists that covers both Clouds simultaneously, reaches their extended periphery, and samples both young and old stellar populations. Spectroscopic samples exist only a few thousand RGB stars observed with different instruments, spectral resolutions, and calibration relations, introducing systematic inhomogeneities that complicate direct comparison (Dobbie et al. 2014b; Choudhury et al. 2020; De Bortoli et al. 2022). For young stellar populations such as supergiants, metallicity measurements are even sparser, preventing a comparative study of chemical enrichment across different stellar ages. Muñoz et al. (2023) demonstrated, using APOGEE data, that substructures in the LMC periphery carry LMC-like metallicity distribution functions (MDFs), while those near the SMC carry SMC-like MDFs, with the southern LMC periphery showing a complex mixture indicative of debris from both galaxies. A homogeneous, spatially extended metallicity study of both young and old stars, of the Clouds and their peripheral substructures is essentially a next step. This aids to overcome the aforementioned discrepancies and to connect the observed chemical structure to the broader interaction and enrichment history of the system.

Machine learning methods have significantly extended the spatial extent of metallicity studies across the Clouds. Grady et al. (2021) applied these methods to *Gaia* DR2 photometry and produced the first metallicity map spanning the entire area of the Clouds, yielding a shallow LMC gradient of -0.048 ± 0.001 dex kpc^{-1} and evidence for SMC tidal disruption towards the LMC. Moreover, Frankel et al. (2024) constructed mono-age and mono-abundance maps of the LMC from *Gaia* DR3, and Li et al. (2024) employed the tip of the RGB to map metallicities across both Clouds with reduced sensitivity to interstellar reddening. *Gaia* DR3 (Gaia Collaboration et al. 2016a, 2022; Recio-Blanco et al. 2023) provides low-resolution ($R = 20$–80) spectrophotometry for around 220 million sources, opening a new avenue for large-scale metallicity mapping. Andrae et al. (2023) exploited these spectra alongside infrared data and *Gaia* parallaxes to derive data-driven metallicities for ~175 million sources using the XGBoost algorithm trained on APOGEE, though their vetted RGB sample excluded the most distant sources, limiting its direct applicability to the Clouds owing to their distance. Although, this method demonstrates considerable promise, its capacity is presently constrained by systematic uncertainties in the spectra and limitations in the modelling framework, which are anticipated to be mitigated with subsequent data releases from *Gaia*. Additionally, the application of these methods to the younger population was still limited due to the available sparse samples.

This thesis bridges this gap by constructing a spatially resolved, homogeneous photometric metallicity map traced by both young (supergiants) and old (RGB) stars, spanning both Clouds and their substructures simultaneously. This provides a unified chemical perspective, enabling a coherent characterisation of chemical enrichment and the dynamical origin of the features to better understand their prolonged interaction history.

1.4.6 Photometric metallicities: Synthetic Strömgren photometry

An alternative approach to derive metallicities is via synthetic photometry, from observed spectrophotometric data. It is a valuable tool for obtaining magnitudes and colours within standard photometric systems. It enables the gain of insights from the spectral properties of stars, star clusters and even distant galaxies. This approach involves the process of deriving photometric quantities such as magnitudes, colours and corresponding colour indices, based on stellar spectra, by convolving observed spectrophotometric fluxes with standard passbands, rather than relying on direct observations in those specific bands. One of the key advantages of using synthetic photometry is that it allows us to estimate the stellar metallicities for a large number of individual stars in a galaxy, without the necessity of high-resolution spectra. Thus, significantly reduces telescope time compared to traditional spectroscopic observations.

In this thesis (Chapter 2), we employed synthetic Strömgren photometry to estimate photometric [Fe/H] of individual stars in the Clouds. The Strömgren photometric system devised by astronomer Bengt Strömgren (Strömgren 1963, 1964), consists of four medium-width passbands covering the visible and near-ultraviolet regions. Compared to the UBV system, the Strömgren system exploits narrower filters designed intentionally to match the specific signatures in the spectra of stars that directly relate to the physical properties like effective temperature, surface gravity and metallicity (Árnadóttir et al. 2010; Narloch et al. 2021, 2022). A particularly important parameter is the metal–line index defined as ($m_1 = (v - b) - (b - y)$), which measures of the total intensity of the metal lines in the v band. The v filter covers a wavelength region rich in iron lines around 4100 Å, along with a CN absorption blend, making it especially sensitive to metallicity. Consequently, Strömgren photometry has been proven to be a reliable metallicity indicator, particularly for giant stars.

The procedure followed in this work can be summarised as follows. First, we obtained the transmission curve of the *Gaia* BP filter together with the response functions for the Strömgren v, b, and y filters. Low-resolution (R = 20–80) *Gaia* BP (330–680 nm) spectra were then obtained for each star in our sample. These spectra were convolved with the BP filter transmission curve, and the integrated flux over the convolved region was calculated to derive magnitudes and colour indices. To perform these steps, we employed the standardised *GaiaXPy* tool (Gaia Collaboration et al. 2022). This tool enables the generation of synthetic photometry across multiple photometric systems from internally calibrated, continuously represented mean *Gaia* BP/RP spectra. Using this method, we derived synthetic Strömgren magnitudes (v, b, and y) and calculated the corresponding colours and indices necessary for the determination of photometric metallicities. Hence, Strömgren photometry is a very useful technique to infer the intrinsic properties of stars when high-resolution spectra are unavailable. Through established calibration relations (e.g. Calamida et al. 2007; Grebel & Richtler 1992; Piatti et al. 2019), photometric metallicities of individual stars can be estimated efficiently, thereby contributing to a detailed understanding of the metallicity distribution across stellar populations.

Bellazzini et al. (2023) demonstrated the power of this approach by deriving photometric metallicities for 694 233 Galactic giant stars using synthetic Strömgren photometry from *Gaia* DR3 XP spectra. A key advantage of the Strömgren method is its applicability beyond old giant stars: appropriate calibration relations also exist for young supergiant stars (Grebel & Richtler 1992; Piatti et al. 2019), making it possible to estimate metallicities for multiple stellar populations from the same homogeneous photometric system, a capability that is especially valuable in the context of the Clouds, where populations spanning a wide range of ages coexist and their comparative metallicities carry direct information about the chemical enrichment history of the system. In this thesis, we present the homogeneous photometric metallicity map of the Clouds constructed from synthetic Strömgren photometry derived from *Gaia* DR3 XP spectra that maps the metallicity of ~20 deg of the LMC and ~11 deg of the SMC, traced by young and old giant stars. By applying a homogeneous method across the Clouds, systematic biases arising from heterogeneous instrumentation are eliminated, enabling a coherent characterisation of radial metallicity gradients across both galaxies and their extended substructures within a homogeneous framework. This includes the identification of gradient breaks tied to structural and interaction features, alongside a direct chemical comparison of peripheral substructures, with the ultimate goal of constraining their origins and illuminating the mutual interaction history of the Clouds and the MW (Chapter 3).

1.4.7 Central region of the Clouds

The central regions of galaxies are amongst the most intriguing yet observationally demanding environments for resolving individual stars. The challenges posed by stellar crowding, interstellar gas and dust, and the potential presence of a massive black hole significantly obstruct observational efforts. Despite substantial progress has been made in characterising their outer regions, survey performance declines markedly towards the centre. For instance, one of the most sensitive ground-based optical imaging survey to date, SMASH (Nidever et al. 2017a), reports a notable deficit in detected stars in the centre in the LMC centre due to crowding (Choi et al. 2018a). Similarly, the pioneering space astrometry, the *Gaia* mission, suffers from incompleteness in high-density regions such as the centre of the Clouds (Rathore et al. 2025b). The Optical Gravitational Lensing Experiment (OGLE) observes an apparent elongation along the line of sight associated with RR Lyrae stars in the inner LMC region, owing to severe blending effects (Jacyszyn-Dobrzeniecka et al. 2017b).

The VMC survey (Cioni et al. 2011) provides enhanced access to the densest regions of the Clouds through its near-infrared sensitivity and spatial resolution. However, it still falls short of resolving structures in the central regions of the Clouds, critical to understanding their dynamics and evolution. The Clouds also cover a huge area of the sky, rendering the Hubble Space Telescope *(HST)* studies spanning several square degrees impractical. Owing to these limitations, the location of the LMC's centre remains a subject of ongoing debate, with different tracers and selection methods yielding notably different results (see Fig. 9 and Table 2 of Niederhofer et al. 2022a). H I rotation studies suggest the centre is situated at ($\alpha_0 = 78.13°$, $\delta_0 = -69.00°$) and ($\alpha_0 = 79.40°$, $\delta_0 = -69.03°$), on the western side of the bar (Luks & Rohlfs 1992; Kim et al. 1998). In contrast, photometric and analyses of carbon star kinematics, favour positions closer to the bar centre at ($\alpha_0 = 81.28°$, $\delta_0 = -69.78°$) and ($\alpha_0 = 81.91°$, $\delta_0 = -69.87°$), respectively (van der Marel & Cioni 2001b; van der Marel et al. 2002). Proper motion studies utilizing both *HST* data Kallivayalil et al. (2006); Kallivayalil et al. (2013) and *Gaia* data yield intermediate positions, broadly consistent with the H I centre (van der Marel & Kallivayalil 2014; Gaia Collaboration et al. 2021b). More recently, Niederhofer et al. (2022a) report a stellar rotation centre derived from near-infrared data of VMC survey, that aligns closely with estimates obtained from *HST*. These discrepancies underscore the disturbed nature of the LMC and the highlight how the inferred centre is contingent on both the selected tracer population and the spatial coverage of the sample. Owing to the observational limitations outlined above, several key properties of the LMC centre remain poorly constrained. The disc centre may be displaced from the bar centre as a result of tidal interaction with the SMC (Pardy et al. 2016), evidence for a central black hole remains tentative (Boyce et al. 2017), and *Gaia* DR2 data suggest that stars near the centre follow elongated orbits along the bar (Gaia Collaboration et al. 2018b), a precise characterisation of the central dynamics has yet to be understood.

Of the two systems, the SMC exhibits a markedly more disturbed morphology, characterised by an elongated structure and substantial line-of-sight depth in its eastern regions. A bimodal red clump RC population was first identified in the eastern SMC, extending towards the Magellanic Bridge and LMC (Hatzidimitriou & Hawkins 1989; Nidever et al. 2013), with subsequent studies confirming the presence of a foreground population located ~ 10–12 kpc in front of the SMC main body (Subramanian et al. 2017; Tatton et al. 2021; Omkumar et al. 2021; El Youssoufi et al. 2021; Gatto et al. 2024; Parisi et al. 2024; Oden et al. 2025). Although this feature has been traced as far as 10 deg from the SMC centre (El Youssoufi et al. 2021), no study has yet achieved sufficient data quality to investigate it within 2.5 deg of the centre. Previous studies of the bimodal feature have detected it only beyond ~2.5 deg from the SMC's centre. In Chapter 5, we address this gap by examining signatures of this substructure in the central region of the SMC, utilising luminosity distributions of RC stars and data from the VMCDeep Survey, which is an extension of the VMC survey aiming to acquire deeper, higher spatial resolution, multi-epoch images of the centre of the Clouds (Cioni & Omkumar et al., submitted; presented in Chapter 4). Characterising this feature in the crowded central regions of the SMC will provide crucial evidence of historical gravitational interactions between the Clouds and the MW, which have stripped stellar material and transformed the morphology and kinematics of both systems.

1.5 Overview of the thesis

The core chapters of this thesis discuss the research work undertaken during the course of my PhD, with a main emphasis on studying various sub-structures in and around the Clouds to understand the dynamical evolution of the Clouds. The work is structured as follows:

- **Chapter 2:** I present the work to produce the Strömgren photometric metallicity catalogues of young and old stars in the Clouds using the low-resolution XP spectra from *Gaia* DR3 data. Utilising the GaiaXPy tool, I compute synthetic photometry and then apply literature calibration relations to estimate radial metallicity gradients, which revealed interaction-driven breakpoints.

- **Chapter 3:** By leveraging these photometric metallicity catalogues, I investigate the origin of the peripheral stellar sub-structures by comparing their metallicities, metallicity distribution functions and stellar kinematics against the main-body populations. This chemo-dynamical dissection elucidates tidal stripping histories linking the LMC, SMC, and MW.
- **Chapter 4:** I introduce the VMCDeep dataset and present the photometry, covering 1.77 deg^2 inner regions of the Clouds to probe the galactic centres of the Clouds with improved depth and homogeneity compared to previous surveys.
- **Chapter 5:** In this chapter, I use the VMCDeep dataset (PSF) to probe the foreground substructure traced by RC stars in the central (inner) regions of the SMC.

2 Strömgren photometric metallicity map of the Magellanic Cloud stars using Gaia DR3–XP spectra

Abinaya O. Omkumar, Maria-Rosa L. Cioni, Smitha Subramanian, Jos de Bruijne, Aparna Nair, Bruno Dias

This chapter has been published in the Astronomy & Astrophysics, Volume 700, A7

2.1 Introduction

Galaxies are a multi-component (bar, bulge, disc, spiral arms, halo made of baryonic and dark matter) diverse class of objects with distinct structural, kinematical, and chemical properties. They are found both in isolation as well as in groups and clusters. Morphologically, they have been classified as ellipticals, spirals and irregulars. The low mass and less luminous counterparts of these objects are classified as dwarfs, which are the most abundant type of galaxies in the Universe. Observationally, groups and clusters of galaxies are ubiquitous. A cluster is dense, populous and typically consists of a few tens to hundreds of galaxies bound by gravity. Whereas, a galaxy group consists of a few massive galaxies surrounded by many satellites, mostly dwarfs that have not yet dissolved or merged with their host galaxy. In the environment of galaxy clusters and groups, dynamical processes such as tidal and ram-pressure stripping play a vital role in driving galaxy evolution. The Λ cold dark matter model suggests that the dark matter halos grow hierarchically (bottom-up scenario); that is, larger halos are formed by the merging of smaller ones (Fall & Efstathiou 1980; van den Bosch 2002; Agertz et al. 2011). A detailed exploration of how this physical process affects the host and satellite galaxy is required to understand galaxy evolution in general. A system involved in both dwarf-dwarf interactions and interactions with its host (a more massive galaxy) is then an excellent place to explore the implications of both phenomena.

One such pair of interacting galaxies is the Large Magellanic Cloud (LMC) and the Small Magellanic Cloud (SMC), which are two prominent satellites of the Milky Way (MW). They are both gas-rich dwarf irregulars and are collectively known as the Magellanic Clouds. The LMC is characterised by an inclined disc, a major spiral arm and an off-centred bar (Bekki 2009; Subramaniam & Subramanian 2009), along with having evidence of warps (Olsen & Salyk 2002; Choi et al. 2018a; Saroon & Subramanian 2022). It is located at a distance of 50±2 kpc (de Grijs et al. 2014a) and is in proximity of the SMC (62±1 kpc; de Grijs & Bono 2015a). The SMC is characterised by an irregular shape, a wing towards the LMC and a large line-of-sight depth (Scowcroft et al. 2016; Jacyszyn-Dobrzeniecka et al. 2016, 2017a; Ripepi et al. 2017; Muraveva et al. 2017; Oliveira et al. 2023). Low-density stellar structures have been identified at the galaxy's front (Leading Arm; Putman et al. 1998) and trailing (Magellanic Stream; Putman et al. 2003) ends as well as between the LMC and SMC (Magellanic Bridge). These features are also prominent in H I maps (Putman et al. 2003). In addition, several stellar sub-structures have been found using various tracers, which exhibit themselves as signatures of dynamical interactions (Mackey et al. 2016, 2018; El Youssoufi et al. 2019; El Youssoufi et al. 2021; Omkumar et al. 2021; James et al. 2021; Almeida et al. 2024; Massana et al. 2023). Some of these sub-structures have also been associated with the influence of the MW. Hence, the Magellanic Clouds (hereafter, 'the Clouds') can serve as an excellent laboratory to study dwarf-galaxy interactions utilising resolved stellar populations.

We expect the stellar structures that formed during the origin of the Bridge (~300 Myr ago) and Stream (~1.5 Gyr ago) to show old stars stripped from the galaxies through dynamical interactions. Previous studies (Nidever et al. 2011; Bagheri et al. 2013; Noël et al. 2013; Skowron et al. 2014; Noël et al. 2015; Belokurov et al. 2017; Jacyszyn-Dobrzeniecka et al. 2017a, 2020a; Massana et al. 2020) found intermediate-age or old stars (> 2 Gyr old) around the Bridge, but the interpretation of their location is inconsistent. Noël et al. (2013, 2015) and Carrera et al. (2017) support a tidal origin for the presence of intermediate-age stars, while Jacyszyn-Dobrzeniecka et al. (2017a) and Wagner-Kaiser & Sarajedini (2017) suggest them as part of the overlapping stellar halos of the Clouds. Since the Stream is vastly spread in the sky, it is not trivial to identify any star associated with a tidally stripped population. Some Stream debris was discovered by Chandra et al. (2023), and more recently, a sample of about 40 very metal-poor stars were tentatively associated with the Stream (Viswanathan et al. 2024).

Metallicity and abundance estimates are key parameters to determining the chemical composition and also hint at the formation history and evolution of galaxies. Recent studies have significantly advanced our understanding of the metallicity distribution in Clouds by using both photometry and spectroscopy. Photometric metallicity maps of the LMC (~ 4 deg from the centre; Choudhury et al. 2016a) and the SMC (~ 2.5 deg from the centre; Choudhury et al. 2018) have been produced using the slope of the red giant branch (RGB) as an indicator of the average metallicity of a sub-region and calibrated using spectroscopic data. Building upon this work, another study extended the analysis to a larger area of the SMC (~ 4 deg from the centre; Choudhury et al. 2020) and the LMC (~ 5 deg from the centre; Choudhury et al. 2021). Grady et al. (2021) chemically mapped the entire Clouds using data from *Gaia* Data Release 2 (DR2). They utilised machine learning methods and obtained photometric metallicity estimates for the selected RGB stars using the spectroscopic metallicities from the Apache Point Observatory Galactic Evolution Experiment (APOGEE) as training samples. More recently, Frankel et al. (2024) used *Gaia* Data Release 3 (DR3) data to construct mono-age and mono-abundance maps of the LMC, while Li et al. (2024) used the tip of the RGB stars, which has less sensitivity to interstellar reddening, to create metallicity maps of the Clouds.

Spectroscopic metallicities are available for only a few thousand giant stars, and for other young populations, metallicities are available for even fewer stars. These measurements were also obtained using various facilities and from different instruments with varying spectral resolutions that may collectively introduce systematic uncertainties in the study of metallicity distributions. For example, Dobbie et al. (2014b) estimated the metallicity gradient from the observation of RGB stars to be -0.075 ± 0.011 dex deg^{-1} out to 5 deg from the centre of the SMC. Choudhury et al. (2020) obtained a gradient of -0.031 ± 0.005 dex deg^{-1} in the inner 2.5 deg region, flattening to 4 deg. De Bortoli et al. (2022) investigated the metallicities of SMC stellar clusters and surrounding field stars, finding that there is a bimodal distribution comprising metal-poor and metal-rich group of clusters, which is contrary to the unimodal metallicity for the SMC field stars. In addition, various studies have used different calibration relations to estimate the metallicities of similar and other stellar tracers in the Clouds (Cioni 2009; Feast et al. 2010; Narloch et al. 2021, 2022). In general, there is a lack of homogeneous and spatially extended metallicity samples that represent both the young and old stellar populations of the Clouds. These samples are essential for studying the sub-structural features in the outskirts, which will help in determining their origins and mutual association.

Gaia DR3 (Gaia Collaboration et al. 2016a, Gaia Collaboration et al. 2022, Recio-Blanco et al. 2023) provides low-resolution (R=20−80) spectrophotometry for around 220 million sources, in the ranges 330−680 nm (BP) and 640−1050 nm (RP), which together are referred to as XP. A recent study by Andrae et al. (2023) used these spectra to obtain data-driven stellar metallicities of ∼175 million sources, including sources in the Clouds. They estimated the metallicities of the stars using the XGBoost algorithm utilising the infrared photometric data from the ALLWISE[1] programme and *Gaia* parallaxes by training their algorithm also on the APOGEE sample. In their work, the addition of the parallaxes as one of the input parameters improved the metallicity estimates by ∼10%. They presented a vetted sample with just the RGB stars after applying quality cuts mainly using the parallax values to remove the most distant sources, especially those in the Clouds. The potential of this full-spectrum fitting method will further improve with subsequent data releases from *Gaia* by fixing the systematics in the spectra and aspects of the modelling. Another way of estimating the stellar metallicities from the XP spectra is by using synthetic photometry, where the transmission curve of the chosen photometric bands are completely covered by the *Gaia* DR3−XP realm, to obtain the magnitudes and colour indices from GaiaXPy and then by using relevant calibration relations to estimate the photometric metallicities. This has also been demonstrated in Gaia Collaboration et al. (2022). Although this is an indirect way of inferring the metallicities of stars, it does have advantages over traditional spectroscopic metallicities. It is less time-consuming, and hence the metallicity estimates can be made for a large sample using the same method. Bellazzini et al. (2023) used this method and the available calibration relations from the literature to estimate photometric metallicities for 694 233 Galactic giant stars from *Gaia* DR3 synthetic Strömgren photometry. The advantage of this method is that it can also be expanded and applied to young stars, such as supergiant stars, by using appropriate calibration relations from the literature to estimate their metallicities. This is especially useful in the case of the Clouds, where there are stellar populations of different ages and where a comparison of their metallicities can provide details about the chemical enrichment process within the galaxies.

In this work, we utilise the homogeneous data sample from the *Gaia* DR3−XP spectra, encompassing the entire LMC and SMC, to estimate their photometric metallicities ([Fe/H]) of both young and old stars, therefore expanding the method utilised by Bellazzini et al. (2023). We compare these metallicities with the APOGEE estimates to validate our method, and we also estimate the metallicity gradients. In Section 2.2, we provide details on the selection of our data sample. In Section 2.3, we discuss the synthetic photometry method, and in Section 2.4, we explain the estimation of the photometric metallicities.

---

[1] https://wise2.ipac.caltech.edu/docs/release/allwise/

In Section 2.5, we present our results, and we discuss their interpretation in Section 4.7, which concludes our study.

2.2 Data

We describe below our initial selection of the most probable SMC and LMC sources used in our study. As we aim to estimate the photometric metallicities of both the RGB and supergiant stars, we also show their further selection from the entire sample.

2.2.1 Gaia DR3–XP spectra for SMC sources

Our initial SMC sample is selected to cover a circular area with a radius of ∼11 deg from the SMC centre (RA = 12.80 deg and Dec = −73.15 deg, Cioni et al. 2000) and to include sources with magnitudes $G < 20.5$ from the *Gaia* archive[2]. This resulted in 4 709 622 sources, which are further reduced to 761 736 after removing sources without *Gaia* XP spectra. To further eliminate the contamination from the foreground (MW) sources and only use the most probable SMC sources, we applied the additional criteria on parallax and proper motions by following the selection procedure described in Gaia Collaboration et al. (2021b) and retain 158 255 sources which satisfy the selection criteria. We also applied a 5 σ cut to the flux-signal-to noises in all three *Gaia* bands, resulting in sources with magnitude errors ≤ 0.22 mag, where magnitude error = 1.086 / flux_over_error (*Gaia* DR2 primer[3], Section 6). We further selected sources which have astrometric excess noise values ≤ 1.3 mas (Omkumar et al. 2021, Section 2). We also estimated the photometric excess factor correction (c_*) by following the method suggested in the Appendix B of Gaia Collaboration et al. (2021a), and selected stars that pass a 2 σ criteria (Riello et al. 2021, Equation 18). After all these quality filters, we obtained 156 428 sources. The RA and Dec of these sources are then converted into the zenithal equidistant projection coordinates X and Y using the transformation equations in van der Marel & Cioni (2001b).

Our SMC sample consists of stellar populations of different ages as shown in the colour-magnitude diagram (CMD) on the top-left panel of Figure 2.1. As stellar populations with different ages might have different metallicities from one another, we further distinguish the RGB stars from the supergiants in our initial sample. RGB stars in the SMC are old or intermediate-age stars typically > 3 Gyr old (e.g. Rubele et al. 2018a) and one of the most abundant and also homogeneously distributed stellar populations across the galaxy. Although we do not have spectra for the entire sample, as the faint limit of the *Gaia* DR3–XP spectra is ∼17.65 mag, we can study the majority of bright RGB sources. To select these RGB stars, we utilised the selection criteria provided by Gaia Collaboration et al. (2021b), which define polygonal regions in the CMD occupied by different types of sources. The bright RGB sources are enclosed within the area defined by these CMD vertexes [$G_{BP}-G_{RP}$, G]: [0.65, 20.50], [0.80, 20.00], [0.80, 19.50], [1.60, 19.80], [1.60, 19.60], [1.00, 18.50], [1.50, 15.843], [2.00, 16.00], [1.60, 18.50], [1.60, 20.50] and [0.65, 20.50]. Further, we selected the supergiant stars. The typical age range of supergiants in

---

[2] https://gea.esac.esa.int/archive/

[3] www.cosmos.esa.int/documents

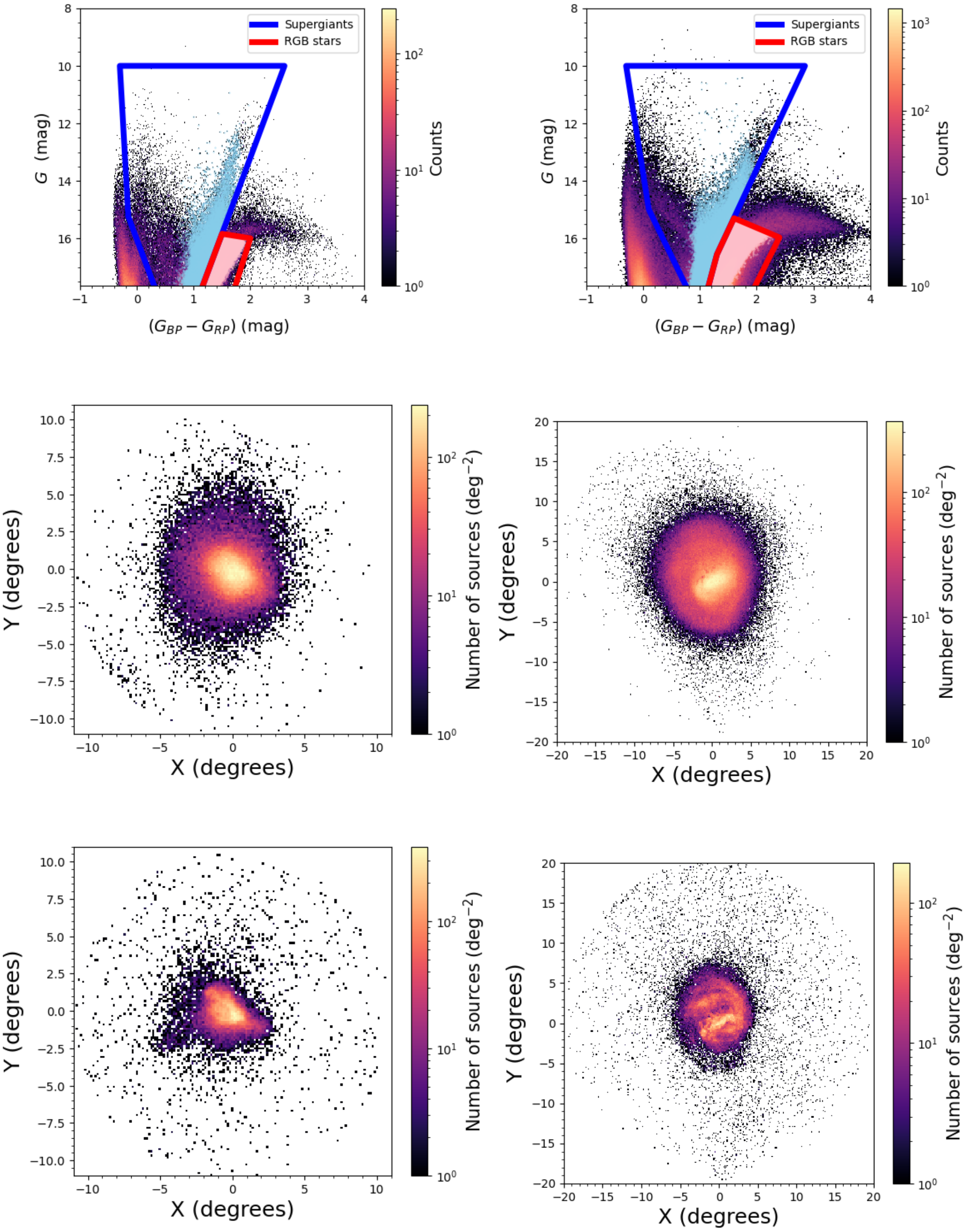

Figure 2.1: *Gaia* DR3 CMD of the SMC (top-left) and the LMC (top-right) sources. In the plots, the regions used to select the supergiants (blue) and the RGB stars (red) are marked. The respective final selections (see text for details) of the RGB stars (pink) and supergiants (light blue) of the Clouds are also over-plotted. The middle-left and bottom-left show the number density distribution of the selected RGB and supergiant sources within ~11 deg of the SMC from its centre (RA = 12.80 deg and Dec = −73.15 deg; Cioni et al. 2000). The middle-right and bottom-right panels show the distribution of the RGB and supergiant sources within ~20 deg of the LMC from its centre (RA = 81.24 deg and Dec = −69.73 deg; van der Marel & Cioni 2001b). The distributions are shown in zenithal equidistant projection coordinates X and Y, as defined in van der Marel & Cioni (2001b). For the LMC we show a de-projected spatial distribution (refer to Section 2.2.2). The colour bar from black to yellow represents the increasing stellar densities in all the plots.

the Clouds is 30–250 Myr (e.g. Gaia Collaboration et al. 2021b). By using the following polygon selection, we separated our supergiant stars which fall in the Blue Loop region from the entire SMC sample, [G_{BP}−G_{RP}, G]: [0.40, 18.15], [−0.15, 15.25], [−0.3, 10.00], [2.60, 10.00], [1.00, 18.50], [0.80, 18.50] and [0.40, 18.15]. Finally, there are 78 833 RGB stars and 39 324 supergiants in our sample. Their spatial distribution is shown in the middle- and bottom-left panels of Figure 2.1, respectively.

2.2.2 Gaia DR3–XP spectra for LMC sources

A similar procedure to the one adopted for the SMC in the previous section is followed to select the LMC sources, but using a 20 deg radius from its centre (RA = 81.24 deg and Dec = −69.73 deg; van der Marel & Cioni 2001b). Our base LMC sample consists of 27 231 400 objects, which includes stellar populations of different ages as shown on the top-right panel of Figure 2.1. Since there are many objects in the LMC and our interest lies in the RGB and supergiant stars, we initially applied the selection criteria provided by Gaia Collaboration et al. (2021b) for extracting these two populations from the CMD. To select LMC RGB sources we use as vertexes of the polygon [G_{BP}−G_{RP}, G]: [0.80, 20.5], [0.90, 19.5], [1.60, 19.8], [1.60, 19.0], [1.05, 18.41], [1.30, 16.56], [1.60, 15.3], [2.40, 15.97], [1.95, 17.75], [1.85, 19.0], [2.00, 20.5] and [0.80, 20.5] and to select LMC supergiants we use instead [G_{BP}−G_{RP}, G]: [0.90, 18.25], [0.1, 15.00], [−0.30, 10.0], [2.85, 10.0], [1.30, 16.56], [1.05, 18.41] and [0.90, 18.25]. The panels on the middle- and bottom-right of Figure 2.1 show the distribution of the selected 520 338 RGB and 99 323 supergiant stars of the LMC, respectively.

The LMC is an inclined disc galaxy, and it is important to de-project the spatial distribution from the sky plane to the galaxy plane. Hence, the inclination (i) of the LMC disc with respect to the sky plane and the position angle of the line of nodes (θ) are taken into account to estimate the de-projected X′ and Y′ coordinates. We applied the recent estimates of i = 23.26 deg and θ = 160.43 deg from *Gaia* Early DR3 (Saroon & Subramanian 2022) and used the distance estimate of ∼50 kpc from de Grijs et al. (2014a). The de-projected spatial distribution is used hereafter for the LMC during the entire analysis.

2.3 Synthetic Strömgren photometry using *Gaia* DR3–XP spectra

Bengt Strömgren introduced a narrow-band photometric system with four (u: 350 nm, v: 410 nm, b: 467 nm and y: 547 nm) bandpass filters (refer to Strömgren 1963, 1964 for more details) covering a similar range as the UBV photometric system. These narrow Strömgren bands are intentionally designed to match the specific signatures in the spectra of stars that directly relate to the physical properties Teff, log g and [Fe/H] and therefore allowed us to classify stars of different spectral classes (Strömgren 1964). Subsequent studies (e.g. Grebel & Richtler 1992) built on the photometric system devised by Strömgren, and derived calibration relations to estimate photometric metallicities of RGB stars (Hilker 2000; Calamida et al. 2007; Hughes et al. 2014; Narloch et al. 2021, 2022; Bellazzini et al.

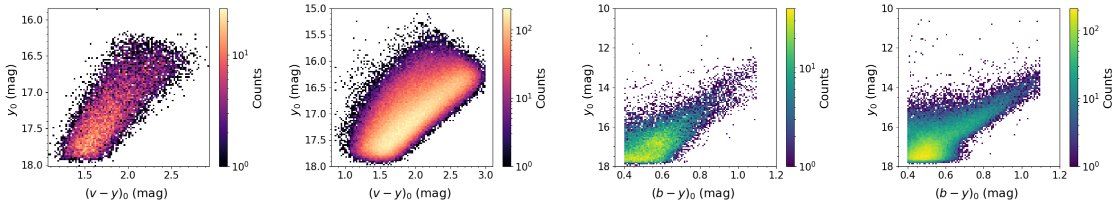

Figure 2.2: Colour-magnitude diagrams depicting the final selection of RGB stars in the SMC (first plot) and those in LMC (second plot), both use Strömgren bands. The third and fourth plots present the CMDs of the final selection for supergiants in the SMC and in LMC, also using Strömgren bands.

2023 and references therein) and supergiants (Grebel & Richtler 1992; Árnadóttir et al. 2010; Piatti et al. 2019). These studies provided metallicity estimates also for stars in the Clouds and of star clusters.

Gaia Collaboration et al. (2022) and De Angeli et al. (2023) explored the details of *Gaia* DR3–XP spectra, and also the generation of synthetic photometry in bands that are covered by the *Gaia* BP/RP wavelength ranges. However, the residual systematics in the externally calibrated XP spectra have larger discrepancies when compared with the existing photometry, notably at $\lambda < 400$ nm. Cordoni et al. (2023) also produced synthetic photometry in BVI bands from the *Gaia* DR3–XP spectra, and validated the accuracy of the synthetic photometric conversion using GaiaXPy by comparing it with literature values. The GaiaXPy is a Python tool from the Data Processing and Analysis Consortium (DPAC) that allows the generation of synthetic photometry in a set of desired systems from the input internally calibrated, continuously represented mean spectra (see Gaia Collaboration et al. 2022 for more details). Gaia Collaboration et al. (2022) used a second-level calibration called standardisation to reproduce existing photometry in several widely used systems to millimag accuracy. Section 4 of Gaia Collaboration et al. (2022) discusses the potential of XP spectra by estimating the synthetic Strömgren magnitudes, as a test case, and deriving photometric metallicities. In our study, we followed a similar method. First, we queried the *Gaia* archive to obtain the *Gaia* DR3–XP spectra for a list of probable SMC and LMC sources. Then, we used the GaiaXPy tool to derive the standardised synthetic Strömgren magnitudes (v, b and y). We note that the standardisation was not done for the u band, and the calibration relations we chose do not utilise it. Hence, we did not use it in our analysis. GaiaXPy also provides us with fluxes and flux errors on each of the Strömgren bands.

2.4 Estimation of photometric [Fe/H]

2.4.1 Calibration relation for RGB stars

In a recent study Bellazzini et al. (2023) estimated the photometric metallicities of Galactic giant stars by utilising synthetic Strömgren magnitudes from *Gaia* DR3–XP spectra. Their metallicities derived from the empirical calibration relations provided by Calamida et al.

(2007), reported in equation (2.1), have a typical accuracy of ≤ 0.1 dex in the range $-2.2 <$ [Fe/H] < -0.4 dex. They also found a systematic trend with [Fe/H] at a higher metallicity, beyond the applicability range of the calibration relation. Metallicities derived using the Hilker (2000) calibration are less precise, and show particularly lower accuracy in the metal-poor regime when compared with the spectroscopic metallicities from APOGEE.

$$[\mathrm{Fe/H}] = \frac{(m_{1,0} - \gamma * (v-y)_0 - \alpha)}{\delta * (v-y)_0 + \beta}, \tag{2.1}$$

where $\alpha = -0.312$, $\beta = -0.096 \pm 0.002$, $\gamma = 0.513 \pm 0.001$, $\delta = 0.154 \pm 0.006$ and $m_1 = (v-b) - (b-y)$.

In this study, we used the Calamida et al. (2007) calibration to calculate the iron abundance [Fe/H] of the SMC and LMC RGB stars. To correct for extinction, we used the reddening maps of the Clouds provided by Skowron et al. (2021), where the extinction is estimated using the red clump giant stars. Their maps cover areas corresponding to a distance from the centre of the galaxies of 2.5 deg for the SMC and 6.5 deg for the LMC. In the outer regions, which are not covered in Skowron et al. (2021) maps, the extinction is corrected by using the all-sky reddening map of the MW provided by Schlegel et al. (1998). The maps provide median $E(B-V)$ values, and for each of the sources in our study, we used the nearest region to obtain their extinction values. The reddening values $E(V-I)$ provided by Skowron et al. (2021) can be converted into $E(B-V)$ by using the recalibration by Schlafly & Finkbeiner (2011). As the recalibration suggests, we translated the $E(V-I)$ into $E(B-V)$ by $E(B-V) = (E(V-I)/1.237) \times 0.86$. We obtain the dereddened colour indices, $m_{1,0} = m_1 + 0.24 \times E(B-V)$, $(v-y)_0 = (v-y) - 1.24 \times E(B-V)$, and $(b-y)_0 = (b-y) - 0.74 \times E(B-V)$ using the equation from Crawford & Mandwewala (1976).

The applicability range of equation (2.1) is $0.85 \leq (v-y)_0 \leq 3$, which reduces our SMC and LMC RGB samples to 78 473 and 512 367 sources, respectively. Then, using equation (2.1), we estimate the photometric metallicities of the SMC and LMC RGB stars, finding a significant spread. On further investigation, it is clear that this is due to those sources with magnitude uncertainties in each band > 0.1 mag; eliminating them resulted in 57 512 SMC and 214 603 LMC RGB stars. The CMDs in Figure 2.2 clearly illustrate the range of $(v-y)_0$ colours of our selected RGB stars in the SMC (first plot) and LMC (second plot) using Strömgren bands, which are also over-plotted in the *Gaia* CMDs (Figure 2.1). We followed the error propagation to estimate the uncertainties on the metallicities, and the estimated median error of both samples is around 0.6 dex. In Figure 2.3, the distribution of the estimated metallicities (top-left) and the estimated errors (bottom-left) for both galaxies are provided. The estimation of [Fe/H] involved multiple quantities, all of which were propagated which resulted in large uncertainties. The distribution shows that the majority of the sources have uncertainties <1 dex, with on average larger values for supergiants than for RGB stars. We did not limit the uncertainties of the metallicities in our study, which is then based on the full sample.

2.4.2 Calibration relation for supergiant stars

To estimate the metallicities of the supergiant stars, we used the empirical relations provided by Grebel & Richtler (1992), and reported in equation (2.2). They successfully performed a feasibility study to apply this equation to the supergiants in the young stellar cluster NGC 330, and also to some field stars of the SMC around the cluster. Later, a study by Piatti et al. (2019) applied this relation to estimate the metallicities of the supergiant stars in selected young clusters of the Clouds.

$$[\mathrm{Fe/H}] = \frac{(m_{1,0} + a_1 * (b-y)_0 + a_2)}{a_3 * (b-y)_0 + a_4}, \tag{2.2}$$

where $a_1 = -1.240 \pm 0.006$, $a_2 = 0.294 \pm 0.030$, $a_3 = 0.472 \pm 0.040$ and $a_4 = -0.118 \pm 0.020$.

We followed the same method as explained in Section 2.4.1 to estimate the reddening values. Then, we estimated the extinction values in the visual band $A_V = 3.1 \times E(B-V)$. We used the translation equation from Cardelli et al. (1989) and we estimated the extinction in each Strömgren band by using $A_v = 1.397 \times A_V$, $A_b = 1.240 \times A_V$ and $A_y = 1.005 \times A_V$. The applicability range of equation (2.2) is $0.4 \leq (b-y)_0 \leq 1.1$ and this reduced the SMC sample to 21 207 sources and the LMC sample to 71 628 sources. Using equation (2.2), we estimated the photometric metallicities of the supergiant sources in both galaxies. Similarly to the RGB stars, we removed sources with magnitude uncertainties in each band > 0.1 mag, which results in 20 713 SMC and 69 083 LMC supergiants. Figure 2.2 shows the range of $(b-y)_0$ colours for our selected supergiant stars in the SMC (third plot) and LMC (fourth plot) using the Strömgren bands. The distribution of the estimated metallicities of the SMC and LMC supergiants are shown on the top-right panel of Figure 2.3. We also estimated the uncertainties for our [Fe/H] values using error propagation, and obtained a median error of around 0.8 dex for the SMC and around 0.6 dex for the LMC samples. The propagated error distribution for both galaxies are shown in the bottom-right panel of Figure 2.3. As for RGB stars, no further reduction has been applied based on the errors.

We chose to utilise the Grebel & Richtler (1992) calibration for supergiants and the Calamida et al. (2007) for our RGB samples for the following reasons. Calamida et al. (2007) offers a new empirical metallicity calibration using $(u-y)$ and $(v-y)$ colours, which are more sensitive to temperature across a broader metallicity range of $-2.2 <=$ $[\mathrm{Fe/H}] <= -0.7$ dex, providing an advantage over Grebel & Richtler (1992). Additionally, Bellazzini et al. (2023) successfully applied the Calamida et al. (2007) calibration for estimating metallicity in Galactic giant stars, yielding accurate results. However, Gaia Collaboration et al. (2023a) noted that this calibration, based on older globular clusters, may introduce systematic offsets when applied to younger systems, such as open clusters, due to intrinsic age differences. In contrast, despite its limited sources, the Grebel & Richtler (1992) calibration is applicable to red supergiants, making it more suitable for our purpose of estimating metallicities for these stars.

2.5 Results

2.5.1 Metallicity distributions

The histograms in the top-left and top-right panels of Figure 2.3 depict the metallicity distributions of the RGB stars and supergiants of the Clouds, respectively. We excluded sources with [Fe/H] and uncertainties outside the broad range illustrated in Figure 2.3, resulted in 271 843 RGB stars and 89 599 supergiants in the Clouds after removing duplicate sources in the outskirts. By comparison, the overall metallicity of the SMC RGB stars is lower than that of the LMC, as expected, which is also the case for the supergiants. For both populations, we obtained unimodal metallicity distributions in agreement with the previous studies (Carrera et al. 2008; Dobbie et al. 2014b; Choudhury et al. 2016b; Grady et al. 2021; De Bortoli et al. 2022). These literature metallicity distributions also show significant asymmetries, with sharp declines towards the metal-rich ends, and extended tails towards the metal-poor ends (see e.g. Grady et al. 2021). We do not see these trends in our metallicity distributions, probably because of the large errors on the individual metallicity estimates (Figure 2.3). We recognise that while the shape of our metallicity distributions may have limitations due to larger uncertainties, our focus is on the mean (median) metallicities because our main goal is to produce maps of the mean metallicity and mean metallicity gradients. To further compare the metallicity distributions, we estimated the peak and dispersion values by fitting a Gaussian to each of the histograms. The peak metallicity and the dispersion of the LMC RGB stars is −1.19±0.51 dex, whereas for the supergiants, it is −0.58±0.77 dex. In the SMC, the RGB stars show a peak metallicity and a dispersion of −1.47±0.49 dex while that of the supergiants is of −1.08±0.54 dex. There could also be larger systematic errors in these estimates, for instance, caused by errors in the calibration or between the RGB stars and the supergiants. Grady et al. (2021) estimated the median metallicity of RGB stars within 12 deg of the LMC to be −0.78 dex. Haschke et al. (2012) obtained a mean [Fe/H] of −1.50±0.24 dex based on RR Lyrae stars in the LMC. Previous studies such as Dobbie et al. (2014b) and Choudhury et al. (2016b) found the median [Fe/H] to be about −1 dex from the analysis of RGB stars in the inner 4–5 deg of the SMC. Carrera et al. (2008) also quotes a similar value of −1 dex for RGB stars in the inner region, but they also note a decrease of the median value towards the outer region of the galaxy. In the SMC, Haschke et al. (2012) obtained −1.70±0.27 dex based on RR Lyrae stars. Our estimates for both the LMC and SMC RGB stars are lower compared to the median values estimated previously. This could be due to the fact that our metallicity distributions include stars in large areas encompassing the SMC and LMC outer regions, which are predominantly populated by metal-poor and old stars. However, a recalibration of our metallicities using the APOGEE data shows a systematic difference of about 0.4 dex (see Section 2.5.2), which would bring our estimates in line with those from previous studies. If we were to limit our sample by applying cuts based on the individual metallicity errors (e.g. 0.3 dex), it would be reduced to only a few thousand sources. Irrespective of our large uncertainties, we see that our median metallicity estimates align with those from previous studies. Hence, we did not apply further cuts in order not to reduce the statistical significance of our analysis. We examined our initial selection of photometric and astrometric cuts to assess

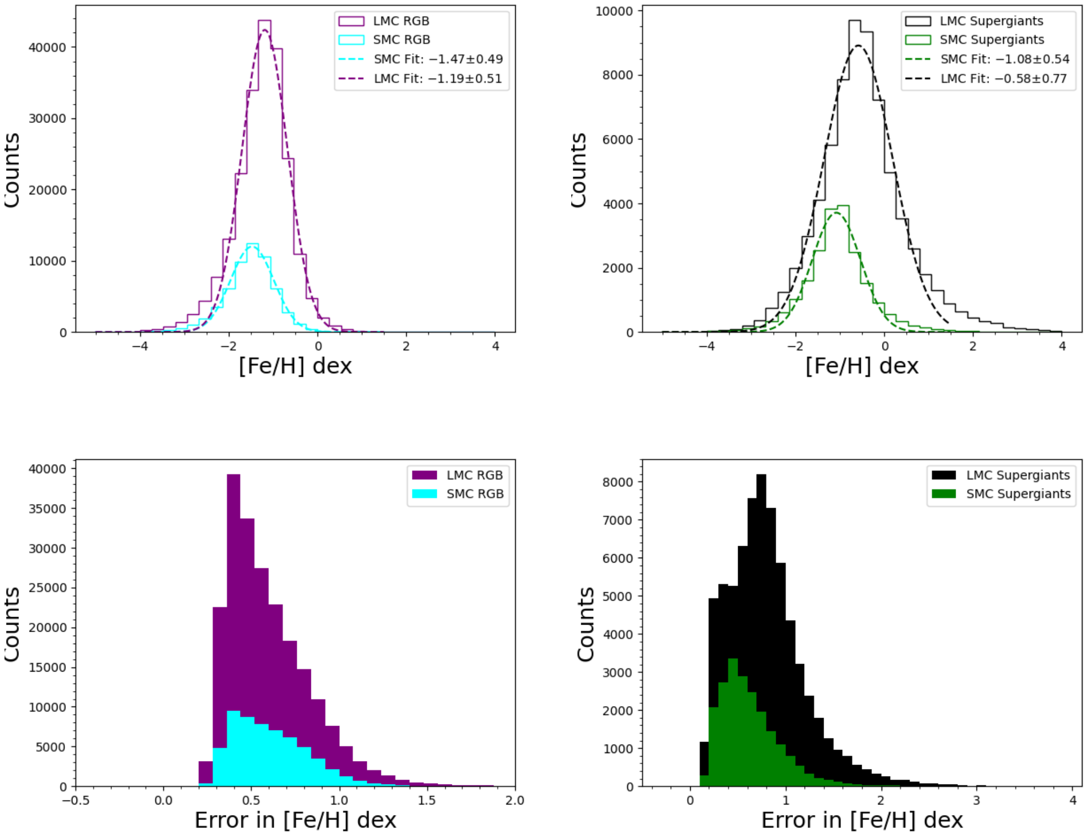

Figure 2.3: Metallicity distributions of RGB (top-left) and supergiant (top-right) stars of the LMC and SMC samples. Best-fit Gaussians for the SMC (cyan) and the LMC (purple) are shown on the histograms. The distributions of the estimated uncertainties are also shown for RGB stars (bottom-left) and for supergiants (bottom-right). Best-fit Gaussians for the SMC (green) and the LMC (black) are marked.

how different criteria impact the resulting metallicity distributions. Our findings indicate that the metallicity distributions (Figure 2.3) remain unchanged when using *ruwe* ≤1.2, and applying a photometric error of <0.1 mag instead of <0.22 mag as adopted in all three *Gaia* bands.

2.5.2 Photometric metallicity recalibration

In order to validate the estimates of the photometric metallicities of the RGB and supergiant samples from our work, we compared them with the spectroscopic metallicities from APOGEE. APOGEE is a high-resolution (R∼22 000), near-infrared (*H* band; 1.51−1.7 μm) spectroscopic sky survey. In the southern sky, observations are performed with the 2.5m du Pont telescope at Las Campanas Observatory, Chile. The initial samples of sources in the LMC and SMC regions were ∼70 000. Though the survey mainly focused on the RGB stars, it also included main sequence stars, asymptotic giant branch (AGB) stars and post-AGB stars. The details on the target selection are explained in Zasowski et al. (2017). The ASPCAP (APOGEE Stellar Parameters and Chemical Abundances Pipeline) calculates the stellar parameters and elemental abundances. We cross-matched the APOGEE sources with the *Gaia* DR3 data, to select the most probable members of the Clouds and retain those with parallax ≤ 0.2 mas which eliminates foreground MW sources within ∼5 kpc. Furthermore, we applied the proper motion selections ($1 \leq \mu_\alpha \leq +2.5$ mas yr^{-1} and $-0.8 \leq \mu_\delta \leq 1.5$ mas yr^{-1}) to identify the most probable LMC sources (Saroon & Subramanian 2022). This selection criteria removes many sources, and we are left with a sample of ∼14 135 sources. Along with the cut in the parallax to remove the foreground contamination from the MW, we also discarded the SMC sources whose proper motions lie outside the expected range ($-3 \leq \mu_\alpha, \mu_\delta \leq +3$ mas yr^{-1}) as predicted by the simulations (Diaz & Bekki 2012) for the main body and stellar tidal features around the SMC. We recalibrated our photometric estimates to match the zero-points of both our samples (Appendix 2.A). This is done by cross-matching the APOGEE sample of the SMC and LMC RGB sources with our samples after the elimination of sources with large photometric uncertainties. The crossmatched sources (4308) then have both the spectroscopic metallicity estimates from APOGEE $[\mathrm{Fe/H}]_{\mathrm{spec}}$ and the photometric metallicity estimates from our study $[\mathrm{Fe/H}]_{\mathrm{phot}}$. We estimated the peak of $[\mathrm{Fe/H}]_{\mathrm{spec}}$ and $[\mathrm{Fe/H}]_{\mathrm{phot}}$ from Gaussian fitting and computed their difference, which is about -0.43 ± 0.02 dex, for both the SMC and the LMC RGB samples. This value is used to obtain the recalibrated metallicities such as $[\mathrm{Fe/H}]_{\mathrm{recal}} = [\mathrm{Fe/H}]_{\mathrm{phot}} + 0.43$ dex. Bellazzini et al. (2023) also used a similar method to recalibrate the metallicity estimates of their MW sources. Following a similar procedure for supergiant stars, we found 1212 crossmatches with APOGEE. The peak difference obtained is -0.35 ± 0.01 dex. Hence, the recalibrated metallicities is obtained as $[\mathrm{Fe/H}]_{\mathrm{recal}} = [\mathrm{Fe/H}]_{\mathrm{phot}} + 0.35$ dex. Bellazzini et al. (2023) found a smaller shift of about 0.14 dex for MW stars. The spatial distribution of the Clouds (see Figure 2.1) indicates that there is a decreasing completeness towards the centre of the galaxies. This suggests an increased level of crowding that can lead to blending and contamination of XP spectra. This may impact our estimation of the photometric metallicities, especially at the centre of the Clouds (Rathore et al. 2025b). In this context, to better understand the larger shifts obtained in our study, we performed a test to determine whether the peak difference between our photometric metallicities and spectroscopic sample decreases as we move away from the centre of the Clouds (refer to Section 2.B and Figures 2.13 and 2.14).

2.5.3 Radial recalibration

To maintain consistency in our recalibration with respect to the spectroscopic sample, it is essential to account for variations in the recalibration zero point. This consideration is particularly significant in regions affected by crowding, as they will experience the most impact from radial bias when applying uniform recalibration throughout the galaxy. Our analysis of the two galaxies was conducted separately for the RGB stars. It is evident from the top two rows of Figure 2.13 that the peak differences change from the centre to the outskirts. In the bottom-left panel of Figure 2.13, we observed that the radial variation of the LMC RGB peak difference is significantly larger at the centre (0.7 dex) than at the outskirts. As we move outward, this difference decreases to 0.3 dex, and then slightly increases to 0.5 dex in the outer regions. However, in the outer bins, the distribution of sources becomes less clear due to the reduced number of stars present. The important factor contributing to these larger shifts could be crowding, causing an increased spectral contamination. Therefore, radial recalibration is applied to the RGB stars in the LMC. For the defined radial bins shown in Figure 2.13, we utilised the corresponding peak difference rather than a constant value. In contrast, the third row of Figure 2.13 shows that the RGB stars in the SMC did not exhibit significant radial differences and have larger standard deviations. As a result, we opted for a consistent recalibration factor of 0.4 dex across the entire SMC.

We encountered limitations regarding the SMC supergiants due to an insufficient number of cross-matched sources from the APOGEE survey. This indicates that significant differences may not be detectable between our photometric and spectroscopic samples. Therefore, we did not further separate the LMC and SMC supergiants (Figure 2.14). The middle plot in the bottom panel of Figure 2.14 primarily represents the SMC supergiant stars based on their radial distance. For all supergiant stars, we observed an overall constant difference of 0.4 dex, with a variation of approximately 0.1 dex only in the bin corresponding to the radial range of 3–4 kpc. Given the large standard deviations, we applied a constant recalibration factor of 0.4 dex.

2.5.4 Metallicity maps of the RGB and supergiant stars

We produced the metallicity maps for the young (supergiants) and the old (RGB stars) stellar populations separately. In order to do that, we combined the RGB sources from both the SMC and the LMC and removed any duplicate sources, as our initial selection of the LMC and SMC areas overlap in their outer regions. Then, we created a two-dimensional Hess distribution (a density plot) colour-coded with the median of the metallicity of each bin, using the recalibrated metallicity estimates, since the median is less prone to the effect of outliers. The left panel of Figure 2.4 shows the metallicity map of the RGB stars, where each bin corresponds to 0.25 deg^2. Although we tend to have fewer sources in the outskirts of the Clouds than in their inner regions, their overall distribution is a large improvement over the stellar density from previous spectroscopic metallicity studies. The central regions of the LMC reveal a metal-rich inner disc and a southern spiral arm. The bar is not obvious, and we note that at its centre, the metallicity is low, but this area is also influenced by a lack of sources in our sample due to crowding. The median value of each bin represents the underlying population accurately only with a sufficient number of stars, especially when individual measurement uncertainties are significant. To address this, we created metallicity maps using Voronoi binning as shown in Figure 2.5. Here, we adopted equal density binning, ensuring that each bin has 100 sources, based on the median error derived from Markov chain Monte Carlo (MCMC) simulations (refer to section 2.C for more details). In the left panel of Figure 2.5, we show the metallicity distribution of RGB stars in the Clouds. The LMC's central region has a higher metallicity (yellow-green shades), while the SMC displays a scattered, lower metallicity distribution (greener to purple regions). The outer regions of both galaxies transition into lower metallicities, consistent with the expectation that older, less metal-enriched stars dominate the outskirts. This spatial variation reflects the galaxies' evolutionary histories, with stronger star formation and chemical enrichment at the centres. The gradient from higher to lower metallicity corresponds to typical dwarf galaxy evolution models, while small-scale variations signal complex star formation histories. We also created Voronoi binning plots for the median uncertainty in each bin (see Figure 2.16).

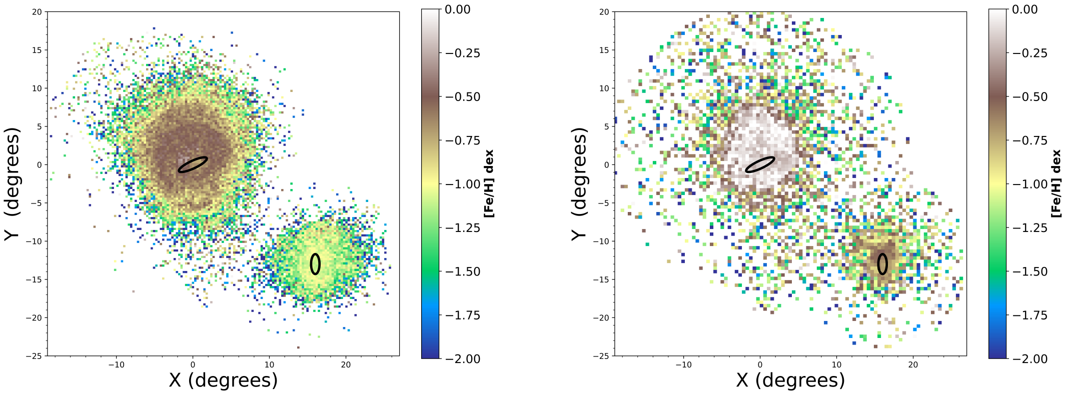

Figure 2.4: Strömgren photometric metallicity maps of RGB (left) and supergiant (right) stars of the Clouds derived from the *Gaia* DR3–XP spectra. Each spatial bin corresponds to 0.25 deg^2 and 0.5 deg^2 for the RGB and supergiant stars, respectively. The maps are centred at RA = 81.24 deg and Dec = −69.73 deg; (van der Marel & Cioni 2001b). The bar regions of both galaxies are marked with black ellipses. The colour-coding from blue to white shows the increasing median metallicity values. We note the larger relative difference between the LMC and SMC metallicity in the supergiants than in the RGB stars. The distribution of RGB stars, which contains fainter sources than that of supergiants, at the core of the galaxies may be affected by a lack of sources due to crowding.

Recently Frankel et al. (2024) produced a metallicity map of the entire LMC using total metallicity estimates ([M/H]) from Andrae et al. (2023). Their maps confirm an extended disc between −1.6 dex and −0.8 dex compared to a smaller disc at metallicities below −1.6 dex or above −0.8 dex. The bar region dominates at all metallicities, but spiral features are not as prominent as in our map. Grady et al. (2021) provided the metallicity maps of the Clouds using the *Gaia* DR2 data. Their maps also reveal a metal-rich LMC bar and a metal-rich SMC centre. In the outer regions, the metallicity further decreases, as we see also in our maps. The right panel of Figure 2.4 provides the metallicity map of the supergiant (young) stars of the Clouds using bins with a size of 0.5 deg^2 due to the reduced number of sources. Similarly to the most metal-rich maps by Frankel et al. (2024), we trace the extent of the inner LMC disc superimposed to a wide metal-poor outer region, but we do not find a clear enhancement corresponding to the bar of the galaxy. In the SMC, our map clearly traces a metal-rich bar-like feature at its centre, which is however, metal-poor than at the centre of the LMC. The young populations are metal-rich than the old ones, as previously noticed (Figure 2.3), and their spatial distribution differs. A similar trend can be seen in the right panel of Figure 2.5, which shows the Voronoi-based metallicity distribution of supergiants in the Clouds. Each bin has 100 stars, and the colour

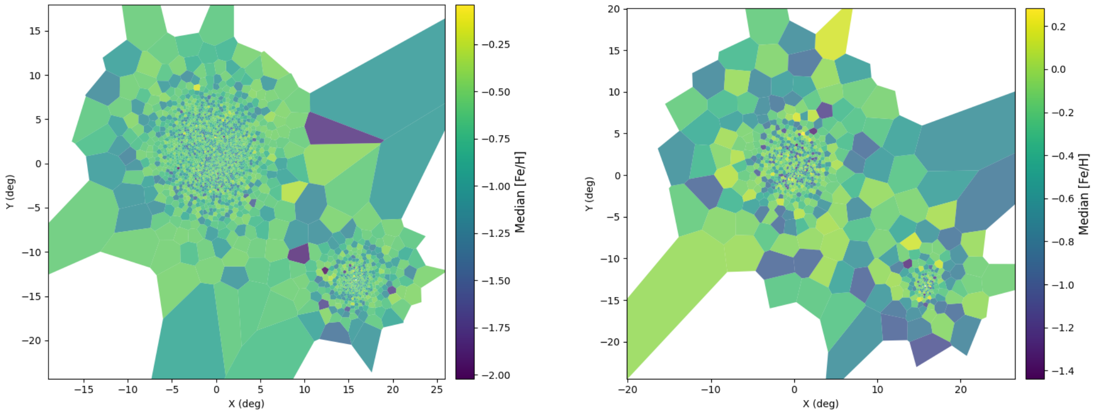

Figure 2.5: Strömgren photometric metallicity maps of RGB (left) and supergiants (right), respectively. These maps were produced using the Voronoi binning method, where each bin has 100 sources. The colour-coding from green to yellow indicates an increase in the metallicity.

scale indicates metallicity levels, with yellow representing high metallicity and purple indicating low metallicity. These findings align with previous research, such as Grady et al. (2021), which highlighted the LMC's inside-out formation and the SMC's bursty star formation history. Additionally, Frankel et al. (2024) noted the impact of interactions between the LMC and SMC on their metallicity distributions, further explaining the observed differences. Both of these works utilised different machine learning methods, which shows dependency on their respective training samples. For example, in Figure 8 of Frankel et al. (2024), it is evident that the difference in [M/H] estimates between their work, and the APOGEE DR17 sources is less than 0.2 dex for G≤16.5 and less than 0.4 dex at fainter magnitudes, which is closer to the 0.43 dex of constant recalibration as we obtained for the RGB sample in our study. But the figure also includes differences from other spectroscopic surveys, which show a wider range than the APOGEE DR17 data. It is important to note that a large number of sources from APOGEE were used to train the XGBoost algorithm (Andrae et al. 2023) utilised by Frankel et al. (2024). Therefore, the observed smaller differences could be biased due to this training on APOGEE DR17 data. Both of these works demonstrate the ability of data-driven methods to estimate the photometric metallicities for a larger sample of stars, but focused exclusively on the older population. This is understandable, as there is a larger amount of spectroscopic data available for the RGB stars to train such models. In contrast, our work aims to estimate the metallicities of a larger sample of stars that includes both young and old stellar populations using the same method. This approach is particularly beneficial for galaxies such as the Clouds, where studying populations of different ages is essential to understanding their complex interaction history.

2.5.5 Metallicity gradient of RGB stars

To further explore the metallicity distribution of the SMC and LMC RGB stars, we derived the metallicity gradients separately for the two galaxies as a function of distance from their corresponding centres. In the SMC, we first converted the distance from degrees

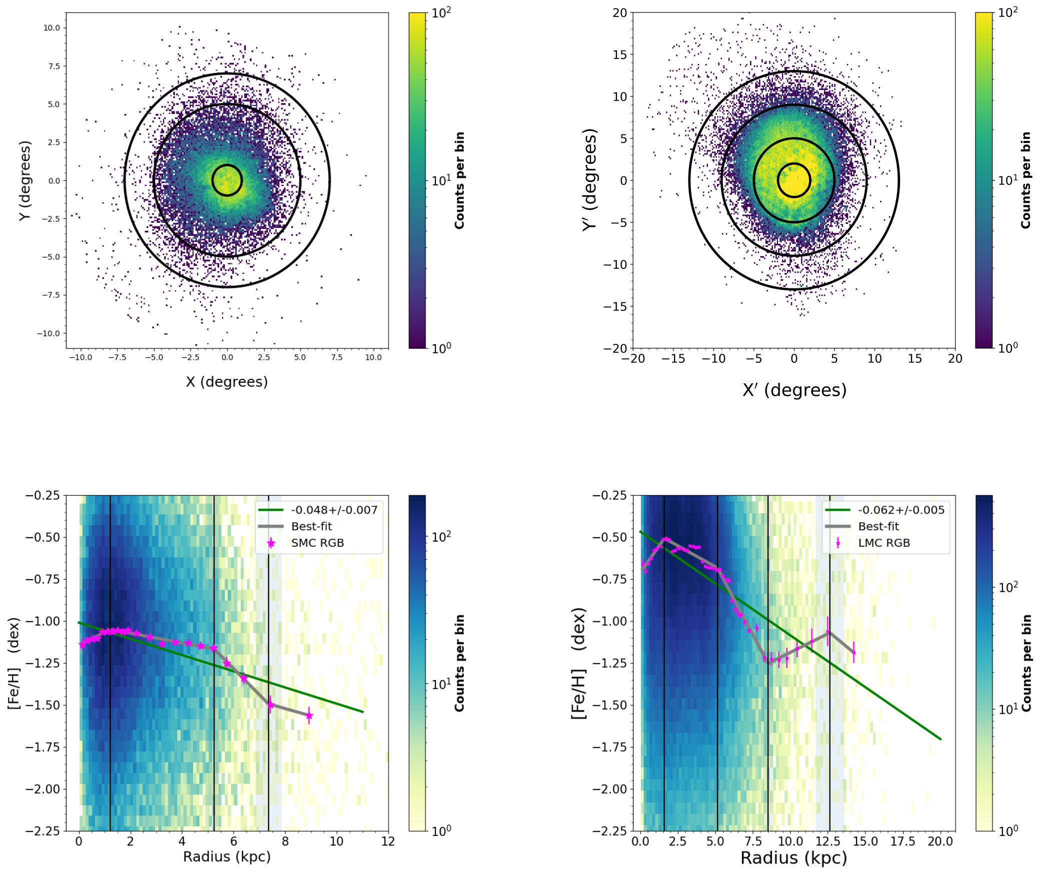

Figure 2.6: Distribution of RGB stars within the SMC (top-left) and the LMC (top-right) with superimposed annular rings of breakpoints marked in the corresponding lower panels. The plots show the metallicity gradients for the SMC (bottom-left) and LMC RGB stars (bottom-right). The median metallicities of the annular bins are marked with pink stars along with their standard errors. Linear best-fits are marked with green and the piecewise-regression fits are marked with grey. The black vertical lines show the division of different segments or the location of the breaks in the gradient. In both panels, a Hess diagram shows the density distribution of the sources colour-coded such that blue shows the regions with the highest stellar density.

into kpc by using 62 kpc × tan(radius), where 62 is the distance to the galaxy from de Grijs & Bono (2015a). Then, we radially binned the sources into 0.2 kpc steps up to 2 kpc from the centre. We used 0.5 kpc steps up to 6 kpc, 1 kpc steps up to 8 kpc and combined the rest of the sources until 11 kpc into a single sub-region. We chose radial bins of different radii due to the decreasing stellar density from the centre towards the outskirts. The number of sources in each bin ranges from around 550 to a few thousand in the central bins to around 270 in the outer ones. The metallicity gradient of the SMC RGB stars as a function of distance is shown in the bottom-left panel of Figure 2.6. For this, we calculated the median metallicities in each of the radial bins and also their respective standard errors. We used the Python module curve-fit to find the estimate of the best-fit metallicity gradient. We observed a linearly decreasing trend, and a negative metallicity gradient of -0.048 ± 0.007 dex kpc^{-1}. In the figure, the gradient is superimposed on the distribution of the estimated individual stellar metallicities.

Table 2.1: Best-fit radial metallicity gradient for the SMC sources.

RGB		Supergiants	
Distance (kpc)	Gradient (dex kpc^{-1})	Distance (kpc)	Gradient (dex kpc^{-1})
0 − 1	0.079±0.014	0 − 1	0.148±0.086
1 − 5	−0.029±0.003	R >1	−0.058±0.008
5 − 7	−0.155±0.014		
R >7	−0.043±0.011		
0 − 11	−0.048±0.007	0 − 11	−0.045±0.007

Although we can estimate the overall gradient by using a linear fit, it is evident from the median values that the slope changes are not uniform across the SMC, but there are breaks in the gradient. To quantify these changes in the slope, we used the Python module piecewise-regression or segmented regression (Pilgrim 2021a). This module is particularly useful in estimating the different slopes in the dataset without having to fit different slopes in different regions. This module uses an iterative method to identify breakpoint positions and simultaneously fits a linear regression model to data that includes one or more breakpoints corresponding to the gradient's changes. This makes it computationally efficient and allows for robust statistical analysis. We iterated the fit over various numbers of breakpoints, starting from zero, which means no breaks in the overall gradient until the model converges. Then we obtain the Bayesian information criterion (BIC), which takes into account the value of the likelihood function to avoid over-fitting and choose the number of breaks where the BIC is minimum as the best-fit model. For the SMC, the best-fit model has three breaks, and we have four regions with different gradient values. All these breakpoints are marked as black concentric circles in Figure 2.6 (top-left). The different regions and their gradients are provided in Table 2.1.

We followed the same procedure to estimate the metallicity gradient of the LMC RGB stars. One difference is that the LMC metallicity gradient is quoted as a function of the de-projected distance. Then, using 50 kpc × tan(radius), where 50 is the distance to the galaxy from de Grijs et al. (2014a), we obtained the de-projected distance in kpc. Also, in comparison with the SMC, our LMC sample is larger, and hence we redefined the size of our radial bins as follows. We radially binned the sources into 0.2 kpc steps up to 7 kpc from the centre. Then, we used 0.5 kpc steps up to 10 kpc, 1 kpc steps up to 13 kpc and combined the rest of the sources until 20 kpc into a single sub-region. The median metallicity of each of these sub-regions is estimated along with their standard errors and shown in Figure 2.6. The linear best-fit for the overall metallicity gradient is also shown and suggests an increasing metallicity until ~2.5 kpc from the centre. Although in these regions we can have the highest stellar density, *Gaia* DR3 is incomplete and sources are still missing. The metallicity gradient corresponds to -0.062 ± 0.005 dex kpc^{-1}. Our best-fit model for the segmented regression returns four breakpoints, and hence five line segments with different gradients are as given in Table 2.2. The overall metallicity gradient for the entire region is also provided at the bottom of the table. The breakpoints are marked as concentric circles in Figure 2.6 (top-right). To facilitate the comparison with previous studies, we repeated the analysis by using radial bins in degrees. The resulting metallicity gradients for the SMC and LMC RGB stars are given in the top-left and top-right panels of Figure 2.17, respectively, and the values are provided in the appendix.

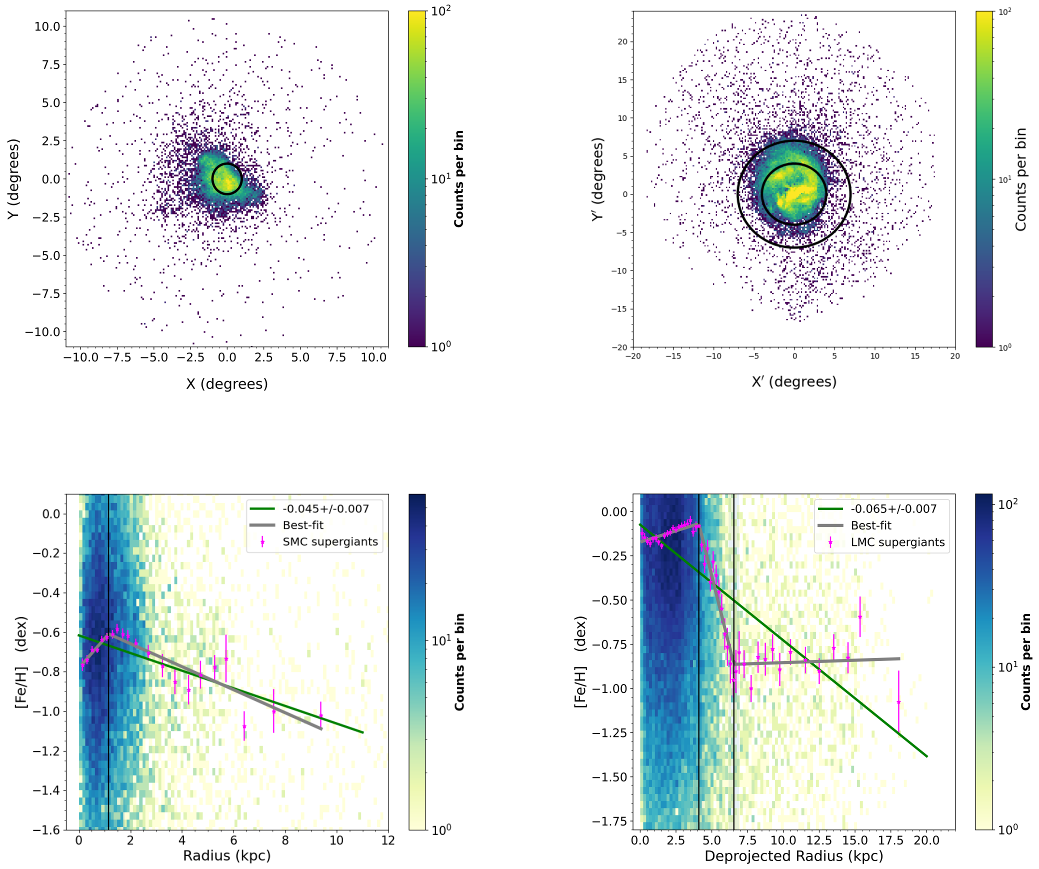

Figure 2.7: Same as Figure 2.6 but for supergiants.

2.5.6 Metallicity gradient of supergiants stars

We present here the metallicity gradient as a function of the distance (kpc) of the young supergiant stars in both the SMC and the LMC. We used the same radial binning that was applied to the SMC RGB sample. The metallicity gradients of the supergiant stars are shown in Figure 2.7 (bottom). We also used the same Python curve-fit module to fit the median metallicities of different radial bins and derive the best-fits. In the SMC, we find a linearly decreasing trend in the metallicity distribution, and the estimated metallicity gradient is −0.045±0.007 dex kpc^{-1}. The best-fit for the piecewise-regression method has only one break around 1 kpc corresponding to two gradient values. We redefined our radial binning for the LMC supergiant sources. For the LMC supergiants, we radially bin the sources into 0.2 kpc steps up to 7 kpc from the centre. Then, we use 0.5 kpc steps up to 10 kpc, 1 kpc steps up to 16 kpc and combined the rest of the sources until 20 kpc into a single sub-region. In the LMC, we find a peculiar trend in the median metallicities of the supergiant stars, which can possibly be due to their intrinsically non-uniform spatial distribution. Most of these sources are concentrated in the bar region and in the major spiral arm of the LMC. At about 5 deg from the LMC centre, the stellar density drops rapidly, where the median metallicities tend to decrease abruptly. Towards the outskirts of the LMC, the stellar density distribution is very low but more or less uniform, and hence the median metallicity values seem to flatten. The estimated metallicity gradient from the LMC supergiants is −0.065±0.007 dex kpc^{-1}. The best-fit for the piecewise-regression is obtained with two breaks and three gradients. In the inner region, we have a positive metallicity gradient, and then we have negative gradients with a break around 4 kpc. Beyond 7 kpc, we obtain an almost flat gradient value. The different regions and their metallicity gradients for the SMC and the LMC supergiants are provided in Table 2.1 and 2.2, respectively.

Table 2.2: Best-fit radial metallicity gradient for the LMC sources.

RGB		Supergiants	
Distance (kpc)	Gradient (dex kpc^{-1})	Distance (kpc)	Gradient (dex kpc^{-1})
0 − 2	0.127±0.026	1 − 4	0.025±0.014
2 − 5	−0.050±0.008	4 − 7	−0.325±0.036
5 − 9	−0.169±0.011	R >7	0.003±0.006
9 − 13	0.044±0.016		
R >13	−0.074±0.027		
0 − 20	−0.062±0.005	0 − 20	−0.065±0.007

2.5.7 Metallicity catalogue

The final catalogues for all the sources with estimated [Fe/H], recalibrated using the APOGEE values, are published with this study. As an example, the estimated [Fe/H] values along with the reddening values and other parameters characterising the individual sources (Gaia DR3 Source IDs, coordinates at the epoch J2016.0, Strömgren magnitudes, and distances from the centre of the galaxies) are shown in Table 2.3.

Table 2.3: Catalogue of the estimated [Fe/H] for RGB stars in the SMC.[†]

Gaia Source ID	RA[‡] (deg)	Dec (deg)	v (mag)	b (mag)	y (mag)	D (deg)	D (kpc)	E(B−V) (mag)	A_*V* (mag)	[Fe/H] (dex)	[Fe/H]_*err* (dex)
4688748623761036544	5.05237	−73.28698	18.829	17.607	16.816	2.413	2.612	0.034	0.106	−0.851	0.418
4688746978787018496	4.79228	−73.23919	19.181	17.931	17.065	2.482	2.687	0.029	0.088	−1.229	0.397
4688748902932208256	5.01639	−73.26982	19.341	18.045	17.223	2.421	2.621	0.034	0.106	−0.811	0.502
4688748078298643072	4.75311	−73.19900	19.238	18.081	17.320	2.490	2.696	0.047	0.144	−0.829	0.549
4688749006011415424	5.11183	−73.25140	19.395	18.305	17.702	2.391	2.589	0.034	0.106	0.147	0.730

[†] The full table and a similar table for the supergiants as well as tables for the LMC sources are available at the CDS.

[‡] The RA and Dec coordinates are truncated here for the purpose of visualisation and are given as obtained from *Gaia* DR3 in the online version.

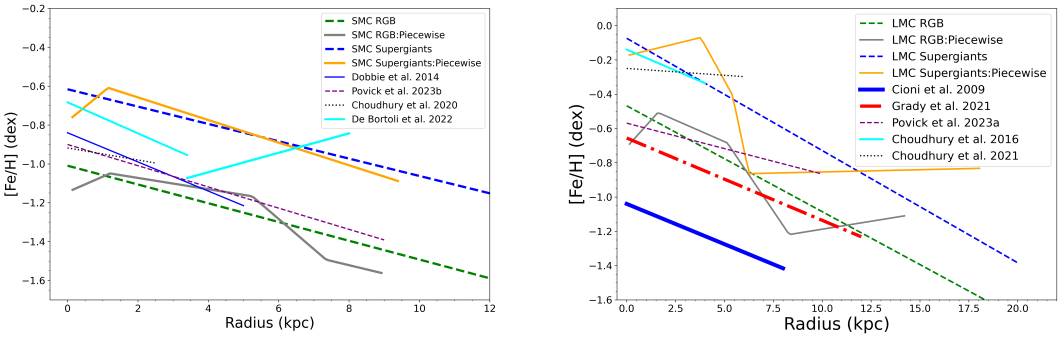

Figure 2.8: Comparison of the radial metallicity gradients of the SMC (left) and the LMC (right) from this work with those from the literature.

2.6 Discussion and conclusions

In this work, we estimated the photometric metallicities from *Gaia* DR3–XP spectra using the synthetic Strömgren photometry. We used the different calibration relations from the literature to derive the [Fe/H] abundance of the RGB (old, >3 Gyr old) and the supergiant (young, <300 Myr old) stars in the SMC and the LMC. We also compared our photometric metallicity estimates with the spectroscopic metallicities from APOGEE to validate our method. We used our photometric metallicities to create metallicity maps with a spatial resolution of 0.25–0.5 deg^2 covering a wide area of the Clouds for both stellar populations. We also computed metallicity gradients with respect to the centres within both galaxies. Our choice of the centres should not influence the gradients because the central and smallest bins correspond to a circular diameter of 0.4 kpc (about 0.4 deg), which includes other estimated centres (e.g. Niederhofer et al. 2021a, 2022b). In the left panel of Figure 2.8, we show the comparison of the radial metallicity gradients obtained in our study for the SMC.

2.6.1 SMC gradient

In our study, the estimated overall metallicity gradient of the SMC RGB stars is −0.048±0.007 dex kpc^{-1}, which is very similar to the gradient obtained for the supergiants (−0.045±0.007 dex kpc^{-1}) out to 11 deg (~10 kpc) from the SMC centre. Povick et al. (2023b) explored the metallicity estimates of the RGB stars from APOGEE and found a similar overall metallicity gradient of −0.0545±0.0043 dex kpc^{-1} for the SMC stars out to ~9 kpc. Previously Choudhury et al. (2020) used the RGB slope as an indicator of the average metallicity and estimated a metallicity gradient of −0.031±0.005 dex deg^{-1} within 2.5 deg of the centre of the galaxy, finding also a rather flat gradient beyond this distance. This is shallower than our current overall estimates but is in good agreement with the gradient we find from RGB stars located within 1–5 deg −0.029±0.003 dex kpc^{-1}. The steeper gradient we find up to 1 kpc from the centre (0.079±0.014 dex kpc^{-1}) might be influenced by the incompleteness of our dataset due to crowding. In the outer regions, the gradient first decreases steeply, the slope is higher than in the innermost regions, and then shows a flattening. A previous study by Parisi et al. (2016) also found, using star clusters, a change of slope at about 5 kpc, suggesting an upturn of the gradient until 8 kpc. In this less gravitationally bound region, the imprints of dynamical interactions are strong and there are existing sub-structures (e.g. El Youssoufi et al. 2021) which may influence the metallicity distribution. The supergiants also show an increase and then a decrease in the metallicity gradient. Our estimated best-fit for the inner region up to 1 kpc is 0.148±0.086 dex kpc^{-1} and beyond that it is −0.058±0.008 dex kpc^{-1}. The only breakpoint we find in the centre could again be the result of crowding and not an actual breakpoint in the metallicity gradient.

The spectroscopic study by Dobbie et al. (2014b) estimated an RGB metallicity gradient of −0.075±0.011 dex deg^{-1} out to 5 deg from the centre. Later, Taibi et al. (2022) derived the radial metallicity gradients of several Local Group galaxies, recalibrating the metallicity estimates from Dobbie et al. (2014b). Although they have not provided metallicity gradients for different regions across the SMC, their smoothed SMC radial metallicity profile excellently matches the metallicity gradient of SMC RGB stars in our study. Interestingly, they also see a positive gradient up until 1 kpc from the SMC centre, which was not clearly seen or noted in other studies. Then, their gradient decreases until 4 kpc, slightly increases until 5 kpc and then decreases further until 7 kpc in line with the trends found in this study. We note that a change of slope at ∼4 kpc could be deduced from Figure 2.6, but it is not sufficiently strong to be picked up in our analysis as a separate breakpoint. De Bortoli et al. (2022) estimated a negative gradient of −0.08±0.03 dex deg^{-1} in the inner region ($<$ 3.4 deg), but a positive or null gradient in the outer region 0.05±0.02 dex deg^{-1} derived from the analysis of SMC field stars. Their values are comparable to the main-body cluster metallicity gradients derived in the same study. However, they do not find any separate metallicity gradient for their metal-rich and metal-poor clusters.

Although our estimated overall metallicity gradient seems to overlap with previous studies, it can still be seen that the gradient in different regions differs considerably. One reason could be how we are projecting the SMC stars and estimating the gradients, as the SMC has a large line-of-sight depth and a complex structure. Taking this into account, Dias et al. (2022) showed that any projected radial metallicity gradient cannot be seen when using the real three-dimensional (3D) physical distances to the clusters. Our dataset does not consist of any standard candles to estimate distances based on them. Also, at the distance of the Clouds, estimating the 3D distances for individual stars is not trivial.

2.6.2 LMC gradient

For the RGB stars across the entire LMC, we obtained an overall metallicity gradient of −0.062±0.005 dex kpc^{-1}, whereas for supergiants we obtained a negative gradient of −0.065±0.007 dex kpc^{-1}. In the right panel of Figure 2.8, we show the comparison of the radial metallicity gradients obtained in our study for the LMC. A recent study by Povick et al. (2023a) estimated a metallicity gradient of the LMC to be −0.02966±0.00171 dex kpc^{-1} out to a radial distance of ∼10 deg using spectra of RGB stars from APOGEE, which is shallower than our estimations. They also detect a steepening of the abundance gradients in the inner region of the galaxy for populations younger than 2 Gyr. Grady et al.

(2021) utilised the *Gaia* DR2 data and estimated metallicities using a machine learning method to obtain −0.048±0.001 dex kpc^{-1} out to ~12 deg. Also, a previous estimate from Cioni (2009) using the AGB stars in the LMC found a linearly decreasing gradient of −0.047±0.003 dex kpc^{-1} out to ~8 kpc from the centre. A study by Choudhury et al. (2016b) estimated photometric metallicities and found a similar [Fe/H] trend in the LMC as −0.049±0.002 dex kpc^{-1} out to ~4 kpc. In a later study using the VMC data of the RGB stars, Choudhury et al. (2021) estimated a metallicity gradient of −0.008±0.001 dex kpc^{-1} out to a radius of ~6 kpc from the LMC centre. This value compares well with our measurement in 2−5 kpc, whereas the overall gradient is somewhat lower compared to the previous studies, probably because our study extends to 20 deg and includes the outskirts of the galaxy, where there is a relatively large number of metal-poor stars.

Our best-fit for the piecewise-regression fit estimates of the metallicity of RGB stars results in four different gradients for the entire LMC. In the very centre until 2 kpc, we get a positive gradient of 0.127±0.026 dex kpc^{-1}. This is the region that mostly encompasses the bar, which has both young and old stars. Also, this is the region that is subject to crowding. In a way, the first breakpoint in the gradient more or less separates the bar from the rest of the galaxy. From 2 to 5 kpc, representing the inner disc of the LMC, we find a gradient of −0.050±0.008 dex kpc^{-1}. A recent study by Rathore et al. (2025b) finds that the angular momentum section of the inner disc is misaligned with respect to the outer disc, which can be reproduced in simulation by a recent collision with the SMC. In our study, a break in the metallicity gradient at 5 kpc corresponds to a transition in the amount of misalignment, which suggests a possible link between the two behaviours. The misaligned inner disc, influenced by the SMC interaction, may have played a role in the chemical enrichment processes, leading to the differing metallicity profiles. In the regions from 5 to 9 kpc, we find a very steep decrease in the gradient corresponding to −0.169±0.011 dex kpc^{-1} and in the outskirts beyond 9 until 13 kpc, we obtained a positive gradient of 0.044±0.016 dex kpc^{-1}. This outer disc region hosts different tidal sub-structures and has been mostly influenced by the interactions from the MW and also the SMC, its closest companion. Beyond 13 kpc, we again see a negative gradient of −0.074±0.027 dex kpc^{-1}.

Our best-fit piecewise-regression fit for the supergiants provides two breaks in the metallicity gradient, and the supergiants look more complex than the RGB stars. In the inner region up to 4 kpc, we obtained a positive gradient of 0.025±0.014 dex kpc^{-1}. Similarly to the RGB stars, we can see that the bar region is enclosed within the first breakpoint. For the region between 4 to 7 kpc, we see a much steeper gradient of −0.325±0.036 dex kpc^{-1}. This region includes part of the prominent northern spiral arm, where young stars are forming. Moreover, it exhibits a significant decline in stellar density, which leads to the steep gradient observed here. Additionally, the breakpoint around 4 kpc also suggests a link with the misalignment of the angular momentum (Rathore et al. 2025a), which implies a connection between the LMC's dynamical response to the collision and its chemical evolution. Beyond 7 kpc, we do not have many stars, but the gradient seems to flatten into 0.003±0.006 dex kpc^{-1}.

Feast et al. (2010) derived the metallicity gradient out to 6 kpc from the LMC centre using two different period-metallicity relations for RR Lyrae stars. They estimated a linearly decreasing gradient of −0.0104±0.0021 dex kpc^{-1} and −0.0145±0.0029 dex kpc^{-1}, whereas Haschke et al. (2012) obtained a gradient of -0.03 ± 0.07 dex kpc^{-1} using RR Lyrae stars up to 14 kpc from the LMC centre. They also estimated the gradient only in the innermost 8 kpc and obtained a shallower value of $-0.010\pm$ 0.014 dex kpc^{-1}. Wagner-Kaiser & Sarajedini (2013) derived instead a gradient of -0.0270 ± 0.02 dex kpc^{-1}. In the inner 2–5 kpc we also find a shallower gradient, from the RGB stars, compared to the measurements by Feast et al. (2010) and Haschke et al. (2012). By including regions further away, we also find a decreasing trend for the overall distribution of stars. We note that the RR Lyrae stars are at least 10 Gyr old and represent a stellar population that is on average older than our RGB stars.

2.6.3 Concluding remarks

The main goal of our study is to validate the potential usage of *Gaia* DR3–XP spectra to estimate the individual [Fe/H] values across a wide area encompassing the Clouds. This method can be applied to sources fainter than 17.65 mag from the next *Gaia* data releases to study even larger samples and confirm or refine our findings. The metallicity gradients estimated in this work and in comparison with the literature values show that different tracers do not show the same trends. Compared to previous studies, different trends are also present for tracers that cover different spatial regions. The metallicity gradient results from the combination of different physical processes: the chemical enrichment from stellar evolution, the accretion of gas or stars and the process of radial migration, as well as dynamical interaction displacing stars within galaxies. The present-day LMC and SMC have a complex structure, and to quantify which process dominates at a given distance and for a given stellar population, we need to also study azimuthal variations, which we plan to address in our next study focused on sub-structures.

In the near future, the [Fe/H] as well as the abundance of other chemical elements for a large number of stars making up the range of stellar populations present in the Clouds will be obtained with the new multi-object spectroscopic facilities 4MOST (de Jong et al. 2019) and MOONS (Gonzalez et al. 2020). In particular, 4MOST will target about 200 000 RGB stars and 60 000 supergiants across ~1000 deg^2 from the One Thousand and One Magellanic Clouds fields survey (Cioni et al. 2019), whereas MOONS will focus on RGB stars at specific locations during guaranteed-time observations. These spectra, combined with photometric investigations, will provide an unprecedented view of the system, increasing not only the size of the statistical spectroscopic samples but also the number of diagnostics to study its origin and evolution. Yuxi et al. (2023) has shown the possibility of inferring birth radii for individual stars using cosmological simulations in galaxies such as the LMC. They obtain ~25% median uncertainties for individual stars if accurate metallicities and ages are available, further supporting a promising application of our results. Our findings highlight the complexity of metallicity gradients and their dependence on different stellar tracers, spatial coverage, and physical processes shaping the evolution of the Clouds.

Acknowledgments

We thank the referee for their constructive and insightful comments on our paper. AOO acknowledges support from the Indian Institute of Astrophysics during her visit. SS acknowledges support from the Science and Engineering Research Board of India through a Ramanujan Fellowship and support from the Alexander von Humboldt Foundation. AOO is grateful to the European Space Agency (ESA) for support via the Archival Research Visitor Programme during her stay at ESTEC. BD acknowledges support by ANID-FONDECYT iniciación grant No. 11221366 and from the ANID Basal project FB210003. This work has made use of data from the ESA mission *Gaia* (https://www.cosmos.esa.int/gaia), processed by the *Gaia* Data Processing and Analysis Consortium (DPAC, https://www.cosmos.esa.int/web/gaia/dpac/consortium). Funding for the DPAC has been provided by national institutions, in particular, the institutions participating in the *Gaia* Multilateral Agreement.

Appendix

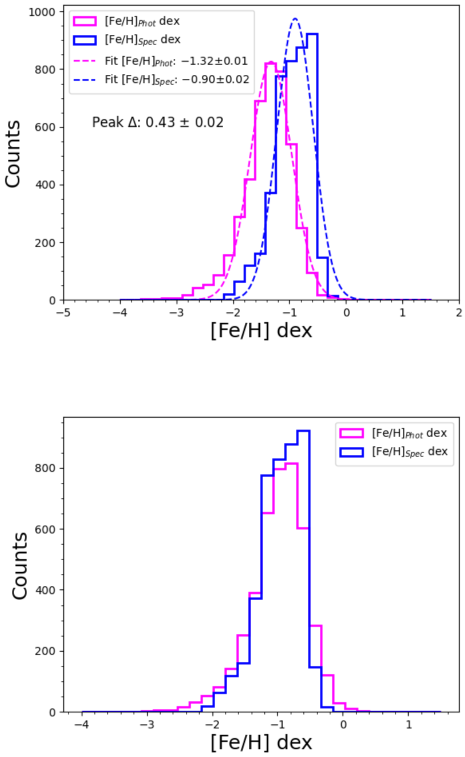

Figure 2.9: Histograms of the LMC and SMC sources used for recalibration. On the top panel, the estimated photometric (Phot; blue) metallicities are plotted together with the spectroscopic (Spec; pink) metallicities as measured. On the bottom panel photometric metallicities are exploited after the addition of systematic difference.

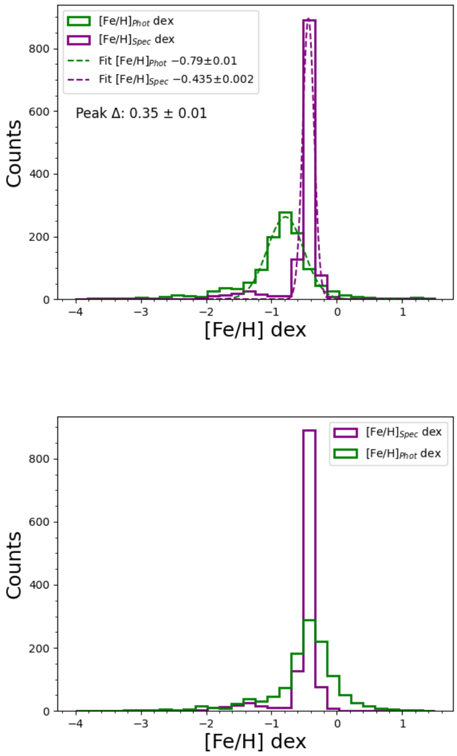

Figure 2.10: Same as Figure 2.9 but for the supergiant sources.

2.A Metallicity recalibration using APOGEE

Figure 2.9 shows the metallicity distribution of the RGB sources in common between our sample and APOGEE. We fitted Gaussians to both histograms and estimated the peak and dispersion of each sample. The photometric metallicity peaks at −1.32±0.01 dex and the spectroscopic metallicity peaks at −0.90±0.02 dex; hence the peak difference is 0.43±0.02 dex. We added this difference to our estimated photometric metallicities. The bottom panel shows that after applying a shift, both samples match. We also provided the metallicity distribution plots for the supergiant sources in the top panel of Figure 2.10. The photometric and spectroscopic peaks of the supergiants are −0.79±0.01 dex and −0.435±0.002 dex. The bottom panel shows that after adding 0.35±0.01 dex to the photometric metallicity, both samples match.

To provide a quantitative idea of the residual bias and dispersion with respect to spectroscopic measures, the top panel of Figure 2.11 shows the density histograms of photometric metallicities vs spectroscopic metallicities of RGB stars in the Clouds. In the bottom panel, we plotted the difference in the photometric and spectroscopic samples over the recalibrated metallicities. We fitted a line and the estimated slope is 0.45 with a constant of −0.33. We tested using these values to recalibrate our metallicities rather than just adding the peak difference estimates. Our overall gradients for the RGB sources of both Clouds did not change even by employing this recalibration, but we noticed larger uncertainties, which would then propagate into the analysis of the gradient. The top panel of Figure 2.12 shows the photometric metallicities vs spectroscopic metallicities of the supergiants in the Clouds. In the bottom panel, the difference is plotted against the recalibrated values. Here, we do not see a clear slope for the RGB stars. The estimated slope for the supergiants is 0.13 with a constant value of −0.41. With this calibration, uncertainties for the supergiants would be ever larger.

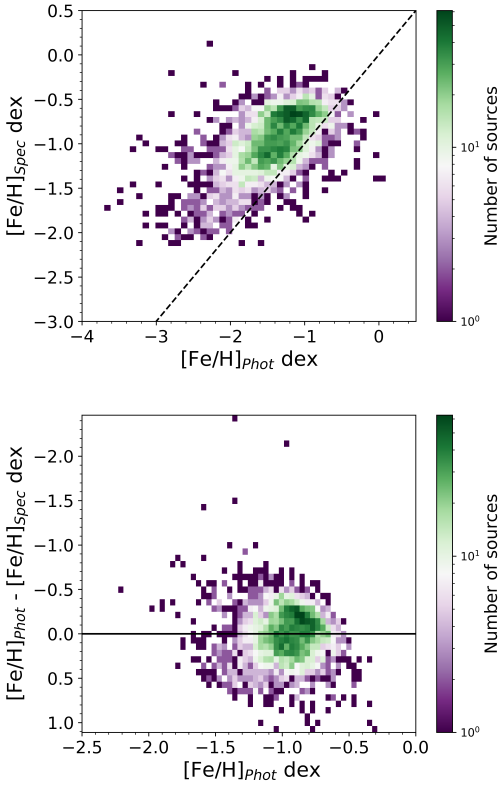

Figure 2.11: Photometric [Fe/H] versus spectroscopic [Fe/H] of the RGB sources are shown on the top panel. The dotted line marks the one-to-one relation. In the bottom panel, photometric [Fe/H] (recalibrated with the slope and constant) is plotted against the difference between them. The colour bar from violet to green shows the increase in stellar density.

2.B Estimation of peak difference based on radius

Crowding can cause blending and contamination of XP spectra, affecting our estimation of photometric metallicities, especially at the centre of the Clouds. To investigate whether we are observing any amplitude shift from the centre to the outskirts of the Clouds, we divided the area into various annular sub-regions from the respective centres. We plotted the distribution of photometric and spectroscopic metallicities for the LMC RGB stars in the top two rows of Figure 2.13, and for the SMC RGB stars in the third row. The radial variation of the shifts from the respective centres are shown in the bottom-left for the LMC RGB stars and bottom-right for the SMC RGB stars. The same analysis was conducted for the supergiant stars and shown in Figure 2.14. For both distributions, we fitted Gaussians to identify the peak and standard deviation values for each radial region.

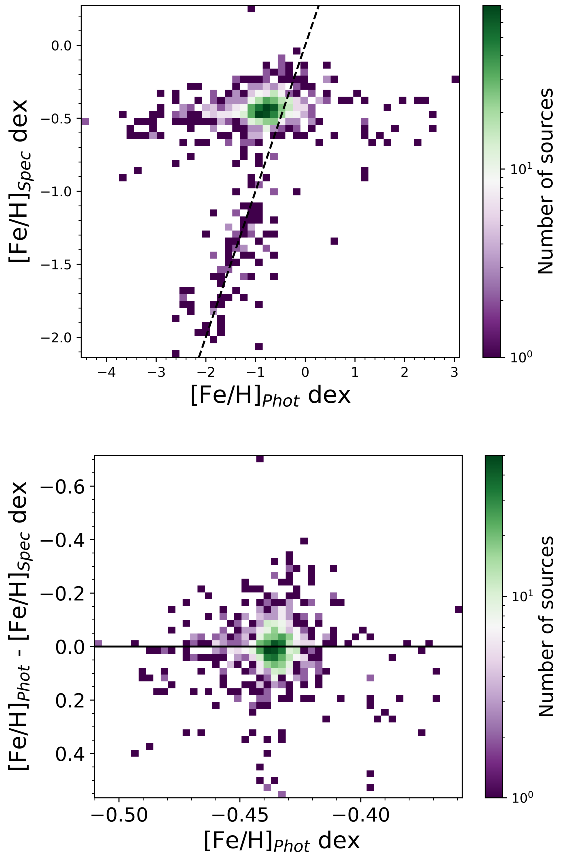

Figure 2.12: Same as Figure 2.11 but for the supergiant sources.

2.C Voronoi binning

In this section, we outline the methodology used to determine an optimal number of sources for plotting the Voronoi metallicity maps of RGB stars and supergiants. To determine a sensible number of sources in each bin, we utilised MCMC simulations. The procedure was as follows: we drew random samples ranging from 10 to 1000, in steps of 10, from our entire dataset and conducted 100 simulations for each sample to determine the median error of [Fe/H]. The results produced a Gaussian distribution, which we fitted to estimate the peak and the associated dispersion, which is our median error for each run. The number of sources is plotted against this error for RGB stars and supergiants (see Figure 2.15). Our analysis revealed that for both RGB stars and supergiants, the error of the sample approached ~0.1 dex when each bin included 100 sources. Consequently, we created a Voronoi metallicity map, ensuring that each of our bins contained 100 sources. Given the significant differences between our LMC and SMC samples, we generated the Voronoi metallicity maps separately for improved visualisation. To facilitate easier interpretation of uncertainties associated with each bin of our Voronoi metallicity maps, we also produced a similar Voronoi binning map where we show the median of the [Fe/H] error in each of the bins. In Figure 2.16, the top (RGB stars) and bottom (supergiants) panels show the median error of our metallicity distributions of the LMC (left) and the SMC (right).

2.D Radial [Fe/H] gradient of the SMC and LMC sources in degrees

The overall metallicity gradient as a function of distance (in degrees) is shown in Figure 2.17. For both populations in the SMC, we first radially binned the sources into 0.2 deg steps up to 2 deg from the centre. Then we used 0.5 deg steps up to 6 deg, 1 deg steps up to 8 deg and combined the rest of the sources until 11 deg into a single sub-region. The estimated overall metallicity gradient for the SMC RGB stars is −0.053±0.007 dex deg^{-1}, and the overall metallicity gradient estimated for the SMC supergiants is very similar −0.047±0.008 dex deg^{-1}. For the LMC RGB stars and supergiants, we divided the sources into radial bins of 0.2 deg up to 7 deg from the centre and then use 0.5 deg bins up to 10 deg. Due to the lower number density, we made some adjustments for the RGB stars and supergiants. For the RGB stars, we used 1 deg bins up to 13 deg, while for the supergiants, we used 1 deg bins up to 16 deg. Finally, we combined the remaining sources into a single sub-region up to 20 deg. The estimated overall metallicity gradient for the LMC RGB stars is −0.055±0.005 dex deg^{-1}. The overall metallicity gradient estimated for the LMC supergiants is −0.066±0.006 dex deg^{-1}.

Table 2.4: Best-fit metallicity gradient of the SMC sources in degrees.

RGB		Supergiants	
Distance (deg)	Gradient (dex deg^{-1})	Distance (deg)	Gradient (dex deg^{-1})
0 − 1	0.100±0.034	0 − 1	0.190±0.126
1 − 5	−0.029±0.005	R >1	0.058±0.008
5 − 7	−0.174±0.024		
R >7	0.065±0.017		
0 − 11	−0.053±0.007	0 − 11	−0.047±0.007

Table 2.5: Best-fit metallicity gradient of the LMC sources in degrees.

RGB		Supergiants	
Distance (deg)	Gradient (dex deg^{-1})	Distance (deg)	Gradient (dex deg^{-1})
0 − 2	0.114±0.02	0 − 5	0.025±0.007
2 − 5.5	−0.044±0.005	5 − 6	−0.192±0.022
5.5 − 10	−0.147±0.008	6 − 8	−0.385±0.076
10 − 12	0.112±0.043	8 − 12	0.026±0.018
R >12	−0.012±0.016	R >12	−0.017±0.008
0 − 20	−0.055±0.005	0 − 20	−0.066±0.006

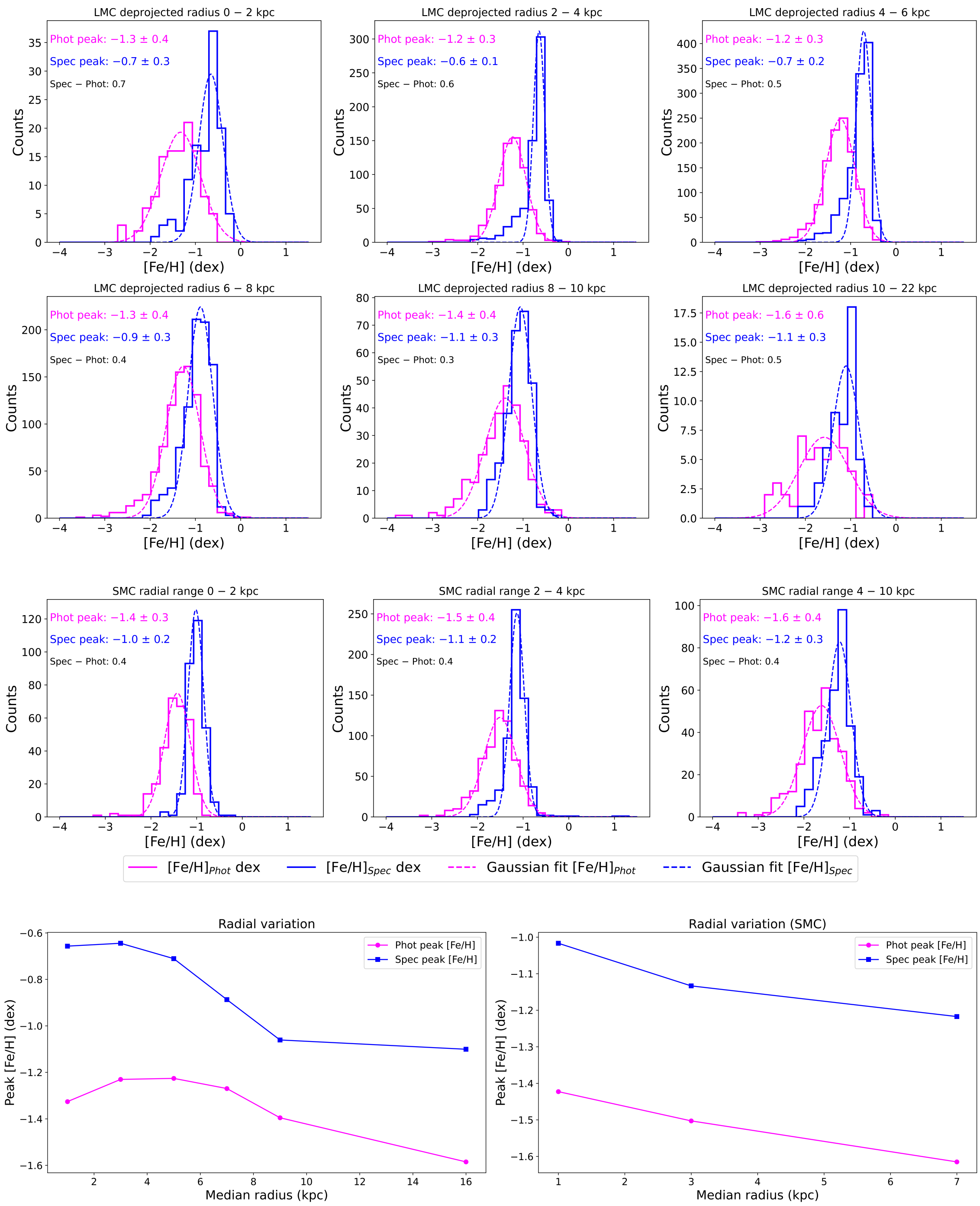

Figure 2.13: Radial variation of Photometric versus Spectroscopic metallicities in RGB Stars of the Clouds. The top and middle rows display the peak differences between the photometric (Phot; blue) and spectroscopic (Spec; pink) RGB samples, calculated for various radial ranges from the centre of the LMC. The third row presents similar data for the RGB stars in the SMC. Both peaks are fitted, and the peak values are shown in the last row: on the left for the LMC and on the right for the SMC, which illustrates the radial variation of the shifts from the respective centres.

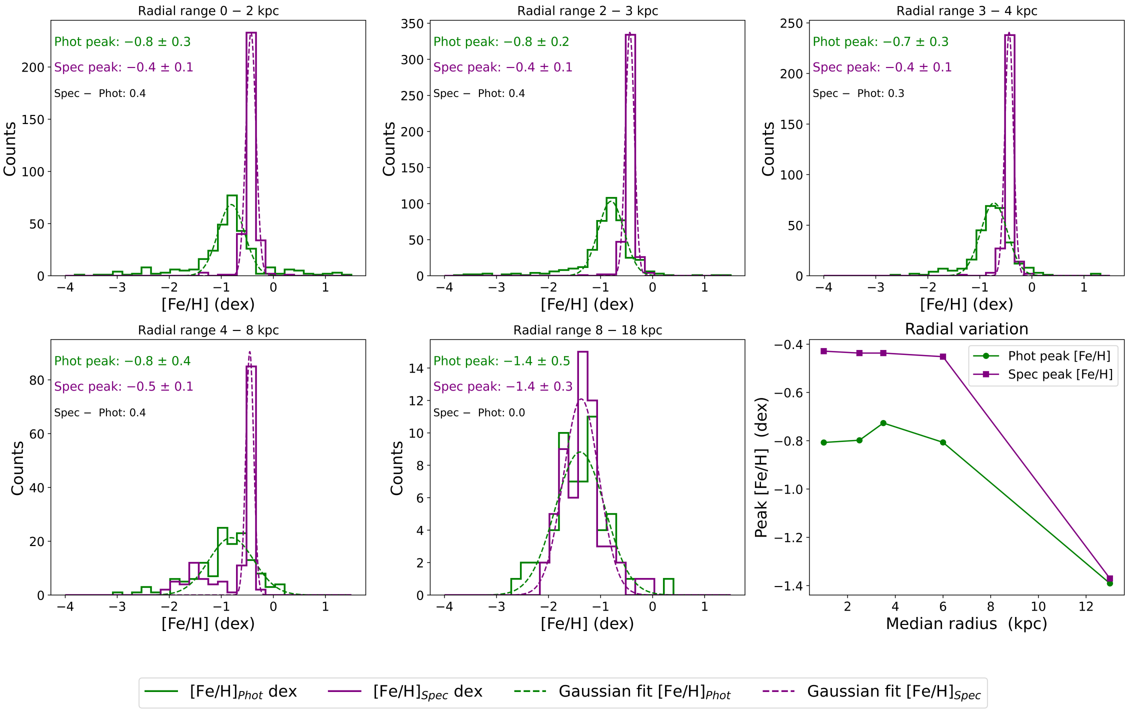

Figure 2.14: Same as Figure 2.13 but for the LMC and SMC supergiant stars together.

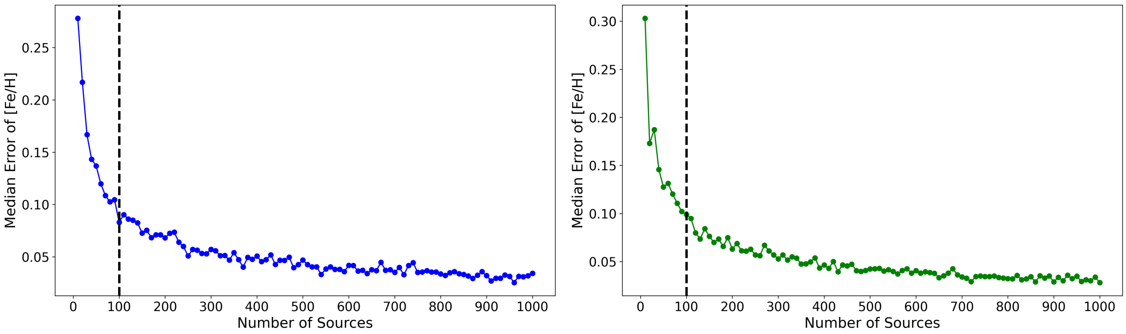

Figure 2.15: Median error of [Fe/H] plotted against the number of sources in each bin for RGB (left) and supergiant (right) stars in the Clouds. Dotted vertical lines at 100 sources indicate the limit adopted in our study.

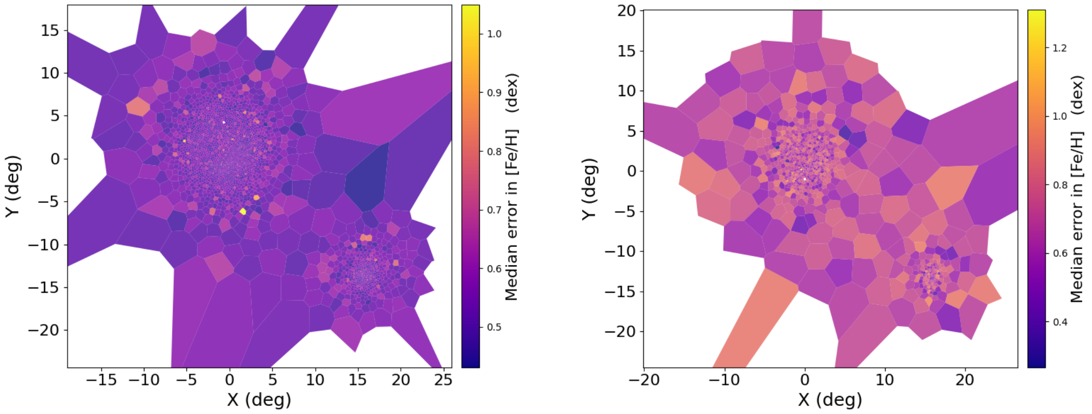

Figure 2.16: Maps showing the median error in the metallicity of RGB stars (left) and supergiants (right) of the Clouds. These maps are produced using the Voronoi binning method, where each bin has 100 sources. The colour-coding from purple to yellow indicates an increase in the median error.

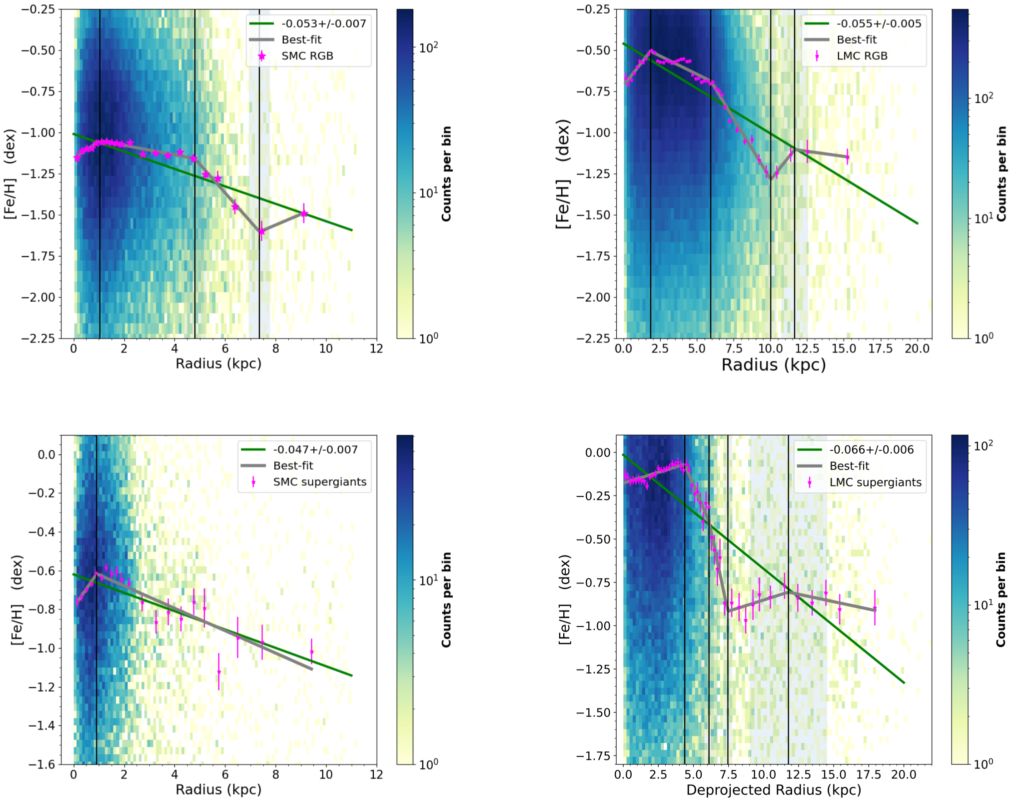

Figure 2.17: Radial metallicity gradient (in degrees) for the RGB (top) and supergiant (bottom) stars for SMC (left) and LMC (right). In all panels, the increasing stellar density is colour-coded from purple to yellow. The median metallicities of the annular regions are marked with pink stars along with their standard errors. Linear best-fits and segmented best-fits are shown in green and grey, respectively. The black vertical lines show the division of different segments at the location of the breaks in the gradients. Underlying Hess diagrams show the source-density distributions.

3 Investigating the origin of periphery stellar substructures of the Clouds using photometric metallicities

Abinaya O. Omkumar, Maria-Rosa L. Cioni, Smitha Subramanian, Jos de Bruijne & Bruno Dias

The draft of this chapter is in preparation for submission in the Astronomy & Astrophysics journal

3.1 Introduction

The Milky Way's two most notable satellites, the Large Magellanic Cloud (LMC) and the Small Magellanic Cloud (SMC), serve as the closest pair of gas-rich interacting galaxies with ongoing star formation. The LMC is situated at a distance of 50 ± 2 kpc (de Grijs et al. 2014a). It features an inclined disc, an off-centred bar (Bekki 2009; Subramaniam & Subramanian 2009), a single spiral arm, and indications of warped structures (Olsen & Salyk 2002; Choi et al. 2018a; Saroon & Subramanian 2022). Nearby to the LMC in the sky, the SMC is located at 62 ± 1 kpc (de Grijs & Bono 2015a) and is categorised as a dwarf irregular galaxy. A wing-like structure extends towards the LMC, also known as the SMC wing. Previous studies have identified a significant line-of-sight depth ~20 kpc in the eastern SMC (Nidever et al. 2013; Dias et al. 2021; Parisi et al. 2024). Another interesting feature is a gaseous bridge, known as the Magellanic Bridge (MB), connecting these two galaxies, which was first observed by Hindman et al. (1963). Later, stellar counterparts were detected (Irwin et al. 1985). Several follow-up studies investigated this and reported that MB is a feature connecting the eastern SMC to the Western LMC (Harris 2007; Bagheri et al. 2013; Mackey et al. 2017; Gaia Collaboration et al. 2021b). Low-density stellar structures were observed at the leading edge of the Clouds, referred to as the Leading Arm, and at the trailing edge, known as the Magellanic Stream. These features are prominently displayed in H I maps (Putman et al. 2003). Understanding the process that led to the formation of various substructures between the LMC and SMC is crucial for unravelling the processes that govern their evolution. These substructures provide a unique laboratory for studying tidal stripping, star formation, and the transfer of gas and stars between dwarf galaxies.

In a recent study, El Youssoufi et al. (2021) investigated the morphology of the stellar periphery of the Magellanic Clouds (hereafter, 'the Clouds') using near-infrared imaging data from the Visible and Infrared Survey Telescope for Astronomy Hemisphere Survey (VISTA VHS; McMahon et al. 2013). In their comprehensive study using both young and old stars, they confirmed the existence of several previously identified structures and identified two, new additional substructures, one on the eastern side of the LMC, towards the Milky Way (MW) namely Eastern substructure 2 (hereafter, 'East 2'), a thin stream-like structure, and the other on the northern side of the SMC, named as Northern Substructure 2 (hereafter, 'SMC North'). They also identified another substructure close to the East 2, namely Eastern substructure 1 (hereafter, 'East 1')– a circular feature, which aligns with a feature previously reported by de Vaucouleurs (1955). According to de Vaucouleurs (1955), the eastern substructures of the LMC appear to extend towards the Galactic disc, suggesting a complex interaction influenced by the MW. These substructures are located at a considerable distance from the LMC centre, indicating that their formation may be a consequence of tidal interactions between the MW and the LMC disc.

A previous study conducted by Mackey et al. (2016) identified an arclike substructure ~13.5 deg north of the LMC. This structure resembles the older population of the LMC disc. Utilising imaging data from the Dark Energy Survey (DES Abbott et al. 2018), their research estimated that this arc-like substructure could be around 1.5 kpc wide and extend as far as 10 kpc to the east. This feature, termed Northern Substructure 1 (hereafter, 'North 1'), was also identified in El Youssoufi et al. (2021), extending ~20 deg in older and to a lesser radial extent in the younger populations. In subsequent research, Mackey et al. (2018) identified two additional substructures in the southern region of the LMC, hereafter, South 1 and South 2, both of which are also prominent within the old stellar population. Their findings suggest a spatial correlation between at least one of these substructures and the RR Lyrae bridge, as described in Belokurov et al. (2017), which connects the Clouds to the south of the MB. Moreover, Belokurov & Erkal (2019a) detected a stream-like structure to the south of the LMC, characterised predominantly by an old stellar population, corroborated by VHS morphological maps. Pieres et al. (2017) identified a stellar overdensity located 8° north of the SMC's centre which was named the SMC Northern Over-Density (SMC NOD). UtUtilising DES data and data from the Magellanic Satellites Survey (MagLiteS Drlica-Wagner et al. 2016), they concluded that this structure exists at a similar distance to the SMC and consists primarily of intermediate-age stars (~6 Gyr old), along with a minor fraction of younger stars (~1 Gyr old).

Several other substructures, like a bimodal red clump (RC) population, have been identified by Nidever et al. (2013) in the eastern SMC, towards the MB and LMC. Later studies (Subramanian et al. 2017; Tatton et al. 2021; Omkumar et al. 2021; El Youssoufi et al. 2021; Gatto et al. 2024; Parisi et al. 2024) found that a foreground population exists at $\sim 10 - 12$ kpc, in front of the SMC main body, which was also confirmed to have a slower tangential velocity. Different studies could trace this feature to varying extent. The farthest it has been traced so far is to a distance of 10° from the SMC centre, utilising near-infrared data from the VHS (El Youssoufi et al. 2021). In an examination of the largest homogeneous dataset (~314 deg^2) from the Gaia Data Release 2 (DR2; Gaia Collaboration et al. 2018a), Omkumar et al. (2021) reported this feature between roughly $2\overset{\circ}{.}5$ and 5–6° from the optical centre of the SMC in the eastern regions. Notably, in their study, the transverse velocity of the foreground substructure is slower compared to the main body RC population.

In the eastern regions of the SMC, where the RC bimodality is evident, Dobbie et al. (2014a) discovered a bimodal distribution in the radial velocity (RV) of red giant branch (RGB) stars through their spectroscopic study. Furthermore, James et al. (2021) integrated the RV data from Dobbie et al. (2014a) and De Leo et al. (2020), along with proper motions derived from Gaia early-DR3, revealing that the proper motions of the lower and higher velocity RGB stars align with the foreground and main body RC populations, respectively. Additionally, they noted a bimodality in the RV distributions of RGB stars in the South-

West regions, which was not observed for the RC stars. Interestingly, El Youssoufi et al. (2021) noted a fainter RC component in the Northern outskirts of the SMC, which they suggest might trace the Counter-Bridge proposed by Diaz & Bekki (2012). Almeida et al. (2024) investigated the metallicities and RV of RGB stars from the Apache Point Observatory Galactic Evolution Experiment (APOGEE, Majewski et al. 2017) infrared spectra across various fields in the SMC. Their RV results indicated that the foreground substructure is approaching us, while the chemical analysis suggests that the disc is the source of the foreground material observed in the eastern side bimodality.

Spatially resolved metallicity maps of the Clouds provide critical insights into the processes of star formation, the effects of tidal stripping and dynamical encounters on the evolution of metallicity gradients, as well as the formation of peripheral substructures. Examining the chemistry and kinematics of these substructures will help us to know about how interactions shaped the galaxies and how that led to the present-day LMC and SMC. Altogether from different instruments, we only have spectroscopic measurements of a few thousand sources in the Clouds, which makes the comparison of elemental abundances a tedious process due to the systematic uncertainties. We currently lack a homogeneous data set that has [Fe/H] estimates of sources from the entire SMC and the LMC to study the various substructures in and around the Clouds to get a clear idea about their origin as well as the chemical history of the entire galaxies. Muñoz et al. (2023) used APOGEE data to show that the metallicity distribution function (MDF) of substructures closer to the LMC is LMC-like MDF and that closer to the SMC is SMC-like MDF. Combining with the kinematics, the LMC southern region has a mixture of debris from both the LMC and SMC, signalling complex interactions. This plethora of substructures is an excellent probe to better our understanding of the multiple mutual interactions of the Clouds and with their host, the MW.

The low-resolution spectra (R = 20–80) provided by the Gaia DR3 (Gaia Collaboration et al. 2016a, Gaia Collaboration et al. 2023a) include about 220 million sources. This data spans two wavelength ranges: 330–680 nm (BP) and 640–1050 nm (RP), which are collectively known as XP. Massana et al. (2023) studied the Magellanic periphery substructures using the metallicities of the RGB stars obtained by a machine-learning methodology (Andrae et al. 2023) applied on the XP spectra. In their analysis, they found that the substructures are mostly dominated by the LMC material. This poses a contradiction as we expect the stars in the SMC to have been tidally stripped during the interaction with the LMC, as the SMC is the less-massive companion. One important thing to note is that Andrae et al. (2023) also presented a vetted sample by applying the parallax criteria to obtain better results from their data-driven method, and this removed most of the distant sources, including those of the Clouds. Despite significant progress, the origin and evolution of substructures remain poorly understood due to the lack of a homogeneous dataset for studying their metallicities and kinematics systematically. El Youssoufi et al. (2021) showed that some substructures are prominent in young stars, and some are present in both old and young distributions. Hence, it is essential to study the metallicities of both young and old stellar populations in the substructures.

In our previous study (Omkumar et al. 2025), we presented large photometric metallicity maps of both old (RGB) and young (supergiant) stars covering the Clouds homogeneously, derived from a *Gaia* DR3–XP spectra using synthetic Strömgren photometry. Our analysis reveals that the overall radial metallicity gradients decrease linearly, consistent with findings from previous studies. With such large stellar samples, we were able to employ piecewise regression fitting to determine breaks in the gradients across different radial regions. In this study, we utilise the photometric metallicity estimates provided in Omkumar et al. (2025) to examine the metallicity of the stars present in several previously studied substructures. Our goal is to determine whether the stellar substructures in the outskirts of the Clouds influence their metallicity gradients and investigate the potential connection between the breaks and the substructures. Additionally, we seek to explore the possible origins of these substructures by examining all peripheral features through a uniform dataset.

In Section 3.2, we present the details of the data used in this study. In Section 3.3, we focus on the results of our analysis on the young and old stellar substructures in the Clouds. In Section 3.4, we provide the comparison of various substructures and their kinematics. In Section 3.5, we provide a discussion on the potential origin of the substructures. Finally, in Section 3.6, we provide a concise summary of our results.

3.2 Data

3.2.1 Photometric [Fe/H] catalogues

This study utilises the photometric metallicity catalogues of the Clouds presented in our previous work, Omkumar et al. (2025), along with astrometric data from *Gaia* DR3. In Omkumar et al. (2025), we used the low-resolution spectra from *Gaia* DR3–XP of the RGB and supergiant stars within ∼11 deg of the SMC and ∼20 deg of the LMC from their respective centres, down to $G = 17.65$ mag, as our initial sample. To remove as many MW contaminants as possible and select the most probable sources of the Clouds, we employed various selection cuts. These include parallax, proper motion cuts following Gaia Collaboration et al. (2021b), astrometric excess noise cut (> 1.3 mas), and photometric excess factor cuts by adopting the Gaia Collaboration et al. (2021a); Riello et al. (2021). Old (RGB; > 3 Gyr) and young (supergiants; 30–250 Myr) stellar populations were further segregated using colour-magnitude diagrams (Gaia Collaboration et al. 2021b, Figure 2) and exploited GaiaXPy[4] to obtain the Strömgren magnitudes. We then applied extinction-corrected magnitudes in the available calibration equations for both the RGB stars (Calamida et al. 2007 and Omkumar et al. 2025, Section 4.1) and the supergiants (Grebel & Richtler 1992 and Omkumar et al. 2025, Section 4.2) to estimate their respective photometric metallicities. Additionally, we recalibrated our estimations using the spectroscopic metallicities from APOGEE DR17 (Abdurro'uf et al. 2022) and provided radially recalibrated photometric metallicities (Omkumar et al. 2025, Section 5.3). The final catalogue comprises ∼90,000 young and ∼270,000 old stars of the Clouds. The catalogues consist of the Gaia Source IDs, right ascension (RA), declination (Dec), Strömgren magnitudes, distances from the centre, and reddening values and are made publicly available at the CDS [5].

[4] https://gaia-dpci.github.io/GaiaXPy-website/

[5] https://cdsarc.cds.unistra.fr/viz-bin/cat/J/A+A/700/A74

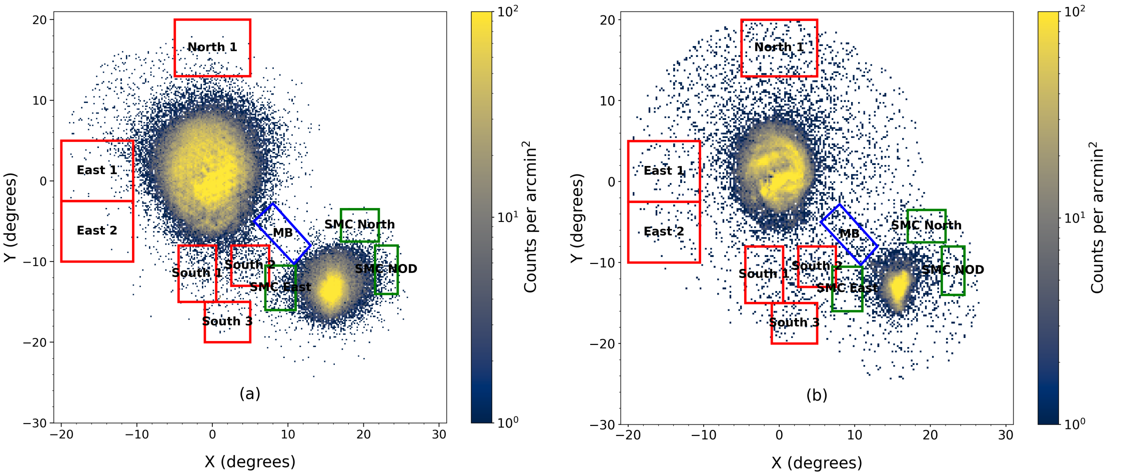

Figure 3.1: Spatial distribution of the RGB (panel a) and supergiants (panel b) stars in the Clouds. In both figures, the map is centred at (RA_0, Dec_0 = 81.24 deg, −69.73 deg), and the colour bar from blue to yellow shows the variation of stellar density. The regions of the various substructures of the LMC are marked with red, and those of the SMC and MB are shown in green and blue, respectively.

3.2.2 Substructure source selection

This study aims to analyse the metallicity of substructures in the periphery of the Clouds and compare them to the metallicity of the main body population of the Clouds. To select the sources belonging to where the substructures are, we plotted the spatial distributions of the RGB and supergiant sources in Figs. 3.1a and 3.1b, respectively. The spatial map is centred on the LMC centre (RA_0, Dec_0) = (81.24 deg, −69.73 deg). The colour bar from blue to yellow shows the increase in number density. The plots show the low stellar density in the outer parts of both Clouds, where these substructures are situated. We identified the regions of the substructures (marked in Fig. 3.1) by using the coordinates given in El Youssoufi et al. (2021) after plotting them in X and Y using the transformation equations in van der Marel & Cioni (2001b). The regions corresponding to the LMC substructures North 1, East 1, East 2, South 1, South 2, and South 3, the SMC substructures SMCNOD, SMC North 2, and SMC East, and the MB are marked in Fig. 3.1. Note that although the MB region has sources from both the Clouds, due to the large number of sources from the LMC, we study it along with the LMC substructures. To analyse the [Fe/H] of the various substructures in the Clouds, we have selected sources in the respective enclosed sub-regions that could be part of the substructures from our data set.

3.3 Results

3.3.1 Old stellar populations in the LMC substructures

To investigate the potential origin of the old stellar substructures in the periphery of the LMC and analyse whether these stellar substructures drive the metallicity gradients, we compared the median metallicities of various substructures with the radial metallicity gradient of the LMC RGB stars. To facilitate comparison, we plot the metallicity gradient from a previous study (Omkumar et al. 2025, Fig. 6), which originally presented the metallicity as a function of the de-projected radius of the LMC, revealing a clear negative gradient. In that work, we calculated the de-projected distance as 50 kpc × tan(radius) from de Grijs et al. (2014a). Due to the large LMC sample, we used varying radial bins: 0.2 kpc to 7 kpc, 0.5 kpc to 10 kpc, and 1 kpc to 13 kpc, combining sources beyond that up to 20 kpc. Then we obtained the median metallicity of each bin and the associated standard errors, as shown with black points in Fig. 3.2a. We obtained an overall radial metallicity gradient of -0.062 ± 0.005 dex kpc^{-1} using a linear fit to the median metallicities. From the plot, it is evident that the linear fit is not the best fit for the data. Hence, we also performed piecewise regression using the Python module piecewise-regression (Pilgrim 2021b), which identifies breakpoints iteratively while fitting a linear model, ensuring computational efficiency, revealing distinct breaks in slope across the LMC. The method also evaluates models with varying numbers of breaks using the Bayesian information criterion (BIC) to select the best fit while preventing over-fitting. After testing different numbers of breakpoints, we found that the best-fit model (lowest BIC value) for the LMC RGB has four breaks, leading to five regions with varying gradients. These breakpoints are marked with black vertical lines in Fig. 3.2a and are summarised in Omkumar et al. (2025).

In this study, we extended the analysis by incorporating the median metallicities of LMC substructures and the MB observed through comparisons with the same dataset. The substructures MB, South 1, and South 3 deviated from both the radial and piecewise gradients. Specifically, MB and South 1 were metal-poorer, while South 3 was metal-richer than expected. East 1, East 2, and North 1 were relatively metal-poorer than the overall gradient, but they aligned with the piecewise gradient in their regions. It is important to note that East 2 contains very few RGB stars; consequently, the resulting analyses derived from this sparse dataset must be interpreted with caution. South 1 showed slight enrichment compared to the piecewise gradient. Beyond 6 kpc, the piecewise gradient steepened, possibly due to interactions enriching the LMC outskirts. Removing substructure sources did not significantly alter the overall gradient, as illustrated in Fig. 3.8a.

To further probe the identified breaks, and whether they are present in all directions or steeper in one region than the other, we looked into the metallicity gradient in different directions across the galaxy. We divided each of the LMC radial bins into 4 quadrants: north-east (NE; $Y > 0$ and $X < 0$), north-west (NW; $Y > 0$ and $X > 0$), south-east (SE; $Y < 0$ and $X < 0$), and south-west (SW; $Y < 0$ and $X > 0$) and estimated median metallicities across each quadrant. The best-fit piecewise metallicity gradients for each quadrant are shown in Fig. 3.2b, with breakpoints and slopes detailed in Table 3.5. The observed metallicity gradients in each quadrant and their respective best fits are provided in the Appendix (Fig. 3.10a for the LMC RGB stars). We notice that the piecewise regression provides the fits that represent the gradients well. The best-fits provided 3 breaks for the NE and SW and 2 breaks for the NW and SE quadrants. The median metallicities of the substructures followed specific quadrant gradients: East 1, East 2, and North 1 aligned with the NE quadrant, while South 1 was metal-richer relative to the NE and metal-poorer compared to the others. South 2 matched the NW quadrant, and South 3 was metal-rich across all quadrants, while MB remained metal-poor. Histograms and Gaussian fits of substructure metallicities are provided in Figs. 3.11a and 3.11b, respectively. From the plot, peaks in substructure metallicities for the MB, East 2, North 1, South 1 and South 2 were similar to the LMC main-body RGB peak (−1.19±0.51 dex; Omkumar et al. 2025), while for East 1 and South 1 they were notably metal poor. However, Gaussian fitting was not optimal for all distributions.

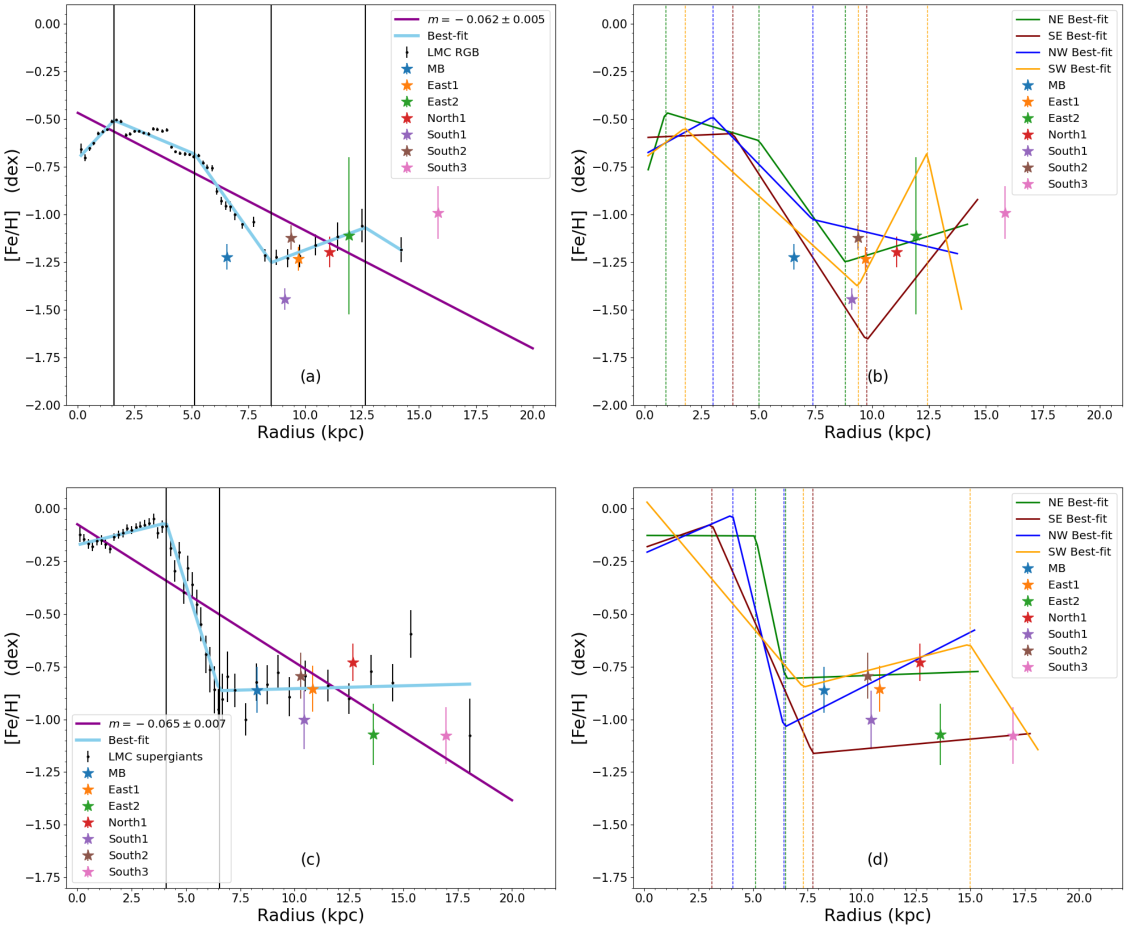

Figure 3.2: Metallicity gradients for LMC RGB (top panels) and supergiant (bottom panels) stars are presented. Panels (a) and (b) show radial metallicity gradients and quadrant-specific gradients for RGB stars. Panels (c) and (d) present the same for LMC supergiants. Panels (a) and (c) include median metallicities marked by black dots with standard errors, linear best-fits in purple, and piecewise-regression fits in pale blue, with black vertical lines indicating segment breaks. Panels (b) and (d) display gradients for the NE (green), NW (blue), SE (brown), and SW (yellow) quadrants, and coloured vertical lines marking quadrant breaks. In all panels, coloured stars denote the median metallicity of the LMC substructures.

3.3.2 Young stellar populations in the LMC substructures

We identified several supergiant stars in the regions of RGB substructures around the LMC, which may also be part of the substructures. According to Omkumar et al. (2025), the radial bins for supergiants were redefined as follows: 0.2 kpc to 7 kpc, 0.5 kpc to 10 kpc, and 1 kpc to 16 kpc, with sources beyond that combined into a single sub-region up to 20 kpc due to the noticeable decline in stellar density at ~5 deg from the LMC centre. Our analysis indicates a trend in median metallicities due to an uneven spatial distribution, particularly in the bar region and major spiral arm, as illustrated in Fig. 3.2c. The overall metallicity gradient was estimated as -0.065 ± 0.007 dex kpc^{-1}, with the best-fit piecewise-regression (minimum BIC value) revealing a positive gradient in the inner region, negative gradients with a break at 4 kpc, and a nearly flat gradient beyond 7 kpc. Additional details are provided in Omkumar et al. (2025, Table 2). After removing substructure sources, the overall fit remains similar but with additional breaks, as shown in Fig. 3.8b.

To compare the metallicities of different young stellar substructures, we overlaid the median metallicities of the LMC substructures identified with supergiants onto the metallicity gradients. Initial observations indicate that all substructures fall within the last section of the piecewise gradient (Radius > 7 kpc), which is nearly flat. However, the overall fit shows a linearly decreasing gradient without flattening. The median metallicities of substructures MB and East 1 align precisely with the piecewise gradient, while North 1 lies slightly above, and East 2, South 1, and South 3 fall below this gradient. South 2 is positioned between the overall and piecewise gradients.

To investigate trends in specific LMC quadrants, we divided each radial bin into NE, NW, SE, and SW quadrants, as described previously. The metallicity gradients in these quadrants are shown in Fig. 3.2d. Piecewise fits reveal that the quadrants show a similar flattening as the radial gradient, except in the NW bin, where we observe a slight enrichment. The quadrant breakpoints and slopes are detailed in Table 3.5. Appendix 3.10b shows that piecewise regression best-fits effectively represent the gradients observed for different quadrants, with two breaks in each quadrant. Substructures MB, East 1, and South 2 align with the NE and SW quadrant gradients, while East 1 and South 3 fall within the SE quadrant gradient, and North 1 follows the NW quadrant. Histograms and Gaussian fits for each substructure are presented in Figs. 3.11c and 3.11d, respectively. Most Gaussian fits appear narrower compared to those for RGB stars. All substructures are metal-poor compared to the peak of LMC supergiants (-0.58 ± 0.77 dex; Omkumar et al. 2025).

3.3.3 Old stellar populations in the SMC substructures

To estimate the metallicity gradients of RGB stars in the SMC, Omkumar et al. (2025) utilised a conversion method from deg to kpc as described in de Grijs & Bono (2015a), applying the formula $62\text{kpc} \times \tan(\text{radius})$. Radial binning was performed with varying bin sizes: 0.2 kpc to 2 kpc, 0.5 kpc to 6 kpc, 1 kpc to 8 kpc, and a final bin encompassing distances to 11 kpc. This approach was adopted to accommodate the declining stellar density towards the periphery. The overall metallicity gradient of SMC RGB stars exhibits a linear decrease of -0.048 ± 0.007 dex kpc^{-1}, as depicted in Fig. 3.3a. Additionally, a piecewise regression analysis identified 3 breakpoints, dividing the gradient into 4 segments with distinct slopes. Median metallicities of SMC substructures, represented by RGB stars, were plotted along with their standard errors on the gradient plot, indicated by differently coloured symbols. The overall gradient suggests that all three SMC substructures are marginally metal-poor. Notably, the gradient steepens between 5 to 7 kpc, where the substructures are located. SMC East is slightly more metal-poor compared to the segment of the piecewise gradient, while SMC NOD aligns closely with the gradient, indicating a similar metallicity to that of the main body of the galaxy. SMC North appears slightly metal-rich but remains within errors.

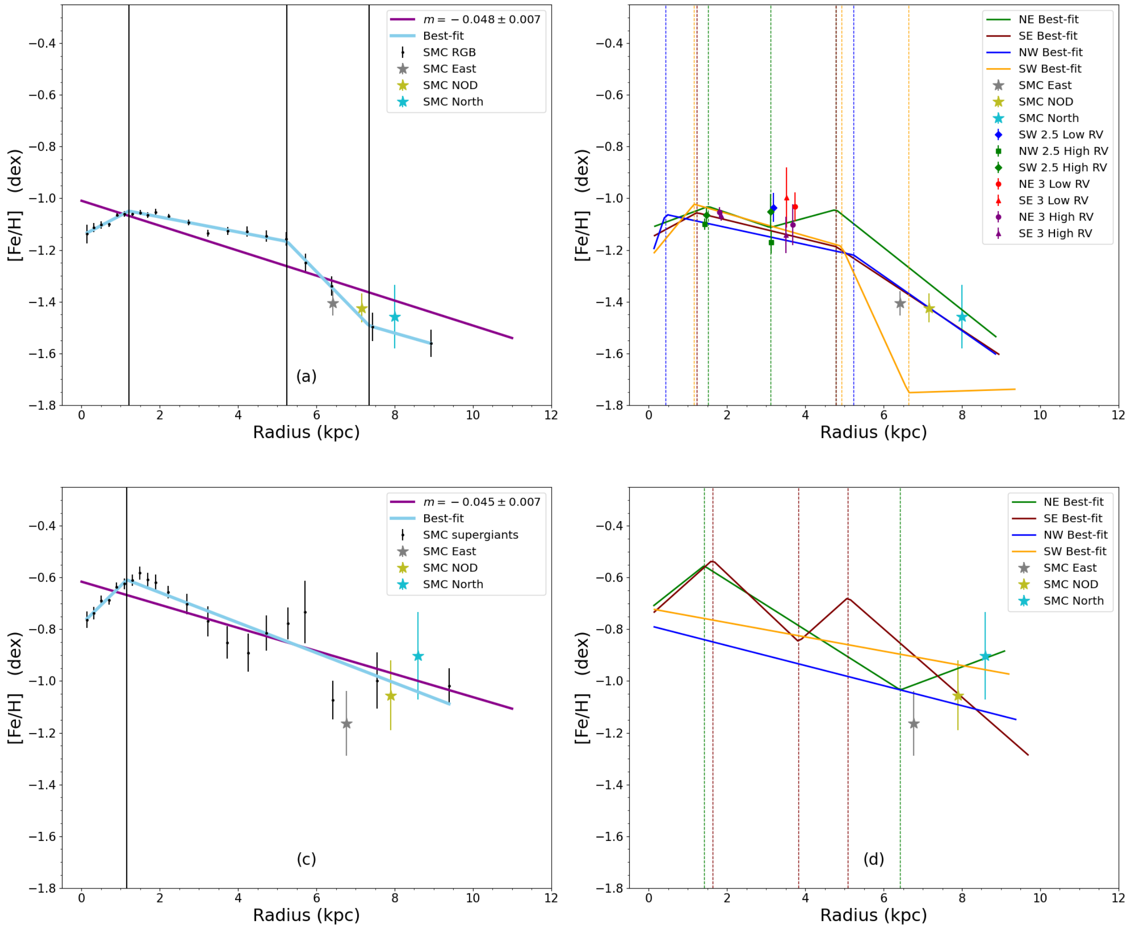

Figure 3.3: Same as Fig. 3.2 but for the SMC stars.

To analyse the metallicity gradients across different directions in the SMC, we divided the SMC into four quadrants, as previously done for the LMC stars. The resulting gradients are illustrated in Fig. 3.3b. We identified 3 breakpoints in the NE and SW quadrants and 2 in the SE and NW quadrants. Individual quadrant fits are presented in Fig. 3.10c. While the overall metallicity gradient shows a slight inversion, the NE region specifically revealed a breakpoint. Parisi et al. (2022) reported a similar finding from their analysis of northern clusters, noting a break and inversion around 3.4 deg, a feature observed in previous studies for SMC clusters and field stars (Parisi et al. 2016, 2022; Bica et al. 2020). These studies suggest that this inversion may be attributed to the intrinsic wing/bridge region or could result from mergers, interactions, or radial migration, marked by the SMC tidal radius (see e.g. Dias et al. 2021). The SMC East substructure is marginally more metal-poor compared to the SE and NW quadrants, whereas the metallicity of the SMC NOD aligns with that of two quadrants. SMC North's metallicity aligns with that of the NE quadrant. To compare the metallicities of various SMC peripheral substructures, we plotted their metallicity distributions in a histogram (Fig. 3.12a) and fitted them with Gaussians (Fig. 3.12b). From the plot, the fitted peak metallicities for SMC East, SMC NOD, and SMC North indicate they are slightly more metal-rich than the SMC RGB stars (−1.47±0.49 dex; Omkumar et al. 2025)

3.3.4 Young stellar populations in the SMC substructures

To study the stellar substructures in the periphery of the SMC in detail, we also analysed the SMC supergiant stars present in the substructure regions. As noted by Omkumar et al. (2025), the same radial binning as the SMC RGB stars was applied to estimate the median metallicities of the supergiants in each bin. The overall best-fit revealed a linearly decreasing metallicity trend for the supergiants, with a gradient of −0.045±0.007 dex kpc^{-1} shown in Fig. 3.3c. The best-fit from the piecewise regression indicated a break at about 1 kpc, resulting in two different gradient values. For comparison, the median metallicities of each of the SMC substructures traced by the supergiants are shown with different coloured stars. Notably, there is an upturn in the median metallicities around 4 kpc, although the substructures lie well beyond this region. This resembles the 3.4 deg breakpoint previously discussed for RGB stars in the SMC. In Oliveira et al. (2023), the classical MB is analyzed in two cluster groups: younger and older than 300 Myr. Interestingly, the older group exhibits an inverted gradient, while the younger group maintains a consistent metallicity. On the outskirts, the overall and piecewise gradients align closely, and the SMC NOD falls along these gradients. A Comparison of the SMC East substructure shows that it is metal-poor, while the SMC North is metal-rich relative to the gradient in the outer regions of the SMC, a trend also observed for the substructures traced by the SMC RGB stars. Figs. 3.9a and 3.9b illustrate the overall metallicity gradients of RGB and supergiant stars in the SMC after excluding substructures from the gradient. The gradients remained largely unchanged, within the error limits of their respective fits. Piecewise fits to these samples showed variations in the number and position of breakpoints compared to when substructures were included.

Metallicity gradients in different quadrants are estimated and shown in Fig. 3.3d. Individual gradients along with their median metallicities are shown in Fig. 3.10d. We identified 2 breakpoints in the NE quadrant and 3 in the SE quadrant. Similar to the inversion in the metallicity gradient of the NE with older stars, our piecewise fits identified an inversion in the SE quadrant. Due to the significant dispersion in the median metallicities, linear fits were used for the western quadrants. The SMC East substructure is metal-poor relative to all quadrant gradients, while SMC NOD aligns with the SE quadrant and SMC North aligns with the NE quadrant. Metallicity distributions and their Gaussian fits for different SMC substructures are shown in Figs. 3.12c and 3.12b. From the plot, the peak metallicities for SMC East and SMC NOD are metal-poorer compared to the overall peak metallicity of SMC supergiant stars (−1.08±0.54 dex; Omkumar et al. 2025). Conversely, SMC North is metal-richer. As expected, the young stars in the substructures are relatively more metal-rich than their older counterparts.

3.3.5 Dual RGB population in the SMC

We investigated the metallicity of the dual RGB population in the SMC to understand its origin. We utilised the RV estimates of 5,664 RGB sources, combining data from Dobbie et al. (2014a) and De Leo et al. (2020), as previously explored in James et al. (2021), to distinguish between the two populations. Notably, while Dobbie et al. (2014a) provides metallicity estimates, De Leo et al. (2020) does not. Cross-matching this sample with the SMC RGB metallicity catalogue by Omkumar et al. (2025) yielded 3,623 sources with both RV estimates and photometric metallicities. The spatial distribution of this sample is shown in Fig. 3.4a. We divided this sample into various quadrants as before. Additionally, the eastern sub-regions (NE and SE) are divided into inner (R ≤ 3 deg) and outer (R > 3 deg) regions, while the western sub-regions (NW and SW) are divided into inner (R ≤ 2.5 deg) and outer (R > 2.5 deg) regions. For each of these sub-regions, we used the peak ± sigma of both the lower and higher RV components provided James et al. (2021) to select the sources that are part of the lower and higher RV components, respectively. Proper motions were quantified using median values and standard errors, as detailed in Table 3.1. Fig. 3.4b illustrates the proper motions for different sub-regions. We see that for this sub-sample, the proper motions are comparable with those of the respective higher and lower velocity components of the RGB stars as noted previously by James et al. (2021).

Table 3.1: Median proper motions of the dual velocity RGB stars.

Regions	Lower velocity RGB		Higher velocity RGB	
	μ_α (mas/yr)	μ_δ (mas/yr)	μ_α (mas/yr)	μ_δ (mas/yr)
NE Inner	-	-	0.760 ± 0.008	-1.209 ± 0.005
NE Outer	0.990 ± 0.025	-1.252 ± 0.017	0.861 ± 0.033	-1.159 ± 0.019
NW Inner	-	-	0.622 ± 0.007	-1.257 ± 0.006
NW Outer	-	-	0.520 ± 0.018	-1.281 ± 0.014
SE Inner	-	-	0.766 ± 0.009	-1.211 ± 0.006
SE Outer	1.124 ± 0.044	-1.340 ± 0.030	0.962 ± 0.032	-1.211 ± 0.027
SW Inner	-	-	0.584 ± 0.008	-1.240 ± 0.006
SW Outer	0.506 ± 0.019	-1.304 ± 0.014	0.448 ± 0.035	-1.259 ± 0.020

To investigate the nature of the metallicities of these dual velocity components in various sub-regions, the median [Fe/H] values and their standard errors are plotted as a function of median radius in Fig. 3.4c and tabulated in Table 3.2. Figures 3.4d and 3.4e display the median proper motions and metallicities of the higher and lower velocity components across each quadrant (NE, NW, SE, and SW), highlighting the separation of these components. The results show that the lower velocity components in the eastern (NE and SE) sub-regions are slightly more metal-rich than their counterparts, suggesting

Table 3.2: Median [Fe/H] of the dual velocity RGB stars.

Regions	Lower velocity [Fe/H] (dex)	Higher velocity [Fe/H] (dex)
NE Inner	-	-1.05 ± 0.02
NE Outer	-1.03 ± 0.06	-1.10 ± 0.08
NW Inner	-	-1.10 ± 0.02
NW Outer	-	-1.17 ± 0.04
SE Inner	-	-1.07 ± 0.02
SE Outer	-1.00 ± 0.12	-1.14 ± 0.07
SW Inner	-	-1.07 ± 0.03
SW Outer	-1.04 ± 0.06	-1.05 ± 0.07

distinct kinematics and metallicities. This supports the hypothesis that the lower velocity component, associated with the tidally stripped foreground RC population, is metal-rich. This conclusion is based on the similarity in the proper motions of the two RC components and the two RGB components (Omkumar et al. 2021; James et al. 2021). This evidence suggests that the lower velocity RGB component was tidally stripped from the inner SMC during its interaction with the LMC.

3.4 Comparison of various substructures

3.4.1 Metallicity distribution Functions

Figure 3.5 illustrates the MDFs for various substructures within the Clouds using Kernel Density Estimation (KDE). We used a simple Gaussian kernel to smooth the MDFs. Panels (a) to (j) depict the MDFs of the main-body RGB stars and identified substructures. The SMC's MDF peak is notably more metal-poor compared to that of the LMC, corroborating earlier observations. Substructures MB, East 1, North 1, and South 2 exhibit MDF peaks similar to the SMC. In contrast, East 2 displays a broader MDF with a peak nearer to the LMC's RGB stars. The South 1 substructure has a peak more metal-poor than the SMC's RGB peak, and South 3 shows a bimodal distribution, with one peak more metal-poor than the SMC and another intermediate between the LMC and SMC peaks. Notably, all SMC RGB substructure MDFs peak at metallicities more metal-poor than the main-body SMC as traced by RGB stars.

Panels (k) to (t) compare the MDFs of the main-body supergiant stars of both Clouds with those of identified supergiant substructures. The MDFs of substructures MB, North 1, and South 2 align with that of the SMC, mirroring the trends observed in RGB stars. East 2 and South 3 present peaks more metal-poor than the SMC. East 1 and South 1 substructures exhibit broader MDFs without bimodality, with peaks more metal-poor than the SMC supergiants. While young SMC substructures generally show more metal-poor peaks than the SMC supergiants, closer inspection reveals additional minor peaks near the LMC's peak in SMC East and SMC NOD.

We also performed a statistical analysis, the Kolmogorov-Smirnov test (KS test), to

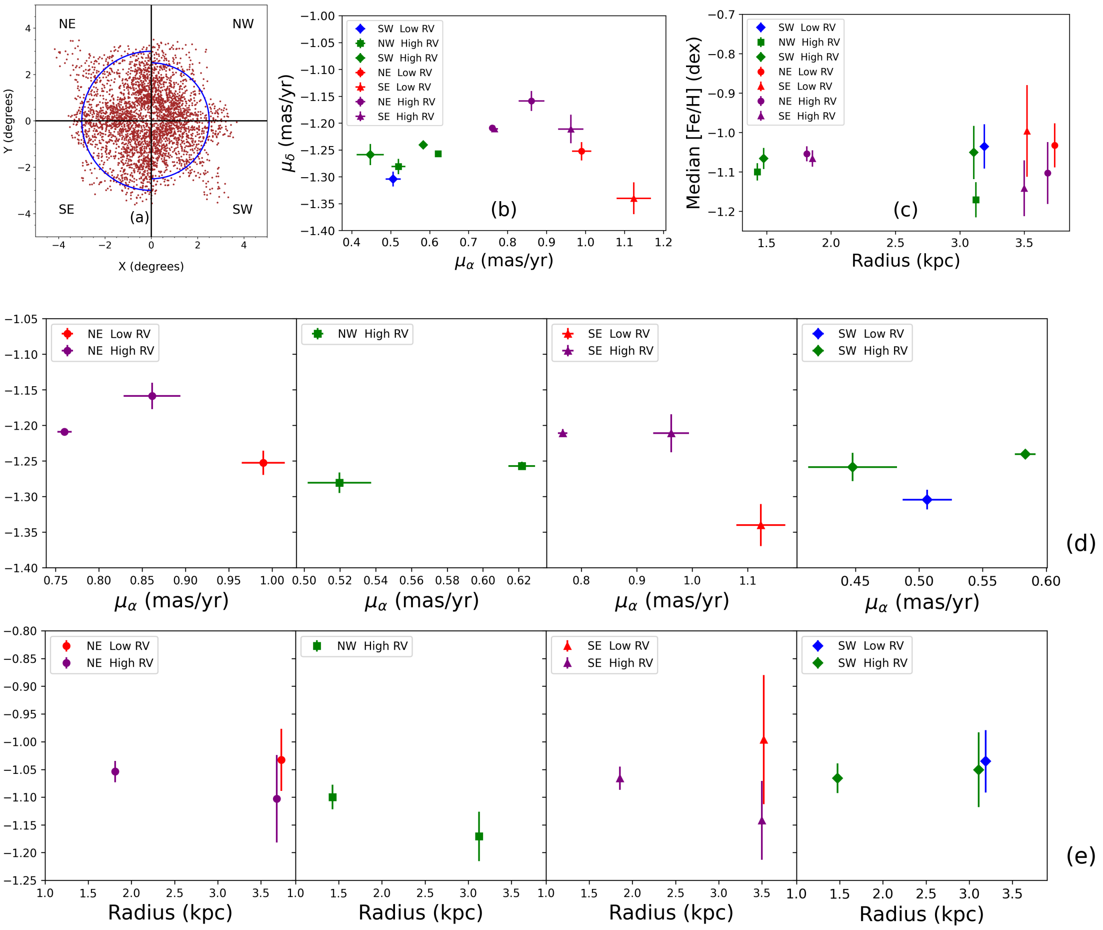

Figure 3.4: (a) Spatial distribution of the dual RGB populations. (b) Median proper motions of the lower and higher RV components. (c) Median [Fe/H] plotted as a function of radius for the dual RV components. (d) Median proper motions of different quadrants. (e) Median [Fe/H] versus radius for different quadrants.

determine the potential origins of the substructures in our study. It is a widely employed method for evaluating the similarity between two distributions. We assume that similar distributions suggest a common origin. Hence, if they are alike, they likely originate from the same parent population. We compared the MDF of each substructure with the corresponding MDFs of the LMC and SMC as presented in Fig. 3.5. The KS test yields two valuable information: a test statistic and a p-value, the latter of which was used to evaluate the null hypothesis and infer whether the substructure's MDF is more consistent with that of the LMC or SMC. The results, summarised in Tables 3.3 and 3.4, indicate that the East 2, North 1, and South 3 RGB substructures are similar to that of the SMC distribution, hence these substructures likely originate from the SMC. Similarly, the young substructures South 1 and SMC North also appear to be associated with the SMC. Substructures whose MDFs do not align with those of either the SMC or LMC may arise from a combination of both origins. For the young substructures, in-situ formation remains a plausible explanation.

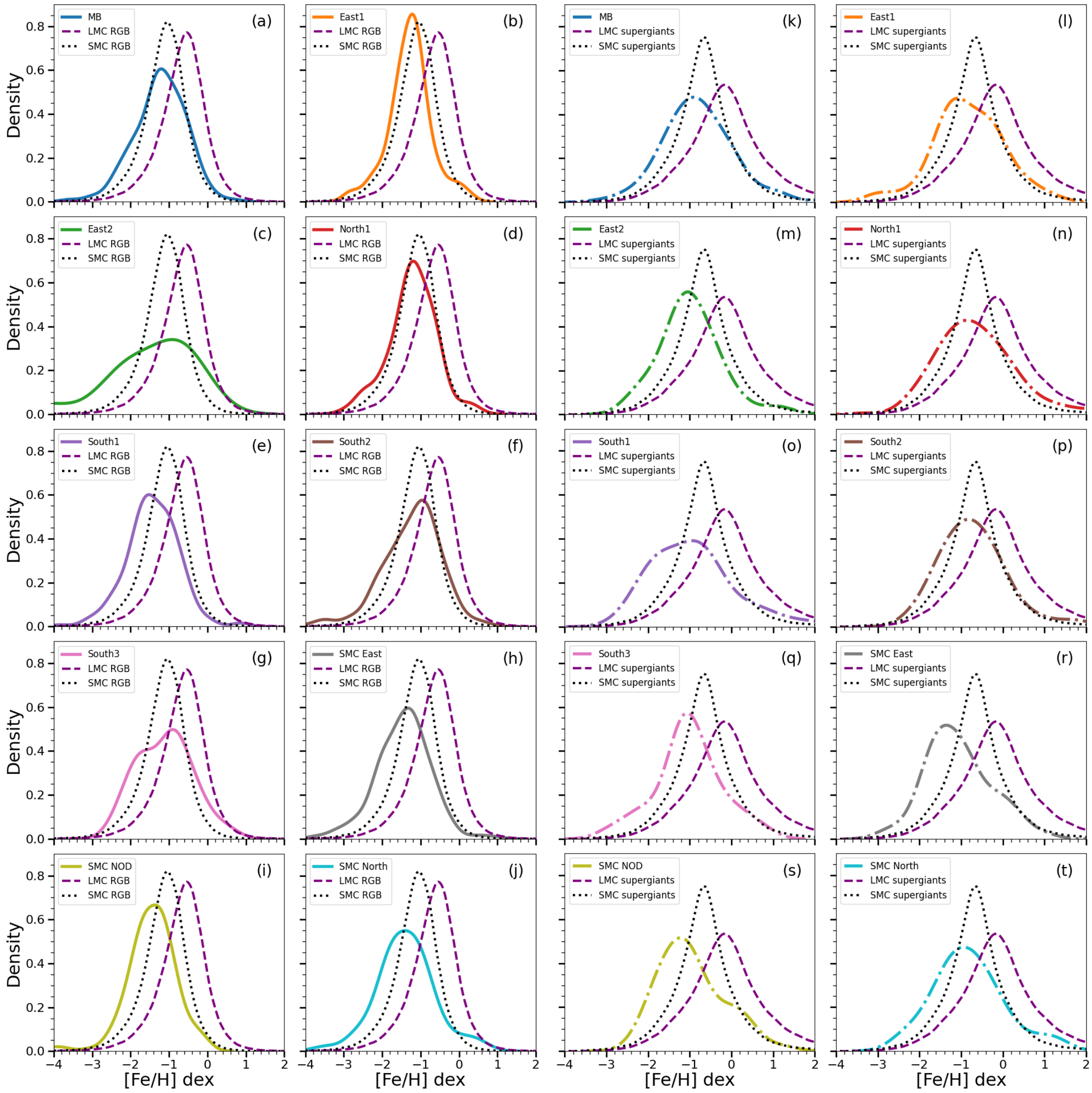

Figure 3.5: Metallicity distribution function of different substructures of the RGB (panels (a) to (j)) and supergiant (panels (k) to (t)) stars are shown in various colours. In each panel, along with each substructure, the respective metallicity distribution of the LMC (dashed magenta line) and SMC (dotted black line) are plotted for comparison.

Table 3.3: Median [Fe/H] of old stellar substructures in the Clouds.

Substructure	N	Median	MAD	KS_{LMC}	KS_{LMC} (P_{value})	KS_{SMC}	KS_{SMC} (P_{value})	Origin
MB	157	−1.22	0.45	0.38	2.51e-21	0.12	2.47e-02	–
East1	130	−1.23	0.26	0.54	3.32e-36	0.21	1.03e-05	–
East2	12	−1.11	0.68	0.39	3.46e-02	0.34	8.91e-02	SMC
North1	93	−1.20	0.36	0.41	1.32e-14	0.13	8.66e-02	SMC
South1	218	−1.44	0.42	0.51	1.08e-52	0.26	1.27e-13	–
South2	216	−1.12	0.44	0.37	3.47e-27	0.11	6.73e-03	–
South3	41	−0.99	0.57	0.35	6.82e-05	0.19	1.01e-01	SMC
SMC East	355	−1.41	0.43	0.52	1.49e-88	0.25	1.23e-20	–
SMC NOD	202	−1.42	0.36	0.54	3.60e-56	0.26	9.28e-13	–
SMC North	57	−1.46	0.40	0.53	2.39e-15	0.27	4.25e-04	–
LMC RGB	213597	−0.61	0.36	0.00	1.00e+00	0.00	1.00e+00	LMC
SMC RGB	56827	−1.09	0.34	0.00	1.00e+00	0.00	1.00e+00	SMC

Table 3.4: Median [Fe/H] of young stellar substructures in the Clouds.

Substructure	N	Median	MAD	KS_{LMC}	KS_{LMC} (P_{value})	KS_{SMC}	KS_{SMC} (P_{value})	Origin
MB	121	−0.86	0.50	0.37	2.04e-15	0.15	1.05e-02	–
East1	93	−0.85	0.51	0.36	1.88e-11	0.19	1.90e-03	–
East2	57	−1.07	0.39	0.50	1.24e-13	0.31	2.71e-05	–
North1	186	−0.73	0.60	0.30	4.80e-15	0.14	2.07e-03	–
South1	86	−1.00	0.64	0.43	1.22e-14	0.24	5.91e-05	–
South2	102	−0.79	0.51	0.33	1.23e-10	0.11	1.64e-01	SMC
South3	55	−1.08	0.45	0.50	3.13e-13	0.32	1.47e-05	–
SMC East	60	−1.16	0.43	0.51	5.36e-15	0.32	6.37e-06	–
SMC NOD	53	−1.05	0.49	0.49	2.09e-12	0.31	3.97e-05	–
SMC North	39	−0.90	0.47	0.40	3.61e-06	0.20	7.95e-02	SMC
LMC supergiants	68346	−0.15	0.54	0.00	1.00e+00	0.00	1.00e+00	LMC
SMC supergiants	20468	−0.67	0.38	0.00	1.00e+00	0.00	1.00e+00	SMC

3.4.2 Comparison with the LMC and SMC gradients

In Section 3.3, our analysis of the metallicity gradients of LMC substructures revealed some to be more metal-poor than expected. To investigate this further, we compared the overall metallicity gradients of the LMC and SMC RGB stars with those of each substructure, as shown in Fig. 3.6a. Notably, median metallicities of all substructures around the Clouds were overplotted on this figure. Notably, the median metallicity of the MB substructure closely aligns with the piecewise fit of the SMC RGB gradient, indicating that it is formed from the SMC during the past interaction between the Clouds. The South 1 substructure around the LMC matches the SMC's radial metallicity gradient at ~10 deg from its centre, suggesting it may have been stripped from the outer SMC during tidal interactions.

Figure 3.6b illustrates the radial metallicity gradients traced by supergiants in both Clouds, alongside their respective substructures. The median metallicities of the young South 1 substructure are notably closer to the SMC's metallicity gradient than to that of the LMC. Similarly, the SMC North substructure has metallicities similar to those of the MB, positioning both between the gradients of the SMC and LMC, but closer to the

LMC's outer regions. The East 2 and South 3 substructures of the LMC, located in the outskirts, exhibit significantly lower metallicities, comparable to those of the SMC NOD.

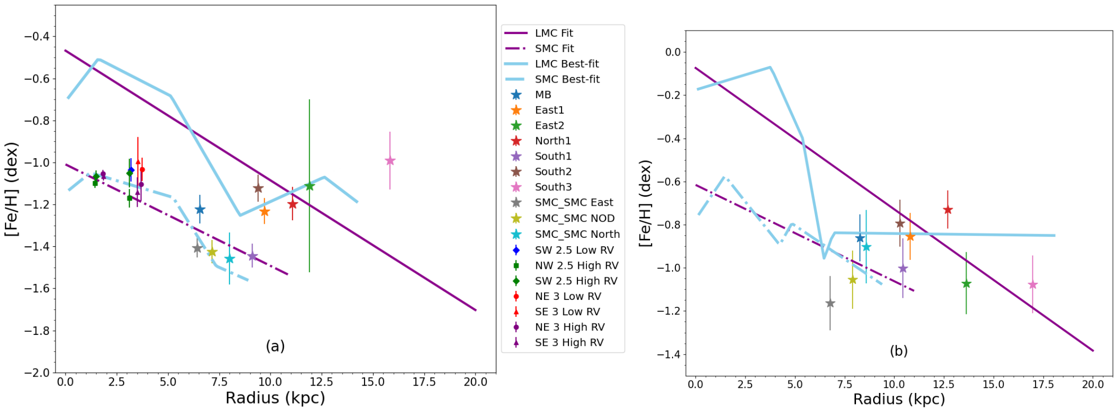

Figure 3.6: Comparison of all the LMC and SMC substructures for the RGB stars (a) and for the supergiants (b) with the respective radial metallicity gradient of the Clouds.

To test the hypothesis that the foreground population in the RGB stars is a result of tidal interactions between the Clouds, leading to the stripping of stars from the SMC's inner disc, we compared the median metallicities of the dual velocity components with the metallicity gradient of the SMC RGB stars (Fig. 3.6a). Most sub-regions exhibit similar metallicities to the main-body RGB population of the SMC, particularly within 1 to 4 kpc from the SMC centre, while the eastern lower velocity components tend to be more metal-rich. Additionally, comparisons with the metallicity of different SMC quadrants (Fig. 3.10c) show that the substructure aligns with the breakpoint in the NE quadrant, near the SMC's tidal radius. This also confirms the metal-rich nature of the lower RV populations in the eastern regions, supporting the hypothesis that the chemical enrichment in this region is due to tidal interactions between the Clouds, which is consistent with the findings from star clusters (e.g. Oliveira et al. 2023). This suggests that the foreground population, traced by older stars (RC and RGB), in the eastern regions of the SMC is both kinematically and chemically distinct. The metal-rich nature of the lower velocity RGB stars indicates that they were stripped from the central region (~3 deg) of the SMC main body. In the SW region, the proper motions of the lower and higher velocity RGB stars indicate that higher-velocity stars are located further behind the main SMC body. Simulations suggest that these higher-velocity stars may correspond to the Counter-Bridge described by Diaz & Bekki (2012), though no significant differences in their metallicities were observed to confirm this, which is also consistent with the findings from star clusters (e.g. Dias et al. 2022; Parisi et al. 2024).

3.4.3 Kinematics of substructures

To gain a comprehensive understanding of the various substructures, we conducted a kinematic analysis, complementing our metallicity analysis in the previous sections. We utilised proper motions in right ascension (μ_α) and declination (μ_δ) from the *Gaia* DR3

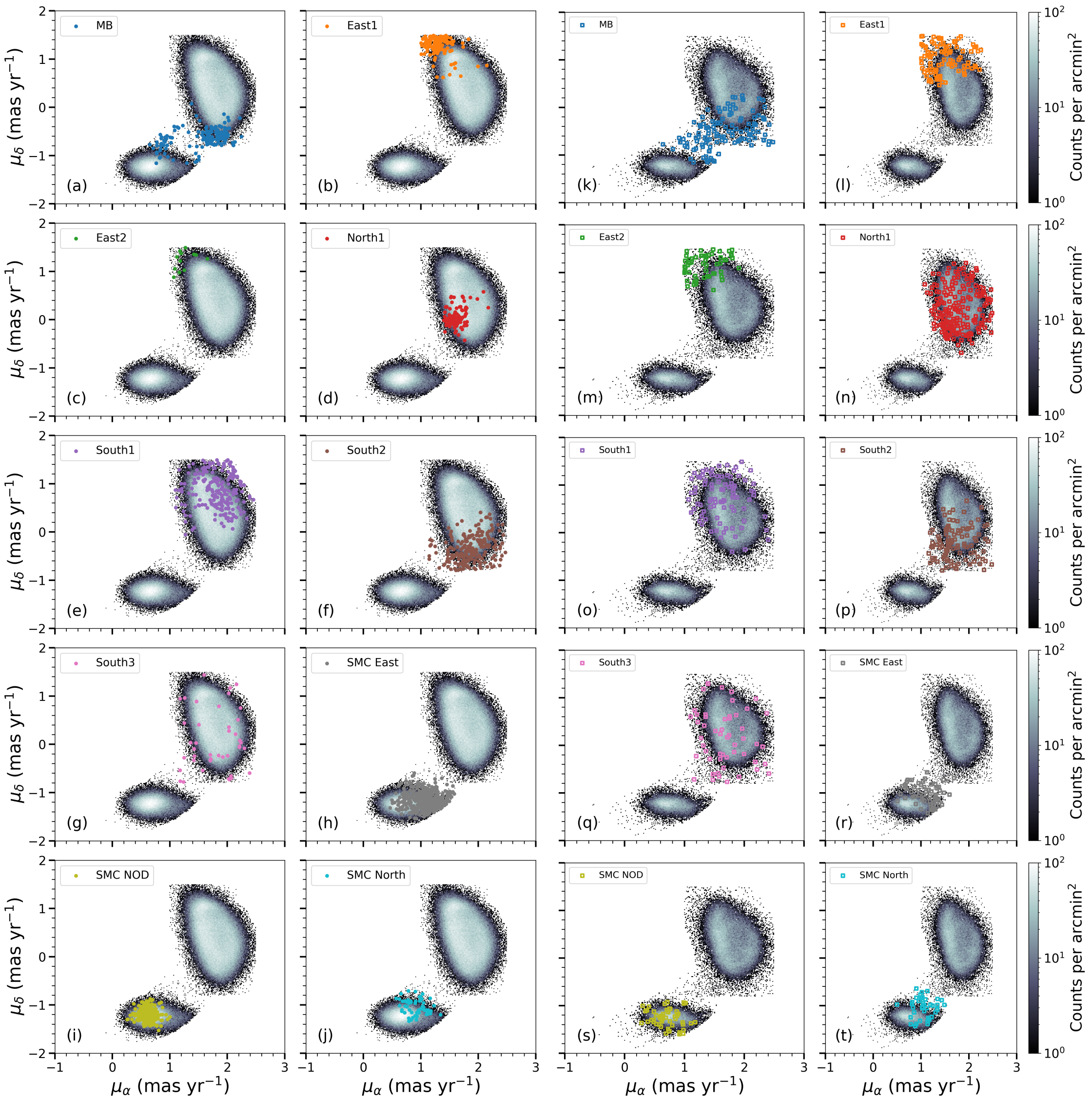

Figure 3.7: Proper motions of various substructures for RGB (panels a to j) and supergiants (panels b to t) along with the overall proper motion of the Clouds obtained from *Gaia* DR3 data. The increase in the stellar density is shown in the grey scale from black to white.

dataset. Figure 3.7 shows the proper motions of RGB stars in the LMC and SMC, represented by larger and smaller density distributions, respectively. These plots distinguish the bulk motions of the two galaxies, with a colour bar from white to black illustrating the decrease in stellar density from the centre to the outskirts. Each panel from (a) to (j) overlays the proper motions of substructures from RGB stars in different colours, while panels (k) to (t) replicate this for supergiant stars.

It is evident that both old and young stars in the MB region (panels (a) and (k)), located between the LMC and SMC, exhibit proper motions consistent with stars dynamically linking these galaxies. The old stellar bridge, known to have been dynamically stripped from the SMC and in-situ formation of young stars along the bridge, is consistent with Harris (2007). All LMC substructures (panels (b) to (f)) display clustered proper motions closely aligned with those of the LMC, a pattern also observed in SMC substructures. This coherent motion implies that, following their interactions, these substructures have become integrated into the respective galaxies from which they are currently identified.

Additionally, we observe that some substructures, such as South 3 and SMC East among the old population, exhibit highly perturbed proper motions, showing a broader distribution across their respective galaxies as well as in the MB region. This suggests that these regions have stars spreading towards the other galaxies, which might be the tidally stripped stars from one galaxy, migrating towards the other. This observation supports the tidal stripping of less-gravitationally bound stars from the outskirts during recent passages. Similar patterns of highly perturbed proper motions are evident in several young substructures, including North 1 and all the southern substructures of the LMC, as well as those of the SMC. These disturbances may result from prior interactions, variations in distance, or slight differences in velocities. It is worth noting that although South 1 and South 2 are located close to each other in the sky, they present highly perturbed but very different kinematics from one another. We utilised *Gaia* proper motions to compare the motions of substructures with those of the Clouds without accounting for internal kinematics. In future, to account for the effect of internal kinematics, we will utilize proper motion maps (e.g., Dhanush et al. 2024, 2025) or established methods (Niederhofer et al. 2021a, 2022b; Vijayasree et al. 2025a) to subtract center-of-mass motion, yielding residual motions for better dynamical comparison.

3.5 Discussions

In this section, we discuss our findings in light of understanding the origins of substructures. We do this by combining their comparisons of metallicities with radial gradients and metallicity gradients across different quadrants, along with their MDFs and kinematic properties. Tables 3.7 and 3.8 provide a tabulated summary of the results for the old (RGB) and young (supergiant) stellar substructures, respectively.

- **MB:** The MB substructure exhibits properties intermediate between the LMC and SMC. The older population is slightly more metal-poor than the LMC but comparable to the SMC, suggesting a metal-poor composition likely formed from stars stripped from the SMC. On the contrary, the younger population is more enriched, indicating a formation from metal-rich gas from the LMC following their mutual interaction. Our results on the kinematics also support this interpretation and align with a recent H I study by Morelli et al. (2025). They used MeerKat Absorption Line Survey data to investigate the similarity between the MB gas-to-dust ratio and that of the LMC and SMC. They concluded that the MB gas-to-dust ratio is similar to the LMC's gas-to-dust ratio and hence the gas has been extracted from the LMC during the direction collision of the Clouds. This is consistent with studies by Harris (2007), Besla et al. (2012), and Zivick et al. (2018), which support the idea that metal-rich gas stripped from the LMC led to in-situ star formation.

- **East 1:** Comparisons of metallicity gradients and kinematics indicate that both the old and young populations of this substructure are similar to those of the LMC, particularly in the NE quadrant. This suggests formation due to MW-induced deflections of the LMC disc during tidal interactions. According to El Youssoufi et al. (2021), the substructure is located at a distance similar to the LMC, supporting its association with the LMC disc. Cullinane et al. (2022b) and Navarrete et al. (2023) found this substructure to be dynamically stable and aligned with the LMC disc, suggesting it arises from a perturbed disc. Cullinane et al. (2022b) suggested that a possible SMC crossing of the LMC disc plane ~400 Myr ago, in combination with the LMC's infall to the MW potential, caused perturbations in the outer disc. Muñoz et al. (2023) and Massana et al. (2023) also classified it as part of the LMC. A recent kinematic study by Vijayasree et al. (2025b) using VMC and *Gaia* proper motions noted an outward radial motion in the northeastern region, indicating the substructure's origin within the LMC disc plane. They suggest that this is due to a tidal influence from the MW combined with the SMC's recent close pericentric passage ~150 Myr ago.

- **East 2:** The old population of the East 2 substructure shares similar properties with that of the East 1 substructure. The older population is slightly metal-poor compared to the LMC, with a broader distribution and a peak closer to the LMC. The younger population, however, is metal-poor and exhibits properties similar to those of the SMC. The older population's metallicity is comparable to that in the NE quadrant, while the younger population's metallicity is closer to that in the SE quadrant. The MDF and kinematics also indicate a strong association with the LMC. This feature was first reported by El Youssoufi et al. (2021), who suggested a similar formation mechanism to that of East 1, potentially originating during significant tidal interactions with the MW. Our results suggest that the old population might have formed from the LMC during these interactions. But the young stars or the gas from which they formed might have reached here from the SMC during the SMC crossing of the LMC disc plane ~400 Myr ago, as discussed in Cullinane et al. (2022b).

- **North 1:** The old stellar population exhibits similar kinematic and metallicity to those of the LMC, particularly to the NE quadrant, while the peak metallicity observed from it's MDF resembles closer to that of the SMC. In contrast, the young population is slightly enriched, similarly to the LMC's NW quadrant, suggesting potential origins through stripping from the inner disc or subsequent star formation following interactions. Notably, the perturbed proper motions of these young stars imply significant influences from both the SMC and the MW's tidal forces, hinting at possible tidal stripping from the LMC disc. Mackey et al. (2016) identified this feature first and proposed that it may have originated from the LMC's outer disc or resulted from close interactions between the Clouds. Cullinane et al. (2022a) conducted an extensive analysis of this northern arm-like structure and found that its metallicity aligns closely with that of the adjacent LMC outer disc. Their models predicted that the MW's tidal forces during the LMC's infall likely account for the observed increase in out-of-plane velocities along this feature. More recent investigations (El Youssoufi et al. 2021; Massana et al. 2023; Muñoz et al. 2023) have also reached similar conclusions.

- **South 1:** The South 1 substructure of the LMC comprises an old population with it's metallicity similar to the SMC, but slightly enriched which is comparable to the LMC's SE quadrant, and exhibits kinematics as the LMC. The young population also has a metallicity similar to the SMC, with a slight enrichment, which on comparison, is similar to the LMC SE quadrant, and shows perturbed proper motions, suggesting an origin from the SMC during past interactions. Distance estimates from (El Youssoufi et al. 2021) indicate proximity to the MB, implying this feature might be a stripped population from the outskirts of the SMC. Both Massana et al. (2023) and Muñoz et al. (2023) attributed the substructure's origin to interactions between the Clouds. Conversely, Cullinane et al. (2022b) found that the substructure's metallicity ([Fe/H] ~-1]) is consistent with that of the outer LMC disc, implying a perturbation of LMC disc material and not from the SMC's outskirts.

- **South 2:** The old and young populations in the South 2 substructure exhibit slightly higher metallicities than the LMC and have their MDFs similar to that of the SMC. The proper motions indicate a distance comparable to the MB region, suggesting that this substructure likely originated from the mutual interaction between the LMC and SMC, with debris from both galaxies. Previous studies (El Youssoufi et al. 2021; Massana et al. 2023; Muñoz et al. 2023) also support this scenario.

- **South 3:** The South 3 substructure traced by old population exhibits a metal-rich bimodal distribution, while the substructure traced by the young population is metal-poor and similar metallicity as the SMC. The old population is metal-rich than that of all the quadrants, while the young one has a metallicity similar to that of the SE quadrant. The proper motions are highly perturbed, and distance estimates from El Youssoufi et al. (2021) indicate a similarity to the MB. This suggests that the old population was likely stripped from the LMC during its interaction with the SMC, while the young population formed from gas stripped from the SMC. Massana et al. (2023) referred to this substructure as the 'Southern arm' and found that it predominantly consists of LMC material based on its MDF. Studies such as Cheng et al. (2022) and Muñoz et al. (2023) identified some metal-poor stars, indicating an origin from both the LMC and SMC, which is consistent.

- **SMC East:** The SMC East substructure, as traced by old stars, exhibits metallicities and kinematics similar to those of the SMC. The associated young population shows similar properties to the SMC but includes a smaller number of stars with metallicities characteristic of the LMC. The young population also displays relatively perturbed proper motions compared to the old population. A similar observation was reported by Massana et al. (2023), who identified a dual population: one consistent with the SMC and another with the LMC, suggesting the substructure originated from debris of both clouds. Interestingly, Cullinane et al. (2023) also observed two stellar populations: one consistent with the SMC main body and a second, highly perturbed population. The latter is on average 0.2 dex more metal-rich and located about 7 kpc in front of the main body population, moving towards the LMC. They concluded that this substructure primarily consists of SMC debris, recently stripped by the LMC.

- **SMC NOD:** The old and young populations associated with the SMC NOD substructure exhibit properties similar to those of the SMC. Specifically, the old population has a metallicity comparable to the SE and NW quadrants of the SMC, while the young population is similar to the SE quadrant. In the MDF, the young population is similar to the SMC East, showing an additional, smaller metal-rich peak that is closer to the LMC peak. This suggests that the old population primarily consists of SMC debris, while the young population might have formed with metal-rich gas from the LMC. Pieres et al. (2017) identified this elliptical structure, containing intermediate and old stellar populations, located at the distance of the SMC. El Youssoufi et al. (2021) concluded that it is the farthest from the SMC with a similar stellar population. Massana et al. (2023) also found bimodality in their analysis of the SMC NOD's MDF, with a metal-poor and old population and an intermediate-age population having metallicities similar to the outer regions of the SMC. They associated it primarily with the SMC, suggesting that it likely originated from it, but has been influenced by tidal interactions with the LMC.

- **SMC North:** The SMC North substructure features a slightly metal-rich older and younger population compared to the SMC, particularly with respect to the SMC's NE quadrant, where this substructure is located. In their MDFs, both populations exhibit a smaller metal-rich peak comparing to the peak metallicity of the LMC. The kinematics of the old population is similar to that of the SMC, while the young population shows highly perturbed motions. This structure was first identified by El Youssoufi et al. (2021), who located it at a distance similar to the SMC main body and associated it with the ellipsoidal structure of the SMC. They suggested that this feature might be undergoing tidal stripping, which removed stars from the SMC. Massana et al. (2023) named this substructure the SMC Leading, as it moves in the same direction as the SMC. They associated it with both the LMC and SMC, reflecting its proximity to the LMC's western region. Our findings align with these results, as we also observe a smaller metal-rich component that may originate from the outskirts of the LMC.

3.6 Summary

In this work, we compared the median metallicity estimates of several previously identified stellar substructures traced by old (RGB) and young (supergiant) stars in the outer regions of the Clouds by using the metallicity catalogues provided by Omkumar et al. (2025). To understand the potential origin of these substructures and how they drive the metallicity gradients of the Clouds, we compared the estimated median metallicities of each substructure with the metallicity gradients. We also analysed their kinematics using the proper motions from *Gaia* DR3.

As observed in our study, a central positive gradient in the SMC was recently observed in a spectroscopic study (Navabi et al. 2025), who attributed it to radial migration or centralised chemical enrichment. In addition to the observed breakpoints in the centre, it is evident from our analysis that the latter breakpoints in the outskirts, appear in the regions where most of these substructures are located. In some cases, we also see a positive metallicity gradient owing to them, which clearly suggests that the mutual interaction between the Clouds and the MW, which created the substructures, is also responsible for the breaks in the metallicity gradient. The MB substructure likely formed from a mix of stars stripped from the SMC and metal-rich gas from the LMC following their mutual interaction, consistent with previous findings. Substructures, East 1 and East 2 appear to have formed due to MW-induced deflections of the LMC disc during tidal interactions with the MW, in combination with the SMC passing over the LMC disc. The North 1 substructure also has a similar formation as the eastern substructures, while the young population might have formed after the interactions. The South 1, South 2, and South 3 substructures likely formed from the mutual interactions between the LMC and SMC, consisting mainly of SMC debris (South 1) and debris from both Clouds (South 2 and South 3). South 3 has a metal-rich old population with a bimodal distribution and a young population that is metal-poorer than the SMC. The SMC East substructure primarily consists of SMC debris, with a smaller number of stars having LMC-like metallicities. The perturbed proper motions of the young population suggest ongoing interactions with the LMC, leading to the formation of a dual population. The SMC NOD substructure likely originated from the SMC, with a bimodal MDF indicating a metal-poor old population and an intermediate-age population with LMC-like metallicity, suggesting tidal interactions with the LMC. SMC North is part of the ellipsoidal structure of the SMC, is located at a distance similar to the SMC main body, and is associated with tidal stripping of the SMC, but also has debris from the LMC outskirts.

Additionally, we also included the analysis of the metallicities of the dual velocity RGB stars found in the eastern and western sub-regions to understand their origin. We find that lower velocity components are slightly metal-rich relative to the higher velocity components in the same regions. Our analysis confirms that the lower velocity RGB component in the eastern region of the SMC, the tidally stripped population, has similar metallicities to the SMC inner disc. Based on the differences in distances between the foreground and main-body RC and velocity difference of two RV components of the RGB, James et al. (2021) estimated that the substructure formed $\sim 307 \pm 65$ Myr ago. This timescale is consistent with predictions of recent interactions between the MCs (Besla et al. 2012; Diaz & Bekki 2012), indicating that the substructure likely formed during a recent tidal interaction, highly likely to be stripped from the inner SMC.

These substructures collectively reflect a complex history of star formation, tidal interactions, and gravitational influences from both the LMC, SMC, and the MW, highlighting the dynamic and interconnected nature of the galaxies.

Data Availability

The photometric metallicity catalogues used in this work are available at the CDS via https://cdsarc.cds.unistra.fr/viz-bin/cat/J/A+A/700/A74.

3.A Metallicity gradient without substructures

We wanted to investigate the influence of substructure sources on the estimation of both overall and piecewise gradients of the clouds. To achieve this, we systematically removed the substructure sources from our analysis and subsequently reevaluated the estimations of the overall and piecewise gradients. This approach allows us to assess the impact of substructure sources on the accuracy of our gradient estimations and to enhance the robustness of our findings. Figures 3.8 and 3.9 show the overall metallicity gradient of LMC and SMC after removing the substructures sources from the overall gradient. Here, we can see that the overall gradient only changes slightly and within errors comparing to the respective overall gradients where the sources of the substructures are included.

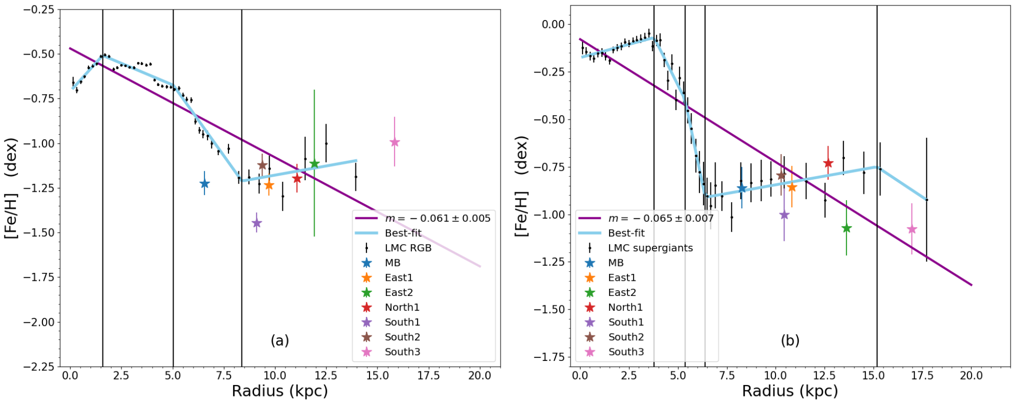

Figure 3.8: Same as Fig. 3.2, but with the sources of the substructures removed from the overall gradient.

3.B Metallicity gradients in different quadrants

To better understand the metallicity gradients of various substructures, we examined the metallicity gradient in different directions across the galaxies. We divided each of the LMC bins into four quadrants: north-east (NE; Y > 0 and X < 0), north-west (NW;

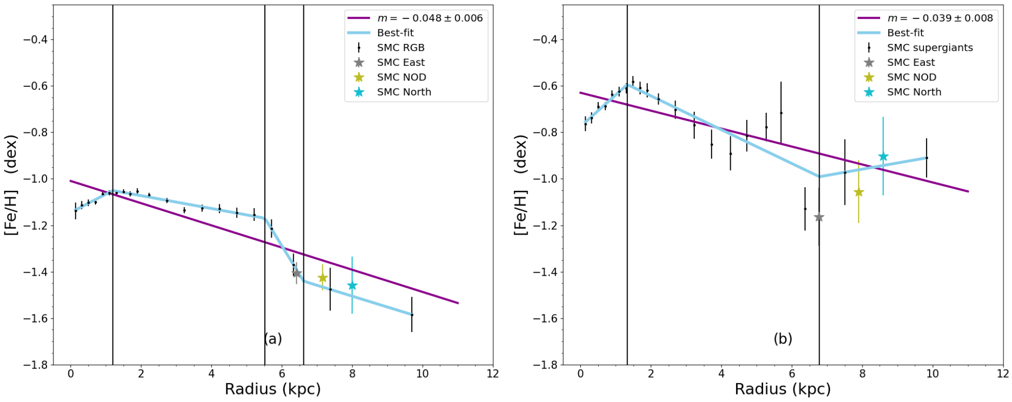

Figure 3.9: Same as Fig. 3.3, but the sources of the substructures removed from the overall gradient.

Table 3.5: Best-fit parameters for the LMC quadrants.

LMC	Quadrant	Slope 1	Breakpoint 1	Slope 2	Breakpoint 2	Slope 3	Breakpoint 3	Slope 4
RGB stars	NE	0.39 ± 0.07	0.9 ± 0.1	−0.04 ± 0.01	5.0 ± 0.2	−0.17 ± 0.01	8.8 ± 0.2	0.04 ± 0.01
	SE	0.01 ± 0.02	3.9 ± 0.4	−0.18 ± 0.02	9.7 ± 0.3	0.15 ± 0.03	–	–
	NW	0.07 ± 0.02	3.0 ± 0.3	−0.12 ± 0.01	7.4 ± 0.6	−0.03 ± 0.01	–	–
	SW	0.09 ± 0.06	1.8 ± 0.3	−0.11 ± 0.01	9.4 ± 0.2	0.23 ± 0.05	12.4 ± 0.2	−0.54 ± 0.09
Supergiants	NE	−0.00± 0.01	5.1 ± 0.2	−0.49 ± 0.11	6.5 ± 0.2	0.00 ± 0.01	–	–
	SE	0.04 ± 0.03	3.1 ± 0.3	−0.23 ± 0.02	7.7 ± 0.4	0.01 ± 0.01	–	–
	NW	0.04 ± 0.02	4.1 ± 0.2	−0.43 ± 0.04	6.4 ± 0.2	0.05 ± 0.01	–	–
	SW	−0.07 ± 0.02	5.1 ± 0.2	−1.13 ± 0.64	5.5 ± 0.1	0.00 ± 0.01	–	–

$Y > 0$ and $X > 0$), south-east (SE; $Y < 0$ and $X < 0$), and south-west (SW; $Y < 0$ and $X > 0$). We estimated the median metallicities across each quadrant. Figure 3.10 shows the metallicity gradient across these quadrants, with each quadrant plotted in a separate panel. The median metallicities for each bin are also indicated in the respective subplots, to show how well these gradients are estimated. Panel (a) refer to the LMC RGB stars and (b) to the LMC supergiants, while panels (c) and (d) refer to the SMC RGB and supergiants stars. Note that we employed the same binning criteria as for their respective radial bins. This led to some bins having null sources and those bins were discarded from the fits. For the SMC supergiants stars, the median metallicities in the western quadrants are very scattered, due to fewer stars present in these regions. Hence, we were not able to obtain any breaks, and we fitted linear fits for these quadrants.

3.C Metallicity distributions

To analyse the metallicities of various substructures traced by RGB stars in the LMC, we created histograms of their metallicity distributions, as illustrated in Figs. 3.11a. Each substructure is represented with a different coloured histogram. We further quantified these distributions by fitting them with Gaussian functions, which are shown in Fig. 3.11b, using the same colours for the fits. Figures 3.11c and 3.11d represent the metallicity

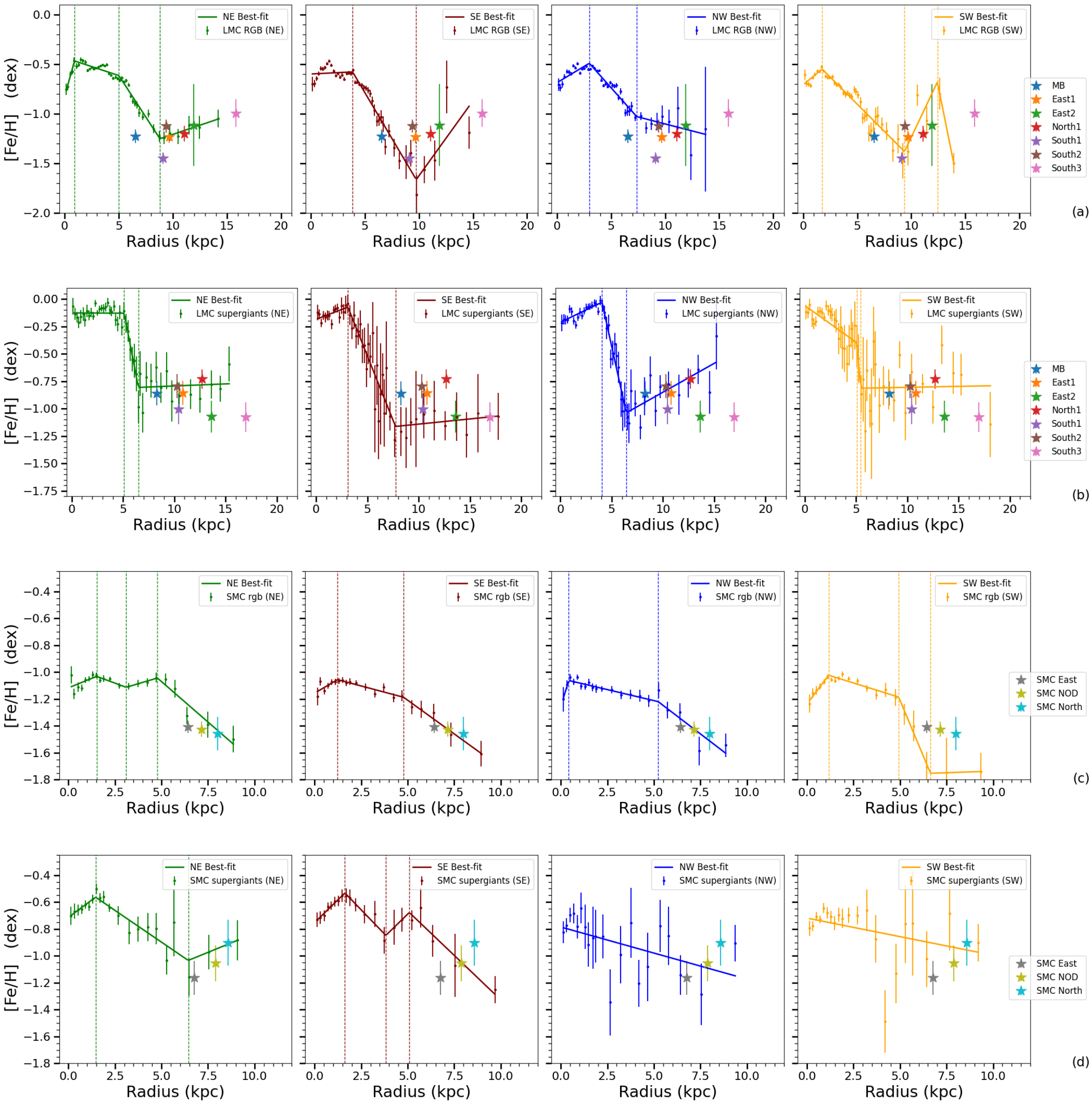

Figure 3.10: Metallicity gradient using piecewise fitting for each quadrant, including the corresponding break points. Panels (a) and (b) for LMC RGB and supergiant stars, while panels (c) and (d) focus on SMC RGB and supergiant stars, respectively. The gradients for the NE, SE, NW, and SW quadrants are arranged from left to right. Each panel features median metallicities and break points in corresponding colours as the piecewise fits, along with over-plotted median metallicities of the identified substructures for comparison.

Table 3.6: Best-fit parameters for the SMC quadrants.

SMC	Quadrant	Slope 1	Breakpoint 1	Slope 2	Breakpoint 2	Slope 3	Breakpoint 3	Slope 4
RGB Stars	NE	0.06 ± 0.05	1.5 ± 0.5	−0.05 ± 0.05	3.1 ± 0.8	0.04 ± 0.04	4.8 ± 0.3	−0.12 ± 0.02
	SE	0.08 ± 0.04	1.2 ± 0.2	−0.04 ± 0.01	4.8 ± 0.5	−0.10 ± 0.01		
	NW	0.45 ± 0.19	0.4 ± 0.1	−0.03 ± 0.01	5.2 ± 0.7	−0.11 ± 0.01		
	SW	0.18 ± 0.04	1.2 ± 0.1	−0.04 ± 0.01	4.9 ± 0.1	−0.33 ± 0.04	6.6 ± 0.2	0.00 ± 0.02
Supergiants	NE	0.10 ± 0.05	1.5 ± 0.3	−0.09 ± 0.02	6.4 ± 1.0	0.06 ± 0.07		
	SE	0.14 ± 0.04	1.6 ± 0.2	−0.14 ± 0.03	3.8 ± 0.4	0.14 ± 0.16	5.1 ± 0.4	−0.13 ± 0.01
	NW	−0.04 ± 0.02	–	–	–	–	–	–
	SW	−0.03 ± 0.02	–	–	–	–	–	–

distributions and their corresponding Gaussian fits for the substructures traced by LMC supergiants, using the same colours for comparison between the same substructure regions traced by young and old stars.

Similarly, to assess the metallicities of different substructures traced by RGB stars in the SMC, we plotted their metallicity distributions in histograms (Figs. 3.12a). Each substructure is represented using distinct colours. We quantified these distributions by applying Gaussian fits, as shown in Fig. 3.12b, with the fits coloured to correspond to the histograms. Figures 3.12c and 3.12d illustrate the metallicity distributions and their Gaussian fits for the substructures traced by SMC supergiants, utilizing same colours for comparison between young and old substructures.

3.D Tabular summary

Tables 3.7 summarises the results obtained from our study of the substructures in the Clouds traced by the old (RGB) stars. The table consists of the metallicity characteristics of old (RGB) stars across different substructures, including radial gradients and the metallicity gradients in different quadrants across each galaxy, as well as the results of the Ks statistical test and an analysis of their stellar proper motions. A similar summary for the substructures traced by the young (supergiant) stars are provided in Table 3.8.

Table 3.7: Summary of the old stellar substructures around the Clouds.

Substructures	Radial gradient (piecewise)	Quadrants	MDF	Ks test	Proper motions
MB	~SMC	Metal-poor than all quadrants	~SMC	–	Between LMC and SMC
East1	~LMC	~NE quadrant and SW quadrant	~SMC	–	LMC
East2	~LMC	~NE quadrant	Broader distribution Peak closer to LMC	SMC	LMC
North1	~LMC	~NE quadrant	~SMC	SMC	LMC
South1	~SMC	~SE quadrant	Metal-poor than SMC	–	LMC
South2	Slightly metal rich than LMC	~NW quadrant	~SMC	–	LMC
South3	Metal rich than LMC	Metal-rich than all quadrants	Bimodal distribution	SMC	Highly perturbed
SMC East	Slightly metal poor than SMC	Slightly metal-poor than SE and NW quadrants	Metal-poor than SMC	–	SMC
SMC NOD	On the gradient	~SE and NW quadrants	Metal-poor than SMC	–	SMC
SMC North	Slightly metal rich than SMC	~NE quadrant	Metal poor than SMC	–	SMC

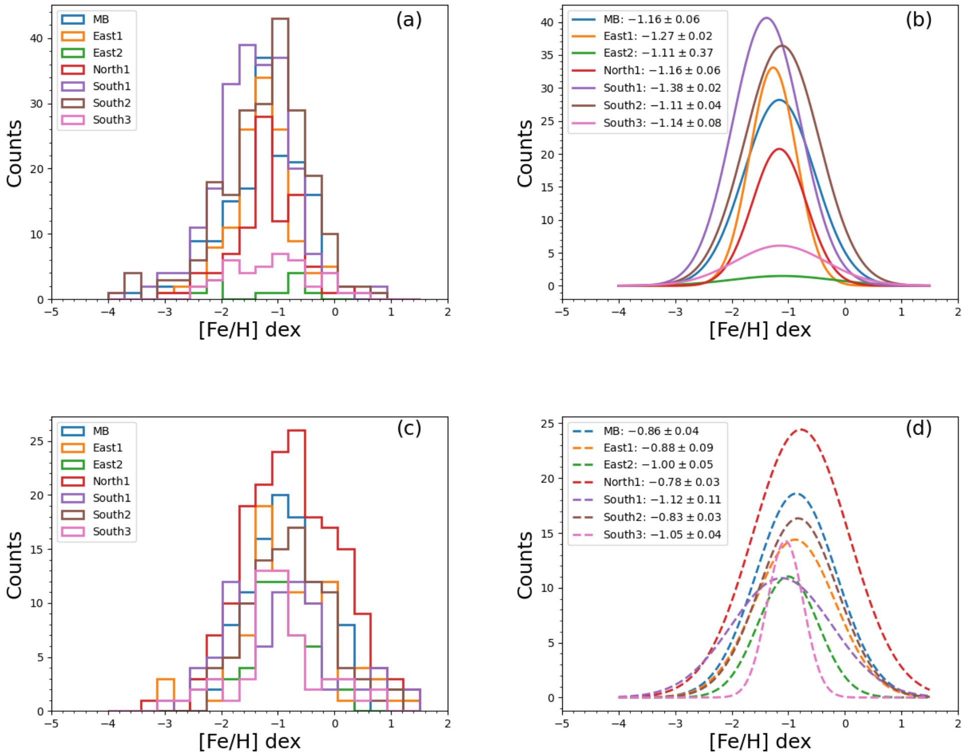

Figure 3.11: Metallicity distributions of different LMC substructures from RGB stars (a) and Best-fit Gaussian for the same distributions are shown (b). Figures (c) and (d) are same as (a) and (b), but for the supergiant sources.

Table 3.8: Summary of all young stellar substructures around the Clouds

Substructures	Radial gradient (piecewise)	Quadrants	MDF	Ks test	Proper motions
MB	~LMC	Slightly metal-poor than NE and SW and metal-rich than NW	~SMC	–	Between LMC and SMC
East1	~LMC	~Slightly metal-poor than NE and western quadrants	Broader distribution Metal poor than SMC	–	LMC
East2	Metal-poor than LMC ~SMC	~SE quadrant	Metal-poor than SMC	–	LMC
North1	Slightly Metal-rich than LMC	~NW quadrant	~SMC	–	Highly perturbed
South1	Metal-poor than LMC ~SMC	Metal-rich than SE	Metal poor than SMC	–	Highly perturbed
South2	Slightly Metal-rich than LMC	NE and SW quadrant	~SMC	SMC	Highly perturbed
South3	Metal poor than LMC ~SMC	~SE quadrant	Metal poor than SMC	–	Highly perturbed
SMC East	Slightly metal poor than SMC	Metal-poor than all quadrants	Metal poor than SMC Small peak closer to LMC	–	Highly perturbed
SMC NOD	On the gradient	~SE quadrant	Metal poor than SMC Small peak closer to LMC	–	Highly perturbed
SMC North	Slightly metal rich than SMC	~NE quadrant	Metal poor than SMC	SMC	Highly perturbed

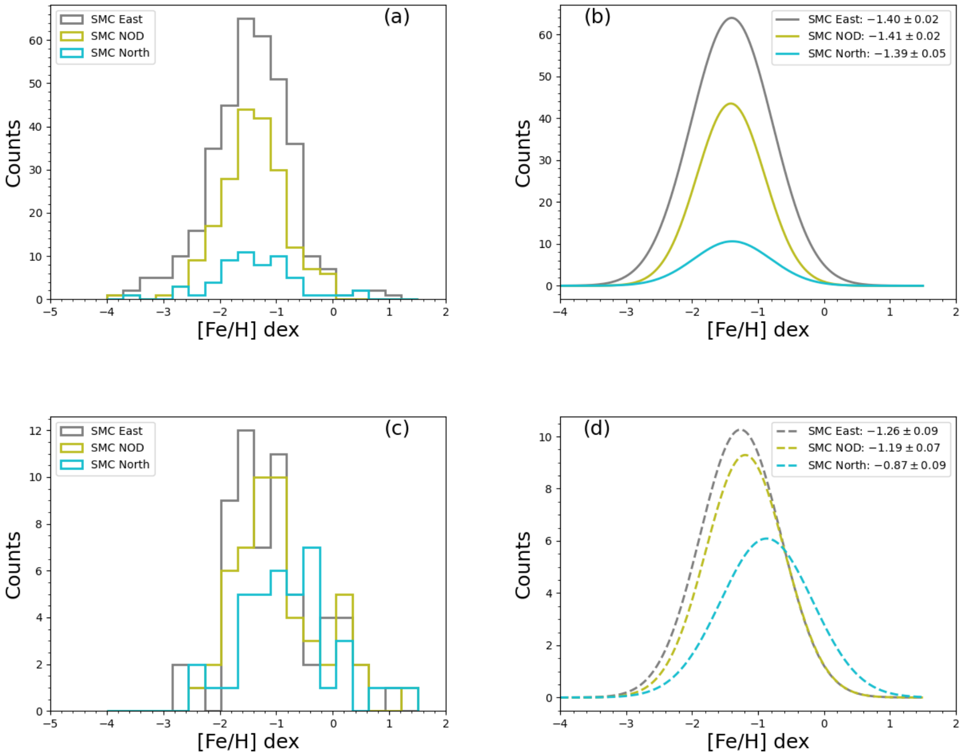

Figure 3.12: Same as Fig. 3.11 but for the SMC sources.

4 Deep VISTA observations of the Magellanic Clouds (VMCDeep)

*M.-R. L. Cioni, **A. O. Omkumar**, N. J. G. Cross, F. Cusano, F. Dresbach, F. Ficara, F. Niederhofer, J. M. Oliveira, V. Ripepi, S. Vijayasree, G. Clementini, R. de Grijs, L. Girardi, M. A. T. Groenewegen, V. D. Ivanov, N. Kacharov, M. Marconi, A. Mazzi, G. Pastorelli, C. M. Pennock, M. Petr-Gotzens, J. Storm, S. Subramanian, J. Th. van Loon, R. P. Blake, M. J. Holliman, J. Irwin, M. J. Irwin, R. G. Mann, M. Read, E. Sutorius*

This chapter is based on a manuscript submitted for publication in Astronomy & Astrophysics journal.

4.1 Introduction

The inner parts of galaxies are among the most challenges places to observe individual stars because they are prone to crowding, contain gas and dust and may host nuclear structures such as a black hole. The Large and Small Magellanic Clouds (LMC and SMC) are our nearest pair (50−60 kpc distance; de Grijs et al. 2014b and de Grijs & Bono 2015b) of interacting dwarf irregular galaxies and locating their centres is not trivial due to their mutual dynamical interaction and their interaction with the Milky Way. These events may cause the Clouds to break apart (e.g. Deason et al. 2017, McClure-Griffiths et al. 2018) and we are witnessing an early stage of this process.

Several multi-wavelength imaging surveys have produced data to unravel properties of the Clouds, their star formation history (SFH), three-dimensional (3D) structure, rotational pattern, tidal tails, and associated satellites (e.g. Sales et al. 2013, Ripepi et al. 2017, Gaia Collaboration et al. 2018b, Mackey et al. 2018, Rubele et al. 2018b, Kallivayalil et al. 2018, Belokurov & Erkal 2019b, El Youssoufi et al. 2019, Mazzi et al. 2021, Massana et al. 2022, Cullinane et al. 2023). Despite major progress in characterising their external regions, our observational capabilities deteriorate in the central regions. The most sensitive ground-based imaging survey to-date, the Survey of the Magellanic Clouds Stellar History (SMASH; Nidever et al. 2017b), shows a lack of stars in the LMC centre (Choi et al. 2018b) due to crowding. The most powerful space astrometry mission, *Gaia*, is also incomplete in the high-density regions (Gaia Collaboration et al. 2016b) although there are in general ∼20% more sources in Data Release 3 (DR3) than in DR2 (Gaia Collaboration et al. 2023b). For example, the incompleteness within a 2.5 deg radius of the LMC centre is at least 50% (Jiménez-Arranz et al. 2023, Rathore et al. 2025a). The most extensive monitoring programme (in the V and I bands), the Optical Gravitational Lensing Experiment (OGLE; Udalski et al. 2015), shows that an apparent extension along the line of sight, as traced by RR Lyrae stars in the inner region, is the result of blending effects (Jacyszyn-Dobrzeniecka et al. 2017b, 2020b). The Visual and Infrared Survey Telescope for Astronomy (VISTA; Sutherland et al. 2015) survey of the Magellanic Clouds system (VMC; Cioni et al. 2011), because of its sensitivity and spatial resolution in the near-infrared, allows to penetrate the dusty and dense regions, but not adequately enough (i.e. sources are still blended and faint stars are not detected) to quantify structures related to the origin, dynamics, and evolution of the galaxies (Niederhofer et al. 2022a). Even the central parts of the Clouds are very extended on the sky and accurate studies with the *Hubble Space Telescope* (HST), (e.g. Kallivayalil et al. 2013, Weisz et al. 2013, van der Marel & Kallivayalil 2014, Zivick et al. 2018), or the *James Webb Space Telescope* (JWST) over several square degrees are impractical, given their small field of view (HST$\sim$ 7 arcmin^2, JWST$\sim$ 5 arcmin^2).

The location of the centre of the LMC, which depends on the type of tracer (stars or gas) and perhaps also on wavelength, is highly debated. The disc-centre may be displaced from the bar-centre due to the interaction with the SMC (Pardy et al. 2016) and there is only tentative evidence of the presence of a central black hole (Boyce et al. 2017; Han et al. 2025). *Gaia* Early DR3 (EDR3) data suggest that the rotational centre is closer to the centre from photometric studies than from the H I gas (Gaia Collaboration et al. 2021b). Using multi-epoch VMC data Niederhofer et al. (2022a) determined the proper motion of stars within the central parts of the LMC. They used a simple flat-rotating disc model to analyse and interpret the proper motion data and found a stellar centre of rotation very close (~10 arcmin) to the position of the tentative central black hole as well as a high inclination (~33.5 deg) of the central parts of the galaxy. Their study confirmed a higher rotational velocity for the young stars (~90 km s^{-1} and <0.5 Gyr old) compared to the intermediate-age/old stars (~70 km s^{-1} and >1 Gyr old), which can be explained by asymmetric drift. They constructed spatially resolved velocity maps of the different (by age) stellar populations which showed that intermediate-age/old stars follow elongated orbits parallel to the bar's major axis whereas young stars show motions along a central filamentary bar structure. In a subsequent study by Vijayasree et al. (2025a), which extends the VMC time baseline from about six to ten years, the position of the centre was refined within the uncertainties of the previous determination. Their study, which covers the entire galaxy, following the analysis method of Niederhofer et al. (2022a), allows to also derive a kinematic centre which turns out to be very close to the dynamical centre of mass obtained by Rathore et al. (2025a). The latter developed a novel solution to tackle crowding-induced incompleteness in the *Gaia* data in order to measure the bar properties (radius, axis ratio, position angle and strength) using red clump stars. They traced the crowding level using the Gaia BP−RP colour excess.

In the SMC Niederhofer et al. (2018, 2021b) showed that stars within the dense core region have a systematically different motion which can be explained either by stretching of the SMC, so the outer parts move differently than the central parts, or by a tidal feature behind the main body of the galaxy. Data from HST support SMC stretching (Zivick et al. 2018) and the *Gaia* data confirm a proper motion dichotomy (Gaia Collaboration et al. 2021b). The apparent anisotropic tangential motion at all radii derived from Gaia DR2 data and spectra of many giant stars corroborate the tidal disruption of the SMC, possibly all the way into the core (De Leo et al. 2020).

Motivated by the excellent astrometric performance of the VISTA camera and inspired by the possibility of finding the cores of the Clouds, we developed an observational programme to obtain more robust proper motions to constrain the central kinematic patterns. We focused on one VISTA *tile* (a region of ~1.77 deg^2) per galaxy and were awarded observations at the European Southern Observatory (ESO) with a better sky quality and an increased number of epochs, at both J and K_s bands, with respect to the

VMC survey. These aspects, including a long time-baseline obtained from the combination of deep and shallow (from VMC) data, will provide an independent and more precise measurement of the stellar proper motions in the densest regions of the Clouds. In this paper, Section 4.2 describes the observations and Section 4.3 presents the data reduction process. A comparison between the new data and those from the VMC survey is given in Section 4.4. Section 4.5 presents the content of the catalogue whereas ongoing scientific applications of the data are presented in Section 4.6. Section 4.7 concludes this study.

4.2 Observations

The VISTA data described here correspond to a total of 160 hours obtained during the period from December 2020 to January 2023 and refer to ESO programmes 105.206M, 106.201G, 108.221P and 109.23G7 (VMCDeep or this programme hereafter). VISTA is a 4 m class alt-azimuth mounting survey telescope which is part of ESO's Paranal Observatory. Until March 2023, VISTA was equipped with an infrared camera (VIRCAM; Sutherland et al. 2015) operating between 0.8 μm and 2.3 μm with a set of broad and narrow band filters. VIRCAM had an array of 16 Raytheon detectors with a mean pixel size of 0.339 arcsec and a 1.65 deg diameter field-of-view. The point-spread function (PSF) of the instrument and camera systems was designed to have a full width at half maximum (FWHM) of 0.51 arcsec. VISTA observed a continuous area of sky by filling in the gaps between the detectors using a sequence of offsets, each by a significant fraction of a detector. In this programme, we combine three fixed offset positions in the "Y" direction of the array, named *pawprints*, to cover an area of $\sim$ 0.9 deg^2 (a VISTA *half tile*); each pawprint covers an area of 0.6 deg^2 excluding the gaps between the detectors. Then, we combine another set of three pawprints which were offset also in the "X" direction, with respect to the previous set. Each half tile corresponds to a stripy coverage of the sky area which is counter-intuitive with respect to the nomenclature used to refer to them in the observations, i.e. left (LFT) and right (RHT). The merging of the two half tiles produces a VISTA *tile* that covers about 1.77 deg^2 (Fig. 4.1).

Observations were obtained in service mode by ESO staff. This mode guarantees efficiency of operations and a high level of data homogeneity, it is also the best method to capture images of high-quality which are needed for this study to disentangle sources in the dense stellar regions at the centres of the Clouds. We requested observations to take place during the following weather conditions: seeing of 0.7 arcsec at 500 nm at zenith, airmass < 1.7, any lunar phase, and a variable/thin cirrus sky transparency. A violation of these observing requirements by 10% is still considered as if observations were obtained within specifications. Table 4.1 describes the main parameters of the VISTA observations. The total exposure time is calculated as follows (number of epochs)×2×(number of jitters)×(number of Detector Integration Time – DITs)×DIT. The factor of two comes from the tiling pattern, during which most points of the sky are observed twice (on average). The exception are the tile edges, observed once, and some areas of extra overlap among the detectors that are observed four or six times. The observations followed the nesting sequence FPJME (see VISTA user Manual[6]). This sequence first sets a filter

---

[6] https://www.eso.org/sci/facilities/paranal/decommissioned/vircam/doc.html

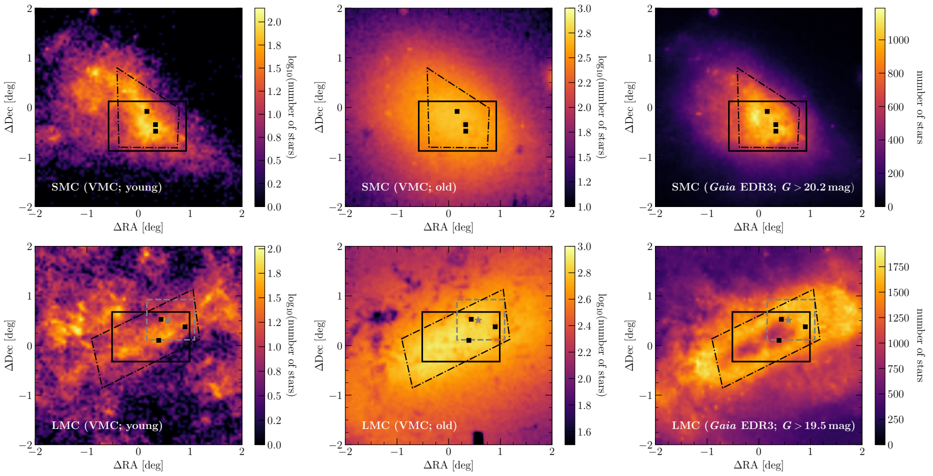

Figure 4.1: Distribution of young (upper main sequence stars, left) and old (red clump and brighter stars, middle) stars from the VMC survey and *Gaia* EDR3 (right) in 3×3 arcmin^2 bins across the SMC (top) and LMC (bottom). The rectangles indicate the VISTA tiles from this programme while the irregular polygons show the areas with special *Gaia* observations designed to overcome crowding issues (see text for details). Small black squares highlight star forming regions while a dashed-grey box shows the location of a suspected central black hole (star).

(F), then obtains images at all jittered positions of the first pawprint (P), before moving to the next pawprint and taking all the jittered images at that position (J), within a microstepping pattern (M) if specified and so on, until all multiple three pawprints that form the half tile are executed (E). The Jitter pattern was *Jitter9s* and the tile patterns were *Tile3nx* and *Tile3px* for the RHT and LFT half-tile observations, respectively. The J- and K_s-band observations were independent from each other and could have been obtained during the same night without restrictions in time of execution except for the wish to distribute observations of the same half tile and filter across multiple nights.

The pawprint mosaic was prepared using the survey area definition tool (SADT; Arnaboldi et al. 2008) using default values for the parameters (maximum jitter = 15 arcsec

Table 4.1: Observing parameters.

Filter	J	K_s	Filter	J	K_s
Central wavelength (μm)	1.25	2.15	Exposure time per epoch (s)	360	900
Bandwidth (μm)	0.18	0.30	Number of epochs	40	40
Detector Integration Time – DIT (s)	10	5	otal exposure time (s)	14400	36000
Number of DITs	2	10	Predicted sensitivity per epoch (Vega mag)	20.5	19.0
Number of exposures	1	1	Signal-to-noise per epoch at depth required	10	10
Microstepping	1	1	Total predicted sensitivity (Vega mag)	22.5	21.0
Number of Jitters	9	9	Total signal-to-noise at depth required	10	10
Paw-prints in half tile	3	3	Saturation limit	12.7	11.4
Pixel size (arcsec)	0.34	0.34	Tile area (deg^2)	1.77	1.77
System FWHM	0.51	0.51	Number of half tiles	80	80

Notes. Jitter pattern = *Jitter9s*. Tile patterns = *Tile3nx* and *Tile3px*.

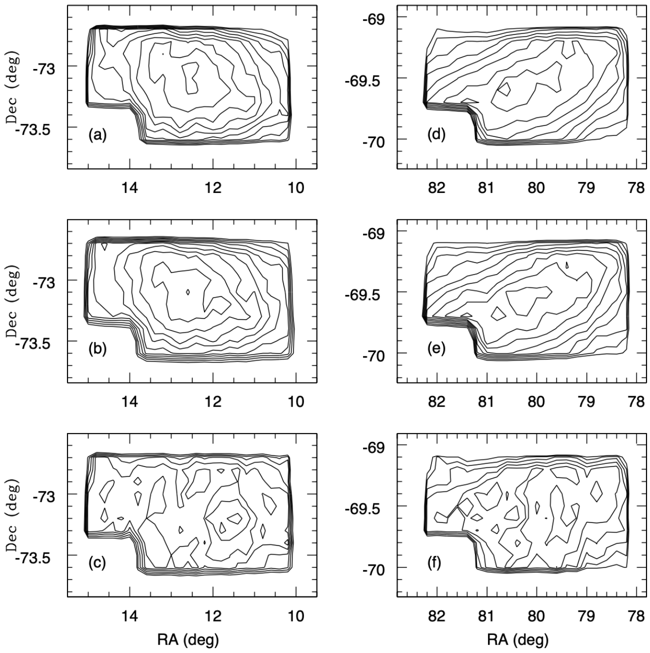

Figure 4.2: Spatial distribution of sources from the SMC (left) and LMC (right) catalogue detected in both J and K_s, and with *ppErrBits*<256. Top panels refer to all sources, middle panels refer to stars and bottom panels refer to galaxies. Contours mark number density levels increasing towards the centres as follows. Panel (a): from 2 000 in steps of 200. Panel (b): from 1 000 in steps of 200. Panel (c): from 500 in steps of 75. Panel (d): from 3 000 in steps of 300. Panel (e): from 2 000 in steps of 250. Panel (f): from 800 in steps of 75. The missing bottom-right corner corresponds to the area covered by detection #16.

and *backtrackStep*=100) and also for the tile orientation (position angle = 0 deg) with the "Y" axis to the North and the "X" axis to the West. The position angle is defined to increase from North to East. This is the best orientation to maximise the coverage of the central areas of the Clouds where Gaia data are not optimal (Fig. 4.1). We created two geodesic rectangles centred at α = 05:20:54.47, $\delta = -69{:}34{:}43.32$ (J2000.0) for the LMC and α = 00:50:16.06, $\delta = -73{:}10{:}40.92$ (J2000.0) for the SMC with width = 1.4753 deg and height = 1.2005 deg. Guide stars were assigned automatically to each tile using the Two Micron All Sky Survey (2MASS) catalogue (Skrutskie et al. 2006).

4.3 Data processing

4.3.1 CASU reduction

The raw VISTA images were reduced using the VISTA Data Flow System (VDFS; Irwin et al. 2004) version 1.5 at the Cambridge Astronomy Survey Unit (CASU[7]). The most relevant steps in the reduction of the VISTA images are: – reset, dark, linearity, flat-field and de-stripe correction (i.e., removing a horizontal pattern in the background);

---

[7] http://casu.ast.cam.ac.uk/surveys-projects/vista

Table 4.2: Quality control parameters for high-quality observations.

Galaxy	α (h:m:s)	δ (°:′:″)	Filter	Half tile	N	Airmass	FWHM (″)	Ellipticity	Zero-point (mag)
SMC	00:50:16.06	−73:10:40.92	J	LFT	43	1.54±0.04	0.80±0.06	0.08±0.02	23.80±0.11
			J	RHT	42	1.57±0.09	0.81±0.07	0.08±0.02	23.82±0.07
			K_s	LFT	40	1.54±0.04	0.74±0.06	0.07±0.02	23.07±0.02
			K_s	RHT	40	1.56±0.05	0.74±0.05	0.07±0.02	23.07±0.02
LMC	05:20:54.47	−69:34:43.32	J	LFT	37	1.46±0.06	0.78±0.04	0.09±0.03	23.75±0.11
			J	RHT	39	1.48±0.07	0.79±0.04	0.09±0.02	23.73±0.12
			K_s	LFT	38	1.47±0.06	0.76±0.05	0.07±0.02	23.03±0.03
			K_s	RHT	38	1.47±0.07	0.75±0.05	0.07±0.02	23.02±0.03

Notes. The coordinates are those of the tile centres. LFT corresponds to the tile pattern *Tile3px* and RHT to *Tile3nx*.

– sky-background correction; – jitter and pawprint stacking; – catalogue generation; – astrometric and photometric calibration. Detector crosstalk and sky fringing as well as persistence effects following the observation of a bright object are negligible or rare and are ignored during pipeline processing. The reduction takes also into account information from all VISTA data obtained during the same night and week regardless of host programme. Observational uncertainties are propagated during the data processing and quality control parameters are calculated to monitor the data to both evaluate the observing conditions (in retrospect) and the individual data reduction steps. Among them are: the zero-point to measure the atmospheric extinction, the FWHM to measure the seeing, the ellipticity to evaluated the quality of the guiding and active optics correction, and the sky level to estimate the background level and its variations. Table 4.2 shows the mean values of some quality control parameters for this programme. The quality parameters for additional observations that do not meet the sky quality conditions are provided in Table 4.5. Overall, 508 sets of pawprint images were obtained, where one set corresponds to the three offset positions that cover a given half tile. There is an excellent consistency among the quality parameters associated to the observations of the two half tiles at the same wave band for both high (Table 4.2) and low (Table 4.5) quality data. A pawprint image is produced by stacking and combining the images obtained at each jitter position. Each image (including a confidence map) and catalogue are delivered in Rice compressed format and are multi-extension FITS files containing each the information for all of the 16 detectors covering the field-of-view. The processing history is recorded directly in the FITS headers.

4.3.2 WFAU reduction

The data produced at CASU using the VDFS are ingested into the VISTA Science Archive[8] (VSA; Cross et al. 2012) which is hosted at the Wide Field Astronomy survey Unit (WFAU[9]). At the WFAU the data are further processed and curated to produce standardised data products using the same software, which guarantees that the data are processed homogeneously throughout the entire processing chain. Multiple epochs in the same

---

[8] http://vsa.roe.ac.ukl

[9] https://ifa.roe.ac.uk/research-areas/wide-field-astronomy-unit

filter and pointing are combined to produce *deepstack* images, which due to the increased exposure time allow to detect faint sources. A *tile* image in a given filter is created by combining all individual images in that filter (also from different pointings) that meet pre-defined quality criteria. Their sky level and individual pawprint astrometric and photometric distortions are adjusted in the grouting process (González-Fernández et al. 2018a). Deepstack and tile images have associated confidence images that contain the relative weighting for each pixel. This includes bad pixel masking, the effects of jittering, seeing and exposure time weighting. Further data products are generated in a database-driven manner. Catalogues are extracted from the deep images and single-filter catalogues are merged to create catalogues of sources, which can be cross-correlated with external catalogues (hosted at the VSA) to produce catalogues of neighbours.

The basic tables which contain information on the deep VISTA data are the *vmcdeepDetection*, which contains the catalogues corresponding to individual observations, and *vmcdeepSource*, which contains the list of sources obtained from deepstack images matched between the J and K_s bands. In the vmcdeepSource table the same source may appear more than once depending on its location with respect to the overlap among the pawprints forming a tile. These duplicates are identified in a *seeming* process and the attribute *priOrSec* allows users to select unique sources. Note that the best detection among the duplicates is defined as the source closest to the optical axis of the camera. The position and magnitude of each source in any given table refers to the astrometrically and photometrically calibrated measurements using the parameters specified in the image headers. The photometric calibration of the VISTA data is described in González-Fernández et al. (2018a) and the precision achieved in the J and K_s filters is better than 2%. All tiles show a 10–20 mas systematic astrometric pattern. Both astrometry and photometry rely on the observation of stars from the 2MASS catalogue within each detector and with magnitudes between 12 and 14 in both bands. In addition, there are quality flags (*ppErrBits*) that identify problems related to the ingestion, incompleteness, and detection of the sources as well as morphological classification flags (*mergedClass*) to indicate stellar, non-stellar, borderline sources and noise. For more details about the columns present within each table readers are referred to the CASU and VSA web pages. Known issues present in the VISTA data, such as bad regions in specific detectors or spurious sources around bright stars, are also described on the web pages. Only images that meet the observing requirements (Table 4.2) are included into the creation of deepstack and tile images as well as their associated catalogues. The other images (Table 4.5) are deprecated and remain only available as single observations/detections. Figures 4.21 and 4.22 show most of the LMC and SMC tiles produced from the stacking of all the good-quality observations.

4.3.3 PSF photometry

Point Spread Function (PSF) photometry is performed separately in the J and K_s bands: per epoch, per half tile and on the stacked images, following the method described in Rubele et al. (2015) (see also 4.B). A band-merged catalogue is subsequently created by associating sources within 1 arcsec in distance. In brief the method works as follows. Calibrated pawprint images are first combined using the SWarp programme (Bertin et al.

2002) to produce a uniform sky subtracted deep tile image. The PSF in each detector on each pawprint image is normalised to a constant PSF reference model before combining them and artefacts are removed by masking contaminated regions. This process aims to render more uniform the limiting magnitude on the final deep tile with respect to intrinsic differences in detector sensitivity and stellar crowding. The PSF magnitudes are aligned with the magnitudes obtained through the VDFS by applying systematic shifts of about 0.46 mag in J and 0.25 mag in K_s (see Appendix 4.C) and are not corrected for reddening. We note that with this process the PSF on individual half-tile images, that refer to a set of observations obtained at a specific epoch during ~1 hour, will be more homogeneous than that resulting from deep and stacked observations combining epochs observed during different sky conditions. While this represents a good average that can serve multiple-scientific applications, a dedicated processing tailored to address specific aspects, such as the determination of the SFH (Sec. 4.6.4) or the detection of semi-resolved star clusters (Miller et al. 2026), may provide better results.

4.4 Differences with respect to VMC

Compared to previous VISTA observations of the Clouds obtained in the VMC survey (Cioni et al. 2011), this programme adopts a larger number of jitter positions (9 versus 5 in VMC) and a reduced number of DITs (2 versus 8 and 10 versus 15 in VMC for the J and K_s band, respectively). This results in less images per pawprint at a given position in the J band (18 vs 40 in VMC, where the number of images is given by the product of the number of DITs and Jitters) and consequently a shorter exposure time per epoch (360 s versus 800 s in VMC). The opposite occurs in K_s (90 vs 75 images in VMC and 900 s versus 750 s exposure time in VMC). This programme uses only two filters (J and K_s) instead of three (VMC also observed in the Y band). The exposure time was designed to detect faint pulsating variable stars in single-epoch images and old main-sequence turn-off stars in stacked images whereas the choice of filters reflects the best calibrated filters (VISTA photometry is calibrated with respect to 2MASS which does not have a Y filter) and those where variable stars obey a clear, and narrow, period-magnitude relation. The centres of the tiles produced with this programme differ from those of the VMC survey. The deep VISTA tile in the LMC from this programme overlaps mostly with VMC tiles LMC 6_4 and LMC 6_5 whereas in the SMC the overlap is with tiles SMC 4_3 and SMC 4_4.

The average parameters indicating the quality of the data, covering the same regions, are given in Table 4.3. Compared to the VMC data, the FWHM of individual sources is about 0.2 arcsec smaller in both bands, which is larger than the standard deviations of the measurements. The difference in ellipticity is comparable to the uncertainties, but the dispersion is larger in this program than in the VMC survey, which could be due to an increased sensitivity to the source profile. The significantly larger number of epochs (about 40 in both J and K_s) obtained with this programme compared to those in the VMC survey (3 in J and 12 in K_s), combined with high-quality sky conditions, produces the deepest and best spatially resolved near-infrared survey for the centres of the Clouds to-date.

Table 4.3: Quality of the data compared to VMC data.

Survey	Band	FWHM ($''$)	Ellipticity
VMC	J	0.99±0.11	0.06±0.01
	$\mathrm{K_s}$	0.93±0.10	0.05±0.01
This work	J	0.79±0.08	0.08±0.04
	$\mathrm{K_s}$	0.75±0.07	0.07±0.05

Table 4.4: Number of detections.

Galaxy	Filter(s)	Star	Galaxies	Stars[a]	Galaxies[a]	Others[b]
SMC	$J + K_\mathrm{s}$	648 000	257100	543 000	199 800	400
	J	63 800	101 100	42 600	63 100	2 100
	K_s	24 300	68 700	19 800	50 500	1 000
	All	736 100	426 900	605 400	313 400	3 500
LMC	$J + K_\mathrm{s}$	789 800	273 500	648 800	215 100	300
	J	38 000	56 200	29 800	39 800	1 500
	K_s	59 000	58 300	25 600	35 000	1 500
	All	886 800	388 000	704 200	289 900	3 300

Notes. Subscript [a] refers to sources with minor quality issues (*ppErrBits*<256) and subscript [b] refers to detections with a 90% probability of being noise or saturated sources.

4.5 Content of the catalogue

The number of unique detections resulting from the deepstack images in J and K_s are given in Table 4.4. There are in total about 2.5 million detections equally split between the SMC and the LMC. The majority (80%) are sources detected in two filters of which 2/3 have a star-like profile and 1/3 a galaxy-like profile. An approximately equal number of sources are detected only in one filter and 0.3% are due to noise or saturated objects. In the SMC, there are more stars detected only in J than in K_s, while the opposite is true in the LMC. The number of extended sources in the SMC is larger than that of stars whereas in the LMC they are not significantly different. Note also that sources in detector #16 appear as single K_s-band detections because the variability of the quantum efficiency is worse in the J band, which impacts the flatfielding process and the ability to detect sources on the affected images. In what follows, we only refer to sources with minor quality issues (*ppErrBits*<256). This criterium excludes sources that lie within detection #16 or an underexposed area of a tile as well as within a dithered offset of a stacked frame boundary. It also excludes sources close to saturation, with a problematic photometric calibration or that while appearing in a tile they are not detected in the corresponding pawprints. At least 80% of the sources detected in two filters satisfy this criterium. In the SMC, this is also true for single detections in K_s whereas in J they drop to 65%. In the LMC, there are more good-quality sources detected only in J (75%) than in K_s (50%).

The spatial distributions of sources within the central region of each galaxy are shown in Figure 4.2. They homogeneously cover the central regions of the galaxies, contrary to

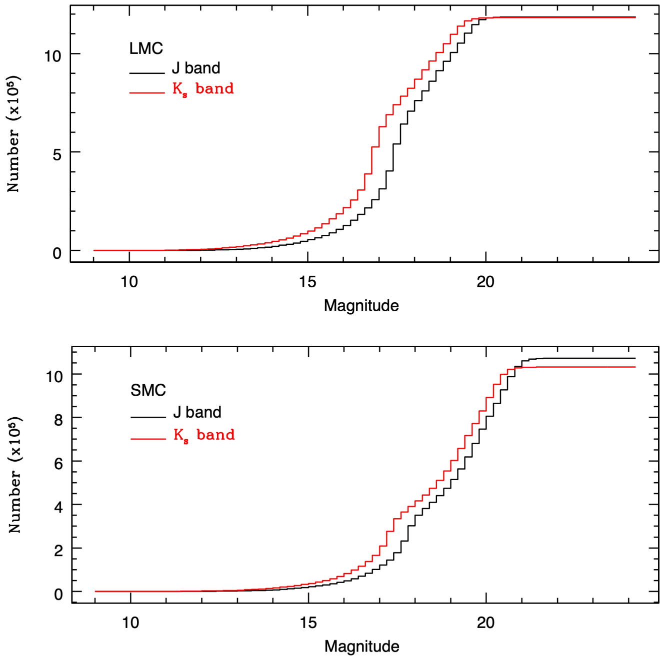

Figure 4.3: Cumulative star counts in bins of 0.2 mag for the entire LMC (top) and SMC (bottom) catalogues in the J (black) and K_s (red) bands.

the VMC survey (Fig. 4.19), which clearly favours the characterisation of morphological structures. They illustrate the expected increase in the number of sources towards the centres. The distribution of galaxies is unstructured, also as expected, whereas stars depict the elongations of the SMC from the south-east to north-west and along the LMC bar.

The number of sources increases as a function of magnitude as shown in Figure 4.3. This indicates that the SMC catalogue is approximately complete until $J \sim 20.5$ mag and $K_s \sim 20.3$, while for the LMC the diminishing trends begin about half a magnitude brighter. Figure 4.4 shows the apparent luminosity functions. The highest peaks in the distributions of stellar sources detected in both filters are created by red clump stars while the second highest peaks are due to RGB stars. Detections in the SMC reach sources ~1 mag fainter than in the LMC, which explains the double peaks in the distributions of single-filter detections. Separate luminosity functions for the LMC and SMC are shown in the Appendix. The luminosity functions of the VMC sources within the same regions are very similar; see Cioni et al. (2025) for luminosity functions across the entire VMC footprint. Many of the sources with a galaxy-like profile (galaxies hereafter) are likely stellar blends because compared to less dense stellar regions, where background galaxies are more easily distinguished from stars, the background galaxies dominate for J>20 mag and K_s>19 mag. The number of background galaxies in the high stellar density regions along the LMC bar can drop to 10–20 galaxies per detector (Niederhofer et al. 2022a).

Figure 4.5 shows the colour-magnitude diagram from the VMCDeep and VMC catalogues of LMC sources located within a 0.1 deg^2 region. A comparison of the magnitudes and the uncertainties does not show any systematic effect (Fig. 4.6). The magnitude

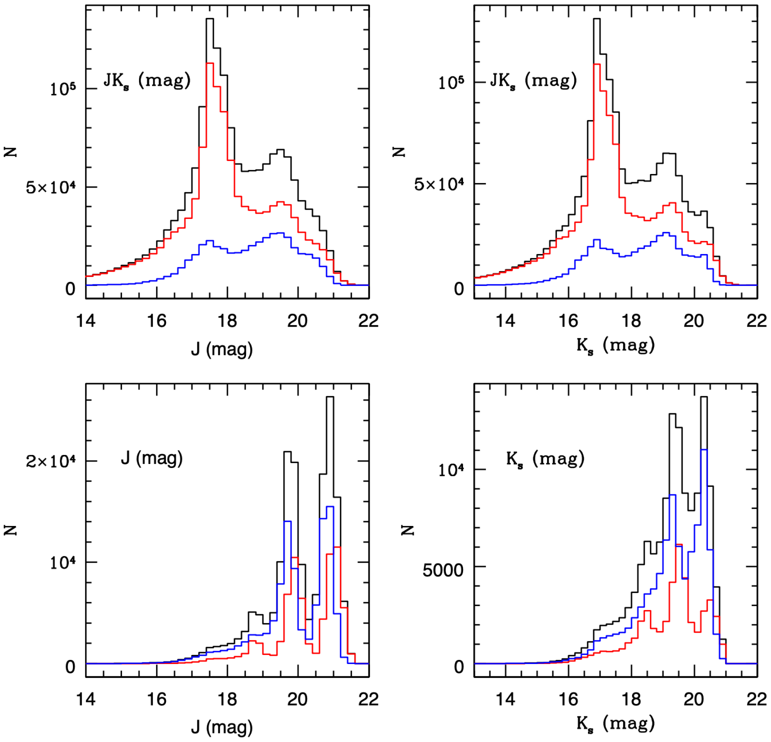

Figure 4.4: Apparent luminosity function in 0.2 mag bins, for sources in the entire catalogue with *ppErrBits*<256, with detections in one (bottom) and two (top) filters, as indicated on the upper left corner of each panel. Sources with a stellar profile are shown in red and sources with a galaxy profile are shown in blue whereas their total is shown in black.

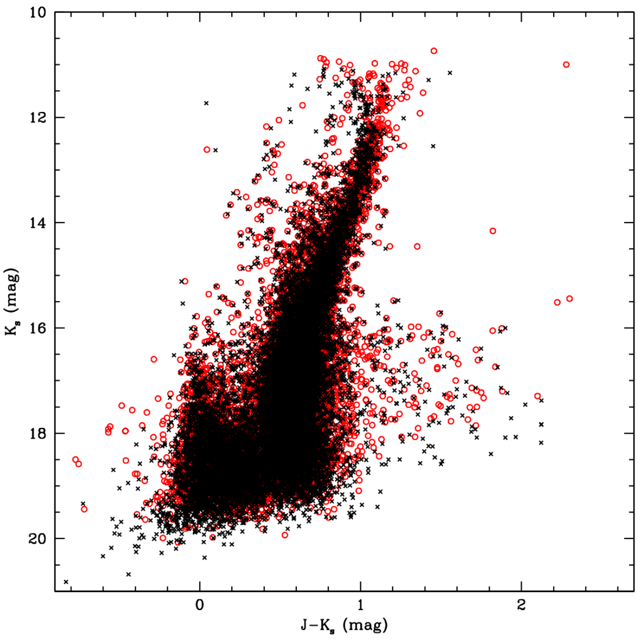

Figure 4.5: Colour-magnitude diagram of 20,000 LMC sources in common between this work (black crosses) and the VMC survey (red circles).

variations at the bright end and at the red clump (~17 mag) are probably due to variable stars while at the faint end are due to a low signal-to-noise (cfg. with Fig. 6 from Cioni et al. 2025). There is a comparable number of good-quality sources detected in both VMCDeep and VMC from the VDFS. However, many more sources are detected using PSF photometry.

4.5.1 Confusion

The improved spatial resolution of the VMCDeep observations combined with the increase in integration time, with respect to the VMC survey, has improved the clarity of the detections. To show this, we computed a qualitative confusion limit by calculating the number of beams per source in regions 0.2×0.1 arcsec^2, where one beam corresponds to the area in arcsec^2 occupied by a source with radius equal to half the FWHM. Using the FWHM values in Tab. 4.3 we obtain the maps shown in Fig. 4.7; similar maps obtained for the VMC survey catalogue (Cioni et al. 2025) are shown in the Appendix (see also Vijayasree et al., submitted). A critical limit corresponds to 20−25 beams, up to 50 beams confusion is high, whereas above 50 beams is low. Confusion can influence both the magnitude and position of faint sources as well as their number. A low confusion level means a high completeness and reliable source detection.

4.5.2 Data availability

Data products resulting from both the CASU and WFAU reductions, which are based on the VDFS, are stored in the VSA. They are made publicly available to the astronomical

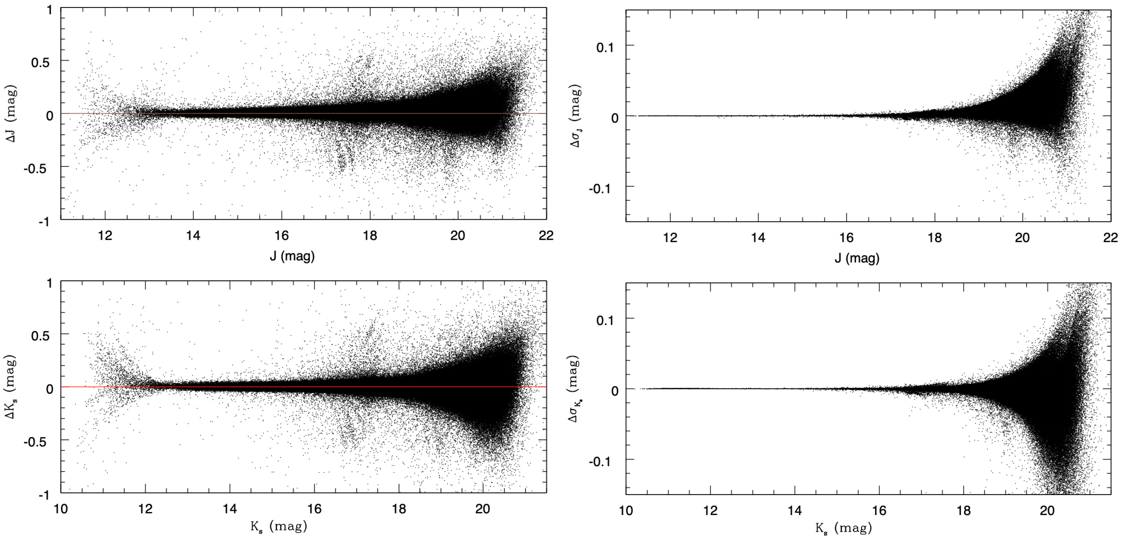

Figure 4.6: Distribution of magnitude differences (left) and uncertainties (right) between this programme and the VMC survey as a function of magnitudes J and K_s from this programme. Only sources in the SMC detected in both filters and with minor quality issues are shown.

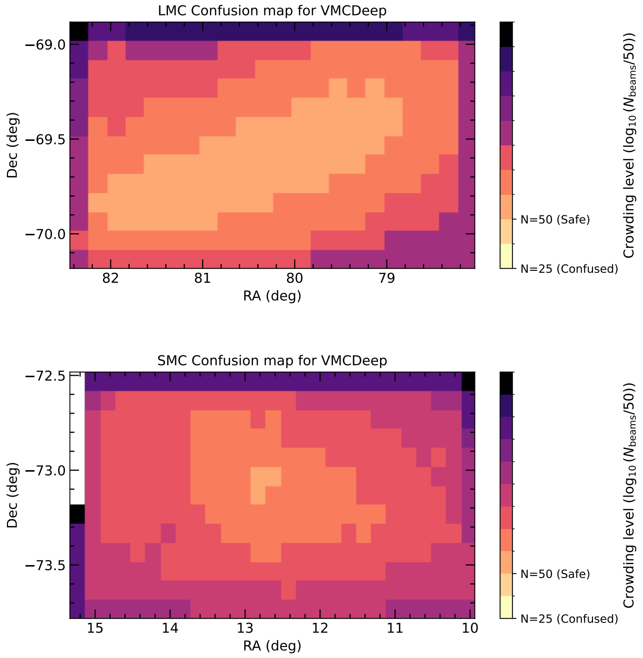

Figure 4.7: Confusion maps for bins of 0.2×0.1 deg^2 in the LMC (top) and SMC (bottom) central regions. The threshold number of beams (N=50) and the critical value (N=25) are indicated in the colour bar.

community through the VSA and the ESO Science Archive Facility (SAF; Romaniello et al. 2023). Catalogues with PSF photometry are not released at this stage because they are still undergoing validation by the science team, which occurs through the application of the catalogues to specific science analysis. They will be made available together with the first respective publications.

4.6 Applications of the catalogue

4.6.1 Stellar kinematics

The main goal of this programme is to constrain the central stellar kinematic patterns of the Clouds through measurements of near-infrared proper motions with better quality observations and spanning a longer time baseline in combination with the VMC survey. In these regions, the VMC survey obtained on average 12 epochs in the K_s band over a time baseline of two years (Niederhofer et al. 2021b, 2022a). One additional epoch was acquired several years later resulting in a time baseline of ~7 years for the SMC and ~11 years for the LMC central regions (Vijayasree et al. 2025a). The VMC survey obtained only a few observations in the J band within the main programme and there were no additional ones that followed them. The VMCDeep programme provides a significant increase in the number of epochs (at least 37 or 40 in the SMC or LMC) and an increase in the time baseline of another 1–3 years, depending on which of the two VMC tiles covering the centres of each galaxy are considered (Sect. 4.2).

Figure 4.8 shows the variation of the celestial coordinates for a random star observed in all three programmes. The slopes of the variations, which correspond to the proper motions in the two directions, are significantly better constrained in the combined data set than in the VMC or VMCDeep programme alone. Preliminary results based on proper motions derived from both bands show that the proper motion precision improves by about 2.5 times, compared to previous studies. In addition, using only sources detected in at least 70% of the epochs adds fainter stars (by about half a magnitude; VMC-only proper motions are limited to sources with $K_s < 18.5$ mag, e.g. Niederhofer et al. 2022a) to the sample of usable stars for statistically addressing the kinematical pattern of the central regions, without significantly diminishing the proper motion precision.

4.6.2 Variable stars

The VMCDeep observations will allow to build well sampled J and K_s light-curves for about 4000 and 500 RR Lyrae stars (M=0.55–0.8 $M_\odot$, age > 10 Gyr) in the LMC and SMC, respectively, and accurately measure their average magnitudes. The magnitude variation of ~1800 δSct (relatively young single stars) and SX Phoenicis (resulting from the merging of old stars) intermediate-mass (1.2–2.6 $M_\odot$) stars will also be sampled, thus enabling to build for the first time near-infrared period-luminosity relations for these classes of pulsating stars in the Clouds and use them as an additional standard candle. Along with their literature optical light curves they will be modelled with updated pulsation models to derive individual distances and intrinsic stellar properties (e.g. McNamara et al. 2007). The incidence of δSct stars in metal-poor environments like the SMC and LMC, a quantity

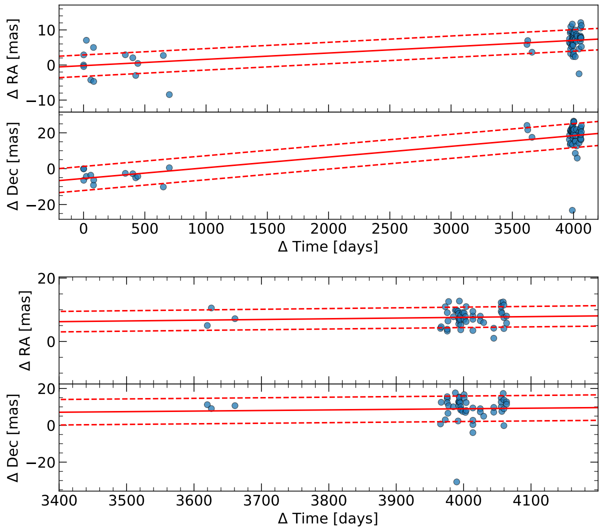

Figure 4.8: Sky position of a single random star as a function of time observed in the standard VMC survey (ΔTime<1000 days), in additional epochs (ΔTime~3600 days) and in this programme (ΔTime~4000 days). The bottom panel is a zoom-in version of the top panel. Both good and bad quality epochs are shown for each programme. The solid line is the best-fitting linear curve to the data. The dashed lines indicate the σ distance of the stars from the fitted line.

with a significant impact on studies of field star and star cluster evolution (Salinas et al. 2016), will also be determined. Moreover, RR Lyrae, δSct and SX Phoenicis stars will be used to measure the 3D structure of the central regions of the Clouds. These stars probe different epochs of star formation at a location where about 10% of the OGLE data are blended. Figures 4.9 and 4.11 show the light-curve examples of Classical Cepheids and RR Lyrae stars differentiating between detections from the VMCDeep and VMC survey programmes. Figure 4.10 shows that VMCDeep provides well-sampled light-curves also for the low-amplitude and faint δSct stars. Note that in these figures the VMCDeep values refer to PSF photometry while the VMC values refer to VDFS photometry, performed on individual epochs. Preliminary results from the analysis of the entire sample of pulsating stars within the central regions of the Clouds show a small dispersion around the respective period-luminosity relations.

4.6.3 Star formation

The central areas of the Clouds include several star forming regions (e.g. N113, N119, and N120 in the LMC and N19, N22, and N36 in the SMC) and massive young stellar objects (YSOs), e.g. over 300 in the LMC (Carlson et al. 2012, Sewiło et al. 2013). The more homogeneous coverage, higher spatial resolution and increased exposure time (by a factor of ~4) in the VMCDeep programme than for the VMC survey, will allow to study the star formation activity on large spatial scales while sampling deeper down the mass function (1.4 $M_\odot$ for ages ≤3 Myr). Using the automated algorithm from Zivkov et al. (2018) we will identify and study low-mass pre-main sequence stars to a similar depth (in mass) as for the outer regions sampled in VMC. Combined with the distribution of

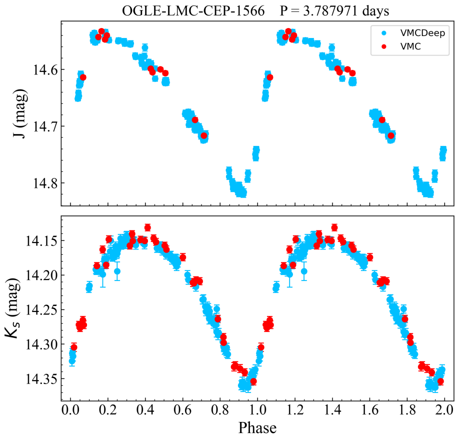

Figure 4.9: VISTA light-curve of a Classical Cepheid in the J (top) and K_s (bottom) bands. Data are folded according to the period and the epoch of maximum light derived from OGLE. The different colours indicate detections from this programme (light blue) and from VMC DR7 (red).

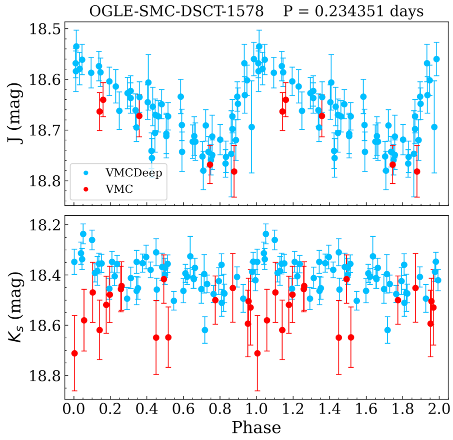

Figure 4.10: As Fig. 4.9 but for a δSct star.

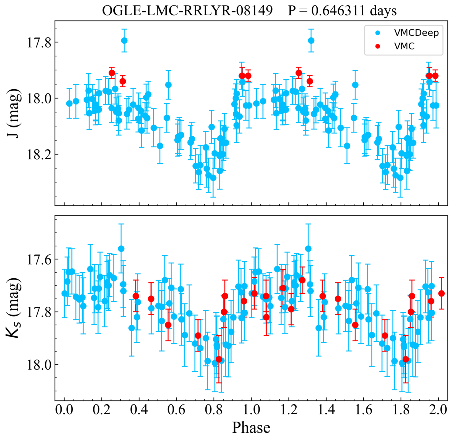

Figure 4.11: As Fig. 4.9 but for an RR Lyra star.

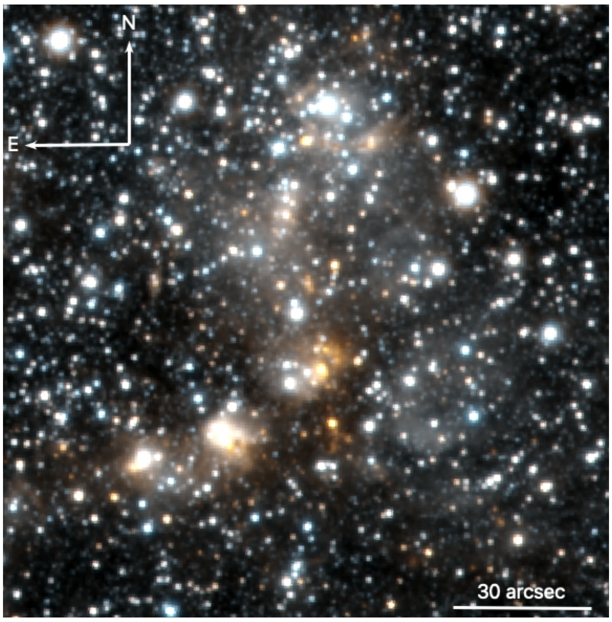

Figure 4.12: Near-infrared two-colour image of the star forming region N113 in the LMC as observed in this programme. The J band is shown in blue and the K_s-band in red.

upper-main sequence stars (Sun et al. 2018) it will provide a comprehensive picture of how star formation was spatially organised. Comparing the morphology and properties of the young populations to the underlying gas and dust distributions will also constrain the star formation rate. Furthermore, multi-epoch observations will improve the analysis of young variables; about 400 counterparts to massive YSOs (detected in the mid-infrared) are expected, more than doubling the current sample, allowing statistically meaningful comparisons with Galactic samples (e.g. Teixeira et al. 2018, Zivkov et al. 2020). Figure 4.12 shows the star forming region N113 in the LMC whereas full-tile images are shown in Figs. 4.21 and 4.22.

4.6.4 Star formation history

The depth and sensitivity of the VMC data have allowed a significant improvement in our knowledge of the space resolved SFH of the Clouds (Rubele et al. 2018b; Mazzi et al. 2021), but in the central regions where the stellar density is high crowding was a major problem. In the LMC central region, the completeness of the source detections corresponded to 75% at K_s<18.5 mag (cfg. their Fig. 12), which means that crowding already influenced stellar populations of ~1.6 Gyr old. In this case, the star formation rate is driven by the RGB and red clump regions rather than the main sequence turn-off and subgiant branch (Mazzi et al. 2021). A similar situation occurred in the SMC, since the completeness in the central regions was significantly worse than in the other regions (Rubele et al. 2018b).

The VMCDeep observations will improve the completeness of the source detections in the central regions of the Clouds and bring them in line with that in the other more external regions probed by the VMC survey. Preliminary results show that at the turn-off of the main sequence both the photometric uncertainties and sharpness distributions are

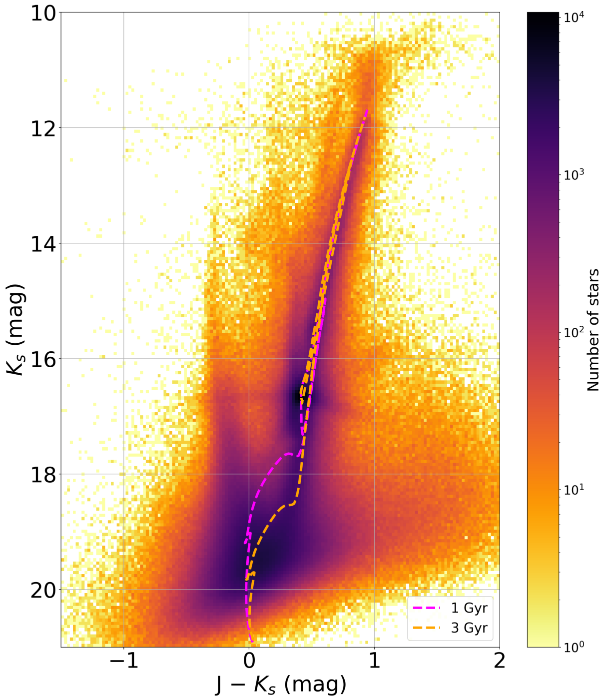

Figure 4.13: Colour-magnitude diagram of the LMC from re-modelled PSF photometry of the deep and stacked observations.

significantly reduced, which will allow us to estimate a robust SFH for the intermediate-age populations (~4 Gyr old) also in the central regions (Fig. 4.13). In this case, the PSF for the deep and stacked observations has been re-modelled, following a different process from the one by Rubele et al. (2015), to better define and trace the CMD features.

4.6.5 Red clump substructure

Low-mass core-helium burning metal-rich stars populate the red-clump feature in the CMD, which has been extensively used to trace the line-of-sight distance and dust content of galaxies (e.g. Girardi 2016). In particular, in the outskirts of the SMC a bi-modal distribution has been attributed to distinct stellar populations ~10 kpc apart. The foreground component, possibly of tidal origin, has been traced between about 2.5 and 10 kpc from the centre of the galaxy (e.g. Nidever et al. 2013; Omkumar et al. 2021; El Youssoufi et al. 2021).

A preliminary study based on the VMCDeep data, which is scrutinising the inner region, suggests that there is a bi-modality in the red clump distribution across the entire central 1.5 deg^2. Figure 4.14 presents an example of the histogram of the stellar distribution, obtained after subtracting stars that have a high probability of belonging to the Milky Way based on the Gaia astrometry (e.g. Gaia Collaboration et al. 2021b), and the best-fits gaussians. The underlying RGB stars are best represented by a quadratic fit, whereas the dual red clump stars show two peaks that are significantly different (0.13±0.01 mag) and appear better defined than in the previous study based on the VMC

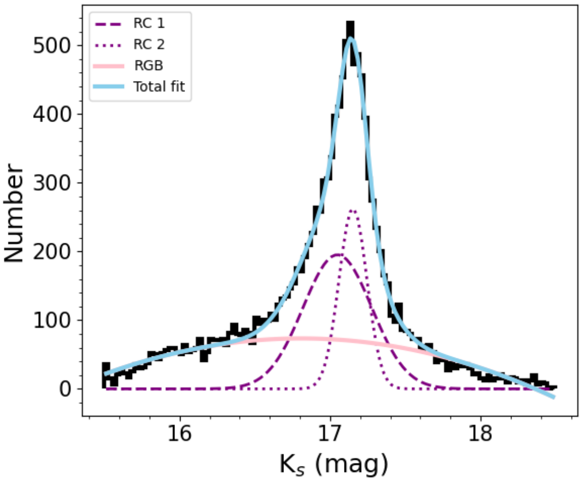

Figure 4.14: Gaussian fits to the magnitude distribution of giant stars (black histogram), excluding Milky Way stars, in a region of ~ 0.16 deg^2 east of the SMC centre. The best-fit total, RGB and two red-clump (RC) populations are shown with lines of different type and colour.

data (Subramanian et al. 2017). By using two rather than one gaussian to represent the red clump, the quality of the fit increases by 64%.

4.7 Conclusions

In this paper, we have described a deep VISTA observational programme designed to probe the stellar content and kinematics of the central ~1.77 deg^2 of the Clouds. Observations were collected during the last three years of operation of the near-infrared camera in the J and K_s bands during excellent sky conditions. The data processed through the VDFS have produced a catalogue of about 2.5 million sources with about 40 epochs per filter. Combined to the VMC survey, which covered the same regions with a mosaic of two tiles per galaxy, the deep observations represent the most spatially homogeneous observations of the Clouds' centres in the near-infrared to date. They have a high potential for studies of the stellar kinematics, the variable star populations and the structure of the galaxies as well as of star formation and the characterisation of young (variable) stellar objects. Detailed comprehensive analyses of these specific topics are ongoing and will be presented in separate subsequent papers. This also includes source catalogues with PSF photometry, which further improve source detection, and will allow us to derive more precise SFHs for the central (crowded) regions.

The data presented in this study provide useful counterparts to observations in the central regions of the Clouds at other wavelengths, for example in the X-ray domain by the extended ROentgen Survey with an Imaging Telescope Array (eROSITA; see Merloni et al. 2024 for the first data release) or in the visual domain by Gaia. The upcoming Gaia DR4 will contain the first products from dedicated observations in regions of high stellar density including the central regions of the Clouds (Fig 4.1; see Gaia Collaboration et al. 2023c for the increase of sources through the analysis of Sky Mapper images).

Ongoing observations with the *Euclid* space telescope will cover the SMC centre (see Euclid Collaboration et al. 2024 for the coverage of the Euclid Wide Survey) before the *Roman* Space Telescope[10]. Several sources will be spectroscopic targets for new multi-fibre spectrographs such as Multi-Object Optical and Near-infrared Spectrograph (MOONS) and 4-metre Multi Object Spectroscopic Telescope (4MOST) which both envisage dedicated observations of the central square degrees of the galaxies (see Gonzalez et al. 2020 and Cioni et al. 2019 for the respective survey strategies). In this context, studies of the central regions of the Clouds are extremely promising.

Acknowledgements

This programme is based on observations made with VISTA at the La Silla Paranal Observatory under programme IDs 105.206M, 106.201G, 108.221P and 109.23G7. We are grateful to C. Bell for producing one figure and to both C. Gonzalez Fernandez and Y. Kupcu Yoldas for processing the first images. We also acknowledge the assistance of Amrit Sedain in the large-scale production of the PSF photometry catalogues. We thank the Cambridge Astronomy Survey Unit (CASU) and the Wide Field Astronomy Unit (WFAU) in Edinburgh for providing calibrated data products under the support of the Science and Technology Facility Council (STFC).

Appendix

4.A Additional (low-quality) observations

During the observing period additional observations were obtained that did not meet the required sky conditions. This data, except for a few observations that were interrupted due to bad weather or technical problems for which not all offset positions could be obtained, are of comparable quality to the data obtained for the VMC survey in the outer regions of Clouds. Table 4.5 lists their average quality control parameters. These observations may be useful to address specific scientific questions, for example, the light-curve analysis of variable stars or the determination of proper motions which benefit from extra epochs for relatively bright sources.

4.B VMCDeep: PSF photometry

Point Spread Function (PSF) photometry is a valuable tool for determining the magnitudes of stars especially in crowded fields. We utilised the VMC pipeline to produce PSF catalogues in J and K_s bands, which employs the DAOPHOT package within the Image Reduction and Analysis Facility (IRAF). The pipeline was executed in a fully automated manner in a *docker* environment, non-interactive mode. Unlike the standard VMC survey (which observes in Y, J, and K_s bands), the VMC Deep data comprise only two bands

---

[10] https://science.nasa.gov/mission/roman-space-telescope/

Table 4.5: Quality control parameters for low-quality observations.

Galaxy	α (h:m:s)	δ (°:′:″)	Filter	Half tile	N	Airmass	FWHM (″)	Ellipticity	Zero-point (mag)
SMC	00:50:16.06	−73:10:40.92	J	LFT	16	1.59±0.06	1.05±0.29	0.09±0.05	23.80±0.16
			J	RHT	23	1.60±0.05	1.01±0.12	0.10±0.06	23.83±0.03
			K_s	LFT	11	1.54±0.04	0.92±0.16	0.08±0.03	23.08±0.01
			K_s	RHT	11	1.55±0.05	0.92±0.14	0.08±0.02	23.07±0.01
LMC	05:20:54.47	−69:34:43.32	J	LFT	35	1.51±0.08	0.90±0.11	0.10±0.04	23.65±0.55
			J	RHT	38	1.51±0.08	0.91±0.11	0.09±0.04	23.75±0.18
			K_s	LFT	26	1.46±0.07	0.88±0.08	0.06±0.02	23.02±0.13
			K_s	RHT	25	1.47±0.06	0.94±0.16	0.08±0.02	23.04±0.03

Notes. The coordinates are those of the tile centres. LFT corresponds to the tile pattern *Tile3px* and RHT to *Tile3nx*.

(J and K_s). To ensure compatibility with our processing pipeline, we duplicated the available epoch data to create a synthetic third band, enabling seamless execution of the photometry code.

4.B.1 Homogenised deep tile creation

The VMCDeep observations consist of multiple epoch observations, each comprising a set of pawprint images (section 4.2) obtained across different observing nights and under varying atmospheric conditions such as seeing. Temporal fluctuations in seeing introduce spatially variable PSF across the field of view, such that the effective PSF of any given exposure differs not only between epochs but also between the individual detectors of the VIRCAM focal plane array. When exposures acquired under heterogeneous seeing conditions are added without prior correction, the resulting stacked image exhibits a spatially non-uniform PSF. This will significantly complicate accurate source detection, blending of sources, and hence PSF-fitting, particularly in the crowded stellar fields of the SMC centre. To address this challenge, a systematic homogenisation procedure as implemented by Rubele et al. (2015), is applied to obtain spatially uniform PSF for each band.

The homogenisation procedure is initiated by characterising the PSF of each individual pawprint image. PSF modelling is performed in each band using the DAOPHOT (Stetson 1987). A sample of bright, isolated, and unsaturated stars, free from neighbouring contamination, is selected from each pawprint to serve as PSF reference stars. An effective PSF (EPSF) is then fitted to this stellar sample for each detector within every pawprint, obtaining the convolved PSF. A symmetric Moffat profile is adopted as the analytic form for the reference PSF (RPSF), owing to its well-established suitability for representing stellar profiles under a broad range of seeing conditions. For each epoch, the RPSF is constructed by setting its half-flux radius (HFR) equal to the maximum HFR measured across all EPSF models derived from the constituent detectors and pawprints of that epoch. With the RPSF defined, spatially matched convolution kernels are computed individually for each pawprint image via Fourier deconvolution of the EPSF by the RPSF. Each kernel encodes the precise smoothing required to transform the PSF of a given pawprint into the target RPSF. The kernels are applied to the respective pawprint images through direct convolution in the spatial domain, yielding a set of homogenised pawprints.

The homogenised pawprints are subsequently resampled onto a common astrometric grid and co-added using SWarp (Bertin et al. 2002), employing a weighted combination that accounts for the relative depth and image quality of each contributing exposure. The resulting deep tile image possesses a well-defined, spatially uniform PSF characterised by the epoch RPSF. It is acknowledged that this uniformity is achieved at the cost of a moderate degradation in angular resolution relative to the best-seeing individual exposures, as the effective PSF of the co-added image is necessarily set by the broadest PSF among the contributing pawprints. Nevertheless, this is justified, as the homogenisation eliminates systematic photometric biases arising from PSF mismatches between exposures and substantially enhances source deblending and photometric precision in the co-added image, particularly in the densely populated inner regions of the Clouds, where overlapping stellar profiles would otherwise render reliable PSF-fitting photometry impracticable.

4.B.2 PSF using DAOPHOT

For each photometric bandpass, the relevant IRAF parameter sets such as the PSF FWHM in pixels (fwhmpsf), the aperture radius (apertur), the PSF model radius (psfrad), the PSF fitting radius (fitrad) and so on. These parameters were adjusted according to the VMCDeep dataset and provided directly before running IRAF tasks on the homogenised deep tile images of each band, at the start of each filter iteration. Source detection was carried out using the ‘daofind’ task, which convolves each image with a Gaussian derivative kernel matched to the PSF FWHM to identify stellar objects above the defined signal-to-noise threshold. Aperture photometry was subsequently performed on all detected sources using the ‘phot’ task. The resulting aperture photometry database provided accurate centroid positions, local sky background values, and initial aperture magnitudes for every detected source, serving as the primary input catalogue for all subsequent PSF-fitting.

Rather than constructing PSF models within the automated pipeline for each image, pre-computed PSF models were provided from a dedicated PSF reference image constructed in advance for each bandpass using ‘pstselect’ and ‘psf’ on a deep reference frame. The ‘allstar’ task was then applied to each image using the pre-computed PSF model, which groups stars automatically based on their proximity relative to the PSF radius, fits the PSF model simultaneously to all stars within each group, and iterates until convergence or the maximum permitted iteration count is reached. Stars failing to converge were written to a rejection file, and a PSF-subtracted residual image was produced for each field. Subsequently, band-merged PSF catalogues were produced with the final catalogues of each band.

4.C Photometric shifts

The PSF photometry is adjusted to the photometry from the VDFS, which is calibrated as in González-Fernández et al. (2018a), to place it on an absolute scale. Table 4.6 shows

Table 4.6: Median photometric shifts.

Galaxy	J (mag)	K_s (mag)
LMC	0.45±0.03	0.28±0.03
SMC	0.47±0.03	0.22±0.02

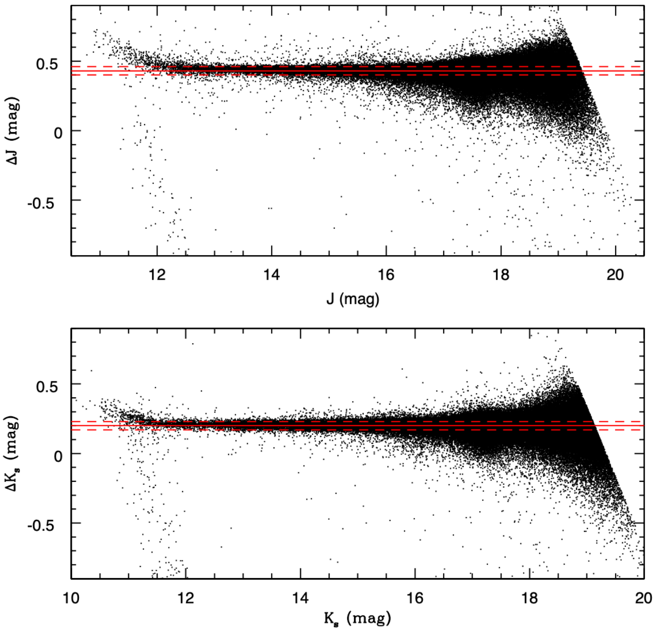

Figure 4.15: Photometric shifts between VMCDeep and VMC sources in the SMC for calibrating the PSF photometry.

the median shifts in the J and K_s filters for the LMC and SMC sources. These are calculated using unique VDFS detections in both filters, with only minor quality issues (*ppErrBits*<256) and with photometric uncertainties <0.1 mag. Figure 4.15 shows as an example, the SMC sources and shifts. Individual shifts for each half-tile image are given in Tab. 4.7 where each line refers to one image and indicates: the name of the catalogue, the corresponding shift and its uncertainty. The name includes the type of galaxy, filter, type of half tile and observing date as well as the number of the first images in the set of offsets that produce the half tile. The filter is followed by a number which identifies the planned epoch of observation. Low-quality observations result in photometric shifts that are systematically below the average of the shifts derived for the high-quality observations, with several measurements outside the 1-σ range and larger individual uncertainties. The individual shifts are also shown in Fig. 4.16 for both high- and low-quality observations. Table 4.7 is only available at CDS.

Table 4.7: Example of individual photometric shifts.

Name	Shift (mag)	Uncertainty (mag)
psf_SMC_LFT_J1_20220808_00251.cat	0.433	0.025
psf_SMC_LFT_J2_20220905_00310.cat	0.441	0.025
psf_SMC_LFT_J3_20220915_00262.cat	0.449	0.026
psf_SMC_LFT_J4_20220915_00289.cat	0.500	0.025
psf_SMC_LFT_J5_20210820_00252.cat	0.422	0.025
psf_SMC_LFT_J5_20220628_01009.cat	0.387	0.028
psf_SMC_LFT_J6_20210820_00333.cat	0.470	0.027
psf_SMC_LFT_J6_20220629_01039.cat	0.534	0.026
psf_SMC_LFT_J7_20210821_00308.cat	0.496	0.024

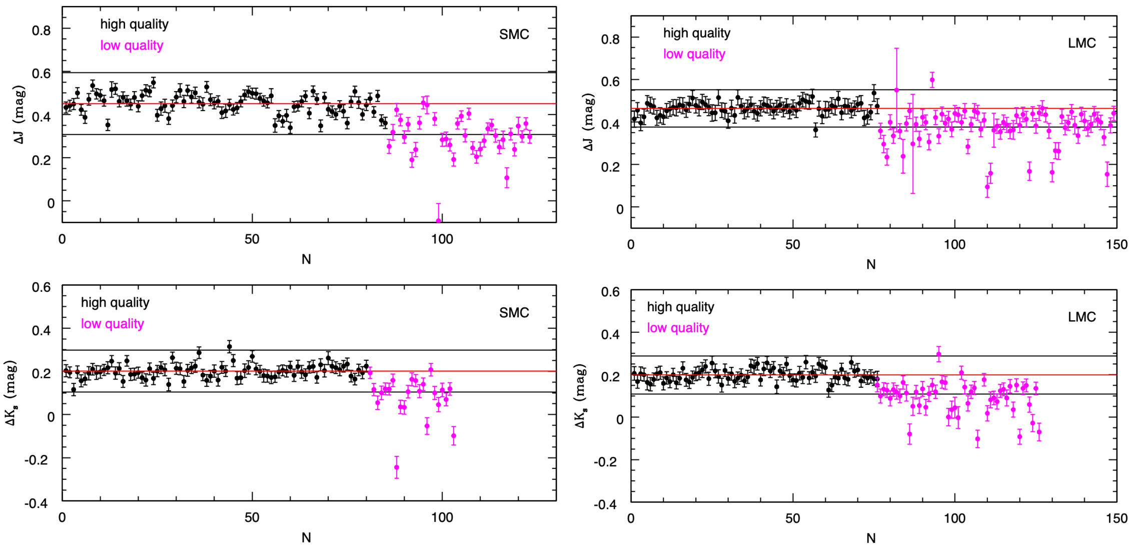

Figure 4.16: Photometric shifts for single half-tile images between VMCDeep and VMC sources in the SMC (left) and LMC (right) for calibrating the PSF photometry. The horizontal axis is a sequential number (N) with high-quality observation first (black) and low-quality observations last (magenta). Horizontal lines show the average of the shifts obtained only from the high-quality observations with the 1-σ range.

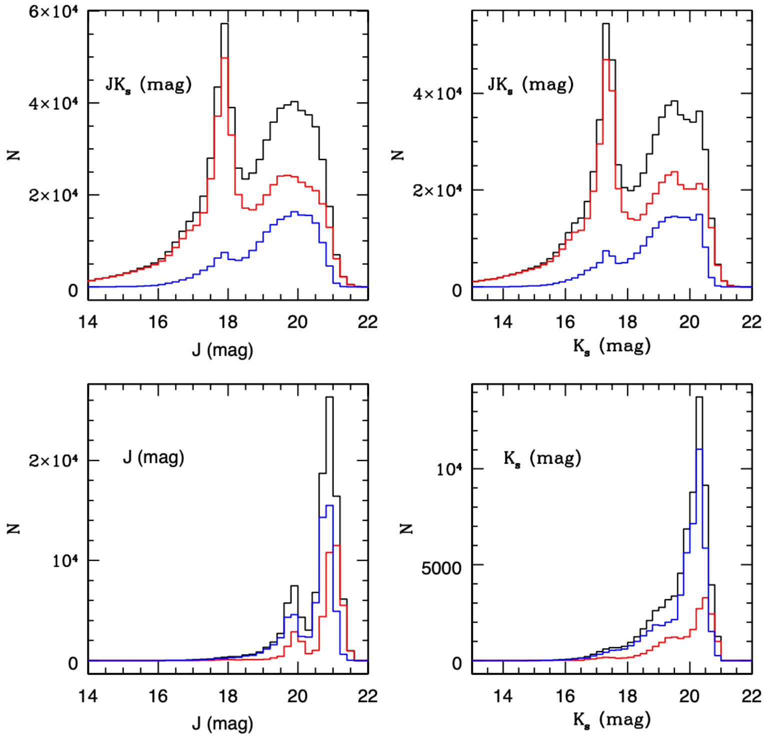

Figure 4.17: As in Fig. 4.4 but for the SMC.

4.D Separate luminosity functions

Luminosity functions of the sources detected in the SMC and LMC observations from this programme are shown in Fig. 4.17 and 4.18, respectively. They can be compared to the overall distribution shown in Fig. 4.4 to explain, in particular, the double peaks in the single-filter detections.

4.E Maps from the VMC survey

The VMC survey observed the Clouds by mosaicing 68 and 27 tiles in the LMC and SMC, respectively. Figure 4.19 shows the coverage of the central regions from this programme by the VMC observations. Both regions result from the observations of two adjacent VMC tiles. The missing rectangular areas are due to detector #16. In the SMC this causes a lack of sources to the south of the centre whereas in the LMC, where the position angle of the tiles is rotated by +90 deg, this is very close to the centre itself. In addition, in the LMC there is a lack of sources along a strip through the centre. This corresponds to the location of the underexposed region of a tile where the exposure time is shared between the adjacent tiles. The same occurs in the SMC in declination. A selection of sources with only minor quality issues (*ppErrBits*<256) excludes stars observed in both detector #16 and the ears of tiles. The tile overlaps for the other sides correspond to 30″, but due to the full depth of the observations at their location there are no obvious discontinuities in the mosaic.

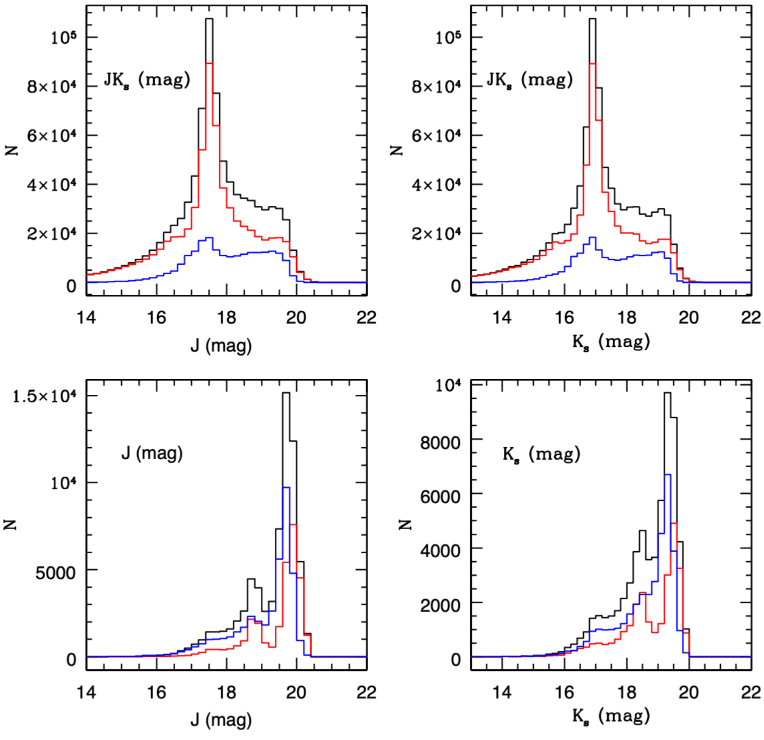

Figure 4.18: As in Fig. 4.4 but for the LMC.

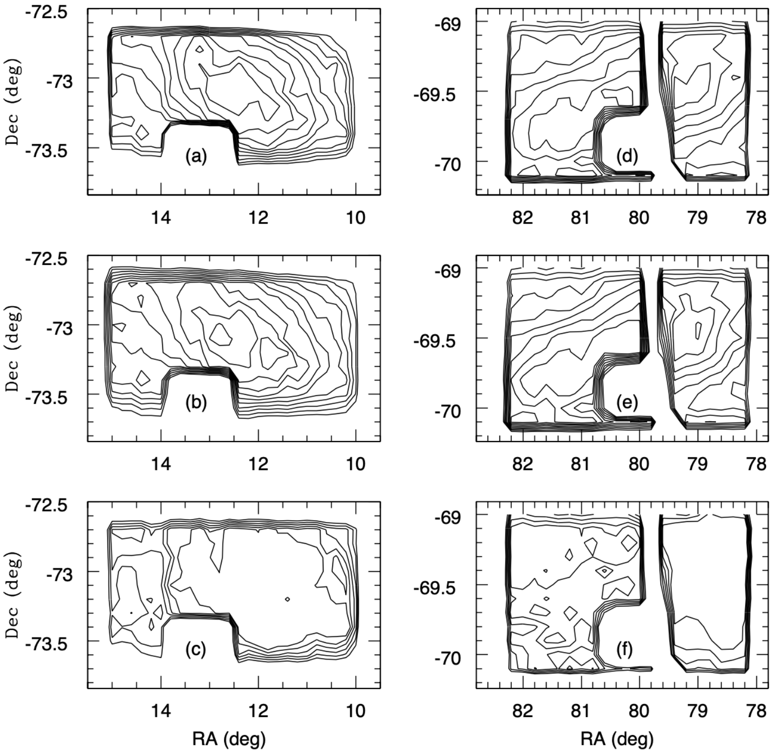

Figure 4.19: As in Fig. 4.2 but using data from the VMC survey.

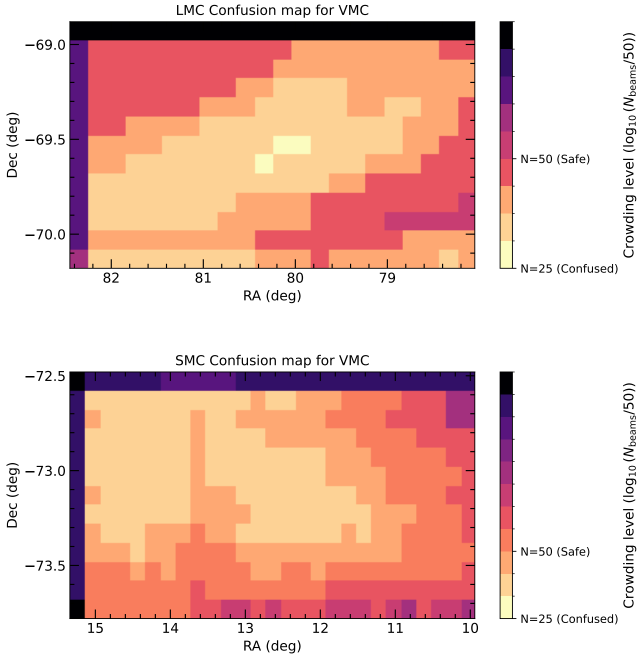

Figure 4.20: Confusion maps for bins of 0.2×0.1 deg^2 in the LMC (top) and SMC (bottom) central regions from the VMC survey. The threshold number of beams (N=50) and the critical value (N=25) are indicated in the colour bar.

4.F Confusion in the VMC survey

Confusion maps of the sources detected in the central regions of the LMC and SMC from the VMC survey are shown in Fig. 4.20. They have been created as in Sec. 4.5.1 and can be compared with those from the VMCDeep observations shown in Fig. 4.7.

4.G Tile images

Figures 4.21 and 4.22 show two-colours mosaic images of the LMC and SMC central regions from this programme. They have been obtained after combining all good-quality observations.

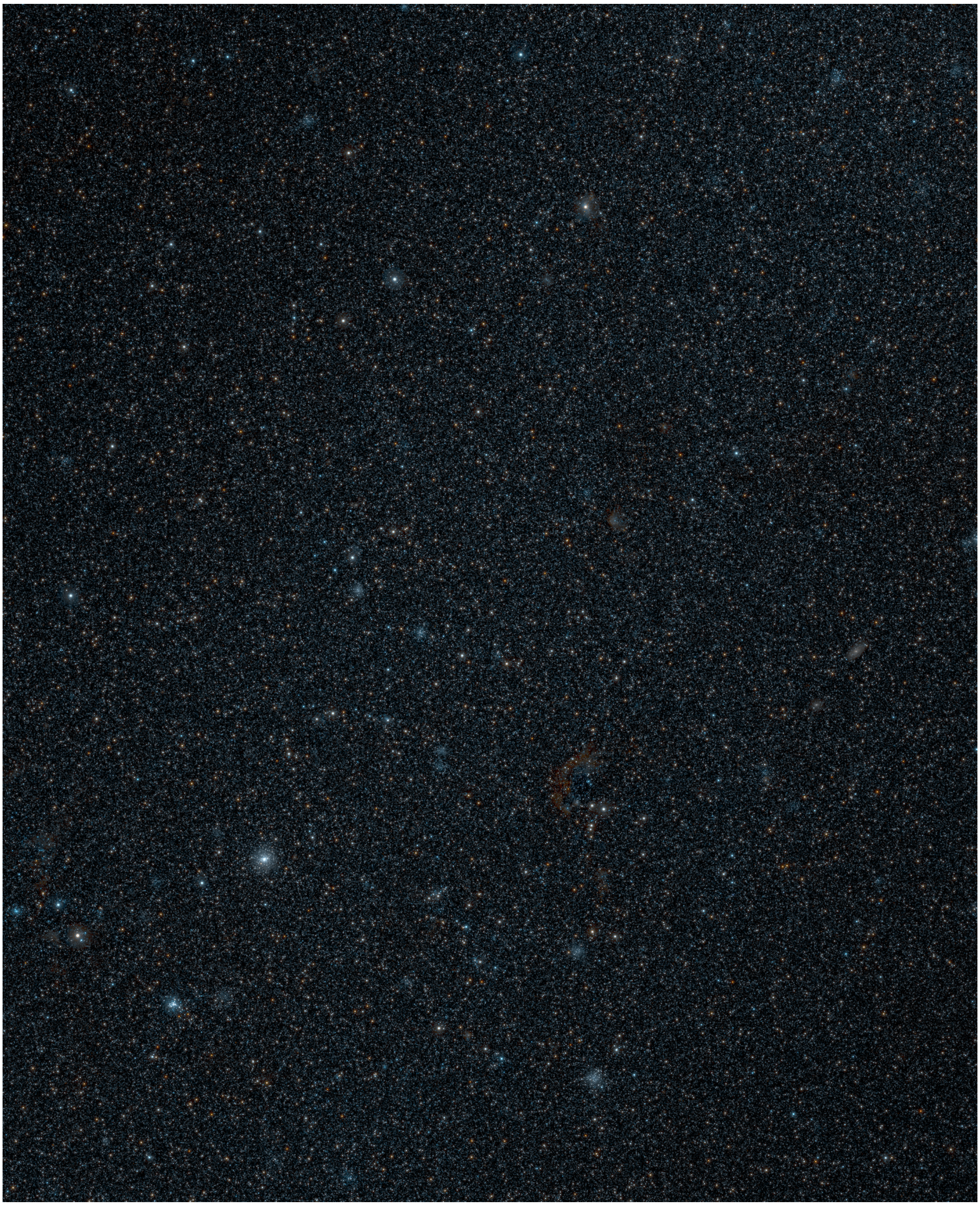

Figure 4.21: Colour-composite image of most of the LMC tile where J is in blue and K_s is in red. East is to the left and North at the top. Several stellar clusters are clearly visible while bright blue stars contrast a red gaseous arc near the centre of the field.

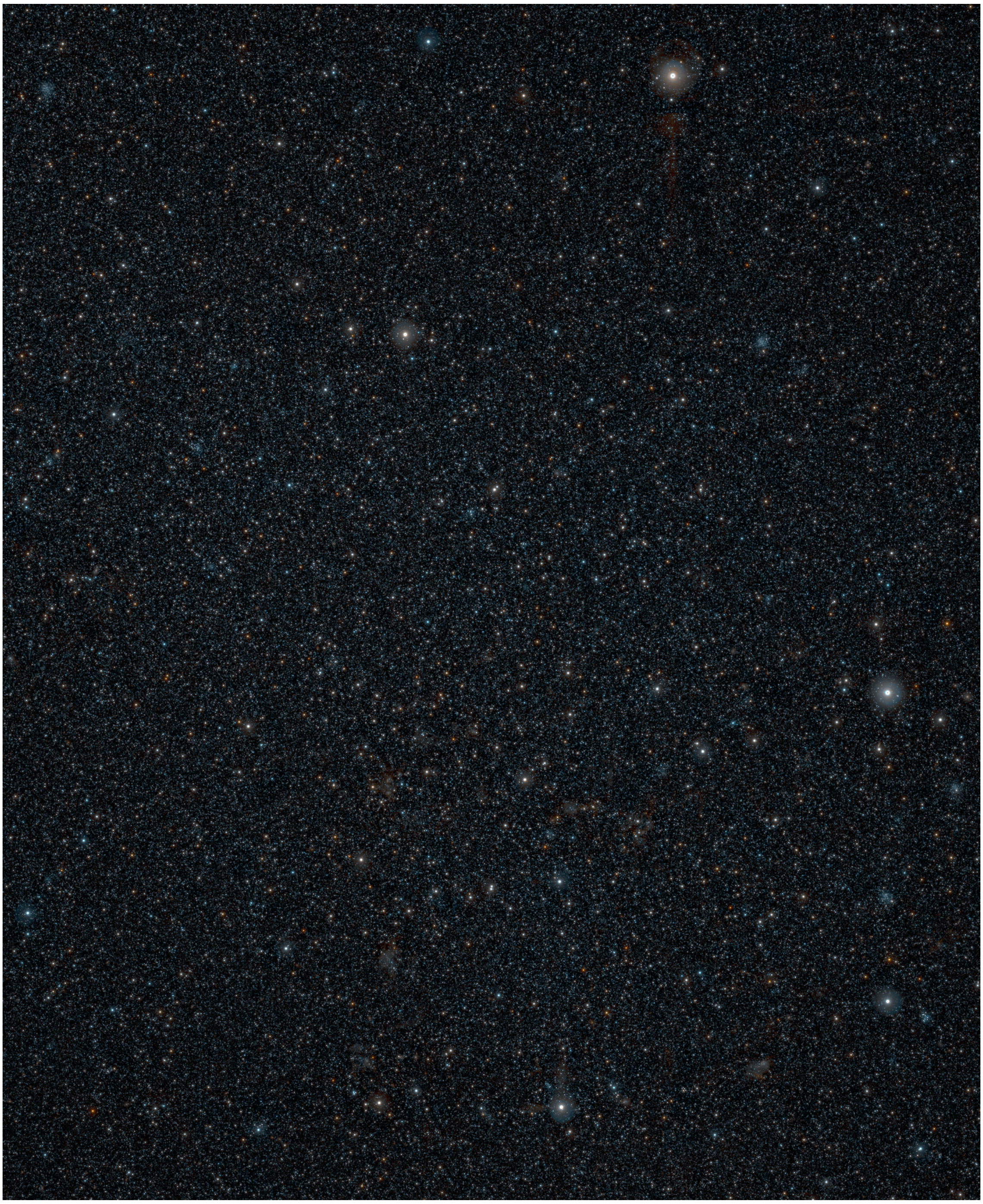

Figure 4.22: Colour-composite image of most of the SMC tile where J is in blue and K_s is in red. East is to the left and North at the top. Bright red stars are scattered in the midst of the density field while the glow of the brightest stars veils the neighbouring sources.

5 Probing the bimodality of Red Clump stars in the centre of the Small Magellanic Cloud

Abinaya O. Omkumar, Maria-Rosa L. Cioni, Smitha Subramanian et al.

The draft of this chapter is in preparation to be submitted for journal publication.

5.1 Introduction

The Large and Small Magellanic Clouds (LMC and SMC) are the closest interacting dwarf satellites of the Milky Way (MW), situated at 50.62±2.32 kpc and 60.75±2.85 kpc, respectively (Oden et al. 2025). Their relative proximity allows us to resolve individual stars even from the ground, identify low-surface-brightness stellar substructures, and makes them an invaluable observational laboratory for investigating fundamental processes such as tidal disruption, interactions among dwarf galaxies, and their evolution (Mackey et al. 2016, 2018; Niederhofer et al. 2021a). Studies of the morphological features of the Magellanic Clouds (hereafter, 'the Clouds'), including warps and structural parameters, provide key insights into the evolutionary processes shaping them over time (Subramaniam & Subramanian 2009; Subramanian & Subramaniam 2012; Choi et al. 2018a; Saroon & Subramanian 2022 and references therein).

The clump of red giants, commonly known as the red clump (RC) stars, was initially identified by Cannon (1970) in their study of open clusters. These stars are characterized by their near-constant absolute magnitude due to helium ignition in a degenerate core, which begins once the stellar core reaches a critical mass of about 0.45 $M_\odot$. RC stars are low-mass (1–2.2 $M_\odot$), intermediate-age (~2–10 Gyr) stars in the core-helium burning phase, and metal-rich counterparts to horizontal branch stars (Girardi & Salaris 2001; Girardi 2016). They occupy a compact, well-defined region in the colour-magnitude diagrams (CMD) of nearby galaxies, owing to their fixed absolute magnitudes. This fixed brightness, combined with their low dispersion in magnitude, makes them reliable standard candles and excellent tracers of galactic structure and kinematics. (Valentini & Munari 2010). Consequently, we utilise RC stars to derive distances and reddening estimates, and to map the three-dimensional structure of their host galaxies (Girardi & Salaris 2001; Girardi 2016; Ruiz-Dern et al. 2018).

Hatzidimitriou & Hawkins (1989) investigated the photometry derived from photographic plates to study the three-dimensional distribution of the northeastern and southwestern regions of the SMC using RC stars as standard candles. They observed significant line-of-sight distances in the northeastern region and discussed the possibility of the existence of two separate entities along the line-of-sight. Subsequently, Nidever et al. (2013) identified a bimodal RC population located at 4 deg from the SMC centre, and termed this feature as "eastern stellar structure". These dual populations were situated at distances ~ 67 kpc (main body) and ~ 55 kpc (foreground), in three distinct fields within the eastern SMC, particularly towards the Magellanic Bridge (MB) and the LMC. Further investigations by Subramanian et al. (2017); Tatton et al. (2021); Omkumar et al.

(2021); El Youssoufi et al. (2021); Gatto et al. (2024); Oden et al. (2025) have explored its extent towards the outer regions. These studies confirmed the presence of a foreground population located at a closer distance of ∼ 10−12 kpc, situated in front of the SMC's main body. The extent to which this feature has been mapped varies among these studies due to limitations in the available data. Currently, the farthest mapping of this feature extends to ∼10 deg from the SMC centre, based on near-infrared (NIR) data from the VISTA Hemisphere Survey (VHS) (El Youssoufi et al. 2021). In an analysis of the largest homogeneous dataset (∼ 314 sq. deg) from the Gaia Data Release 2 (DR2; Gaia Collaboration et al. 2018a), Omkumar et al. (2021) reported tracing this feature between ∼2.5 deg and 5−6 deg from the SMC's optical centre in the eastern regions. This finding has been validated by observations of significantly larger proper motions for the foreground population relative to the main body population. Upon investigating the stellar kinematics, the foreground population was found to be kinematically distinct, ∼ 35 km/s slower tangential velocity relative to the main body RC population. However, no studies had sufficient data quality to probe this feature within 2.5 deg from the SMC centre.

In the eastern regions of the SMC, where the bimodality in the RC is evident, Dobbie et al. (2014a) identified a bimodal distribution in the radial velocities (RV) of red giant branch (RGB) stars through a spectroscopic study. Subsequently, James et al. (2021) combined the RV data from Dobbie et al. (2014a) and De Leo et al. (2020) with proper motions from *Gaia* Early Data Release 3 (EDR3) to analyse the dual RGB populations characterised by lower and higher velocities in the eastern SMC. They found a correlation between the bimodality observed in the RC and RGB stars in the eastern regions of the SMC. Their results indicated that the proper motions of the foreground and main body RC populations correspond to the lower and higher RV RGB stars, respectively. They also detected a bimodality in the RV distributions of RGB stars in the southwestern regions, which they proposed might be associated with the counter-bridge suggested by Diaz & Bekki (2012), a feature not observed among the RC stars.

In Almeida et al. (2024), the authors investigated the kinematics and chemistry associated with the distance bimodality of RGB stars in the eastern side of the SMC using *Gaia* DR3 proper motions and spectra from Apache Point Observatory Galactic Evolution Experiment−2 (APOGEE−2) DR17 data. They examined regions in the eastern, central, and western SMC, finding that the far eastern population displayed normal RV distributions. In contrast, the near eastern population (D_μ = 52 kpc) exhibited skewed RC distributions, which are indicative of motions away from the SMC. These results correlate with the kinematics of the foreground RC stars from Omkumar et al. (2021). Almeida et al. (2024) results further showed that the near eastern stars share a metallicity distribution function (MDF) similar to that of the central SMC, suggesting that these stars represent material drawn from the SMC's centre during tidal interactions with the LMC. More recently, Navabi et al. (2025) estimated the metallicities of the RGB stars from De Leo et al. (2024) and analysed the chemical properties of the eastern substructures. Their findings supported those of Almeida et al. (2024), reinforcing the interpretation that the eastern near (foreground) populations origin from the inner SMC.

Following the several investigations of the bimodal RC and RGB populations in the eastern SMC, it is equally important to explore whether similar structural or dynamical signatures extend into the SMC's central regions. The central areas of galaxies pose significant observational challenges due to their high densities of stars, gas, and dust. Understanding how interactions between the Clouds themselves and with the MW have influenced these most gravitationally bound regions is critical for reconstructing the SMC's evolutionary history. Previous studies of the bimodal feature have detected it only beyond ~2.5 deg from the SMC's centre. In this study, we aim to investigate the SMC's central region to examine whether signatures of bimodality are also present there by studying the luminosity distributions of RC stars. To do this, we use data from the VISTA survey of the Magellanic Cloud (VMC; Cioni et al. 2011) Deep Survey (Cioni & Omkumar et. al., submitted), which is designed to resolve stars fainter than the RC and to analyse star formation, kinematics, and structural features in the innermost regions of the Clouds. Understanding this feature in great detail provides valuable evidence of past gravitational interactions between the Clouds and the MW, which have stripped stellar material and reshaped the morphology and kinematics of the Clouds.

In Section 5.2, we provide details about the observations and the data reduction techniques used in this study. In Section 5.3, we discuss our analysis methodology to investigate the presence of bimodality. In Section 5.4, we present the findings of the study and discuss their implications. Finally, in Section 5.5, we give a concise summary of our work.

5.2 Observations and data reduction

disturbed

5.2.1 VMCDeep survey

We utilised data from the VMCDeep survey (Cioni & Omkumar et. al., submitted) of the SMC, observed with the Visible and Infrared Survey Telescope for Astronomy (VISTA; Sutherland et al. 2015). VISTA is a 4-m class alt-azimuth telescope at ESO's Paranal Observatory, equipped with the wide-field VISTA infrared camera (VIRCAM; Dalton et al. 2006). The survey employs the VIRCAM instrument to acquire deep multi-epoch J (1.25 μm) and K_s (2.15 μm) band data. VIRCAM comprises 16 Raytheon detectors with gaps between them, with a mean pixel scale of 0.339 arcsec and a 1.65 deg field of view. The instrument's point-spread function (PSF) has a full width at half maximum (FWHM) of 0.51 arcsec.

VISTA observes continuous sky areas by filling gaps between detectors via a sequence of offsets, each by a significant fraction of a detector size. The VMC Deep survey targets deep imaging under high-quality sky conditions to resolve sources in the LMC centre (RA: 05:20:54.47; Dec: −69:34:43.32; J2000.0) and the SMC centre (RA: 00:50:16.06; Dec: −73:10:40.92; J2000.0), covering a contiguous area of 1.77 sq. deg. The required seeing is 0.7 arcsec in K_s and 0.8 arcsec in J, at 500 nm at zenith and airmass $\leq$ 1.7 arcsec. For the VMC Deep survey, we combine three fixed offset positions in the "Y" direction of the array, termed pawprints, to cover ~0.9 sq. deg. and this produces a VISTA half tile. We then observe another set of three pawprints, which also has an offset in the "X" direction relative to the first set, producing another half tile. Each half-tile, left (LFT) and right (RHT) provides stripe-like coverage of the sky. Merging the two half tiles yields a full VISTA tile covering approximately 1.77 sq. deg. Observations were conducted in service mode to ensure efficiency and data homogeneity, using half tiles with 58.8 min exposures in both bands across ∼40 epochs. Total exposure times are 14400 s in the J band and 36000 s in the K_s band, with per-epoch integration times of 360 s (J) and 900 s (K_s). For a detailed description of the observing strategy and data reduction, see Cioni & Omkumar et al. (submitted). In this study, we utilise the data obtained for the SMC centre, to investigate the presence of bimodality in the RC stars.

5.2.2 Data reduction

The raw images obtained from the VMC Deep survey were processed and reduced using the VISTA Data Flow System (VDFS), which handles pipeline calibration, sky subtraction, and initial quality assessments for all VISTA observations. The central regions of the SMC we targeted are severely affected by source crowding due to the high stellar density, rendering traditional aperture photometry unreliable and necessitating PSF photometry to accurately measure fluxes from individual stars. Accordingly, we performed PSF photometry on each individual epoch half-tile image as a first step.

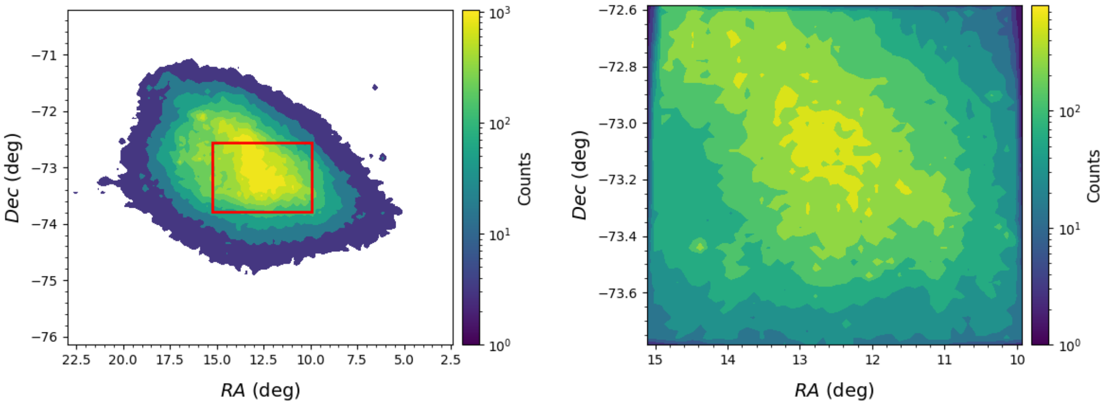

Figure 5.1: *Left Panel*: Density plot illustrating the *Gaia* DR3 sources within the central 3 deg of the SMC, with the area covered by the VMC deep survey indicated by a red rectangle. *Right Panel*: Contour density plot of the VMC deep sources analysed in this study is shown. In both panels, the colour bar from violet to yellow shows the increase in number density.

For each epoch, we classified the observation quality as either ‘good-quality’ or ‘low-quality’ based on quantitative metrics, including the seeing and ellipticity. Depending on this classification, we specified the appropriate PSF model parameters (FWHM) and followed the precise homogenisation and PSF photometry procedure established by Rubele et al. (2015) for VMC data. We then compiled a list of all good-quality epochs to produce a deep tile image to perform PSF photometry. Using this selection, we combined the good-quality images via multi-epoch stacking: first applying global homogenisation to normalise zero-points, sky flats, and PSF variations across epochs; then stacking them into deep J and K_s tile images with the SWARP tool, which resamples and mosaics the input frames onto a common astrometric grid.

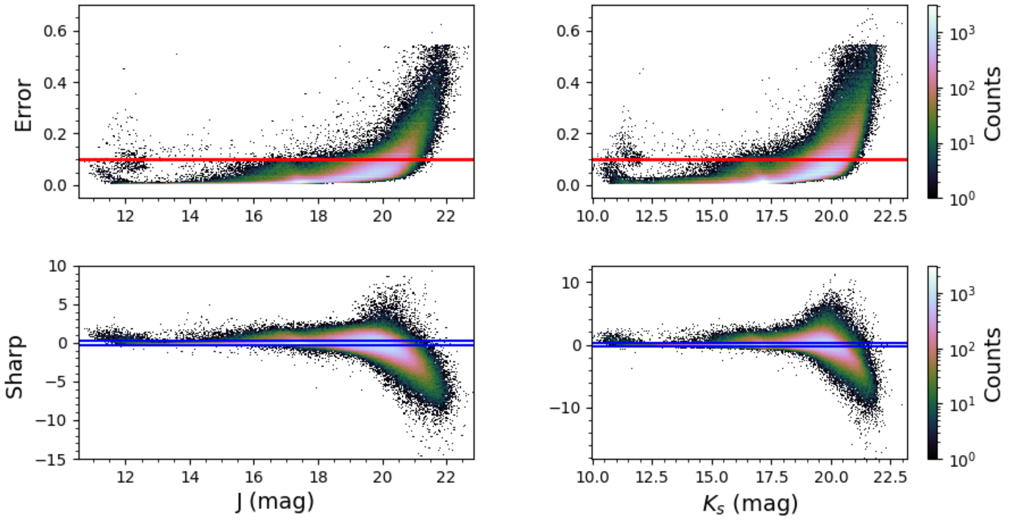

Figure 5.2: Error distribution of SMC deep sources in *J* (top-left) and K_s (top-right) bands are shown The red line indicates the selection limit of 0.1 mag. Sharpness distribution of SMC deep sources in *J* (bottom-left) and K_s (bottom-right) bands is shown. The blue lines indicate the selected sources between −0.3 to 0.3 mag in both bands.

Finally, we performed PSF photometry on these deep stacked tiles using the IRAF DAOPHOT/ALLSTAR package, which is specifically optimised for resolving stars in highly crowded fields through iterative PSF fitting. This process yielded our final deep *J* and K_s PSF catalogues. For a complete description of the PSF catalogue production methodology refer to Chapter 4 (see Section 4.3.3 and Appendix 4.B). Another important consideration is the photometric completeness of the PSF catalogues used in this analysis. Completeness corrections based on artificial star tests are currently being computed and will be incorporated. However, given that the RC lies well above the survey's limiting magnitude, we do not expect this to affect our results. The contour density plot of all the PSF sources of the VMC Deep survey of the SMC is shown on the right panel of Fig. 5.1. For comparison, the contour density plot from *Gaia* DR3 of the central 3 deg of the SMC is shown in the left panel, where the VMC Deep survey is marked with a red rectangle. The estimated error and sharpness distributions of *J* and K_s of the obtained PSF sources are shown in Fig. 5.2.

5.3 Analysis of VMC deep data

In this section, we describe our methodology for selecting probable SMC member stars and subsequently identifying RC stars within the VMC Deep photometric catalogues of the SMC's central regions.

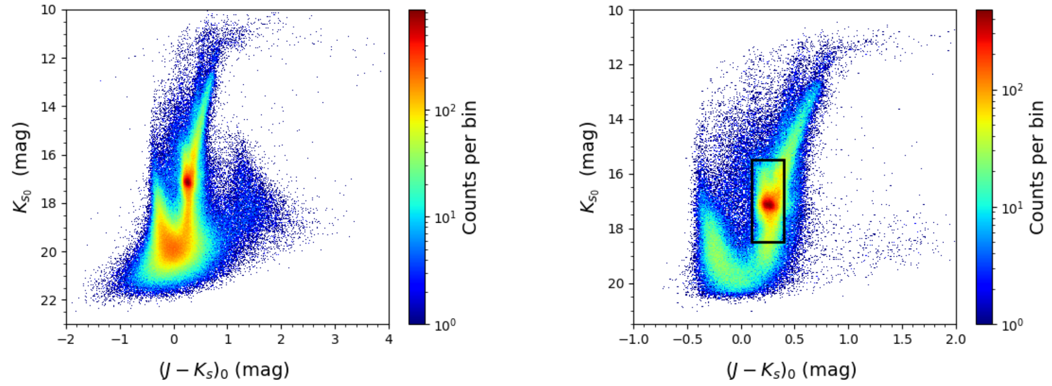

Figure 5.3: *Left*: Extinction corrected CMD of all SMC deep sources. *Right*: Extinction corrected CMD of all SMC deep sources with magnitude and sharpness cuts applied. The selection box, indicating the region of RC stars, is shown using a black rectangle.

5.3.1 Extinction correction

The magnitudes obtained from our PSF catalogues are not corrected for reddening. Although extinction effects are reduced in the near-infrared regime, it remains essential to account for them in precision photometric studies of the SMC. We therefore adopted the interstellar reddening maps for the Clouds constructed by Skowron et al. (2021), who derived $E(V-I)$ values by subtracting the intrinsic RC colour from the observed colour.

To apply these corrections, we first converted the $E(V-I)$ values to $E(B-V)$ using the relation $E(B-V) = E(V-I)/1.237$. For each source, we interpolated the nearest-neighbour $E(B-V)$ value from the map and computed band-specific extinction coefficients according to González-Fernández et al. (2018b): $A_J = 0.705\times E(B-V)$ and $A_{K_s} = 0.308\times E(B-V)$. The de-reddened magnitudes J_0 and $K_{s,0}$ were then obtained by subtracting these extinction values. Left panel of Fig. 5.3 presents the extinction-corrected CMD for all sources in the SMC deep PSF catalogue.

5.3.2 Selection of probable SMC members

In PSF photometry, photometric error and sharpness are used as key criteria to identify good-quality sources. These parameters were estimated during the production of the PSF catalogues. To refine our selection, we applied a sharpness criterion within the range $-1 \leq$ sharpness $\leq +1$ for both the J and K_s bands (Subramanian et al. 2017; Tatton et al. 2021). Sources with sharpness values below -1 were considered to correspond to bad pixels, while those exceeding $+1$ were likely extended sources.

Applying the sharpness filter, along with a photometric error limit of 0.1 mag, reduced the sample to 863,771 sources from 1,268,268 sources. We chose to impose stricter quality criteria, further limiting the sharpness range to $-0.3 \leq$ sharpness $\leq +0.3$, while maintaining the same photometric error threshold of 0.1 mag. This additional filtering yielded a refined sample of 455,885 sources, which were retained as our final set of high-quality PSF sources. The selection range is shown in the error and sharpness distributions of our SMC sample in Fig. 5.2. We constructed Hess diagrams of $(J - K_s)_0$ vs $K_{s,0}$, using bin sizes of ~ 0.02 mag in colour and 0.04 mag in magnitude. The CMD corresponding to this selection of all SMC sources is shown on the right panel of Fig. 5.3.

To select probable SMC sources, we addressed the contamination from MW foreground sources within this refined sample. To remove as many MW contaminants as possible while maximising completeness in the central regions, we employed two complementary approaches. In the first approach, we selected sources from *Gaia* DR3, within a 3 deg radius from the SMC centre and applied parallax and proper motion cuts following Gaia Collaboration et al. (2021b), an astrometric excess noise cut (> 1.3 mas), and photometric excess factor cuts based on the criteria from Gaia Collaboration et al. (2021a); Riello et al. (2021). These quality cuts yielded 1,352,775 sources of *Gaia* DR3 data. A subsequent cross-match between this *Gaia* dataset and the VMC refined catalogue containing 455,885 sources, using a matching radius of 1 arcsec, resulted in 238,394 matched sources. The $(J - K_s)_0$ vs. $K_{s,0}$ CMD for these cross-matched SMC Deep sources is shown in Fig. 5.11d. The CMD demonstrates that many of the fainter sources were removed through this cross-match, as the *Gaia* data is incomplete at the central regions. Although this method efficiently eliminated MW contaminants, it also excluded some faint RC sources from the SMC sample.

To mitigate this effect and retain a more complete RC sample, especially towards the fainter magnitudes, we implemented a different cross-matching procedure to preserve as many fainter sources as possible. First, we selected all *Gaia* sources (both SMC and MW) within the VMC Deep tile region of the SMC, resulting in 1,290,899 sources. The same filtering criteria as in the first method were then applied (Gaia Collaboration et al. 2021b), including the astrometric excess noise cut, which yielded 386,277 *Gaia* SMC sources in the VMC region. We then cross-matched the combined (SMC + MW) sample with the SMC-only subset and removed the overlapping sources, which corresponds to SMC, thereby retaining 904,672 MW sources from the *Gaia* DR3 dataset within the VMC Deep tile region. This MW dataset was then cross-matched with our SMC Deep dataset (after applying the quality cuts) to remove sources identified as MW contaminants, resulting in a final sample of 261,624 sources. The CMD corresponding to this dataset is shown in Fig. 5.11g. Although this second method yielded fewer total sources than the first, the resulting CMD reveals a larger sample of faint sources. Consequently, this approach provides a more complete sample of RC stars, particularly at the fainter end, improving the reliability of subsequent analyses of the SMC RC population.

5.3.3 Selection of RC stars

In this study, our primary objective is to probe the bimodality within the RC population; therefore, we focus our analysis on RC stars. First, we selected RC stars from our refined sample of SMC sources, after removing MW contaminants as described in the previous section. RC stars can be distinctly identified in the CMDs of nearby galaxies by defining a selection box (e.g: Subramanian et al. 2017; Tatton et al. 2021; Omkumar et al. 2021). Specifically, stars within the colour range $0.1 \leq (J - K_s)_0 \leq 0.4$ mag and the magnitude range $15.5 \leq K_{s,0} \leq 18.5$ mag were selected after visual inspection of the VMC Deep CMD

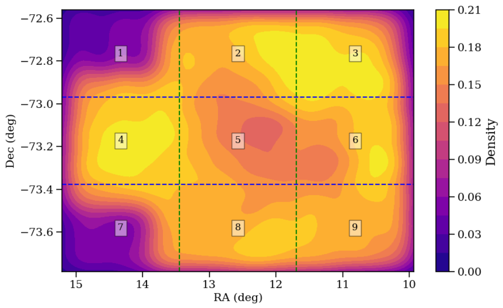

Figure 5.4: Spatial distribution of the probable SMC deep sources RC sources after removing MW sources using *Gaia* DR3 data. The division of the segments are shown with blue and green dashed lines, with segment numbers marked on them, respectively.

of the SMC. This selection yielded a total of 134,786 RC stars, as illustrated in Fig. 5.11g, where the selection box is marked in black.

Table 5.1: Estimated best-fit parameters for single Gaussian fit for RC stars in the SMC deep tile after removing MW sources.

Region	Amplitude	Peak	Sigma	$\chi^2_{reduced}$
Segment 1	240 ± 6	17.093 ± 0.004	0.161 ± 0.005	5.099
Segment 2	386 ± 11	17.109 ± 0.005	0.159 ± 0.005	22.014
Segment 3	394 ± 10	17.110 ± 0.004	0.153 ± 0.005	5.956
Segment 4	440 ± 11	17.123 ± 0.004	0.149 ± 0.005	11.389
Segment 5	280 ± 10	17.118 ± 0.006	0.165 ± 0.007	29.890
Segment 6	390 ± 9	17.113 ± 0.004	0.156 ± 0.005	6.632
Segment 7	245 ± 7	17.121 ± 0.004	0.149 ± 0.005	3.658
Segment 8	391 ± 10	17.130 ± 0.004	0.154 ± 0.005	6.352
Segment 9	397 ± 8	17.120 ± 0.003	0.151 ± 0.004	3.573

The spatial distribution of the selected RC sample, used for subsequent analysis, is presented as density contours in Fig. 5.4. To enable a more detailed investigation, we subdivided the VMC deep tile into nine distinct segments, as shown in Fig. 5.4. The segmentation follows a 3×3 grid scheme, determined by computing midpoints along both RA and Dec. Specifically, two midpoints were calculated along each axis, thereby dividing the full range into three parts in both dimensions. The resulting nine segments are numbered from 1 to 9, and their boundaries are denoted with blue and green dashed lines. The segmentation strategy was designed such that, given the sufficient RC sample coverage across the tile, we could study the distribution of RC stars in different regions, spanning the eastern, western, and central parts of the SMC. This division is also motivated by the fact that bimodal RC stars are primarily detected in the eastern regions of the SMC; thus, the left-hand segments (1, 4 and 7) correspond to the eastern regions, the right-hand segments (3, 6 and 9) to the western regions, and the central segments (2, 5 and 8) covers the core of the SMC. Each segment is analysed individually in the following sections.

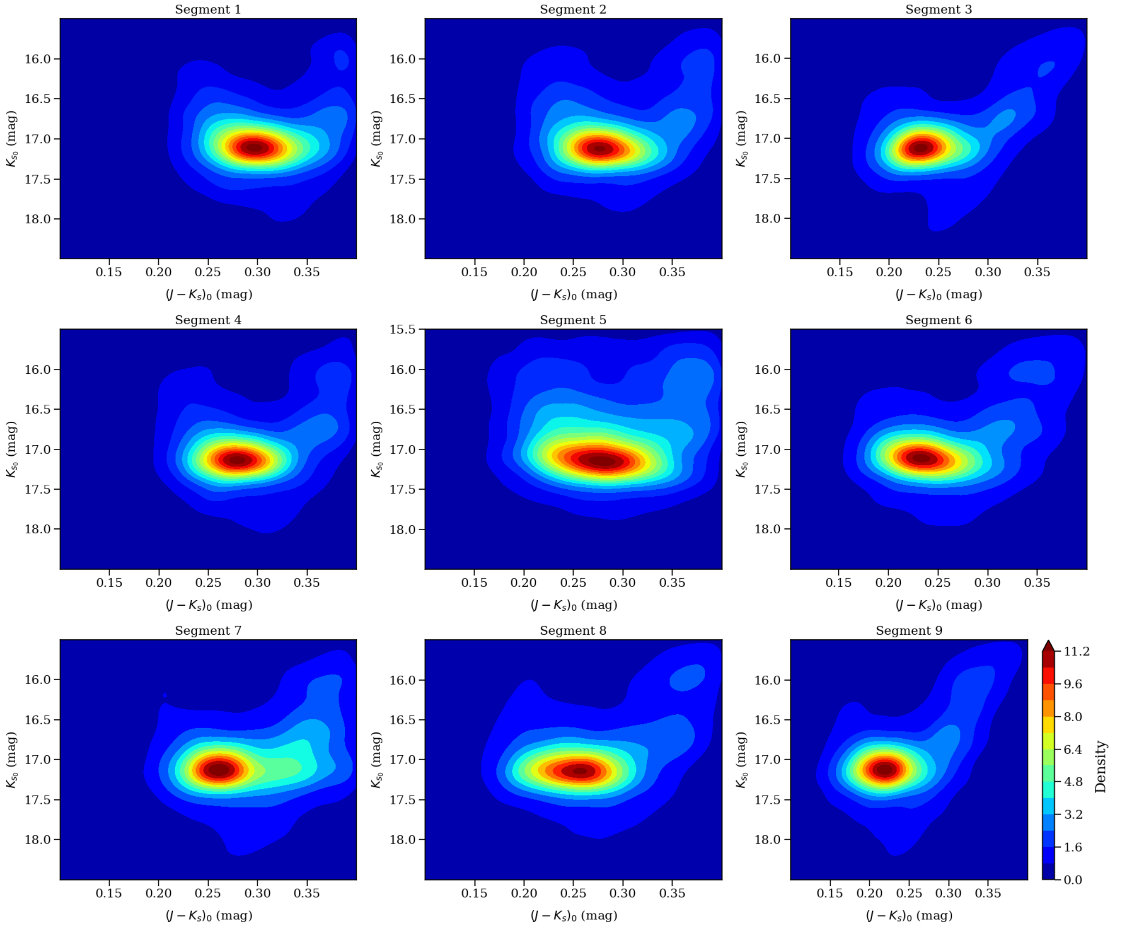

Figure 5.5: Contour density plot of the RC stars in each segment of the SMC deep tile, after removing MW sources using *Gaia* DR3 data, within the analysis region of the RC stars indicated by a black rectangle in Fig. 5.12.

From the density contour plot, it is evident that the eastern regions contain relatively more sources than the central ones. The apparent deficiency of sources in segments 1 and 7 arises from the detector pattern, as discussed in (Cioni & Omkumar et. al. in prep.).

The corresponding density contours of the RC region for each segment are shown in Fig. 5.5. From the CMDs of the various segments, we observe that the RC stars exhibit larger vertical and horizontal extensions in the eastern and central segments than in the western ones. Notably, the central segment (Segment 5) shows the largest extension in both. It is important to note that, although we defined the RC selection box to isolate RC stars for further analysis, the selection also includes some RGB stars, which can be clearly seen in all CMDs. The distribution of stellar populations in each segment is shown in Fig. 5.12, where the RC selection box is marked in black. From both the CMDs and the RC density contours, it is evident that the stellar distribution is not uniform across all segments. To further investigate the observed differences in the CMD (Fig.5.4), which reveals a non-uniform distribution across different segments, we produced differential images (residual) to compare the central regions (Segment 5) with the other segments,

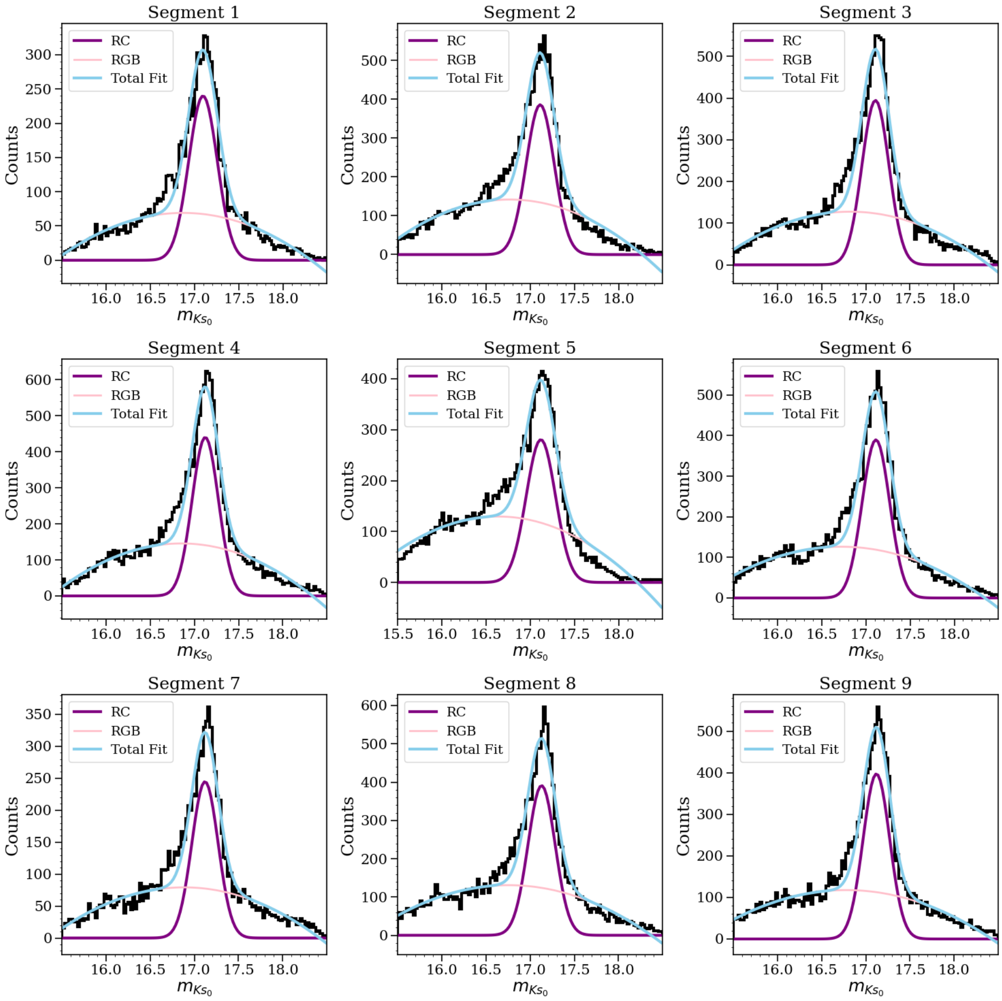

Figure 5.6: A single Gaussian fit to the magnitude distribution of the selected RC stars in each segment of the SMC deep tile after removing MW sources using *Gaia* DR3 data. In all plots, the total fit is shown as a blue line, while single Gaussian fit is indicated by a solid line. A pink line represents the quadratic polynomial fit for RGB stars.

as illustrated in Fig.5.13. In the following section, we discuss the contribution of the underlying RGB stars to our RC sample in more detail.

5.3.4 Presence of RGB stars

In Fig. 5.5, we can see that the selected RC region includes contributions from RGB stars. It is important to account for this contamination in our RC sample. To perform a thorough RC analysis, we adopted two complementary approaches. In the first method, the RGB stars were retained along with the RC sample, and their contribution was modelled using a quadratic polynomial while fitting the RC luminosity function (e.g., Omkumar et al. 2021; Gatto et al. 2024). In the second method, we modelled the RGB stars in each segment separately and subtracted them from the sample to obtain a cleaner RC distribution (e.g., Subramanian et al. 2017).

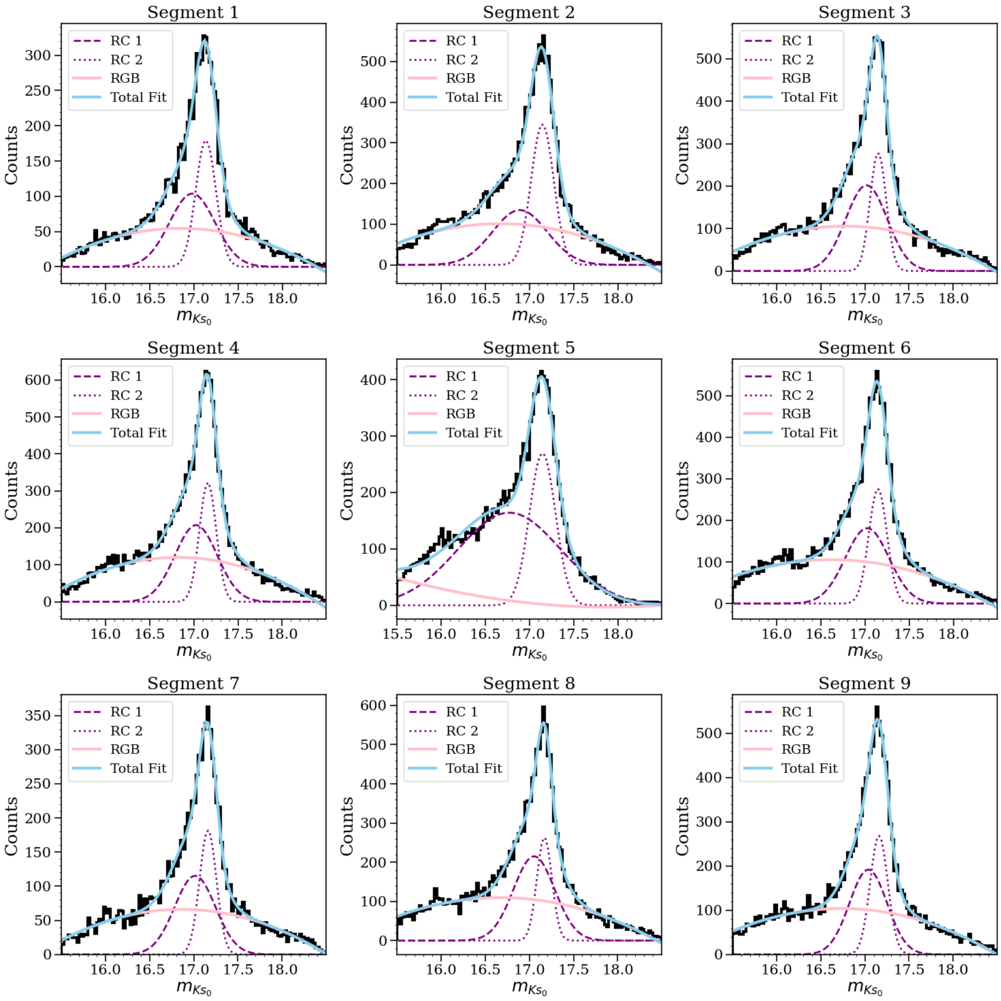

Figure 5.7: A bimodal fit to the magnitude distribution of the selected RC stars in each segment of the SMC deep tile after removing MW sources using *Gaia* DR3 data. In all plots, the total fit is shown as a blue line, while the double Gaussian fits are indicated by dashed magenta lines. A pink line represents the quadratic polynomial fit for RGB stars.

In the first approach, we constructed histograms of the $K_{s,0}$ magnitude distributions of the selected RC stars across the nine segments, using a bin size of 0.025 mag. The observed magnitude distribution was initially modelled with a single Gaussian function to represent the RC stellar distribution, combined with a quadratic polynomial to account for the RGB component within the RC selection box. The magnitude distributions of the RC stars (black), along with the best-fit single Gaussian (magenta), the quadratic polynomial representing the RGB stars (pink), and the total luminosity fit (pale blue), for each segment are shown in Fig. 5.6. The RC peak magnitudes, sigma values, and their associated fit errors for each segment are listed in Table 5.1. The table also provides the best-fit Gaussian amplitudes along with fit errors, and the reduced chi-squared (χ^2_{reduced}) values, which quantify the goodness of fit.

To investigate the possible bimodality in the RC distribution, we added a second

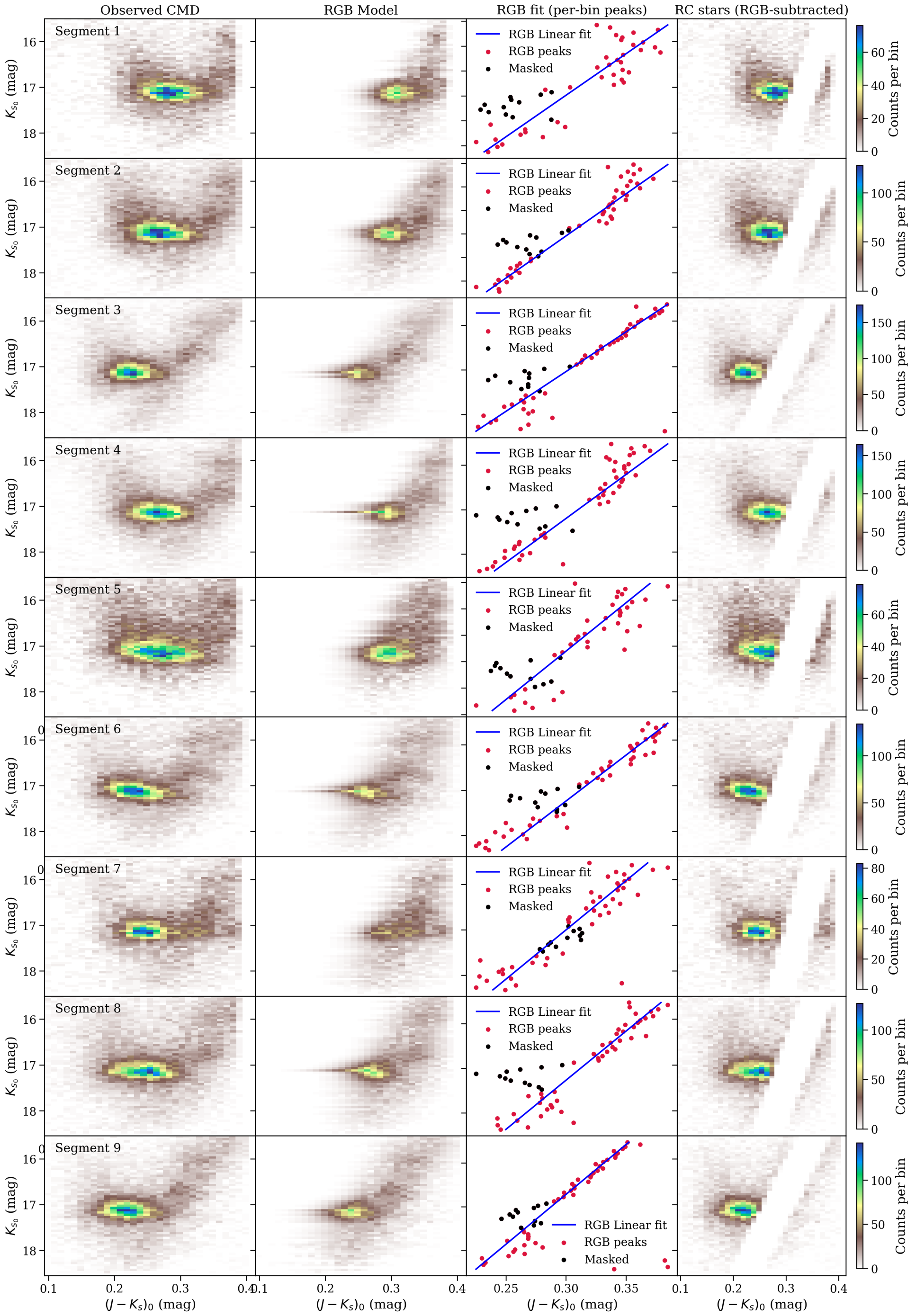

Figure 5.8: Plot displays the observed CMD (panel 1), the modelled RGB component (panel 2), the per-bin RGB peaks along with linear fit (panel 3), and the resulting RC stars after RGB-subtraction (panel 4). The panels are ordered from top to bottom, corresponding to segments numbered 1 through 9. In panel 3, per-bin peaks excluded from the RGB fit are marked with black points, while those retained in the fit are shown as red points; the blue line represents the linear fit to the selected red points and defines the RGB slope. The colour bar indicates the source density in each segment.

Table 5.2: Estimated best-fit parameters for bimodal Gaussian fit for RC stars in the SMC deep tile after removing MW sources.

Region	Amplitude 1	Peak 1	Sigma 1	Amplitude 2	Peak 2	Sigma 2	$\chi^2_{reduced}$	Percentage	Peak difference
Segment 1	104 ± 11	16.978 ± 0.022	0.257 ± 0.016	179 ± 12	17.131 ± 0.005	0.114 ± 0.006	1.692	66.825	0.153 ± 0.022
Segment 2	135 ± 14	16.888 ± 0.035	0.308 ± 0.027	346 ± 17	17.144 ± 0.004	0.128 ± 0.005	4.949	77.520	0.255 ± 0.036
Segment 3	202 ± 12	17.019 ± 0.011	0.235 ± 0.009	279 ± 13	17.150 ± 0.003	0.091 ± 0.004	2.085	64.997	0.132 ± 0.011
Segment 4	208 ± 13	17.026 ± 0.011	0.239 ± 0.009	323 ± 14	17.159 ± 0.003	0.095 ± 0.004	4.047	64.464	0.133 ± 0.012
Segment 5	164 ± 33	16.770 ± 0.031	0.580 ± 0.065	270 ± 7	17.146 ± 0.004	0.147 ± 0.005	1.513	94.939	0.376 ± 0.031
Segment 6	181 ± 16	17.025 ± 0.014	0.248 ± 0.013	276 ± 16	17.147 ± 0.004	0.103 ± 0.005	2.568	61.275	0.122 ± 0.015
Segment 7	115 ± 10	17.015 ± 0.017	0.231 ± 0.012	182 ± 11	17.162 ± 0.004	0.096 ± 0.005	1.468	59.866	0.146 ± 0.017
Segment 8	215 ± 13	17.053 ± 0.010	0.234 ± 0.010	264 ± 14	17.170 ± 0.004	0.085 ± 0.005	2.445	61.507	0.117 ± 0.011
Segment 9	192 ± 18	17.039 ± 0.015	0.213 ± 0.010	268 ± 20	17.160 ± 0.004	0.100 ± 0.006	1.525	57.301	0.121 ± 0.015

Gaussian component to the luminosity distribution of RC stars, along with a quadratic polynomial fit to represent the RGB contamination, and the total fit is overplotted for comparison. The resulting bimodal Gaussian fits are shown in Fig. 5.7, where the bright RC component (foreground population) is indicated by a broken magenta line, and the faint RC component (foreground population) by a dotted magenta line. The best-fit parameters from these bimodal fits are listed in Table 5.2. This table also includes two additional columns: *Percentage* and *Peak Difference*. The *Percentage* column indicates the improvement in χ^2_{reduced} when an additional Gaussian component is introduced, showing an increment between 57% and 94% across the segments. The *Peak Difference* column gives the magnitude difference between the faint and bright RC peaks (Peak 2 − Peak 1), along with the propagated uncertainties from each fit. From the peak values and the bimodal Gaussian plots, it is evident that the amplitude of the bright RC component is lower with a broader width and the faint RC component has a larger amplitude with a narrower width in all segments. Furthermore, although the two Gaussian components overlap in all panels, distinct peaks are still distinguishable, a signature not previously observed in studies of the central regions of the SMC. The magnitude difference between the faint and bright peaks ranges from 0.121 mag to 0.376 mag across the different segments. In the next section, we discuss another approach to quantify the luminosity distribution of RC stars.

5.3.5 Exploring the effect of RGB contamination

In this section, we discuss the second approach, where we performed a comprehensive analysis to separate the RGB stars from the RC stars in each segment by modelling the RGB contribution from the observed CMD, subtracting the RGB model to isolate the RC stars, and fitting the resulting RC luminosity function as described in the previous section (see Section 5.3.4). We retained the same selection criteria for the colour and magnitude ranges of RC stars as before, and this method was applied to each segment separately, as shown in Fig. 5.8.

We plotted the observed CMD for the RC stars in each segment (panel 1), with bin sizes set to 0.01 mag in $(J - K_s)_0$ colour and 0.05 mag in $K_{s,0}$ magnitude, creating a fine grid suitable for detailed modelling of the RGB stars. Then, we estimated the RC and RGB peaks within each magnitude bin. To distinguish the RGB and RC stars, we assumed that the first (bluer) peak always corresponds to the RC stars, and the second (redder) peak corresponds to the RGB stars. We iterated over each magnitude bin and applied a

Table 5.3: Segment-wise statistics for the RGB modelling and final selection of RC stars.

Region	Total RC	RGB slope$\pm\sigma_{\text{med}}$	Error$_{\text{min}}$	Error$_{\text{max}}$	RC stars	RGB (removed)
Segment 1	9162	-0.0288 ± 0.0271	0.0017	0.0077	6437	2725
Segment 2	17107	-0.0350 ± 0.0279	0.0016	0.0070	12277	4830
Segment 3	16492	-0.0456 ± 0.0300	0.0018	0.0166	11281	5211
Segment 4	17921	-0.0337 ± 0.0286	0.0013	0.0090	12883	5038
Segment 5	14698	-0.0292 ± 0.0345	0.0016	0.0111	9733	4964
Segment 6	16499	-0.0317 ± 0.0355	0.0020	0.0114	11074	5425
Segment 7	10089	-0.0239 ± 0.0301	0.0022	0.0087	6826	3263
Segment 8	16860	-0.0329 ± 0.0347	0.0015	0.0098	11400	5460
Segment 9	15958	-0.0439 ± 0.0348	0.0022	0.0238	10214	5744

Table 5.4: Estimated best-fit parameters for single Gaussian fit for RC stars in the SMC deep tile after removing MW sources and RGB stars.

Region	Amplitude	Peak	Sigma	$\chi^2_{reduced}$
Segment 1	184 ± 5	17.081 ± 0.004	0.164 ± 0.005	5.247
Segment 2	319 ± 8	17.100 ± 0.004	0.156 ± 0.005	22.094
Segment 3	363 ± 7	17.106 ± 0.003	0.151 ± 0.004	6.318
Segment 4	392 ± 8	17.119 ± 0.003	0.149 ± 0.004	12.546
Segment 5	186 ± 7	17.088 ± 0.007	0.174 ± 0.008	25.646
Segment 6	342 ± 7	17.101 ± 0.003	0.145 ± 0.004	5.728
Segment 7	203 ± 5	17.123 ± 0.004	0.147 ± 0.004	2.486
Segment 8	336 ± 8	17.125 ± 0.004	0.143 ± 0.004	7.808
Segment 9	341 ± 6	17.113 ± 0.003	0.148 ± 0.003	3.230

Gaussian Mixture Model (GMM) to the colour distribution within that bin; if the GMM fitting failed, a peak-finding algorithm was used as a fallback method to estimate the per-bin peak and dispersion of the RC and RGB stars. We subsequently built the RGB model Hess diagram by interpolating the amplitudes and dispersions for each magnitude bin and constructing the model using Gaussian profiles, with the resulting modelled RGB component shown in panel 2 of Fig. 5.8.

For each segment, we extracted the RGB peak positions, widths, and amplitudes as functions of magnitude and plotted the per-bin RGB peaks (panel 3). A linear fit was then performed to trace the RGB slope, using iterative sigma-clipping to remove outliers and obtain a robust fit. In the central region of the CMD, where the RC is located, identifying the RGB peaks was more challenging, and noticeable in panel 3, where plots show that the RGB peak in K_s shifts noticeably in these regions. Therefore, we excluded the magnitude range $16.9 \le K_{s,0} \le 17.5$ mag (shown in black) and fitted the linear track outside this interval to estimate the slope of the RGB stars. Using this RGB slope $\pm 1\sigma$, we defined the underlying RGB contribution and subtracted it from the original (RGB + RC) Hess diagram to obtain a clean Hess diagram comprising the RC stars (panel 4). The corresponding plots are shown in Fig. 5.8.

The segment statistics, including the RGB slope along with the σ and error ranges, the

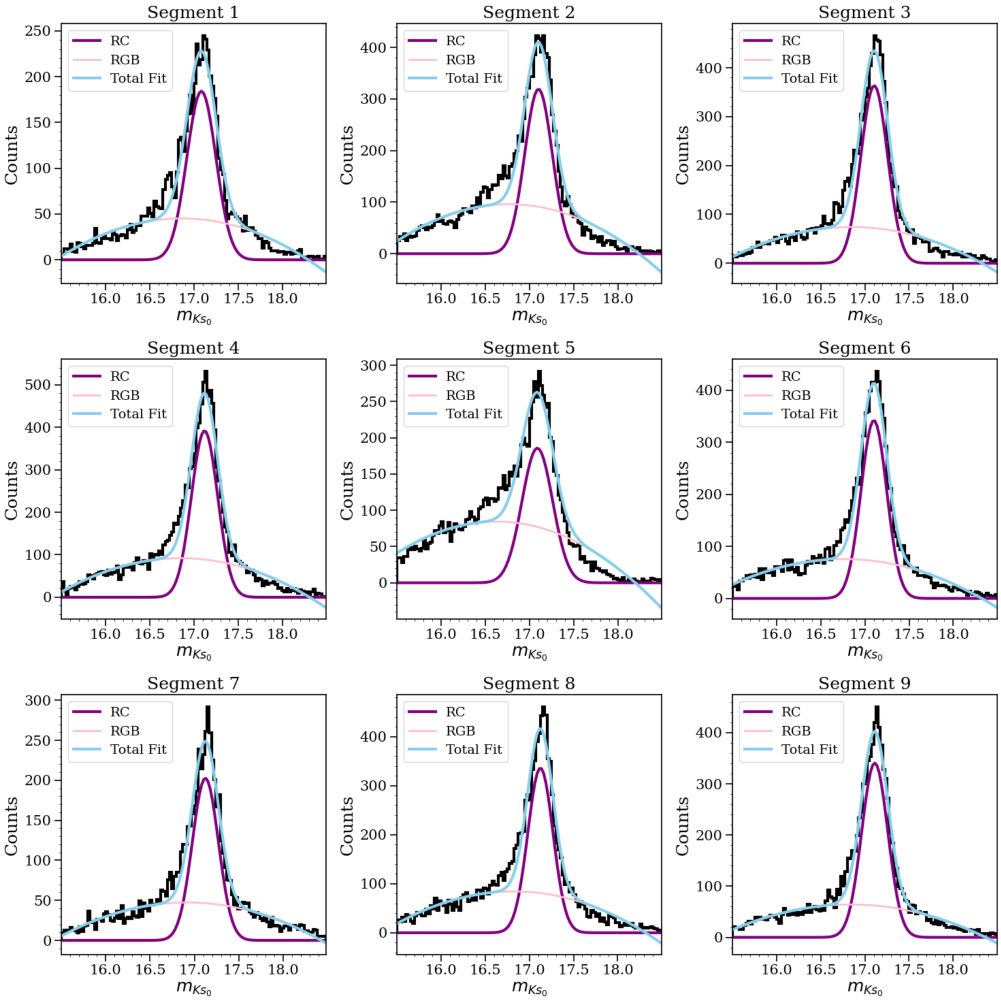

Figure 5.9: Same as Fig. 5.6, but after modelling RGB stars and removing them from the RC sample.

total number of sources in the observed CMD, the number of RGB stars removed, and the final RC sample size, are summarised in Table 5.3. Furthermore, we estimated the RC luminosity function as explained in the previous section to accurately characterise the RC components, and the results are presented in Figs. 5.9 and 5.10. The corresponding best-fit parameters obtained from this method are listed in Tables 5.4 and 5.5. The results from this method are consistent with those obtained when retaining the RGB sources and modelling their contribution to the RC luminosity function, with smaller amplitude as expected. Note that we still kept the quadratic polynomial in our total fits as before, to account for the residual RGB stars in our final RC sample.

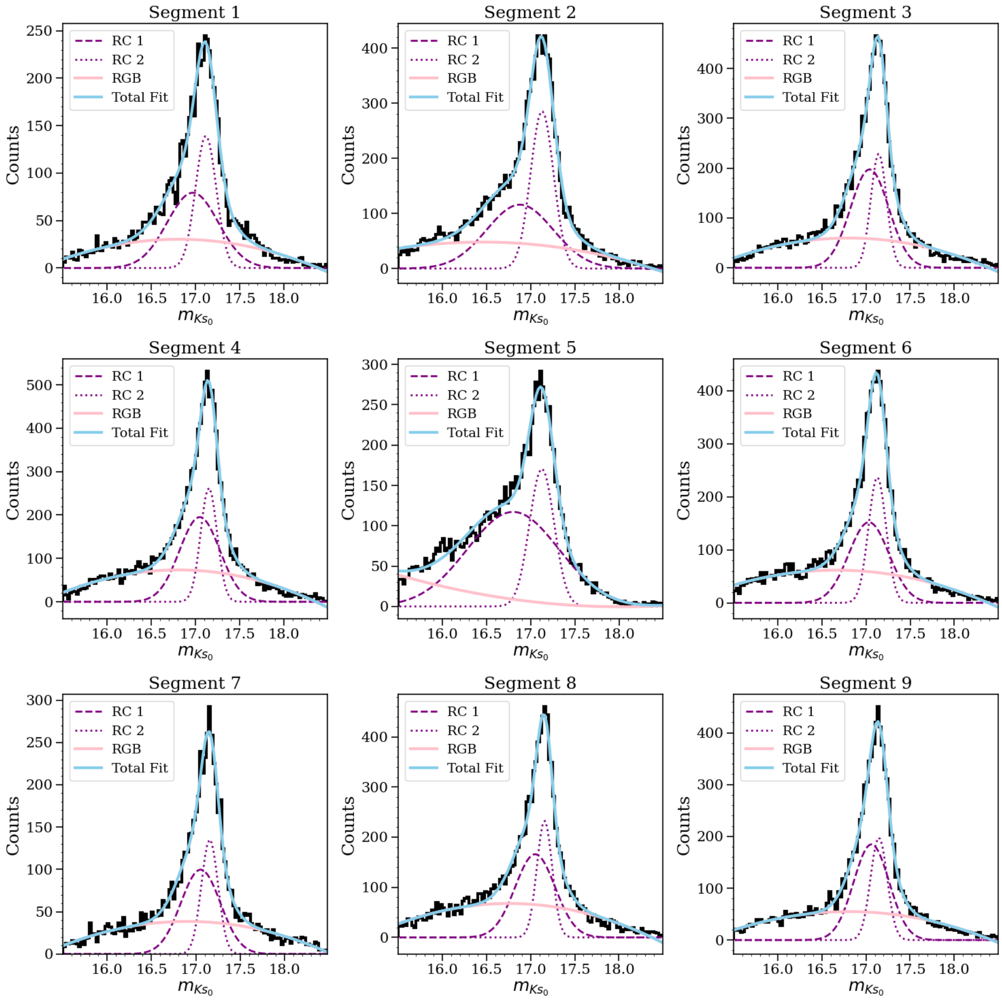

Figure 5.10: Same as Fig. 5.7, but after modelling RGB stars and removing them from the RC sample.

5.4 Results and discussions

In this section, we provide an overview of the results obtained from our study. We will analyse these findings in detail and discuss their implications in the context of the existing literature.

5.4.1 Presence of distance bimodality?

The vertically extended RC region observed in the CMD of nearby galaxies primarily arises from the considerable line-of-sight depth of the host galaxy, as RC stars serve as standard candles. Previous studies have explored potential explanations for the vertically extended RC feature identified in the eastern regions of the SMC. Possible causes include population effects, such as the presence of a younger (brighter) RC population that may appear as a dual RC in the CMD; evolutionary effects involving Blue Loop (BL) stars

Table 5.5: Estimated best-fit parameters for bimodal Gaussian fit for RC stars in the SMC deep tile after removing MW sources and RGB stars.

Region	Amplitude 1	Peak 1	Sigma 1	Amplitude 2	Peak 2	Sigma 2	$\chi^2_{reduced}$	Percentage	Peak difference
Segment 1	79 ± 8	16.968 ± 0.021	0.289 ± 0.020	139 ± 8	17.116 ± 0.005	0.117 ± 0.006	1.630	68.938	0.148 ± 0.021
Segment 2	116 ± 9	16.876 ± 0.021	0.377 ± 0.024	286 ± 7	17.126 ± 0.003	0.130 ± 0.004	2.061	90.670	0.250 ± 0.021
Segment 3	197 ± 12	17.042 ± 0.008	0.217 ± 0.007	229 ± 12	17.145 ± 0.003	0.089 ± 0.004	2.611	58.681	0.102 ± 0.009
Segment 4	195 ± 13	17.049 ± 0.009	0.228 ± 0.009	263 ± 13	17.152 ± 0.003	0.093 ± 0.004	4.757	62.086	0.103 ± 0.010
Segment 5	117 ± 15	16.800 ± 0.024	0.518 ± 0.043	171 ± 5	17.125 ± 0.004	0.139 ± 0.005	1.258	95.094	0.325 ± 0.024
Segment 6	152 ± 14	17.032 ± 0.012	0.228 ± 0.011	237 ± 15	17.128 ± 0.003	0.100 ± 0.005	2.450	57.226	0.095 ± 0.012
Segment 7	100 ± 10	17.054 ± 0.014	0.222 ± 0.012	135 ± 10	17.156 ± 0.005	0.094 ± 0.006	1.232	50.437	0.103 ± 0.015
Segment 8	166 ± 12	17.051 ± 0.011	0.226 ± 0.010	233 ± 12	17.158 ± 0.003	0.087 ± 0.004	3.372	56.819	0.107 ± 0.011
Segment 9	185 ± 17	17.062 ± 0.009	0.202 ± 0.008	198 ± 17	17.147 ± 0.004	0.094 ± 0.006	1.552	51.936	0.085 ± 0.010

near the red end, which could mimic an elongated RC feature; or the effect of extinction, causing the elongation.

Nidever et al. (2013) constructed synthetic CMDs of one eastern and one western field in the SMC to model the Blue Loop and RC populations to eliminate the possibility of the presence of BL stars causing the observed vertical elongation. They demonstrated that BL could not cause the observed extended RC feature in the eastern regions; they attributed this feature to a significant spread of RC stars ∼ 12 kpc in distance. Using NIR data from the VMC survey, Subramanian et al. (2017) studied the 20 deg of the SMC data and tested single- and double-distance models by fitting linear combinations of stellar partial models to reproduce the observed CMDs. The single-distance model failed to reproduce the magnitude difference in the RC feature and also produced a colour spread among the fainter RC stars, whereas the double-distance model showed good agreement with the observed CMD feature and yielded lower normalised $\chi^2_{\text{normalised}}$ values. Although the extinction effects are minimal in the NIR, they further investigated the colour distributions of the RC stars. They argued that extinction could not account for the feature, since the observed magnitude difference of ∼ 0.4 mag would produce a substantial colour spread that was not observed. Their study concluded that the RC peak difference between the foreground and main-body SMC population corresponds to a ∼ 11 kpc difference between the two RC populations from ∼ 2 to 2.5 deg from the SMC centre.

In a subsequent study, Tatton et al. (2021) used the complete VMC coverage of the SMC to map its 3-dimensional structure using RC stars as tracers, obtaining results consistent with those of Subramanian et al. (2017) and thereby confirming the presence of dual RC populations in the eastern regions. Additionally, El Youssoufi et al. (2021) identified the same distance bimodality of RC stars and traced this feature out to nearly 10 deg from the SMC centre using VHS data. Using optical data from *Gaia* DR2, Omkumar et al. (2021) analysed RC stars and traced the feature across ∼ 2 to 6 deg in the eastern regions. They also examined the colour distribution of the RC stars and found only a minimal colour difference, insufficient to account for the observed magnitude separation between the faint and bright RC components expected from differential extinction. More recently, Gatto et al. (2024) confirmed the presence of bimodality among RC stars at about 2.8 deg from the SMC centre in the eastern region using deep optical photometric data from the VLT Survey Telescope. Very recently, Oden et al. (2025) mapped the 3-dimensional structure of the Clouds using RC stars using *Gaia* DR3 data and further confirmed the presence of a dual RC population in the SMC, consistent with the results from previous studies (e.g., Hatzidimitriou et al. 1993; Nidever et al. 2013; El Youssoufi et al. 2021; Omkumar et al. 2021.

These studies collectively concluded that the elongated RC feature results from distance bimodality caused by past tidal interactions between the Clouds. The tidal interactions stripped stars from the SMC, creating a stellar substructure located $\sim 10-12$ kpc in front of the SMC main body in the direction of the MB and the LMC. Previous studies such as Omkumar et al. (2021); James et al. (2021) have revealed distinct kinematic differences between the two RC populations, identified by proper motion differences and line-of-sight distance separations. James et al. (2021) also showed that the RGB stars having lower and higher radial velocities have proper-motions comparable with that of the foreground and main-body RC stars, separated by distance. Recent studies by Almeida et al. (2024); Navabi et al. (2025) and Omkumar et al. (in prep.,) confirms these two RGB populations exhibit similar kinematic properties as the dual RC populations. They differ not only photometrically and kinematically but also chemically. Metallicities derived for the kinematically separated RGB populations show that the foreground substructure (moving towards us) is more metal-rich than the main body stars. This finding suggests that the metal-rich RGB stars and hence the foreground RC stars were stripped from the inner SMC during recent tidal interactions with the LMC (Almeida et al. 2024; Navabi et al. 2025; Omkumar et al. (in prep.)).

So far, all these studies have investigated and established the presence of RC bimodality in the outer regions from about $2-2.5$ deg from the SMC centre. However, central region does not show any signature of bimodality, and most studies have found that a single Gaussian provides an adequate fit to the RC distributions. Studies like Subramanian et al. (2017) and Omkumar et al. (2021), where a bimodal RC distribution has been reported, the two Gaussian components largely overlap, and no significant peak separation is obtained, so no convincing evidence for a dual population in the centre has been reported. Since previous studies concluded that the foreground population was stripped from the inner regions, some level of perturbation in the central parts of the SMC is nevertheless expected. Crowding and incompleteness in the central regions of the Clouds could also explain why even studies using *Gaia* data have not been able to detect clear signatures of this interaction.

In our study, with the VMC Deep catalogue, we were able to detect signatures of bimodal RC populations within the central regions of the SMC. In Fig. 5.10, we find a significant improvement in the $\chi^2_{\rm reduced}$, when a second Gaussian component is included, and all our segments are best described by a double Gaussian fit representing dual RC populations. However, from the plots and the Table 5.5, we see that the peak separation in the central regions is smaller, in the range of ~ 0.12 mag to 0.3 mag, than that reported for the outer regions in previous studies. This evidence implies that the inner regions of the SMC may still exhibit perturbations left behind by the tidal interactions. The smaller magnitude separation between the bright and faint RC peaks in the centre, compared to the outer parts, suggests that the stronger gravitational potential in these regions likely reduces the distance separation between the foreground and main-body RC stars.

Although, the bimodal RC distribution is interpreted as evidence of stellar populations at distinct distances, the potential contribution of stellar population effects cannot be neglected, particularly given that the inner SMC have a star formation history distinct from the outer regions (Nidever et al. 2013; Subramanian et al. 2017). As demonstrated by Girardi (2016), young RC stars (age ~1–2 Gyr) can be intrinsically brighter than older counterparts by up to ~0.5 mag in K_s and also have a larger width, potentially mimicking a foreground population. To distinguish between distance and population effects, we examine the widths (σ) of the two Gaussian components. If the young RC stars are present, this can show up as a wider width in their magnitude distribution than their compact width of the primary RC. Notably, in most of our segments, the RC widths are broadly similar, supporting a distance interpretation, with a notable exception (Segment 5), exhibiting a significantly broader bright component, suggesting that population effects may dominate in the innermost region where recent star formation is more prevalent (Rubele et al. 2018a).

For the other regions, under the assumption that the separation is purely due to distance, the observed separations of ~0.12–0.3 mag imply line-of-sight distance differences of ~ 3–7 kpc (except the central segment 5), substantially smaller than the ~10–12 kpc reported for the outer SMC (Subramanian et al. 2017; Nidever et al. 2013; Omkumar et al. 2021; Gatto et al. 2024), consistent with a deeper gravitational potential in the inner regions. A definitive characterisation of the RC bimodality requires comparison with synthetic CMDs from spatially resolved SFH models of the inner SMC, which will be incorporated in future. With the availability of VMCDeep data, proper motions can now be derived and used to test this scenario further and improve our understanding of the origin of the dual RC population, we may expect similar trends in their proper motion signatures as well.

5.5 Summary

Studies of the SMC have identified bimodality in the distribution of RC stars, mainly in the eastern outer regions (~ 2 – 2.5 deg outward), with the bright component traced up to large radii and interpreted as a foreground stellar substructure located about 10 – 12 kpc in front of the main body (e.g., Nidever et al. 2013; Omkumar et al. 2021). Previous studies have concluded that the feature reflects a distance bimodality caused by past tidal interactions between the Clouds, which stripped relatively metal-rich SMC stars present in the inner regions, and formed this foreground sub-structure. Kinematic studies using proper motions and, more recently, including metallicity analyses, show that the two RC components differ photometrically, kinematically, and chemically, with the foreground population moving north-west relative to the main-body and being more metal-rich than the main-body RC, supporting a tidally stripped origin. In previously studied central SMC regions, the RC generally appeared consistent with a single Gaussian, or any bimodality was too weak (strongly overlapping Gaussians) to claim a clear dual population, likely exacerbated by crowding and incompleteness. Even studies using the NIR data could not find any signatures of a dual RC population in the centre of the SMC. Thanks to the VMC Deep dataset, which was observed with better sky conditions, we were able to identify the signature of the dual RC population. This feature could not be traced with previous releases of Gaia data, as the centre of the Clouds is affected by crowding. In the future, Gaia Focused Product Releases may confirm this feature optically.

Using the deeper VMC data in the central SMC, our analysis finds statistically significant bimodal RC distributions in all central segments, with improved fits when a second Gaussian is included. The central peak separations are smaller (about 0.12 − 0.3 mag) than in the outer regions, suggesting that the stronger central gravitational potential reduces the line-of-sight distance separation between the foreground and main-body RC stars. These results indicate that the central SMC still bears perturbation signatures from the same tidal interactions, and forthcoming proper motion analysis with deep data may reveal corresponding kinematic differences. By leveraging VMC Deep data, we have identified the dual RC feature more accurately than previous studies, offering new insights into the dynamics and structure of the SMC's inner regions.

5.A CMD and Gaia selection

In this section, we show the different CMD of the SMC based on our *Gaia* selection and removal of the foreground sources from our catalogue to retain most probable SMC sources.

Table 5.6: Estimated best-fit parameters for single Gaussian fit

Region	Amplitude	Peak	Sigma	RChi
SMC Deep	5559 ± 102	17.124 ± 0.003	0.158 ± 0.004	30.041
SMC Deep (MW removed)	3161 ± 70	17.116 ± 0.004	0.155 ± 0.004	60.149
SMC Deep (Gaia cross-matched)	3211 ± 72	17.115 ± 0.004	0.155 ± 0.004	69.999

Table 5.7: Estimated best-fit parameters for bimodal Gaussian fit

Region	Amplitude 1	Peak 1	Sigma 1	Amplitude 2	Peak 2	Sigma 2	RChi	Percentage
SMC Deep	2650 ± 91	17.050 ± 0.005	0.262 ± 0.006	3841 ± 95	17.154 ± 0.002	0.103 ± 0.002	5.656	81.172
SMC Deep (MW removed)	1394 ± 70	16.999 ± 0.011	0.247 ± 0.008	2403 ± 78	17.155 ± 0.002	0.106 ± 0.003	16.730	72.185
SMC Deep (Gaia cross-matched)	1406 ± 74	16.996 ± 0.011	0.247 ± 0.008	2456 ± 83	17.155 ± 0.002	0.106 ± 0.003	19.704	71.850

5.B Residual RC distribution

In Fig.5.4, the distribution of RC stars, as observed from the CMD, reveals a non-uniform distribution across different segments. Notably, certain regions exhibit a greater vertical extension, while the central areas demonstrate significant horizontal extension. To further elucidate the RC distribution, we produced differential images (residual) of the CMD of RC stars across various segments. Our primary focus was to compare the central regions (Segment 5) with the other segments, as illustrated in Fig.5.13. The residual KDE, highlight where each region contains excess RC stars relative to the central region of the SMC.

First, we computed the binned Hess diagram for both the reference segment (Segment 5) and every other RC segment. By subtracting the Hess diagram of Segment 5 from those of the other segments, residual Hess diagrams are derived, which reflect the differences in the CMD densities between the segments. These residuals are then flattened and utilized to calculate a kernel density estimate (KDE), providing a smoothed representation of the residual density differences. Contour plots are generated from these KDEs, with color gradients indicating varying density differences, facilitating direct comparison across different segments. The Gaussian kernel is chosen because it offers a smooth and continuous density estimation, making it easier to interpret the distribution of differences between the segments and the reference segment. We notice that the residual plots in the eastern regions (left panels) look similar and the residual plots in the western regions (right panels) are analogous. This can hint us the intrinsic differences between the east and west regions. Although we notice a vertical extension in all panels, the western regions exhibits the most concentrated excess. These findings further demonstrate the non-uniform 3-D structure of the SMC, with significant line-of-sight complexity in the outer regions.

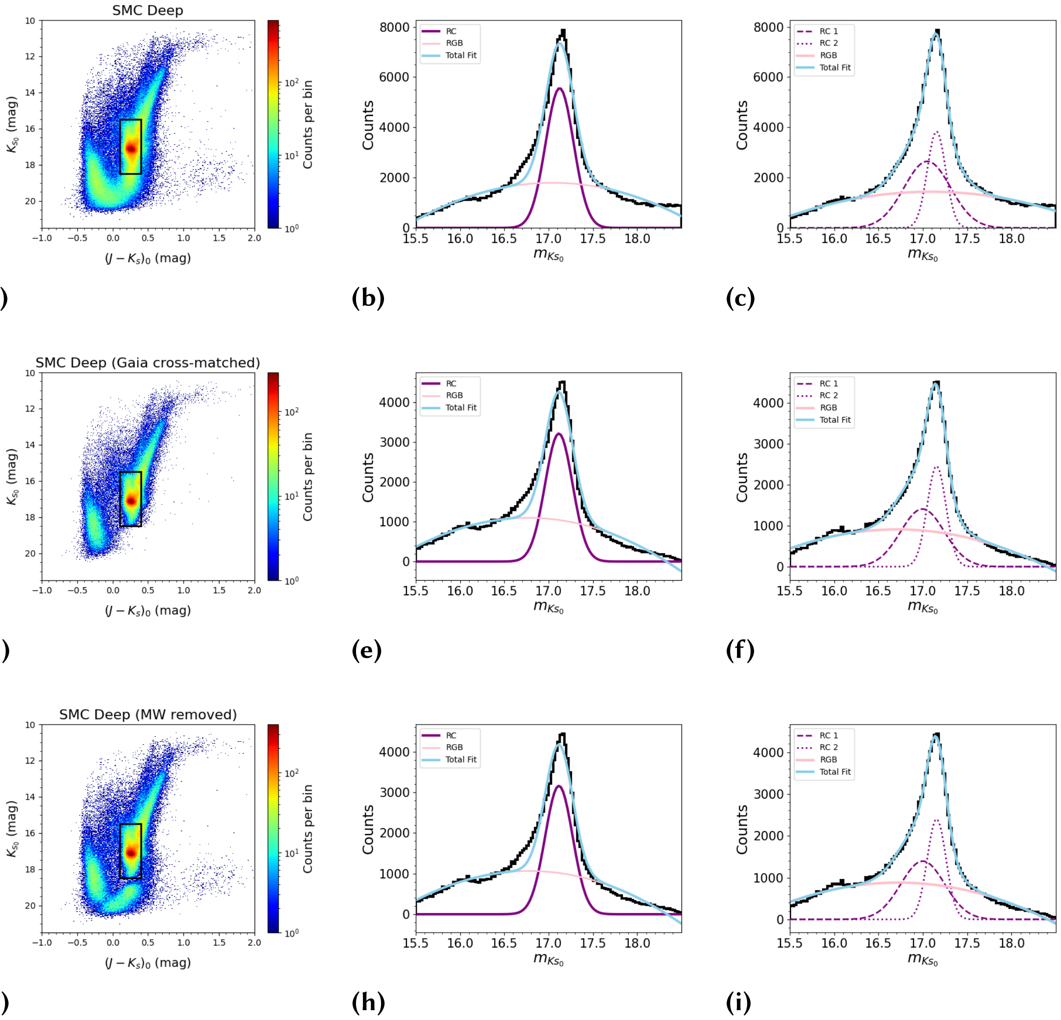

(a) (b) (c)

(d) (e) (f)

(g) (h) (i)

Figure 5.11: (a) The CMD of probable SMC stars after crossmatching with *Gaia* DR3 data, with the analysis region of the RC stars indicated by a black rectangle. (b) A single Gaussian fit to the magnitude distribution of the selected RC stars in the SMC deep tile. (c) A bimodal fit to the same distribution. In (b) and (c) the total fit is shown as a blue line, while single and double Gaussian fits are indicated by solid and dashed magenta lines. A pink line represents the quadratic polynomial fit for RGB stars.

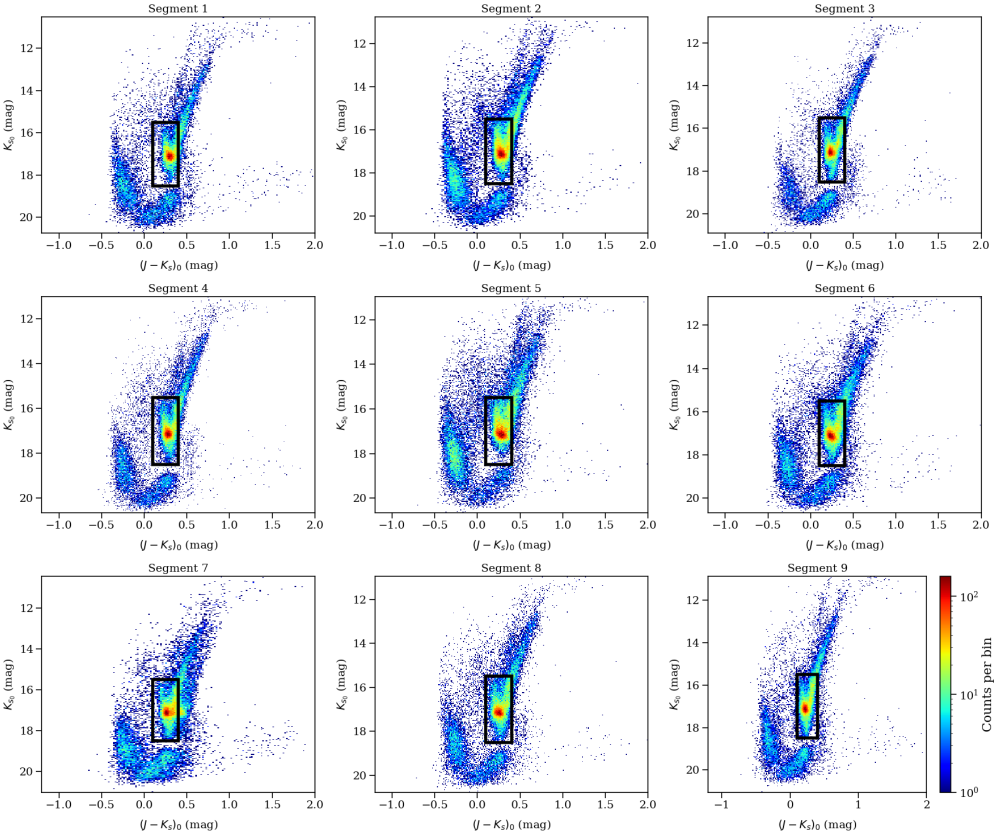

Figure 5.12: The CMD of probable SMC stars in each segment of the SMC deep tile, after removing MW sources using *Gaia* DR3 data, with the analysis region of the RC stars indicated by a black rectangle.

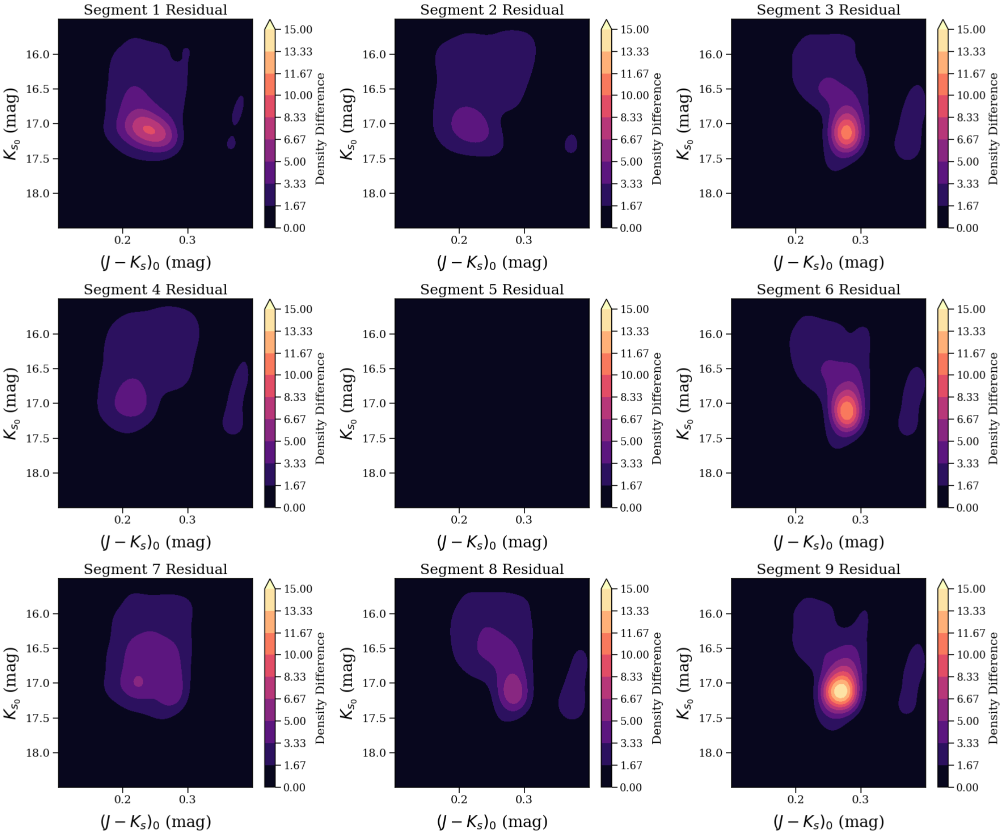

Figure 5.13: Residual CMD after subtracting the hess diagram of individual segments from the central segement (5).

6 Conclusions and future prospects

In this thesis, my primary focus was to decipher the evolution of the LMC and SMC, our closest neighbouring interacting galaxies, through detailed studies of their stellar substructures. This work highlights the importance of studying these substructures using homogeneous datasets and in-depth photometric observations to gain valuable insights into the formation, evolution, and dynamical history of the Clouds. In this final section, I summarise the key contributions of this thesis and the primary results of each chapter, tracing the history of debris-rich outskirts to crowded centres.

6.1 Conclusions

In the standard cosmological model (ΛCDM), galaxies, including the dwarfs such as the Clouds, evolve through repeated interactions that imprint distinct chemical and structural signatures. In this context, the Clouds, owing to their distance, are a unique laboratory to trace how such interactions shape galaxies over time. This thesis demonstrates that repeated interactions between the LMC, SMC, and MW have sculpted distinct chemical and structural signatures across the various stellar populations of the Clouds, from debris-rich outskirts to their dense cores. These imprints, evident in radial metallicity breaks, substructures, and central distance bimodality, reveal a shared history of dwarf-dwarf and host-satellite dynamics that has driven their morphological and chemical evolution. Our results confirm the interaction-driven evolution as predicted by the ΛCDM model.

To enable probing the stellar substructures comprising both young (supergiant) and old (RGB) stars situated mainly in the outskirts of the Clouds, I estimated the photometric metallicities ([Fe/H]) and determined the radial metallicity gradients for both populations. In Chapter 2, I show the detailed methodology, results and discussions of the study, which has been published in Omkumar et al. (2025). To accomplish this, I utilised the XP spectra from *Gaia* DR3 along with the GaiaXPy tool to derive synthetic Strömgren magnitudes. Then, by applying relevant calibration relations from the literature for young (Grebel & Richtler 1992; Piatti et al. 2019) and old (Calamida et al. 2007) stellar populations, I estimated the photometric metallicities for $\sim$ 90,000 young stars and $\sim$ 270,000 old stars situated within the $\sim$ 11 deg of the SMC and $\sim$ 20 deg of the LMC. The resulting radial metallicity gradients decrease linearly, aligning with the results from previous studies, validating the derived photometric metallicities. However, the largest sample of young and old populations also enabled me to apply piecewise regression analysis, revealing multiple breakpoints and varying slopes across radial regions. Overall, the findings of this study demonstrate that the breakpoints reflect the structure of present-day Clouds, star formation and chemical evolution histories signalling repeated interactions leading to episodic star formation and mixed tidal debris in both Clouds.

A key focus of my work is to provide a comprehensive view of the origin of the unique morphological imprints, such as the various stellar substructures, resulting from numerous interactions between the Clouds and their host over the past. Additionally, building on the observed breakpoints in the metallicity gradient, I further investigated their connection to the stellar substructures to elucidate how these interactions have critically shaped their structure and dynamics in Chapter 3 (*Omkumar et al.*, in prep.). For this, I utilised the photometric metallicity maps (Omkumar et al. 2025) and selected sources that belong to the previously identified stellar substructures in the periphery of the Clouds (El Youssoufi et al. 2019). I investigated their metallicities in relation to the main-body metallicities and the radial metallicity gradients. Furthermore, I compared their metallicity distribution functions with those of the LMC and SMC, performed statistical analysis tests such as the KS test, and examined their stellar kinematics to shed light on their potential origins. The results confirm the hybrid origin of the Magellanic Bridge, influenced by both the LMC and SMC, with slightly metal-poor old stellar populations. The East 1, East 2, and North 1 substructures are linked to the LMC disc and show signs of tidal interactions with the MW and the SMC passing over the LMC disc. The southern LMC substructures reveal a complex mix of debris from both Clouds. The SMC East and SMC Northern Over-Density (SMC NOD) substructures primarily consist of SMC debris with minor contributions from the LMC, while the SMC North substructure results from tidal stripping of SMC influenced by the LMC. Low-velocity RGB stars, which are associated with the foreground substructure in the SMC, appear metal-rich relative to their high-velocity counterparts (main-body), suggesting that recent tidal interactions (~250 Myr) stripped these stars from the inner SMC. Thus, the analysis of the substructures confirms several of the previous trends and demonstrates that the observed breaks in the metallicity gradient of the LMC and the SMC are likely due to the mutual interactions between the LMC, SMC, and the Milky Way, which have created the peripheral stellar substructures.

Finally, in Chapters 4 and 5, I focused on the central regions of the Clouds, which present significant observational challenges due to the high density of stars, gas, and dust. Having learned how crucial it is to investigate interaction imprints in the outskirts, it is equally important to understand how interactions between the Clouds and the Galaxy have influenced their gravitationally-bound, crowded regions. In Chapter 4, I presented data from the VMCDeep survey (Cioni & *Omkumar et al.*, submitted), which details observations of high-quality deep images covering ~1.77 deg^2 of both Clouds. I performed PSF photometry on 40 multi-epoch J and K$_s$ half-tile images using IRAF DAOPHOT (following the VMC pipeline). Observations were carried out in half-tiles, necessitating the processing of double the number of images. I employed automated fitting per half-tile, after applying homogenisation across paw-prints for each half-tile and combined good-quality images into deep-tile images for band-merged catalogues. Subsequently, I performed PSF photometry on these deep-tile images and generated a band-merged catalogue for this crowded field. A comparison of the VMC dataset with the newly acquired VMCDeep dataset highlights its more homogeneous spatial coverage of the same regions. This improvement enables diverse science cases and demonstrates enhancements in the obtained preliminary results.

In Chapter 5, I probed signatures of bimodality in RC stars within the core using the VMCDeep dataset, previously identified in the SMC outskirts. I accomplished this via PSF photometry, an invaluable tool for determining magnitudes of stars in crowded fields like the centres of the Clouds. From the VMCDeep PSF catalogues presented in Chapter 4, I selected RC stars from the CMD covering the centre of the SMC. After removing foreground contamination, I modelled and subtracted the RGB stars in the selected RC sample. Analysis of the luminosity distribution of RC stars across central segments reveals statistically significant peak separation, unlike prior single/overlapping Gaussian fits, confirming a subtle dual RC population even in high-density regions of the SMC. These results strongly support the origin of this dual RC population from the inner SMC disc (*Omkumar et al.*, in preparation). Thus, VMCDeep observations reveal bimodality in the distance distribution of RC stars, providing clear evidence of complex internal structure even within the SMC's core and extending signatures of LMC-SMC interactions inward.

Together, these findings portray the Clouds as dynamically evolving systems where repeated interactions have left hierarchical imprints, offering direct insight into dwarf galaxy evolution in a cosmological context. They highlight how tidal interaction histories are encoded in metallicity and structure.

6.2 Future prospects

Building upon the significant results presented in this thesis, several promising areas for future research become apparent, each offering the potential to further disentangle the interaction history of the Clouds. By delving into these areas, we can enhance our understanding of not only the Clouds themselves but also the role these interactions play in the broader context of cosmic evolution.

Advances with future *Gaia* datasets

On 15 January 2025, the *Gaia* mission completed the collection of astrometric, photometric, and spectroscopic data for ~2.5 billion sources. On 27 March 2025, the spacecraft was passivated, marking the formal end of its operational phase. The most recent release, DR3, however, encompasses observations spanning only 34 months, whereas *Gaia* DR4, anticipated towards the end of 2026, will release the observations made over the full nominal mission period of 5.5 years (66 months). Compared to DR3, DR4 is expected to yield parallax precision improvements by a factor of $\sqrt{2}$ and proper motion improvements by $2\sqrt{2}$ across all magnitudes, together with enhanced BP/RP spectra and refined photometric passband calibrations (Brown 2025). This will translate into improved astrophysical parameters inferred from photometry and spectra. The *Gaia* DR5 will have the observations over 10.5 years, nearly double the observational baseline of DR4, which will push precision further. The positions, parallaxes, photometry, and radial velocities will improve by a factor of $t^{0.5}$ (~40%), whilst proper motions will advance considerably more rapidly, scaling as $t^{1.5}$, representing a factor of ~2.8 improvement over DR4 (Brown 2025).

Beyond the standard astrometric catalogues, DR4 will provide specialised astrometry for nine crowded sky regions (Gaia Collaboration et al. 2023d), including the central regions of the LMC and SMC. These improvements will help overcome the crowding issues, extend analyses to fainter sources, particularly within the dense central fields, thereby refining our understanding of the Clouds' structure and kinematics.

Metallicity gradients and calibration relations: Integrations with large spectroscopic surveys

Despite the advances presented in this work, certain limitations remain in the synthetic Strömgren metallicity calibrations, particularly about crowding effects in the central region of the Clouds. The positive radial metallicity gradient observed in the centres of the Clouds has yet to be confirmed spectroscopically, due to smaller samples. A recent study by Navabi et al. (2025) reported a tentative positive gradient in the central SMC; however, its origin remains uncertain, whether driven by tidal interactions, radial migration, or stellar crowding.

Looking ahead, the combination of future *Gaia* datasets with the 1001MC survey (Cioni et al. 2019), proposed within the 4MOST consortium (de Jong et al. 2019), aims to provide kinematic and chemical abundance information for nearly half a million stars spanning diverse stellar populations with $G \leq 19.5$ mag across ~1000 deg^2 of the Clouds. These spectroscopic observations will substantially advance our understanding of the chemical enrichment history of the Clouds. Complementing this survey, the MOONS survey (Gonzalez et al. 2020) offers broad wavelength coverage across the optical and near-infrared (0.6–1.8 μm), utilising 1000 fibres over a 25-arcmin field-of-view. Through mosaic observations, MOONS will extensively target the central regions of both the LMC and SMC, providing precise kinematic and chemical abundance measurements in the densest fields.

A further objective is the development of improved metallicity calibrations for younger stellar populations, made possible by the large spectroscopic samples that 4MOST and MOONS will provide. These calibrations will enhance photometric [Fe/H] estimates and aid in bridging the gap between large-scale photometric and spectroscopic studies. Altogether, the continued synergy between major photometric surveys such as *Gaia* and spectroscopic facilities such as 4MOST and MOONS will prove instrumental in refining our picture of the structure, kinematics, chemical evolution, and interaction history of the Clouds.

Spectroscopic follow-up to study extremely metal-poor stars

Extremely metal-poor (EMP) stars ($-4 \leq$ [Fe/H] < -2.8 dex), having formed from gas, enriched by the first (metal-free) stars, are probes for studying initial conditions of star formation and hence considered as unique tracers of chemical enrichment in the early universe (Bonifacio et al. 2025). In the MW, EMPs exhibit a wide range of chemical properties, often enhanced in carbon or other α-elements such as Mg and Ca, and neutron-capture elements, which allows detailed studies of nucleosynthesis processes, early star formation, and Galactic assembly (Lucey et al. 2023; Karinkuzhi et al. 2021; Sneden et al. 2023 and references therein). In dwarf galaxies, EMPs are typically α-poor, likely due to slower or bursty star formation and show little or no carbon enhancement, suggesting different early enrichment pathways, with simulations further indicating that

r-process-enhanced stars form in systematically different environments in low- versus high-mass galaxies (Bonifacio et al. 2025; Hirai et al. 2025).

In this context, it is highly essential to study EMP stars in external and/or dwarf galaxies. EMPs in the Clouds remain extremely rare, only 11 spectroscopically confirmed EMPs, all in the LMC, and none yet in the SMC (Oh et al. 2024; Chiti et al. 2024), despite the SMC being less massive and more metal-poor on average. We therefore proposed a medium-resolution ($R \sim 20{,}000$) spectroscopic follow-up of four metal-poor candidates in the SMC using the GHOST spectrograph on Gemini-S, selected from the Strömgren metallicity catalogues of the Clouds (Omkumar et al. 2025). This and follow-up observations with larger sample will yield spectroscopic [Fe/H] measurements accurate to ~ 0.2 dex, help expand the small number of spectroscopically confirmed metal-poor stars in the SMC, thereby constraining early chemical enrichment in a low-mass external galaxy.

Future follow-up of substructure analysis

In the kinematic analysis presented in Chapter 2, *Gaia* proper motions were employed to compare the on-sky motions of the substructures with those of the Clouds; however, internal kinematics were not removed prior to this comparison. Future work will address this by either exploiting existing proper motion maps (e.g., Dhanush et al. 2024, 2025), or by following established methods (Niederhofer et al. 2021a, 2022b; Vijayasree et al. 2025a) to estimate the centre-of-mass motion as a function of position. Subtracting this from the observed proper motions will yield residual fields for both the Clouds and the substructures, facilitating a more direct dynamical comparison.

A natural extension is to progress from projected motions to full 3D phase-space information, combining *Gaia* tangential velocities with radial velocities from forthcoming spectroscopic facilities. This will enable a clearer distinction between bound components and tidally stripped material.

3D characterisation of RC substructure

To fully elucidate the origin of the RC substructure, a comprehensive 3D characterisation utilising proper motions and radial velocities is essential, and future facilities will be pivotal in advancing this work. In addition to standard *Gaia* observations, full Sky Mapper images covering $\sim$1.6 deg^2 of the central SMC were recorded, with a dedicated software pipeline exploiting these Service Interface Function images to enhance source recovery in this crowded region (Gaia Collaboration et al. 2023d). This will be complemented by the Euclid Wide Survey (Euclid Collaboration et al. 2024) and the Roman Space Telescope. Together, MOONS (Gonzalez et al. 2020) and 1001MC (Cioni et al. 2019) surveys will enable the first full 6D chemo-dynamical characterisation of these substructures, offering definitive constraints on their formation mechanisms and the interaction history of the Clouds.

Bibliography

Abadi, M. G., Moore, B., & Bower, R. G. 1999, MNRAS, 308, 947

Abbott, T. M. C., Abdalla, F. B., Allam, S., et al. 2018, ApJS, 239, 18

Abdurro'uf, Accetta, K., Aerts, C., et al. 2022, ApJS, 259, 35

Agertz, O., Teyssier, R., & Moore, B. 2011, MNRAS, 410, 1391

Almeida, A., Majewski, S. R., Nidever, D. L., et al. 2024, MNRAS, 529, 3858

Andrae, R., Rix, H.-W., & Chandra, V. 2023, ApJS, 267, 8

Annibali, F., Beccari, G., Bellazzini, M., et al. 2020, MNRAS, 491, 5101

Arnaboldi, M., Dietrich, J., Hatziminaoglou, E., et al. 2008, The Messenger, 134, 42

Árnadóttir, A. S., Feltzing, S., & Lundström, I. 2010, A&A, 521, A40

Bagheri, G., Cioni, M. R. L., & Napiwotzki, R. 2013, A&A, 551, A78

Battaglia, G., Taibi, S., Thomas, G. F., & Fritz, T. K. 2022, A&A, 657, A54

Bekki, K. 2009, MNRAS, 393, L60

Bekki, K., Couch, W. J., & Shioya, Y. 2002, ApJ, 577, 651

Bellazzini, M., Massari, D., De Angeli, F., et al. 2023, A&A, 674, A194

Bellazzini, M., Oosterloo, T., Fraternali, F., & Beccari, G. 2013, A&A, 559, L11

Belokurov, V., Erkal, D., Deason, A. J., et al. 2017, MNRAS, 466, 4711

Belokurov, V. A. & Erkal, D. 2019a, MNRAS, 482, L9

Belokurov, V. A. & Erkal, D. 2019b, MNRAS, 482, L9

Bertin, E., Mellier, Y., Radovich, M., et al. 2002, in Astronomical Society of the Pacific Conference Series, Vol. 281, Astronomical Data Analysis Software and Systems XI, ed. D. A. Bohlender, D. Durand, & T. H. Handley, 228

Besla, G., Hernquist, L., & Loeb, A. 2013, MNRAS, 428, 2342

Besla, G., Kallivayalil, N., Hernquist, L., et al. 2007, ApJ, 668, 949

Besla, G., Kallivayalil, N., Hernquist, L., et al. 2012, MNRAS, 421, 2109

Bica, E., Westera, P., Kerber, L. d. O., et al. 2020, AJ, 159, 82

Blumenthal, G. R., Faber, S. M., Primack, J. R., & Rees, M. J. 1984, Nature, 311, 517

Bonifacio, P., Caffau, E., François, P., & Spite, M. 2025, A&A Rev., 33, 2

Boyce, H., Lützgendorf, N., van der Marel, R. P., et al. 2017, ApJ, 846, 14

Brown, A. G. A. 2025, arXiv e-prints, arXiv:2503.01533

Brown, W., Patton, D. R., Ellison, S. L., & Faria, L. 2023, MNRAS, 522, 5107

Bullock, J. S. & Johnston, K. V. 2005, ApJ, 635, 931

Bullock, J. S., Kravtsov, A. V., & Weinberg, D. H. 2001, ApJ, 548, 33

Byrne-Mamahit, S., Hani, M. H., Ellison, S. L., Quai, S., & Patton, D. R. 2023, MNRAS, 519, 4966

Calamida, A., Bono, G., Stetson, P. B., et al. 2007, ApJ, 670, 400

Cannon, R. D. 1970, MNRAS, 150, 111

Cao, C., Xu, C. K., Domingue, D., et al. 2016, ApJS, 222, 16

Cardelli, J. A., Clayton, G. C., & Mathis, J. S. 1989, ApJ, 345, 245

Carlson, L. R., Sewiło, M., Meixner, M., Romita, K. A., & Lawton, B. 2012, A&A, 542, A66

Carrera, R., Conn, B. C., Noël, N. E. D., Read, J. I., & López Sánchez, Á. R. 2017, MNRAS, 471, 4571

Carrera, R., Gallart, C., Aparicio, A., et al. 2008, AJ, 136, 1039

Chandra, V., Naidu, R. P., Conroy, C., et al. 2023, ApJ, 956, 110

Chauhan, R., Subramanian, S., Kudari, D. A., Amrutha, S., & Das, M. 2025, A&A, 702, A222

Cheng, X., Choi, Y., Olsen, K., et al. 2022, ApJ, 928, 95

Chiti, A., Mardini, M., Limberg, G., et al. 2024, Nature Astronomy, 8, 637

Choi, Y., Nidever, D. L., Olsen, K., et al. 2018a, ApJ, 866, 90

Choi, Y., Nidever, D. L., Olsen, K., et al. 2018b, ApJ, 866, 90

Choi, Y., Olsen, K. A. G., Besla, G., et al. 2022, ApJ, 927, 153

Choudhury, S., de Grijs, R., Bekki, K., et al. 2021, MNRAS, 507, 4752

Choudhury, S., de Grijs, R., Rubele, S., et al. 2020, MNRAS, 497, 3746

Choudhury, S., Subramaniam, A., & Cole, A. A. 2016a, MNRAS, 455, 1855

Choudhury, S., Subramaniam, A., & Cole, A. A. 2016b, MNRAS, 455, 1855

Choudhury, S., Subramaniam, A., Cole, A. A., & Sohn, Y. J. 2018, MNRAS, 475, 4279

Cioni, M. . R. L., Storm, J., Bell, C. P. M., et al. 2019, The Messenger, 175, 54

Cioni, M. R. L. 2009, A&A, 506, 1137

Cioni, M. R. L., Clementini, G., Girardi, L., et al. 2011, A&A, 527, A116

Cioni, M.-R. L., Cross, N. J. G., Ripepi, V., et al. 2025, A&A, 699, A300

Cioni, M. R. L., Habing, H. J., & Israel, F. P. 2000, A&A, 358, L9

Cohen, R. E., McQuinn, K. B. W., Murray, C. E., et al. 2024a, ApJ, 975, 43

Cohen, R. E., McQuinn, K. B. W., Murray, C. E., et al. 2024b, ApJ, 975, 42

Cooper, A. P., Cole, S., Frenk, C. S., et al. 2010, MNRAS, 406, 744

Cordoni, G., Marino, A. F., Milone, A. P., et al. 2023, A&A, 678, A155

Crawford, D. L. & Mandwewala, N. 1976, PASP, 88, 917

Cross, N. J. G., Collins, R. S., Mann, R. G., et al. 2012, A&A, 548, A119

Cullinane, L. R., Mackey, A. D., Da Costa, G. S., et al. 2022a, MNRAS, 510, 445

Cullinane, L. R., Mackey, A. D., Da Costa, G. S., et al. 2022b, MNRAS, 512, 4798

Cullinane, L. R., Mackey, A. D., Da Costa, G. S., Koposov, S. E., & Erkal, D. 2023, MNRAS, 518, L25

Dalton, G. B., Caldwell, M., Ward, A. K., et al. 2006, in Society of Photo-Optical Instrumentation Engineers (SPIE) Conference Series, Vol. 6269, Society of Photo-Optical Instrumentation Engineers (SPIE) Conference Series, ed. I. S. McLean & M. Iye, 62690X

De Angeli, F., Weiler, M., Montegriffo, P., et al. 2023, A&A, 674, A2

De Bortoli, B. J., Parisi, M. C., Bassino, L. P., et al. 2022, A&A, 664, A168

de Grijs, R. & Bono, G. 2015a, AJ, 149, 179

de Grijs, R. & Bono, G. 2015b, AJ, 149, 179

de Grijs, R., Wicker, J. E., & Bono, G. 2014a, AJ, 147, 122

de Grijs, R., Wicker, J. E., & Bono, G. 2014b, AJ, 147, 122

de Jong, R. S., Agertz, O., Berbel, A. A., et al. 2019, The Messenger, 175, 3

De Leo, M., Carrera, R., Noël, N. E. D., et al. 2020, MNRAS, 495, 98

De Leo, M., Read, J. I., Noël, N. E. D., et al. 2024, MNRAS, 535, 1015

de los Reyes, M. 2023, Physics Online Journal, 16, 152

de Vaucouleurs, G. 1955, AJ, 60, 126

de Vaucouleurs, G. 1959, Handbuch der Physik, 53, 275

Deason, A. J., Belokurov, V., Erkal, D., Koposov, S. E., & Mackey, D. 2017, MNRAS, 467, 2636

Dennefeld, M. 2020, The Messenger, 181, 37

Dhanush, S. R., Subramaniam, A., & Subramanian, S. 2024, ApJ, 968, 103

Dhanush, S. R., Subramaniam, A., & Subramanian, S. 2025, ApJ, 980, 73

Dias, B., Angelo, M. S., Oliveira, R. A. P., et al. 2021, A&A, 647, L9

Dias, B., Parisi, M. C., Angelo, M., et al. 2022, MNRAS, 512, 4334

Diaz, J. D. & Bekki, K. 2012, ApJ, 750, 36

Dobbie, P. D., Cole, A. A., Subramaniam, A., & Keller, S. 2014a, MNRAS, 442, 1663

Dobbie, P. D., Cole, A. A., Subramaniam, A., & Keller, S. 2014b, MNRAS, 442, 1680

D'Onghia, E. & Lake, G. 2008, ApJ, 686, L61

Drlica-Wagner, A., Bechtol, K., Allam, S., et al. 2016, ApJ, 833, L5

Dubois, Y., Beckmann, R., Bournaud, F., et al. 2021, A&A, 651, A109

El Youssoufi, D., Cioni, M.-R. L., Bell, C. P. M., et al. 2021, MNRAS

El Youssoufi, D., Cioni, M.-R. L., Bell, C. P. M., et al. 2019, MNRAS, 490, 1076

Ellison, S. L., Patton, D. R., Simard, L., et al. 2010, MNRAS, 407, 1514

El Youssoufi, D., Cioni, M.-R. L., Bell, C. P. M., et al. 2019, MNRAS, 490, 1076

Eneev, T. M., Kozlov, N. N., & Sunyaev, R. A. 1973, A&A, 22, 41

Erkal, D., Belokurov, V., Laporte, C. F. P., et al. 2019, MNRAS, 487, 2685

Euclid Collaboration, Mellier, Y., Abdurro'uf, et al. 2024, arXiv e-prints, arXiv:2405.13491

Fakhouri, O., Ma, C.-P., & Boylan-Kolchin, M. 2010, MNRAS, 406, 2267

Fall, S. M. & Efstathiou, G. 1980, MNRAS, 193, 189

Feast, M. W., Abedigamba, O. P., & Whitelock, P. A. 2010, MNRAS, 408, L76

Ferreras, I., Trujillo, I., Mármol-Queraltó, E., et al. 2014, MNRAS, 444, 906

Fontana, A., Salimbeni, S., Grazian, A., et al. 2006, A&A, 459, 745

Frankel, N., Andrae, R., Rix, H.-W., Povick, J., & Chandra, V. 2024, arXiv e-prints, arXiv:2403.08516

Gaia Collaboration, Brown, A. G. A., Vallenari, A., et al. 2018a, A&A, 616, A1

Gaia Collaboration, Brown, A. G. A., Vallenari, A., et al. 2021a, A&A, 649, A1

Gaia Collaboration, Brown, A. G. A., Vallenari, A., et al. 2016a, A&A, 595, A2

Gaia Collaboration, Helmi, A., van Leeuwen, F., et al. 2018b, A&A, 616, A12

Gaia Collaboration, Luri, X., Chemin, L., et al. 2021b, A&A, 649, A7

Gaia Collaboration, Montegriffo, P., Bellazzini, M., et al. 2023a, A&A, 674, A33

Gaia Collaboration, Montegriffo, P., Bellazzini, M., De Angeli, F., & et al. 2022, A&A

Gaia Collaboration, Prusti, T., de Bruijne, J. H. J., et al. 2016b, A&A, 595, A1

Gaia Collaboration, Vallenari, A., Brown, A. G. A., et al. 2023b, A&A, 674, A1

Gaia Collaboration, Weingrill, K., Mints, A., et al. 2023c, A&A, 680, A35

Gaia Collaboration, Weingrill, K., Mints, A., et al. 2023d, A&A, 680, A35

Gatto, M., Ripepi, V., Bellazzini, M., et al. 2024, A&A, 690, A164

Girardi, L. 2016, ARA&A, 54, 95

Girardi, L. & Salaris, M. 2001, MNRAS, 323, 109

Gonzalez, O. A., Mucciarelli, A., Origlia, L., et al. 2020, The Messenger, 180, 18

González-Fernández, C., Hodgkin, S. T., Irwin, M. J., et al. 2018a, MNRAS, 474, 5459

González-Fernández, C., Hodgkin, S. T., Irwin, M. J., et al. 2018b, MNRAS, 474, 5459

Grady, J., Belokurov, V., & Evans, N. W. 2021, ApJ, 909, 150

Grebel, E. K. 1997, Reviews in Modern Astronomy, 10, 29

Grebel, E. K. & Richtler, T. 1992, A&A, 253, 359

Gunn, J. E. & Gott, III, J. R. 1972, ApJ, 176, 1

Hammer, F., Yang, Y. B., Flores, H., Puech, M., & Fouquet, S. 2015, ApJ, 813, 110

Han, J. J., El-Badry, K., Lucchini, S., et al. 2025, ApJ, 982, 188

Harris, J. 2007, ApJ, 658, 345

Haschke, R., Grebel, E. K., Duffau, S., & Jin, S. 2012, AJ, 143, 48

Hatzidimitriou, D., Cannon, R. D., & Hawkins, M. R. S. 1993, MNRAS, 261, 873

Hatzidimitriou, D. & Hawkins, M. R. S. 1989, MNRAS, 241, 667

Helmi, A. 2020, ARA&A, 58, 205

Hernquist, L. 1989, Nature, 340, 687

Herschel, Sir, J. F. W. 1847, Results of astronomical observations made during the years 1834, 5, 6, 7, 8, at the Cape of Good Hope; being the completion of a telescopic survey of the whole surface of the visible heavens, commenced in 1825

Higgs, C. R. & McConnachie, A. W. 2021, MNRAS, 506, 2766

Hilker, M. 2000, A&A, 355, 994

Hindman, J. V., Kerr, F. J., & McGee, R. X. 1963, Australian Journal of Physics, 16, 570

Hirai, Y., Beers, T. C., Lee, Y. S., et al. 2025, ApJ, 990, 125

Hopkins, P. F., Cox, T. J., Hernquist, L., et al. 2013, MNRAS, 430, 1901

Hopp, U., Schulte-Ladbeck, R. E., & Kerp, J. 2003, MNRAS, 339, 33

Hubble, E. P. 1926, ApJ, 64, 321

Hubble, E. P. 1936, Realm of the Nebulae

Hughes, J., Wallerstein, G., Dotter, A., & Geisler, D. 2014, MNRAS, 439, 788

Irwin, M. J., Kunkel, W. E., & Demers, S. 1985, Nature, 318, 160

Irwin, M. J., Lewis, J., Hodgkin, S., et al. 2004, in Society of Photo-Optical Instrumentation Engineers (SPIE) Conference Series, Vol. 5493, Optimizing Scientific Return for Astronomy through Information Technologies, ed. P. J. Quinn & A. Bridger, 411–422

Jacyszyn-Dobrzeniecka, A. M., Mróz, P., Kruszyńska, K., et al. 2020a, ApJ, 889, 26

Jacyszyn-Dobrzeniecka, A. M., Mróz, P., Kruszyńska, K., et al. 2020b, ApJ, 889, 26

Jacyszyn-Dobrzeniecka, A. M., Skowron, D. M., Mróz, P., et al. 2016, Acta Astron., 66, 149

Jacyszyn-Dobrzeniecka, A. M., Skowron, D. M., Mróz, P., et al. 2017a, Acta Astron., 67, 1

Jacyszyn-Dobrzeniecka, A. M., Skowron, D. M., Mróz, P., et al. 2017b, Acta Astron., 67, 1

James, D., Subramanian, S., Omkumar, A. O., et al. 2021, MNRAS, 508, 5854

Jiménez-Arranz, Ó., Roca-Fàbrega, S., Romero-Gómez, M., et al. 2024, A&A, 688, A51

Jiménez-Arranz, Ó., Romero-Gómez, M., Luri, X., et al. 2023, A&A, 669, A91

Kado-Fong, E., Greene, J. E., Greco, J. P., et al. 2020, AJ, 159, 103

Kado-Fong, E., Robinson, A., Nyland, K., et al. 2024, ApJ, 963, 37

Kallivayalil, N., Sales, L. V., Zivick, P., et al. 2018, ApJ, 867, 19

Kallivayalil, N., van der Marel, R. P., Alcock, C., et al. 2006, ApJ, 638, 772

Kallivayalil, N., Van der Marel, R. P., Besla, G., Anderson, J., & Alcock, C. 2013, ApJ, 764, 161

Karachentsev, I. D., Makarov, D. I., & Kaisina, E. I. 2013, AJ, 145, 101

Karinkuzhi, D., Van Eck, S., Goriely, S., et al. 2021, A&A, 645, A61

Kim, S., Staveley-Smith, L., Dopita, M. A., et al. 1998, ApJ, 503, 674

Koda, J., Yagi, M., Yamanoi, H., & Komiyama, Y. 2015, ApJ, 807, L2

Koposov, S. E., Belokurov, V., Torrealba, G., & Evans, N. W. 2015, ApJ, 805, 130

Kormendy, J. & Kennicutt, Jr., R. C. 2004, ARA&A, 42, 603

Krishnarao, D., Fox, A. J., D'Onghia, E., et al. 2022, Nature, 609, 915

Larson, R. B., Tinsley, B. M., & Caldwell, C. N. 1980, ApJ, 237, 692

Lelli, F., Verheijen, M., & Fraternali, F. 2014, MNRAS, 445, 1694

Li, Y., Jiang, B., & Ren, Y. 2024, AJ, 167, 123

Lucchini, S. 2024, Ap&SS, 369, 114

Lucchini, S., D'Onghia, E., & Fox, A. J. 2021, ApJ, 921, L36

Lucchini, S., D'Onghia, E., Fox, A. J., et al. 2020, Nature, 585, 203

Lucey, M., Al Kharusi, N., Hawkins, K., et al. 2023, MNRAS, 523, 4049

Luks, T. & Rohlfs, K. 1992, A&A, 263, 41

Lynden-Bell, D. 1967, MNRAS, 136, 101

Mackey, A. D., Koposov, S. E., Da Costa, G. S., et al. 2017, MNRAS, 472, 2975

Mackey, A. D., Koposov, S. E., Erkal, D., et al. 2016, MNRAS, 459, 239

Mackey, D., Koposov, S., Da Costa, G., et al. 2018, ApJ, 858, L21

Majewski, S. R., Schiavon, R. P., Frinchaboy, P. M., et al. 2017, AJ, 154, 94

Marasco, A., Belfiore, F., Cresci, G., et al. 2023, A&A, 670, A92

Martin, G., Jackson, R. A., Kaviraj, S., et al. 2021, MNRAS, 500, 4937

Martínez-Delgado, D., Vivas, A. K., Grebel, E. K., et al. 2019, A&A, 631, A98

Massana, P., Nidever, D. L., & Olsen, K. 2023, MNRAS, 527, 8706

Massana, P., Noël, N. E. D., Nidever, D. L., et al. 2020, MNRAS, 498, 1034

Massana, P., Ruiz-Lara, T., Noël, N. E. D., et al. 2022, MNRAS, 513, L40

Masters, K. 2025, arXiv e-prints, arXiv:2502.09610

Mathewson, D. S., Cleary, M. N., & Murray, J. D. 1974, ApJ, 190, 291

Mazzi, A., Girardi, L., Zaggia, S., et al. 2021, MNRAS, 508, 245

McCarthy, I. G., Frenk, C. S., Font, A. S., et al. 2008, MNRAS, 383, 593

McClure-Griffiths, N. M., Dénes, H., Dickey, J. M., et al. 2018, Nature Astronomy, 2, 901

McConnachie, A. W. 2012, AJ, 144, 4

McMahon, R. G., Banerji, M., Gonzalez, E., et al. 2013, The Messenger, 154, 35

McNamara, D. H., Clementini, G., & Marconi, M. 2007, AJ, 133, 2752

McWilliam, A. 1997, ARA&A, 35, 503

Mellinger, A. 2009, PASP, 121, 1180

Merloni, A., Lamer, G., Liu, T., et al. 2024, A&A, 682, A34

Miller, A. E., Slepian, Z., Lada, E. A., et al. 2026, MNRAS, 546, stag081

Mishra, S., Fox, A. J., Krishnarao, D., et al. 2024, ApJ, 976, L28

Mishra, S., Fox, A. J., Smoker, J. V., Lucchini, S., & D'Onghia, E. 2025, ApJ, 984, 104

Moore, B. & Davis, M. 1994, MNRAS, 270, 209

Moore, B., Katz, N., Lake, G., Dressler, A., & Oemler, A. 1996, Nature, 379, 613

Morelli, A. P. M., Kerp, J., Gupta, N., et al. 2025, A&A, 702, L11

Muñoz, C., Monachesi, A., Nidever, D. L., et al. 2023, A&A, 680, A79

Muraveva, T., Subramanian, S., Clementini, G., et al. 2017, MNRAS, 473, 3131

Naab, T. & Ostriker, J. P. 2017, ARA&A, 55, 59

Narloch, W., Pietrzyński, G., Gieren, W., et al. 2021, A&A, 647, A135

Narloch, W., Pietrzyński, G., Gieren, W., et al. 2022, A&A, 666, A80

Navabi, M., Carrera, R., Noël, N. E. D., & De Leo, M. 2025, MNRAS, 544, 3980

Navarrete, C., Aguado, D. S., Belokurov, V., et al. 2023, arXiv e-prints, arXiv:2302.04579

Nidever, D. L., Majewski, S. R., Butler Burton, W., & Nigra, L. 2010, ApJ, 723, 1618

Nidever, D. L., Majewski, S. R., Muñoz, R. R., et al. 2011, ApJ, 733, L10

Nidever, D. L., Monachesi, A., Bell, E. F., et al. 2013, ApJ, 779, 145

Nidever, D. L., Olsen, K., Walker, A. R., et al. 2017a, AJ, 154, 199

Nidever, D. L., Olsen, K., Walker, A. R., et al. 2017b, AJ, 154, 199

Nidever, D. L., Price-Whelan, A. M., Choi, Y., et al. 2019, ApJ, 887, 115

Niederhofer, F., Cioni, M. R. L., Rubele, S., et al. 2018, A&A, 613, L8

Niederhofer, F., Cioni, M.-R. L., Rubele, S., et al. 2021a, MNRAS, 502, 2859

Niederhofer, F., Cioni, M.-R. L., Rubele, S., et al. 2021b, MNRAS, 502, 2859

Niederhofer, F., Cioni, M.-R. L., Schmidt, T., et al. 2022a, MNRAS, 512, 5423, (Paper XLVI)

Niederhofer, F., Cioni, M.-R. L., Schmidt, T., et al. 2022b, MNRAS, 512, 5423

Noël, N. E. D., Conn, B. C., Carrera, R., et al. 2013, ApJ, 768, 109

Noël, N. E. D., Conn, B. C., Read, J. I., et al. 2015, MNRAS, 452, 4222

Oden, S. J., Nidever, D. L., Povick, J., et al. 2025, arXiv e-prints, arXiv:2512.04200

Oh, W. S., Nordlander, T., Da Costa, G. S., Bessell, M. S., & Mackey, A. D. 2024, MNRAS, 528, 1065

Oliveira, R. A. P., Maia, F. F. S., Barbuy, B., et al. 2023, MNRAS, 524, 2244

Oliveira, R. A. P., Maia, F. F. S., Barbuy, B., et al. 2023, MNRAS, 524, 2244

Olsen, K. A. G. & Salyk, C. 2002, AJ, 124, 2045

Olsen, K. A. G., Zaritsky, D., Blum, R. D., Boyer, M. L., & Gordon, K. D. 2011, ApJ, 737, 29

Omkumar, A. O., Cioni, M.-R. L., Subramanian, S., et al. 2025, A&A, 700, A74

Omkumar, A. O., Subramanian, S., Niederhofer, F., et al. 2021, MNRAS, 500, 2757

Pardy, S. A., D'Onghia, E., Athanassoula, E., Wilcots, E. M., & Sheth, K. 2016, ApJ, 827, 149

Parisi, M. C., Geisler, D., Carraro, G., et al. 2016, AJ, 152, 58

Parisi, M. C., Gramajo, L. V., Geisler, D., et al. 2022, A&A, 662, A75

Parisi, M. C., Oliveira, R. A. P., Angelo, M. S., et al. 2024, MNRAS, 527, 10632

Piatti, A. E., Pietrzyński, G., Narloch, W., Górski, M., & Graczyk, D. 2019, MNRAS, 483, 4766

Pieres, A., Santiago, B. X., Drlica-Wagner, A., et al. 2017, MNRAS, 468, 1349

Pilgrim, C. 2021a, Journal of Open Source Software, 6, 3859

Pilgrim, C. 2021b, Journal of Open Source Software, 6, 3859

Povick, J., Nidever, D., Hasselquist, S., Hayes, C., & Majewski, S. 2021, in American Astronomical Society Meeting Abstracts, Vol. 53, American Astronomical Society Meeting Abstracts, 156.03

Povick, J. T., Nidever, D. L., Majewski, S. R., et al. 2023a, arXiv e-prints, arXiv:2309.12503

Povick, J. T., Nidever, D. L., Massana, P., et al. 2023b, arXiv e-prints, arXiv:2310.14299

Povick, J. T., Nidever, D. L., Massana, P., et al. 2023c, arXiv e-prints, arXiv:2306.06348

Privon, G. C., Stierwalt, S., Patton, D. R., et al. 2017, ApJ, 846, 74

Putman, M., Gibson, B., Staveley-Smith, L., et al. 1998, Nature, 394, 752

Putman, M. E., Staveley-Smith, L., Freeman, K. C., Gibson, B. K., & Barnes, D. G. 2003, ApJ, 586, 170

Rathore, H., Besla, G., Daniel, K. J., & Beraldo E Silva, L. 2025a, arXiv e-prints, arXiv:2504.16163

Rathore, H., Choi, Y., Olsen, K. A. G., & Besla, G. 2025b, ApJ, 978, 55

Recio-Blanco, A., de Laverny, P., Palicio, P. A., et al. 2023, A&A, 674, A29

Riello, M., De Angeli, F., Evans, D. W., et al. 2021, A&A, 649, A3

Ripepi, V., Cioni, M.-R. L., Moretti, M. I., et al. 2017, MNRAS, 472, 808

Romaniello, M., Arnaboldi, M., Barbieri, M., et al. 2023, The Messenger, 191, 29

Rubele, S., Girardi, L., Kerber, L., et al. 2015, MNRAS, 449, 639

Rubele, S., Pastorelli, G., Girardi, L., et al. 2018a, MNRAS, 478, 5017

Rubele, S., Pastorelli, G., Girardi, L., et al. 2018b, MNRAS, 478, 5017

Ruiz-Dern, L., Babusiaux, C., Arenou, F., Turon, C., & Lallement, R. 2018, A&A, 609, A116

Sakowska, J. D., Martínez-Delgado, D., Pearson, S., et al. 2026, A&A, 707, L1

Sales, L. V., Wang, W., White, S. D. M., & Navarro, J. F. 2013, MNRAS, 428, 573

Salinas, R., Pajkos, M. A., Strader, J., Vivas, A. K., & Contreras Ramos, R. 2016, ApJ, 832, L14

Sandage, A. 1975, in Galaxies and the Universe, ed. A. Sandage, M. Sandage, & J. Kristian, 1

Saroon, S. & Subramanian, S. 2022, A&A, 666, A103

Sawala, T., Scannapieco, C., Maio, U., & White, S. 2010, MNRAS, 402, 1599

Schlafly, E. F. & Finkbeiner, D. P. 2011, ApJ, 737, 103

Schlegel, D. J., Finkbeiner, D. P., & Davis, M. 1998, ApJ, 500, 525

Scowcroft, V., Freedman, W. L., Madore, B. F., et al. 2016, ApJ, 816, 49

Scudder, J. M., Ellison, S. L., Torrey, P., Patton, D. R., & Mendel, J. T. 2012, MNRAS, 426, 549

Sewiło, M., Carlson, L. R., Seale, J. P., et al. 2013, ApJ, 778, 15

Shah, E. A., Kartaltepe, J. S., Magagnoli, C. T., et al. 2022, ApJ, 940, 4

Shapley, H. 1940, Harvard College Observatory Bulletin, 914, 8

Sheng, Y., Ting, Y.-S., & Xue, X.-X. 2025, MNRAS, 544, 2434

Simon, J. D. 2019, ARA&A, 57, 375

Skowron, D. M., Jacyszyn, A. M., Udalski, A., et al. 2014, ApJ, 795, 108

Skowron, D. M., Skowron, J., Udalski, A., et al. 2021, ApJS, 252, 23

Skrutskie, M. F., Cutri, R. M., Stiening, R., et al. 2006, AJ, 131, 1163

Sneden, C., Boesgaard, A. M., Cowan, J. J., et al. 2023, ApJ, 953, 31

Stanimirović, S., Staveley-Smith, L., & Jones, P. A. 2004, ApJ, 604, 176

Stetson, P. B. 1987, PASP, 99, 191

Stierwalt, S., Besla, G., Patton, D., et al. 2015, ApJ, 805, 2

Strateva, I., Ivezić, Ž., Knapp, G. R., et al. 2001, AJ, 122, 1861

Strömgren, B. 1963, QJRAS, 4, 8

Strömgren, B. 1964, Rev. Mod. Phys., 36, 532

Subramaniam, A. & Subramanian, S. 2009, ApJ, 703

Subramanian, S., Mondal, C., & Kalari, V. 2024, A&A, 681, A8

Subramanian, S., Rubele, S., Sun, N.-C., et al. 2017, MNRAS, 467, 2980

Subramanian, S. & Subramaniam, A. 2009, A&A, 496, 399

Subramanian, S. & Subramaniam, A. 2012, ApJ, 744, 128

Sun, N.-C., de Grijs, R., Cioni, M.-R. L., et al. 2018, ApJ, 858, 31

Sutherland, W., Emerson, J., Dalton, G., et al. 2015, A&A, 575, A25

Taibi, S., Battaglia, G., Leaman, R., et al. 2022, A&A, 665, A92

Tatton, B. L., van Loon, J. T., Cioni, M.-R. L., et al. 2021, MNRAS, 504, 2983

Teixeira, G. D. C., Kumar, M. S. N., Smith, L., et al. 2018, A&A, 619, A41

Tepper-García, T., Bland-Hawthorn, J., Pawlowski, M. S., & Fritz, T. K. 2019, MNRAS, 488, 918

Tillaboev, K., Tadjibaev, I., Mamadaliyev, K., et al. 2025, Galaxies, 13, 117

Toomre, A. 1977, in Evolution of Galaxies and Stellar Populations, ed. B. M. Tinsley & R. B. G. Larson, D. Campbell, 401

Toomre, A. & Toomre, J. 1972, ApJ, 178, 623

Tremaine, S. D. 1976, ApJ, 203, 72

Tully, R. B. & Fisher, J. R. 1977, A&A, 54, 661

Tully, R. B., Rizzi, L., Dolphin, A. E., et al. 2006, AJ, 132, 729

Udalski, A., Szymański, M. K., & Szymański, G. 2015, Acta Astron., 65, 1

Urbano, M., Duc, P.-A., Saifollahi, T., et al. 2025, A&A, 700, A104

Valentini, M. & Munari, U. 2010, A&A, 522, A79

van den Bergh, S. 1976, ApJ, 206, 883

van den Bosch, F. C. 2002, MNRAS, 331, 98

van der Marel, R. P., Alves, D. R., Hardy, E., & Suntzeff, N. B. 2002, AJ, 124, 2639

van der Marel, R. P. & Cioni, M.-R. L. 2001a, AJ, 122, 1807

van der Marel, R. P. & Cioni, M.-R. L. 2001b, AJ, 122, 1807

van der Marel, R. P. & Kallivayalil, N. 2014, ApJ, 781, 121

Vasiliev, E. 2024, MNRAS, 527, 437

Venhola, A., Peletier, R., Laurikainen, E., et al. 2019, A&A, 625, A143

Vera-Ciro, C. & Helmi, A. 2013, ApJ, 773, L4

Vijayasree, S., Niederhofer, F., Cioni, M.-R. L., et al. 2025a, A&A, 700, A279

Vijayasree, S., Niederhofer, F., Cioni, M.-R. L., et al. 2025b, A&A, 700, A279

Viswanathan, A., Byström, A., Starkenburg, E., et al. 2024, arXiv e-prints, arXiv:2408.17250

Vogelsberger, M., Genel, S., Springel, V., et al. 2014, MNRAS, 444, 1518

Wagner-Kaiser, R. & Sarajedini, A. 2013, MNRAS, 431, 1565

Wagner-Kaiser, R. & Sarajedini, A. 2017, MNRAS, 466, 4138

Wang, J., Hammer, F., & Yang, Y. 2022, MNRAS, 515, 940

Wang, J., Hammer, F., Yang, Y., et al. 2019, MNRAS, 486, 5907

Weinberg, M. D. 2000, ApJ, 532, 922

Weisz, D. R., Dolphin, A. E., Skillman, E. D., et al. 2013, MNRAS, 431, 364

Wheeler, C., Oñorbe, J., Bullock, J. S., et al. 2015, MNRAS, 453, 1305

Whiting, A. B., Hau, G. K. T., Irwin, M., & Verdugo, M. 2007, AJ, 133, 715

Woods, D. F., Geller, M. J., Kurtz, M. J., et al. 2010, AJ, 139, 1857

Yuxi, Lu, Buck, T., et al. 2023, arXiv e-prints, arXiv:2312.07219

Zaritsky, D., Chandra, V., Conroy, C., et al. 2025, The Open Journal of Astrophysics, 8, 16

Zaritsky, D., Harris, J., Grebel, E. K., & Thompson, I. B. 2000, ApJ, 534, L53

Zasowski, G., Cohen, R. E., Chojnowski, S. D., et al. 2017, AJ, 154, 198

Zivick, P., Kallivayalil, N., van der Marel, R. P., et al. 2018, ApJ, 864, 55

Zivkov, V., Oliveira, J. M., Petr-Gotzens, M. G., et al. 2018, A&A, 620, A143

Zivkov, V., Oliveira, J. M., Petr-Gotzens, M. G., et al. 2020, MNRAS, 494, 458

Publications

I have successfully published 4 refereed journal articles, including 2 as the first author and 2 as a co-author. I am currently preparing 2 first-author manuscripts and 2 co-author manuscript for submission to journals. Additionally, I have made my photometric catalogues publicly available, further contributing to the research community.

Journal Articles

1. **Abinaya O. Omkumar** et al., "Strömgren photometric metallicity map of the Magellanic Cloud stars using Gaia DR3–XP spectra" 2025, A&A 700, A74. DOI:10.1051/0004-6361/202452510. Link
   Presents the homogenous photometric metallicity maps of old (red giant branch) and young (supergiant) stellar stars in the Magellanic Clouds.

2. M.-R. L. Cioni, N. J. G. Cross, V. Ripepi, ... **Abinaya O. Omkumar**, et al., "The VMC survey: LII. Data release #7: Complete survey data and data from additional programmes", 2025 A&A 699, A300. DOI:10.1051/0004-6361/202554254. Link
   Presents the complete VISTA survey data of the Magellanic Clouds. Produced PSF (point spread function) photometry catalogue for a GAP tile in the Small Magellanic Cloud (SMC).

3. Dizna James, Smitha Subramanian, **Abinaya O. Omkumar**, .. et al., "Presence of red giant population in the foreground stellar substructure of the Small Magellanic Cloud", 2021 MNRAS 508.4, pp. 5854–5863. DOI:10.1093/mnras/stab2873. Link
   Discusses the study of dual radial velocity population in front of the SMC and its connection with the dual red clump population. Trained the first author to use the Gaia data and radial velocity data. Performed the analysis in Section 3.2 and co-wrote the analysis and discussion.

4. **Abinaya O. Omkumar** et al., "Gaia view of a stellar sub-structure in front of the Small Magellanic Cloud", 2021 MNRAS 500.3, pp. 2757–2776. DOI:10.1093/mnras/staa3085. Link
   Presents the photometric and kinematic study of the dual red clump population in the SMC.

Conference Proceedings

- **Abinaya O. Omkumar** et al., "Strömgren photometric metallicity map of the Magellanic Cloud stars using Gaia DR3–XP spectra" 2025, Dynamical Masses of

Local Group Galaxies. Ed. by Piercarlo Bonifacio et al. Vol. 379. IAU Symposium, pp. 221–225. DOI:10.1017/S1743921323001400 Link

Public Catalogues

- **Abinaya O. Omkumar** et al., 2025 VizieR Online Data Catalog: Metallicity maps of the Magellanic Clouds (Omkumar+ 2025). VizieR On-line Data Catalog: J/A+A/700/A74. Link
- M.-R. L. Cioni, N. J. G. Cross, V. Ripepi, .. **Abinaya O. Omkumar**, .. et al., "The VMC survey: LII. Data release #7: Complete survey data and data from additional programmes", 2025 VizieR On-line Data Catalog: J/A+A/699/A300. Link

Statement of own contribution

This thesis is the result of my own work and includes nothing which is the outcome of work done in collaboration except as declared and specified as follows:

- Chapter 2 has been published under the title “Strömgren photometric metallicity map of the Magellanic Cloud stars using Gaia DR3–XP spectra” 2025, in the Astronomy & Astrophysics journal, 700, A74.
  Authors:
  As the lead author of this paper, I conducted the research presented in this paper and wrote the entire manuscript.
- Chapter 3 is based on the work titled "Deep VISTA observations of the Magellanic Clouds (VMCDeep)" submitted to the Astronomy & Astrophysics for publication and is currently under review.
  Authors: As the second author of this manuscript, I have performed the photometry based on the Point Spread Catalogues for all the high- and low-quality data for both J and Ks bands and is used by the VMC team for various science cases. To introduce the dataset and establish the potential, this has been included as a chapter in this thesis.

It is not substantially the same as any that I have submitted, or am concurrently submitting, for a degree, diploma, or other qualification at the University of Potsdam or any other university or similar institution except as declared here in the specified text. I confirm that the above statements are true and complete to the best of my knowledge.

Potsdam, March 2026

Abinaya Ondivillu Omkumar

Acknowledgements

My PhD has been anything but straightforward, and reaching this point is not possible with just my own perseverance, but to the many wonderful people who walked alongside me. I am fortunate and grateful beyond words to each one of them.

I am deeply grateful for the opportunity to undertake this PhD and would like to express my sincere thanks to my supervisors, Prof. Dr. Maria-Rosa Cioni and Dr. Smitha Subramanian, for your trust and support throughout this journey. The countless discussions we shared throughout the development of this work have been invaluable, and your guidance proved instrumental in seeing this PhD through to its successful completion. Smitha, thank you for always believing in me, from the very first day I arrived as a visiting student right through to this moment; this journey was not an easy one, and during the most difficult times, your kindness and encouragement helped me a lot.

I am immensely grateful to the International Office of the University of Potsdam and the DAAD for providing financial support through the completion scholarship, which made it possible for me to extend my visa, stay in Germany, and dedicate myself fully to completing this thesis. I would also like to thank the Welcome Centre of the University of Potsdam, whose support made navigating life and bureaucracy here as an international student, much more manageable.

I would like to thank all members of the DGGH for fostering a warm working atmosphere, and the members of the MWLV group for generously sharing your expertise during our joint group meetings. A special thank you to Florian, Nikolay, and Alexey for always being so approachable and helpful. A special thanks to Florian for helping with the German abstract for this thesis. I am glad to have been part of the VMC team and thank all its members for their support, in particular Francesca, whose dedication during the frequent meetings over zoom was greatly appreciated. I am also thankful to have shared my office with Bridget and Sergey for their kindness and support, and to Marica for her guidance and encouragement throughout.

Amba and *Baaba*, no words could ever truly capture the depth of my gratitude for all your sacrifices, your hard work, and the support you have given me in pursuing my education and my dreams. Sriram, though you are my younger brother, you have taught me more, thank you for sharing so many responsibilities, so that I could keep moving forward. This journey would have been impossible without the love and support of you and my extended family. Ramya *Bei*, I am who I am because of your love and sisterhood. You have always believed in me, even when I struggled to believe in myself, and for that I am eternally grateful.

There are certain people in life whose goodness simply cannot be measured, and I feel truly fortunate to have met some. Saraswathi, Erasmo, and Shreevathsa, no words would ever do justice to how deeply thankful and grateful I am to each of you, and I hope you

know how much your company means to me. Your constant support has given me the strength to smile through the difficult days and keep going, one step at a time, until I finally arrived here, with a completed thesis in hand.

Spending time with like-minded people is truly one of life's greatest gifts, and I feel so glad to have found that in Azlizan, Mariana, Léa, and Léna. Every lunch, dinner, movie evening, and art evening we shared became a source of comfort during the more challenging moments of this PhD. Good food and genuine laughter have a way of making everything feel lighter, thank you all for bringing both into my life so generously.

One of the upsides of splitting my PhD time between Germany and India has been the remarkable people I have had the privilege of meeting along the way, those who were generous with their time and kindness, and always willing to engage in meaningful scientific discussions. I am truly glad to have met Renu, Saili, Shashank, and Rakshit. The group meetings and lunches we shared remain some of my most cherished memories. I am equally grateful to Akhil, Parvathy, Payel, Sipra, Sowmyaranjan, Neeraj, and everyone else who made my time in Bengaluru so warm and memorable. A very warm regard to the Director of IIA, Prof. Dr. Annapurni Subramaniam, from whom I have learnt enormously. Your kindness and the way you inspire those around you have left a lasting impression on me. To those I had the pleasure of getting to know during my time in Germany, Martina, Özgün, Sreepriya, Ruchi, Amy, Ranjith, Desmond, Sabela and Judy, I cherish all the wonderful times we shared.

I have also been incredibly fortunate to have friends who never let the distance or the time differences stand in the way, Ruthra, Sabari, Kavya, Keerthana, AK, Raza, Sathya, and Vishnu, your friendship and encouragement have meant the world to me. Ritu, thank you for opening your home to me, I will always treasure our dates, cooking sessions and late-night conversations that stretched well past midnight. Rike, thank you for being there in the very beginning, helping me settle in and making me feel so welcome, I always enjoyed our conversations and I miss your cakes more than I can say!

I would also like to acknowledge the ESA fellowship that gave me the wonderful opportunity to visit ESA and collaborate on a fascinating project, it was an experience I thoroughly enjoyed and learnt a lot. I gratefully acknowledge the Archival Research Visitor Programme for providing the necessary funding that made this possible. A warm thank you to Jos and Guido for all your support during my time there.

I would also like to thank EDUC for funding and organising the PhD retreat, which brought together doctoral students from a wide range of disciplines to share and learn from one another's experiences. Alain and Eva, thank you for a great company.

Finally, but most importantly, I dedicate this thesis to my beloved grandmother. Though I lost her before I could share this exciting journey with her, I carry her love and courage with me in everything I do.